Zeeman Splitting Caused by Localized sp-d Exchange Interaction in Ferromagnetic GaMnAs Observed by Magneto-Optical Characterization

A dissertation presented to

the faculty of

the Russ College of Engineering and Technology of Ohio University

In partial fulfillment

of the requirements for the degree

Doctor of Philosophy

Hiroki Tanaka

December 2015

This dissertation titled

Zeeman Splitting Caused by Localized sp-d Exchange Interaction in Ferromagnetic GaMnAs Observed by Magneto-Optical Characterization

by

HIROKI TANAKA

has been approved for

the School of Electrical Engineering and Computer Science

and the Russ College of Engineering and Technology by

Wojciech M. Jadwisienczak

Associate Professor of Electrical Engineering and Computer Science

Dennis Irwin

Dean, Russ College of Engineering and Technology

ABSTRACT

TANAKA, HIROKI, Ph.D., December 2015, Electrical Engineering

Zeeman Splitting Caused by Localized sp-d Exchange Interaction in Ferromagnetic GaMnAs Observed by Magneto-Optical Characterization

Director of Dissertation: Wojciech M. Jadwisienczak

The field of spintronics is considered as the next generation of spin-based electronics rather than the flow of charges utilized in electronics. It is expected that it will have some advantages in areas of information storage densities, switching speed, power consumption, manufacturing costs and others. One of the alternatives in developing a successful spintronics materials is the transition metal (TM)-doped III-V diluted magnetic semiconductors (DMSs) and GaMnAs is the proto-type ferromagnetic DMSs. Currently, the origin of ferromagnetism in GaMnAs is not fully clarified yet due to the complexity of an electronic band structure after doping of the Mn into GaAs. However, the magneto-optical characterization, especially, magnetic circular dichroism (MCD), is a very powerful technique to investigate DMS because one can obtain the information of the electronic band structure. Thus, we have performed systematic investigations of the MCD spectra and optical absorption spectra of the $Ga_{1-x}Mn_xAs$ with different concentrations of Mn. In this project, we have conducted the measurement using the transmission-mode MCD, the reflection-mode MCD and the magneto-optical Kerr effect (MOKE) for three different kinds of GaMnAs samples fabricated with the same growth conditions; GaMnAs on sapphire, GaMnAs on InP, and free-standing GaMnAs, respectively. We have successfully estimated the Zeeman splitting energy of both L (E_1 and $E_1+\Delta_1$) and Γ

(E_0 and $E_0+\Delta_0$) critical points (CPs) for these materials. We utilized an energy derivative of the Gaussian function to decompose the MCD spectrum into the impurity band (IB) related background and two dispersion components around *L*-CPs which are expected in theory. Then, using the rigid band shift model we calculated the Zeeman splitting energy of E_1 (*L*-CP). The Zeeman splitting energy at E_1 (*L*-CP) was estimated to be larger than ~ 4 meV in $Ga_{0.97}Mn_{0.03}As$ on sapphire, ~ 0.6 meV in $Ga_{0.97}Mn_{0.03}As$ on InP, and ~ 6.5 meV in free-standing $Ga_{0.97}Mn_{0.03}As$ measured at 6 K. To calculate the Zeeman splitting energy at E_0 (Γ-CP), an experimentally reported parameter of a II-VI paramagnetic DMS, $Cd_{1-x}Mn_xTe$, was used due to some similarities of their electronic band structure. The Zeeman splitting energy at E_0 (Γ-CP) of $Ga_{0.97}Mn_{0.03}As$ on sapphire, $Ga_{0.97}Mn_{0.03}As$ on InP, and free-standing $Ga_{0.97}Mn_{0.03}As$ was ~ 64 meV, ~ 9.6, meV and ~ 104 meV at 6 K. In addition, we found that MCD spectra around *L*-critical points shifted toward lower energy whereas the corresponding absorption spectra did not shift toward lower energy with an increase of Mn concentration. These results indicate that the *sp-d* exchange interaction in $Ga_{1-x}Mn_xAs$ has a very localized nature, because MCD is only active in a region where a band structure is affected by Mn spins, and optical absorption results from the overall sample response. This means that the *sp-d* exchange interactions are only generated within the sphere of influence.

DEDICATION

This work is dedicated to my father; Kiyotaka Tanaka, and my mother; Yoshiko Tanaka.

ACKNOWLEDGEMENTS

First of all, I would like to thank my academic advisor, Dr. Wojciech M. Jadwisienczak for giving me the great opportunity to work on his research project and supervising me during both my MA and Ph.D. programs. He has always encouraged and motivated me to work hard. I recognized the support by the National Science Foundation (NSF) CAREER Award under contact No. DMR-1056493 he has offered me during this project. I am sure that everything that I learned from him will be worthwhile for the rest of my engineering career.

Also, I would like to give a very special thanks to Dr. Koji Ando and Dr. Hidekazu Saito working at the semiconductor spintronics team in Advanced Industrial Science and Technology (AIST) in Tsukuba Japan. Without their kind support, I could not finish up my research project. Furthermore, I acknowledge other AIST members and staffs who kindly supported me during my visiting at AIST.

Moreover, I express my appreciation to Dr. Savas Kaya, Dr. Faiz Rahman, Dr. Kodi, Avinash, Dr. Arthur Smith and Dr. Marty Kordesch for serving as my committee and giving me critical suggestions for my research and dissertation. In addition, I appreciate the encouragement from my great friends, Jingzhou Wang, and Mohammed Bsatee during my Ph.D. program at Ohio University. I would also like to recognize the Chubu University in Japan for giving me an opportunity to study at Ohio University.

Finally, I would like to thank my family and especially my parents for giving me unlimited love and support throughout my life.

TABLE OF CONTENTS

Page

LIST OF TABLES

Page

LIST OF FIGURES

Page

1. INTRODUCTION

1.1 Motivation for this project

Over the past 65 years, electronic technology has been remarkably revolutionized. This period of time until now commonly recognized as silicon technology or the microelectronics era, was based on digital logic devices using electrons. In 1947, William B. Shockley, John Bardeen, and Walter H. Brattain invented the first practical transistor which was a "*PNP point-contact germanium transistor*" [1]–[4]. Since then, the conventional microelectronics technology has drastically improved to achieve a higher performance, faster speed, smaller architectures, lower energy compunctions, and cheaper fabrications as predicted by Moore's Law [5]. However, when the size of the transistor continually keeps decreasing, some severe problems start to arise; thermal noise, leakage current, breakdown of dielectrics, electromigration of copper wires, *etc* [6]. Even if these issues can be solved, the relevance of Moore's Law may become obsolete when the size of the single transistor approaches the dimension of atoms, and that would be the limitation of conventional microelectronics technology we know today.

To overcome this limitation, one of the alternative approaches is introducing another degree of freedom, which is the electrons spins rather than utilizing only the flow of charges in current electronic applications and devices. This alternative technology is called *spintronics* [7]. However, to make spin-based electronic applications and devices successfully, suitable materials are required, which can meet spintronics technological demands. The main constraints can be briefly summarized and related to: (1) current microelectronics heavily relies on complementary metal–oxide–semiconductor (CMOS)

technology which consists of *p*-type and *n*-type semiconductors. The CMOS transistors are essentially being used for conductivity change, signal amplifications, and switching (transistor actions). In spintronics these functions should be performed or related to electron spin. (2) For the electron spin manipulation, magnetic materials are required. In general, electron spins can be controlled in magnetic materials because they have partially-filled orbitals by electrons, which are sources of the magnetism. (3) From an economic standpoint, it is beneficial to fabricate the new materials with current existing manufacturing technology and processes. To change this paradigm the diluted magnetic semiconductors (DMSs) have to be developed and made technologically practical.

DMS is a material that can be created by introducing magnetic ions into a non-magnetic semiconductor (*e.g*. II-VI and III-V semiconductors) so that one can have both magnetic and semiconductor properties in a single material [8]. By doping the magnetic ions into a non-magnetic semiconductor, the DMSs can be either *p*-type or *n*-type materials and as such may be able to be adapted by the CMOS technology [8]–[12]. In addition, since DMSs are semiconductor-based materials, in general, the fabrication and manufacturing process does not need to significantly change. Furthermore, DMSs are expected to cause magnetism due to the effect of the magnetic ions.

The advantages of DMSs are not limited to those mentioned above. Unlike only metallic-based material systems, this semiconductor-based material system can provide the capability of the manipulation of the magnetic state via optical, electrical and structural means [13]. Moreover, a longer mean free path of the spin-polarized charges and larger spin-orbit coupling are also expected in DMSs [13].

The $Ga_{1-x}Mn_xAs$ is one of the ferromagnetic transition metal (TM)-doped III-V DMSs and it has gained a lot of attention not only because of the physics itself but also its technological and economical potentials for future spin-based electronics. Even though a lot of research in the past has been focused on $Ga_{1-x}Mn_xAs$ to improve this material system property, the remaining main drawback today is the relatively low Curie temperature T_c as well as the lack of comprehensive understanding of the origin of the ferromagnetism in $Ga_{1-x}Mn_xAs$ and other III-V DMSs. This is primarily because the GaAs material system becomes complex after Mn doping, making characterizations of the material and interpretations of the results not straightforward. It was shown that magneto-optical characterization has some benefits in investigating the DMSs and it can provide some extra information (*i.e.* electronic band structure) relevant to the origin of the magnetism in the $Ga_{1-x}Mn_xAs$. Thus, this dissertation aims to investigate $Ga_{1-x}Mn_xAs$ using a constructed multifunctional magneto-optical system as well as to demonstrate new data analysis techniques.

This dissertation has the following layouts:

In Chapter 1, an overview of spintronics technology is explained and it includes some examples of current and future spin-based electronic applications. Also, an overview of different kinds of diluted magnetic semiconductors is provided in chronological order. Particular focus is given to $Ga_{1-x}Mn_xAs$ on different substrates having different Mn content. A brief discussion of selected theories and models which try to explain the origin of ferromagnetism in $Ga_{1-x}Mn_xAs$ are mentioned.

In Chapter 2, different types of theories and models are explained for describing used magneto-optical experimental setups and measured data analysis. Specifically, Mueller and Jones matrix formalisms are introduced as needed in the process of experimental facility design and operation. Furthermore, the theoretical background of *s*, *p-d* exchange interaction, Zeeman splitting, the rigid band shift model, and energy derivative of the Gaussian function fitting method are introduced and link with the collected data analysis.

In Chapter 3, the growth process of $Ga_{1-x}Mn_xAs$ materials is briefly explained. Three types of samples were prepared; $Ga_{1-x}Mn_xAs$ on sapphire, $Ga_{1-x}Mn_xAs$ on InP, and free-standing $Ga_{1-x}Mn_xAs$ with different concentrations of Mn by a molecular beam epitaxy (MBE).

In the beginning of Chapter 4, the operation of the transmission-mode MCD setup is described. Then, the development and operation of reflection-mode MCD and polar/longitudinal MOKE setups follows. The Mueller and Jones matrix formalism introduced in Chapter 2 are used here to support the construction of the experimental setup.

Chapter 5 and 6 show the results measured by the transmission-mode and reflection-mode MCD setups for $Ga_{1-x}Mn_xAs$ on sapphire, $Ga_{1-x}Mn_xAs$ on InP, and free-standing $Ga_{1-x}Mn_xAs$. For the analyses of the results, the theories described in Chapter 2 were implemented. Especially, the rigid band shift model was directly used to analyze the MCD and derivative of the absorption (reflection) spectra. In addition, the Zeeman splitting energies of the samples were estimated using the fitting method.

Finally, the last chapter provides the conclusion, and summarizes the importance of this project. The main outcomes generated during this project are:

1. The constructions and development of a multifunctional magneto-optical facility for reflection-mode MCD and polar/longitudinal MOKE spectroscopy,

2. Systematic investigations of MCD spectra for $Ga_{1-x}Mn_xAs$ materials over a wide range of photon energy needed to extract information of both Γ- and L-critical points of Brillouin zone,

3. Introducing a new mathematical method to extract accurate MCD values by background subtraction and a fitting with a derivative of the Gaussian function.

4. Estimation of Zeeman splitting energy of $Ga_{1-x}Mn_xAs$ for Γ- and L-critical points using some theoretical and experimental assumptions. In addition, Appendix G summarizes the major outcomes in this project.

1.2 Overview of spintronics technology

Spintronics is considered as the next generation of electronics, where the spin polarity of electrons rather than its charge is utilized [7], [14]–[22]. It is considered as a new complementary technology and expected to provide some benefits for the current electronics in areas of information storage densities, switching speed, power consumption, manufacturing costs and others.

The era of spintronics began after the discovery of giant-magneto resistance (GMR) by Grünberg *et al.* [23] [24] and Fert *et al.* [25] in Fe/Cr/Fe tri-layers and Fe/Cr multilayer, respectively. It is known, that the Fe layer is ferromagnetic material whereas

the Cr layer is non-magnetic material. When a magnetic field is applied to positive maxima or negative minima of the GMR spectrum, the resistance becomes very small. On the other hand, the resistance becomes very large at the zero magnetic fields. This is due to the ferromagnetic coupling (small resistance) and antiferromagnetic coupling (large resistance) of two ferromagnetic Fe layers separated by a non-ferromagnetic Cr layer.

It was demonstrated that a GMR effect can be utilized for developing spin-valve devices consisting of two ferromagnetic layers (free layer and pinned layer) separated by a non-magnetic space layer and an additional layer which is an antiferromagnetic layer [26]–[31]. This antiferromagnetic layer causes exchange bias in the pinned layer so that the GMR can occur in a very small magnetic field. Thus, the devices capitalizing on the spin-valve operation are currently used in commercial hard drives as reading-heads.

The next new technology base on novel magnetic materials developed utilizes tunnel magneto-resistance (TMR) effect [32]. The TMR involves a significantly changing tunneling current in a device. In general, two ferromagnetic materials forming a device called magnetic tunnel junctions (MTJs) are separated by a thin insulating layer (typically few nanometers thick). When the magnetization of the two ferromagnetic materials in the device is the same (parallel), a tunneling current can flow between them. However, when the magnetization of the two ferromagnetic materials is opposite (anti-parallel), the tunneling current can be significantly reduced. The TMR effect is purely a quantum mechanical phenomenon.

Since the discovery of the room temperature TMR effect in Al-O based MTJs [33] [34], a new type of non-volatile memory, called magneto-resistive random access memory (MRAM), was developed starting in the early 1990's. Initially, the TMR ratio reported by Miyazaki *et al.* [33] [34] was very small between 2.7 % to 18 % at 300 K. In 2004, significant improvement was achieved in generating a large TMR ratio by developing a new method of magnetization switching in Al-O based MTJs [35], called the spin transfer torque (SST) method [36] [37]. Unlike the conventional way which relies on applying a magnetic field (MRAM switching field), the orientation of the magnetization in the magnetic layer can be switched by a spin-polarized current due to the magnetization precession. This can reduce the size of the memory cell because one writing wire can be omitted and the current driven to the cell can be reduced due to the assistance of the magnetization precession to changing the orientation of the magnetization in the magnetic layer. This type of MRAM is called spin transfer torque MRAM (STT-RAM). At the same time, significant improvements of the TMR ratio was independently reported by Parkin *et al.* [38] and Yuasa *et al.* [39] independently using Fe/MgO/Fe junction. The reported TMR ratio was over 200 % at 300 K. Shortly after, the STT switching caused by perpendicular magnetization MTJ was reported in 2007 [40] and 2008 [41]. This approach offers more advantages than the in-plane magnetization MTJ because the perpendicular magnetization MTJ can scale down to 20 nm without a thermal fluctuation problem, and SST-switching efficiency of the perpendicular magnetization MTJ is one order magnitude larger than that of in-plane devices [42]. On the other hand, in-plane magnetization MTJ starts to have a problem in maintaining the

volatility below 50 nm scale because thermal fluctuation starts to increase, and the SST-switching of in-plane devices are less efficient than that of perpendicular devices [42]. In 2008, the TMR ratio of ~600 % in CoFeB/MgO/CoFeB junction at 300 K [43]. Hence, the perpendicular SST-TMR for reading heads and MRAM devices has been intensively studied over the past two decades, and they are the most mature metal-spintronics technology.

While developing the memory devices using spintronics technology, spin-based transistors have also been studied. In 1985-1994, the development of all-metal spin transistor (spin-based bipolar junction transistor (BJT)). was reported by Johnson *et al.* [44] [45]. Even though this had advantages to increase packing densities and reduce power consumption as compared to traditional semiconductor-based BJTs, it could not eventually convert to a field effect transistor (FET) because no signal amplification took place in spin-based BJT having all metal components. In 1989, Datta *et al.* introduced a spin field-effect transistor [46]. It involved InAlAs/InGaAs heterostructure as a body, and source and drain were Fe layers. The heterostructure creates a two-dimensional gas (2DEG) channel between the source and drain. Due to the spin-orbit (OS) coupling and structural inversion asymmetry, an effective magnetic field can be generated based on this relation: $\boldsymbol{B} = -(\hbar/mc^2)(\boldsymbol{k} \times \boldsymbol{E})$, where $\hbar$ is the Planck constant, m is the particle's mass (either electron or hole), c is the speed of light, $\boldsymbol{k}$ is the particle's wavevector, and $\boldsymbol{E}$ is the electric field [47]. This is called the Rashba effect [48] [49] which can control electron spins by applying an electric field which generates the effective magnetic field and this effect can be further increased by applying the gate voltage in spin-FET or spin-

MOSFET [50]. In general, the *Rashba* effect is observed at an interface of a heterostructure or at the edge of the material surface because of structural inversion asymmetry. In the InAlAs/InGaAs-based FET, particular electron spins are injected through the source (Fe layer) and the *Rashba* effect causes the spin precession of the spin-polarized electrons in the channel when the gate voltage is applied [46] [47] [50]. Finally, the electrons can or cannot pass through the detector (drain) if the spins are parallel (or anti-parallel) to the polarization direction of the detector.

Based on the pioneering work of Datta and Das, other metal-semiconductor FET's have also been developed including Fe/GaAs system [51]–[56]. This approach seemed to be somewhat promising for a spin-FETs because the Curie temperature of the involved material system was higher than 300 K [57]–[59]. However, the spin injection efficiency of the spin-FET remained a challenge and was relatively low due to a large lattice mismatch between metal and the semiconductor interface [60]–[63].

Since the spin injection from metal to semiconductor is not efficient, the alternative material to resolve this issue can be using diluted magnetic semiconductors (DMSs). It is known that DMSs maintain a better lattice mismatch to the body of MOSFET and contains magnetic moment needed for spin injections [14] [50] [64] [65]. Furthermore, DMSs are not only the prospective materials for spin-FETs or -MOSFETs but also are considered for spin light emitting diodes (spin-LEDs), spin-TMR, MRAM, spin-solar cells, and *etc.* [7] [15] [16] [22] [50] [66]. However, currently to the best of our knowledge, there is only one successful practical application using II-VI-based DMS for an optical isolator [67]. Despite existing scientific and technological challenges in

manufacturing DMSs and controlling their desired properties, these materials are very promising in modern information technology, and as such, possess potential to succeed as semiconductor-based spintronics technology.

1.3 Overview of diluted magnetic semiconductors

The concept of the magnetic semiconductor is relatively old. It was introduced in the late 1960's to search for new functional material(s) which would combine semiconductor and magnetic characteristics. Even though numerous research was conducted on Cr-chalcogenide spinels (*e.g.*, $CdCr_2Se_4$, $CdCr_2S_4$, $HgCr_2S_4$, $HgCr_2Se_4$) [68] and Eu-chalcogenides (*e.g.*, EuTe, EuO, EuSe, EuS) [69], these materials could not be utilized in practical applications mostly due to the low Curie temperature (T_c) observed in these material systems.

In the 1980's, new magnetic semiconductors started to be popular. These are transition metal (TM)-doped II-VI magnetic semiconductors called diluted magnetic semiconductors (DMSs) [70]–[82]. In these types of materials' systems, cations replaced with magnetic ions in the semiconducting host and the TM-doped II-VI DMSs were expected to cause ferromagnetic behavior. The well-known TM-doped II-VI DMSs are, for example, ZnMnS, ZMnSe, CdMnS, CdMnSe, HgMnS, HgMnSe *etc*. The main problem limiting the practical application of the TM-doped II-VI DMSs is relatively low T_c*'s*. In 2003, for the first time, Saito *et al.* reported room-temperature ZnCrTe DMS observed by magnetic circular dichroism (MCD) [81]. The significance of this

achievement is primarily due to the fact that there are no other II-VI materials showing room temperature magneto-optical responses caused by an *sp-d* exchange interaction.

In 1989, for the first time, ferromagnetism of TM-doped III-V DMS was reported by Munekata *et al*. in InMnAs grown by low temperature molecular beam epitaxy (LT-MBE) [83] [11]. It was realized later that the LT-MBE is the key technique for fabricating TM-doped III-V DMSs. It should be mentioned here, that the prominent feature of the TM-doped III-V DMS was not only its magnetic property but also a possibility for making effective *n*- or *p*-type conductivity via altering the growth conditions [11] [83] [84]. Since then, other TM-doped III-V DMSs have been also investigated including GaMnSb, GaMnP, GaMnN, CaCrN, InCrN, InMnN systems [84]–[93].

These days the most popular TM-doped III-V DMSs is $Ga_{1-x}Mn_xAs$ because it can offer all advantages of GaAs semiconductor useful in many practical applications. This includes, for example, high electron mobility transistor (HEMT) because the GaAs has a higher electron mobility than a Si. In addition, GaAs can be used for higher frequency devices and applications in harsh environments such as mobile phones, satellite combinations, higher frequency radar systems, solar cells, and space applications because GaAs has a larger band gap than the Si so that GaAs-based devices are less affected by heat.

Even though a large number of research continues to be conducted towards the $Ga_{1-x}Mn_xAs$, the mechanism of ferromagnetism in $Ga_{1-x}Mn_xAs$ is not fully understood because of the complexity of the material after the Mn doping. Therefore, the

characterization of the $Ga_{1-x}Mn_xAs$ as a prospective ferromagnetic DMS is very important, and it has to be carefully and correctly conducted.

1.4 Overview of $Ga_{1-x}Mn_xAs$

$Ga_{1-x}Mn_xAs$ is one of the prototype ferromagnetic DMSs; however, the origin of the ferromagnetism in GaMnAs is not fully clarified yet. If the material system of $Ga_{1-x}Mn_xAs$ is understood and one can observe the ferromagnetism above room temperature, it would open a new area of electronics technology.

Figure 1-1 shows the progress of achieving higher Curie temperature T_c in $Ga_{1-x}Mn_xAs$. It was first demonstrated by Ohno, *et al*. in 1996 and the reported T_c was 60 K [94], which at that time was already higher than what was reported for TM-doped II-VI DMSs (T_c = ~3 K). Since then, a systematic improvement was demonstrated reaching T_c of 110 K in 1998 [95] and T_c of 173 K in 2004 [96] [97]. However, there has not been any drastic improvement for the T_c after that. The highest T_c in $Ga_{1-x}Mn_xAs$ reported till now is close to 180 K [98] which is noticeably far below room temperature needed for practical applications.

Considering the above fact, one can realize that it is very important to understand the physics and the ferromagnetism in $Ga_{1-x}Mn_xAs$ and to make a conclusive consensus regarding its technological relevance.

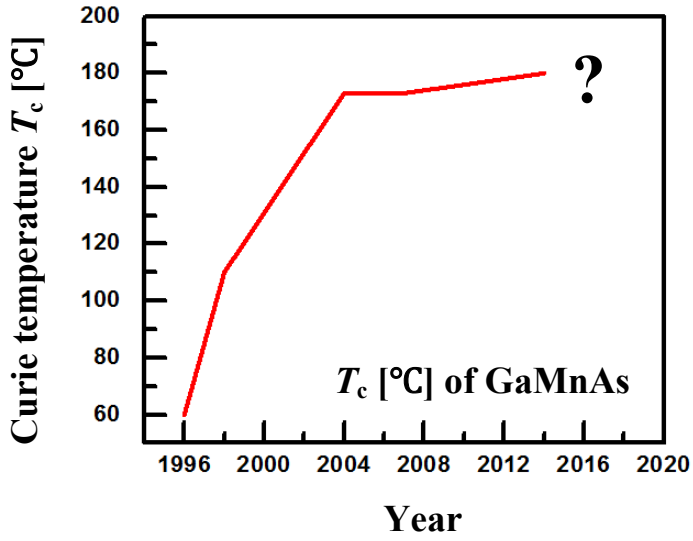

Figure 1-1 The progress of Curie temperature T_c [℃] of $Ga_{1-x}Mn_xAs$ in a chronological order.

In general, the magnetism in TM-doped II-VI and III-V DMSs can be explained by *sp-d* exchange interaction [99]–[103]. This interaction takes place between the *d*-electrons in the magnetic ions and *s-p* electrons in the host semiconductor material resulting in generations of the observed magnetism. It is known that the theory of the *sp-d* exchange interaction can be correctly described using Zener kinetic-exchange and indirect-exchange models [100] explaining the origin of the magnetism in the paramagnetic TM-doped II-VI DMSs [99] [103]. However, currently existing as a mutual consensus in the literature, that TM-doped III-V DMSs, especially $Ga_{1-x}Mn_xAs$, need more advanced theoretical insight to explain the existence of ferromagnetism in these systems, which cannot be explained completely only by *sp-d* exchange interaction [99].

For the past three decades, different, theories, models, and approaches have been introduced to explain the origin of ferromagnetism in $Ga_{1-x}Mn_xAs$ in addition to the *sp-d* exchange approach [65] [101] [104]. These theories, models, and approaches are mostly distinguished depending on the concentration of magnetic impurities (higher concentration (x > 1-5%) or lower concentrations (x <1%)) and the Fermi level position.

When the Mn concentration reaches to x = ~1% in $Ga_{1-x}Mn_xAs$, the system reaches to *Mott insulator-to-metal transition point* (The average distance between the Mn impurities is approximately the same as that of effective Bohr radius of the impurity) [105]. This is the critical point when the $Ga_{1-x}Mn_xAs$ starts to have a ferromagnetic property.

In the case of lower Mn concentration that is when the system is below the Mott insulator-to-metal transition point (the average distance between the Mn impurities is much larger than the effective radius of the impurities) [105], it was expected to have ferromagnetic exchange interactions between local Mn moments through the thermally activated band carriers [106]. However, the most experimental results show paramagnetic behavior when Mn concentration is below a Mott insulator-to-metal transition point (x = ~1% in $Ga_{1-x}Mn_xAs$ system).

Another approach exercised in explaining the ferromagnetic behavior in $Ga_{1-x}Mn_xAs$ is using the *Ruderman-Kittel-Kasuya-Yosida* (RKKY) interaction model [12] [95]. The RKKY model uses the mean-field approximation assuming that the average distance between the carriers is approximately equal to the average distance between spins. When Mn^{2+} ion is doped into GaAs it creates a hole carrier in the host system. Thus, Mn^{2+} ion

acts as the acceptor which is the source of the magnetic moment in $Ga_{1-x}Mn_xAs$. In this case, the carriers (holes) are treated as being itinerant; meaning that they are weakly localized or delocalized in the valence band. Essentially, the holes mediate the ferromagnetic coupling between the localized Mn^{2+} ions spins. Assuming, that the localized Mn^{2+} ions spins and the holes are placed in approximately equal distances (*i.e.* mean-field approximation) one can expect that the localized Mn^{2+} ions spins and holes are anti-ferromagnetically coupled through *p-d* exchange interaction. Thus, ferromagnetic couplings in this case can be expected to happen between the localized Mn^{2+} ions spins.

Another theory widely applied to explain magnetism in the $Ga_{1-x}Mn_xAs$ was the *Moss-Bursten effect* [107] [108]. In this approach, as the concentration of Mn increases, the Fermi level starts to reside inside of the valence band (VB) meaning that extra holes can be created in the valence band (*i.e.* VB-hole model). Then, an extra energy difference ΔE can be created between a heavy-hole and a light-hole VB. It is believed that the ΔE parameter indicates the magnitude of enhancement of the magnetization in the system. However, it should be note here that this was only a qualitative explanation [107]–[109].

Unlike the models described above based on the itinerant nature of the holes, an alternative approach called the impurity band (IB) model (or IB-hole model) was introduced to describe the ferromagnetism in $Ga_{1-x}Mn_xAs$. In the conventional *Zener model* [65] [101] [100] which uses mean-field theory, the ferromagnetism is caused by *p-d* exchange interaction between VB holes and localized 3*d* electrons in Mn^{2+} ions. This model has been widely accepted in the past because it can explain most of the phenomena

in the $Ga_{1-x}Mn_xAs$ system [101] [110]–[113]. In this theoretical framework, it is assumed that the Mn-induced IB is merged with VB and the Fermi level is located ~200 - 300 meV below the top of the VB. However, more recent studies revealed that the Fermi level actually lies in the IB within the band gap of $Ga_{1-x}Mn_xAs$ [104] [114] [115]. This model can be explained by Zener's double-exchange type mechanism which generates the ferromagnetic property by the hopping of a spin-polarized hole in the IB (IB-hole model) [116]–[118]. Originally, this double-exchange mechanism was developed by Clarence M. Zener to explain the exchange interactions between two magnetic ions with different numbers of electrons through oxygen ion involvement [65] [100] [105]. In principle, this concept is described as: "*The double exchange couples magnetic ions in different charge states by virtual hopping of the 'extra' electron from one ion to the other.*" [100] [119]. This theoretical concept was later extended and adopted by Anderson and Hasegawa for the double exchange interaction observed in the DMSs [120] including $Ga_{1-x}Mn_xAs$ [65] [105]. Specifically, when one considers the double exchange interaction, it assumes that: "*Mn^{2+}–Mn^{3+} ions pair with one d-electron hopping virtually from one ion to the other via the p-orbitals of neighboring anions*" [119] [120]. In this case, the spin-polarized holes virtually hop between the Mn ions in the IB and induce observed ferromagnetism.

When the concentration of Mn in $Ga_{1-x}Mn_xAs$ is $x < 1\%$, the resulting IB is above VB, and the Fermi level energy (E_F) starts to decrease as the concentration of Mn increases in the paramagnetic GaMnAs as shown in Fig. 1-2(a) [104] [114]. This behavior of the Fermi level in the paramagnetic $Ga_{1-x}Mn_xAs$ ($x < 1\%$) is caused by the screening effect [104] [121] due to Mn doping. As the concentration of Mn increases

reaching the Mott insulator-to-metal transition point (*i.e.* in $Ga_{1-x}Mn_xAs$ for x = ~1%), Mn-induced IB can be created and it gets close to the VB edge and then starts to overlap with VB as schematically shown in Fig. 1-2 (b) [104] [114]. It was demonstrated using a resonant angle-resolved photoemission spectroscopy that for $Ga_{1-x}Mn_xAs$ with x = 2-10% the IB as well as E_F are located above VB top [115] as is shown in Fig.1-2 (C) [104] [114]. In the last case, the energy separation between the E_F and the VB top increases as the concentration of Mn ions increases. This behavior is known in the literature as the valence band anti-crossing (VBAC) model [122]. Moreover, the IB located near the Fermi level was overlapping with VB in a relatively wider energy range (Fermi level to 400 meV below the top of VB) [104] [115]. Also, resonant angle-resolved photoemission spectroscopy showed that the Fermi level is located 50 meV above the top of VB in $Ga_{1-x}Mn_xAs$ (x = 13%) [123]. These facts also suggest that the carriers (holes) in the IB are another possible candidate to generate a ferromagnetic property in $Ga_{1-x}Mn_xAs$.

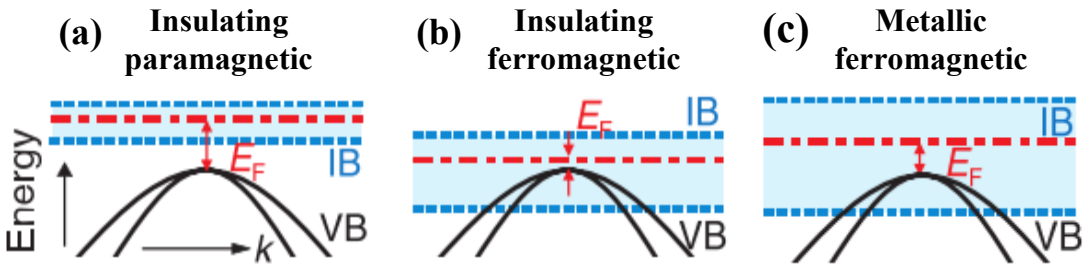

Figure 1-2 The VB and IB diagrams of $Ga_{1-x}Mn_xAs$ derived from in the Refs. [114], [104], and [115]. (a) Insulating paramagnetic (x < 1%), (b) insulating ferromagnetic (x = 1–2%), and (c) metallic ferromagnetic (x > 2%) regions. The black solid curves are the VB. The blue dotted lines are the upper and bottom edges of the IB. The blue region represents the IB region. The red dashed-dotted lines are the Fermi level. After Refs. [104] and [114].

The existence of IB was also supported by the variety of experimental techniques including angle-resolved photoemission spectroscopy [124], hot-electron photoluminescence [125] [126], resonant scanning tunneling spectroscopy (STM) of quantum well [127], infrared and optical spectroscopy [128] [129], and magnetic circular dichroism (MCD) [109] [130] [131]. Especially, the STM analysis showed microscopically inhomogeneous nature of the $Ga_{1-x}Mn_xAs$ electronic structure and confirmed that the origin of the ferromagnetic property in $Ga_{1-x}Mn_xAs$ is more complex than observed in paramagnetic II-VI DMSs [132]. It should be noted here that the MCD measurement technique applied to the $Ga_{1-x}Mn_xAs$ showed an existence of spectral peaks corresponding to the below band gap energy levels [109]. This result, supported by other measurement techniques mentioned above, confirmed unambiguously that the IB is generated inside of the $Ga_{1-x}Mn_xAs$ band gap. In addition, the $Zn_{1-x}Cr_xTe$ system is the only ferromagnetic TM-doped II-VI DMS at 300 K [81] which shows a broad MCD spectral peak below the fundamental absorption edge. This fact further indicates that the IB plays an important role in generating the ferromagnetism in III-V DMSs.

Figure 1-3 shows schematically the concept behind the analysis of the MCD spectroscopic data involving the IB strongly affected by the semiconductor band structure around Γ critical points (CPs) (E_0 and $E_0+\Delta_0$ CPs). It is known that there exists a certain complexity of the $Ga_{1-x}Mn_xAs$ electronic structure around the Γ-CPs [109] which may result in erroneous spectroscopic data interpretations. In the Fig, 1-3, it is seen that the expected MCD background affected by the presence of IB decreases linearly as the photon energy increases toward a higher energy side (L-CPs). This clearly indicates that

one can expect that the IB effect should become much smaller around *L*-CPs simplifying the data analysis [109] [133]. Thus, considering the above mentioned arguments indicating the complexity of theoretical modeling and analysis of the MCD spectra affected by the IB, it would be very interesting to investigate first the MCD spectra structure around *L*-CPs, and later conclude on the features of $Ga_{1-x}Mn_xAs$ around *Γ*-CPs using some theoretical and experimental assumptions. The approach, where MCD spectra collected for $Ga_{1-x}Mn_xAs$ system are first analyzed around *L*-CPs and followed by analysis around *Γ*-CPs presents the essence of the theoretical analysis conducted in this project. The details of our methodology schematically illustrated in Fig. 1-3 are described in Chapter 5 and 6.

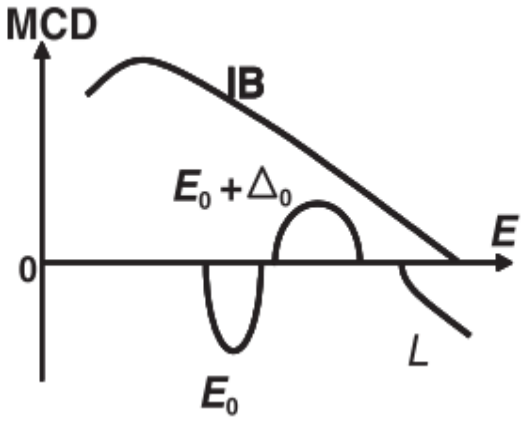

Figure 1-3 Illustration of the decomposed anomalous positive MCD signal into the negative E_0 peak, positive $E_0+\Delta_0$ peak, and broad positive IB peak around the *Γ*-critical points (E_0 and $E_0+\Delta_0$ critical points) of $Ga_{1-x}Mn_xAs$. The negative MCD signal around *L*-critical points (E_1 and $E_1+\Delta_1$ critical points) can be observed in the higher photon energy side. After Ref. [109].

1.5 Characterization of diluted magnetic semiconductors

When it comes to characterization of the DMSs, one has to pay special attention. Most of the DMSs have been investigated using volumetric magnetic measurement techniques like superconducting quantum interference devices (SQUID) or vibrating sample magnetometer (VSM). However, the question that arises, is where does this magnetization actually comes from and how is it generated.

In the past Ando *et al*. [89] has reported that a GaN:Mn can be considered as the DMS. Following this report, Fig.1-4 (a) shows a strong ferromagnetic hysteresis loop in the GaN:Mn measured by SQUID at 300 K indicating that this can presumably be considered as a ferromagnetic DMS. Figure 1-4 (b) shows the MCD spectrum from the GaN:Mn in an energy range from 1 to 4 eV. It is obvious that the MCD signal is enhanced around *L*-CPs in the GaN:Mn due to the *sp-d* exchange interactions occurring between *d*-electrons in magnetic ions, and *s-p* electrons in the host semiconductor [89]. Also, considering the MCD spectrum for the GaN:Mn alone or in conjunction with the SQIUD results, one can assume that this material is a typical DMS. However, as Fig.1-4(c) shows, the MCD hysteresis loop shows linear behavior even at 6 K suggesting that GaN:Mn is actually a paramagnetic and not a ferromagnetic DMS. This leads to the conclusion that the SQUID and the MCD hysteresis loops are contradicting each other. This is because the SQUID technique simply measures magnetic moments of any impurities in the volume of a GaN:Mn sample whereas MCD detects only the *sp-d* exchange interaction between a Mn ion and a GaN host. The last one is the main objective to investigate if a critical determination of a potential material as DMS is

considered. We should emphasize here, that in this project, we define material as DMS which generates *sp-d* exchange interaction inside of the system. This is because the *sp-d* exchange interaction is attractive from a practical applications and devices standpoint. Since the *sp-d* exchange interaction occurs in a visible-spectrum range it can be used for magneto-optical applications, and the spin-FET is another candidate because the *sp-d* exchange interaction enhances the induced magnetic field which is used for the spin manipulation in a channel between source and drain.

Thus, an MCD is a more reliable measurement technique; up to a certain extent, than SQUID or other volumetric magnetic measurement techniques for the investigation of the TM-doped DMS. In addition, the MCD can provide extra information like the electronic band structure enhanced by *sp-d* exchange interaction not accusable by other means.

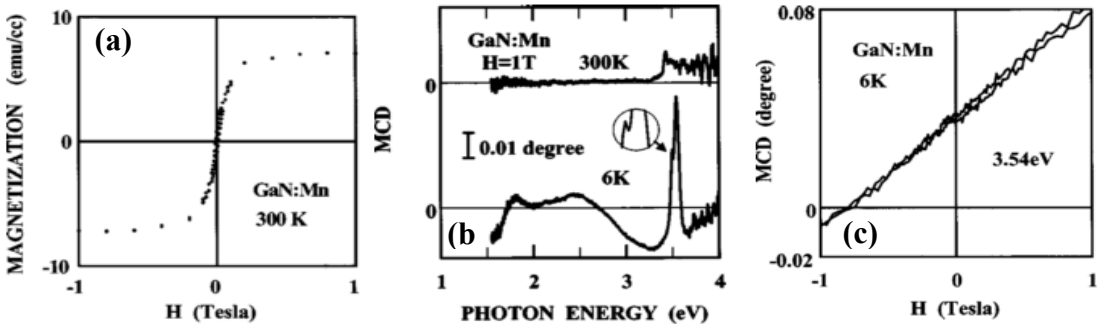

Figure 1-4 Examples for a contradiction results measured by SQUID and MCD (a) Hysteresis loop of GaN:Mn measured by SQUID at 300 K. The magnetic field was applied perpendicular to the sample plane. The diamagnetic contribution was subtracted. (b) MCD spectra of GaN:Mn at 300 K and 6 K. The Γ-CPs of GaN:Mn is around 3.47 eV. The circular inset magnifies the MCD structure for the clarity. (c) Hysteresis loop of GaN:Mn measure by MCD at 6 K. The photon energy of MCD was 3.54 eV. Nonmagnetic circular dichroism (CD) shifts the zero-level of the MCD. After Ref. [89].

Another important aspect of the MCD is its ability to eliminate some of the ambiguity in the DMS experimental data interpretation due to a material contamination. Figure 1-5(a) shows the results of ferromagnetic NiFe and dielectric HfO_2 samples measured by MOKE [134]. It shows the ferromagnetic hysteresis loop from NiFe whereas no magnetic response was observed from HfO_2 due to its nonmagnetic nature. Figure 1-5 (b) shows the results of HfO_2 samples having different thicknesses measured by SQUID. No magnetic responses were observed from any of these samples as expected [134]. However, HfO_2 samples and even a silicon wafer, being not ferromagnetic samples, exhibited ferromagnetic behavior (see Fig.1-5 (c)) after contaminating them by stainless-steel tweezers [134]. It is now understood that SQUID as a very sensitive technique for measuring magnetic property; it detects magnetic responses even from faint surface contamination and creates misleading results. SQUID is a very sensitive and valuable technique to investigate metal or metal alloys; however it may give some wrong interpretations for DMSs as demonstrated in Fig.1-5. Therefore, we would like to emphasize here that the magneto-optical characterization, especially MCD, is a very useful and powerful tool to investigate the DMSs since it can eliminate certain artificial effects and provide extra information of the electronic band structure in the investigated DMSs.

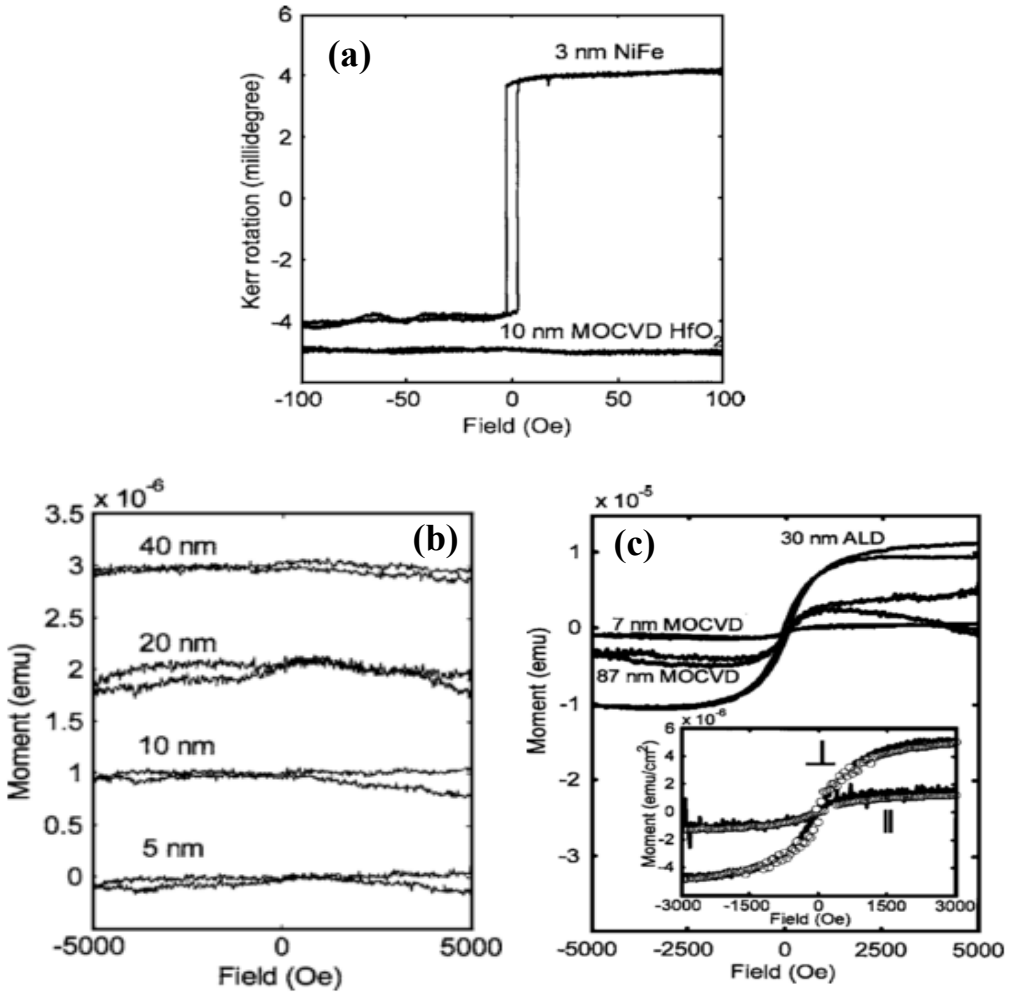

Figure 1-5 (a) Kerr rotations from 10 nm thick HfO_2 film grown by metal-organic chemical vapor deposition (MOCVD), and a 3 nm thick $Ni_{81}Fe_{19}$ film [134]. No moment was observed for any of the Hf-based films. (b) Magnetic moment measured by SQUID and the field applied was parallel to sample plane for 5, 10, 20, and 40 nm thick MOCVD HfO_2 on Si. Diamagnetic background signal has been subtracted from the data. (c) Magnetic moment measured by SQUID and the field applied was parallel to sample plane for three HfO_2 samples made by MOCVD and atomic laser deposition (ALD) after handling with stainless-steel tweezers. Inset: Solid lines show measured moment of a piece of 30 nm thick ALD HfO_2 film on Si after contamination by handling with stainless-steel tweezers, for field applied parallel and perpendicular to sample plane. Open circles show data taken from Ref. [206] with moment scaled to match data in Ref. [134]. After Ref. [134].

2. THEORY

2.1 Theoretical considerations supporting MCD and MOKE measurements

In the following Sections 2.1.1 and 2.1.2, we will focus on theories for the development of MCD and MOKE experimental setups. The detailed derivations of equations used for MCD and MOKE can help an operator choose correct parameters and values for effective experimental investigation. Some of the critical parameters are: polarization of light, phase retardation, frequency of modulated light in photoelastic modulator, angle of incident and reflected light. In addition, the derived equations can be used to calibrate the measured signals [unit less] into MCD [deg], Kerr rotation [deg], or Kerr ellipticity [deg] signals for quantitative analysis. Furthermore, the obtained final equations for MOKE spectra measured in reflection-mode can qualitatively explain unexpected features in the measured spectra as discussed in Chapter 6. First, we will consider the Mueller matrix and Jones matrix formalisms used in developing and understanding the experimental setups. More detailed discussions and derivations of the equations obtained from the Mueller matrix and Jones matrix formalisms are shown in Appendixes A and B. In the following portions of Chapter 2 we will present and discuss only the main theoretical framework.

2.1.1 Mueller matrix formalism used for designing MCD experiment setup

Magnetic circular dichroism (MCD) is one of the magneto-optical effects, and it is essentially the absorption difference between right circularly polarized light and left circularly polarized light. Typically, circularly polarized lights are generated using a

photoelastic modulator (PEM). When considering the transmission-mode MCD setup, all involved optical components can be represented by a Mueller matrix and linearly polarized light can be represented by a Stokes vector. Figure 2-1 shows the generic concept of this experimental arrangement where the *P*, *PEM*, and *S* stand for the polarizer, photoelastic modulator and sample, respectively [135]–[138]. Here, the *Cartesian coordinates* (*x, y, z*), unless mentioned otherwise, represent the orientation of the propagating polarized light optical wave vector $\boldsymbol{k}$ with respect to the sample surface (*i.e.* $\boldsymbol{k}$ //$\boldsymbol{c}$ where $\boldsymbol{c}$ is the sample $\boldsymbol{c}$-axis). Initially, the unpolarized light passes through the polarizer at (-45) degree and the linearly polarized light can be represented by the Stokes vector ($\boldsymbol{I_{-45}}$). Then, the linearly polarized light is modulated by *PEM* to make right and left circularly polarized lights. Therefore, in the transmission-mode MCD, one needs only the Stokes vector representing (-45) degree polarized light ($\boldsymbol{I_{-45}}$) and a Mueller matrix representing a photoelastic modulator ($\widehat{M}_{PEM}$) at 0 degree (*PEM* polarization axes is not tilted). It should be noted here, that the sample ($\boldsymbol{S}$) is a transparent medium and does not contribute an additional polarization effect and phase retardation changes, unless a magnetic field is applied to the sample. The final MCD signal can be derived by multiplying the Stokes vector ($\boldsymbol{I_{-45}}$) and the Mueller matrix of *PEM* ($\widehat{M}_{PEM}$). For the detailed discussion and equation derivations discussed above please refer to Appendix A.

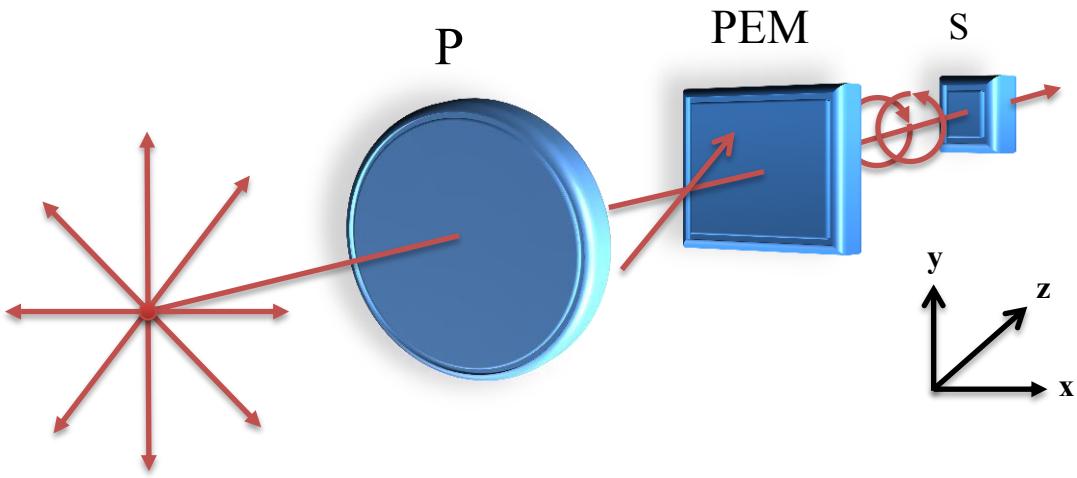

Figure 2-1 Schematic illustration of principles applied to the transmission mode MCD setup and notation of the Muller matrices for each optical component [135]–[138]. *P*: polarizer, *PEM*:photoelastic modulator, *S*:sample, The Cartesian coordinates represent the orientation of magnetic field *B* and the light propagation direction along the *z* axis. The plane of incidence is *x*-*z* plane.

It should be mentioned here that throughout this dissertation we have observed the following notation style in equations: *e.g.* the $\boldsymbol{I_{-45}}$ (in **bold**) represents a vector, the $\widehat{M}_{PEM}$ (in upper accent like ^) represents a matrix and all other symbols are scalars (in *Italic* font style). The equations (2.1) and (2.2) below represent the Stokes vector ($\boldsymbol{I_{-45}}$) and the Mueller matrix of the PEM ($\widehat{M}_{PEM}$) as,

$$\boldsymbol{I_{-45}} = I_0 \begin{pmatrix} 1 \\ 0 \\ -1 \\ 0 \end{pmatrix} \tag{2.1}$$

$$\widehat{M}_{PEM} = \begin{pmatrix} 1 & 0 & 0 & 0 \\ 0 & 1 & 0 & 0 \\ 0 & 0 & cos\delta & sin\delta \\ 0 & 0 & -sin\delta & cos\delta \end{pmatrix} \tag{2.2}$$

where I_0 is the initial intensity of the light before the phase modulation by *PEM* and δ is a phase retardation generated in *PEM*. The phase retardation δ is the phase difference between *x*- and *y*- components of electric field vectors. This δ parameter in *PEM* is used to make right and left circularly polarized light. By multiplying Eqs. (2.1) and (2.2), one can derive an expression for a detected light signal (I_{det}) which can be finally calibrated/converted to an MCD [deg] signal.

It is known that the absorption of light can be represented mathematically using logarithmic forms. Therefore, the absorption represented by base-10 is called *decadic absorption* ($I = I_0 10^{-\Delta A_{MCD}}$) and the absorption represented by base-*e* is called *Eulerian absorption* ($I = I_0 e^{-\Delta \alpha_{MCD}}$). The A_{MCD} and α_{MCD} represent the absorption coefficients for decadic and, Eulerian forms, respectively. The Δ factor indicates absorption coefficient difference between right and left circularly polarized light (*e.g.* $\Delta A_{MCD} = A_R - A_L$). The Eq. (2.3) shows the MCD signal in terms of the Eulerian absorption coefficient (α_{MCD}),

$$\theta_{deg} = \frac{180}{\pi}\frac{\Delta \alpha_{MCD}}{4} \tag{2.3}$$

where 180/π factor represents a calibration factor to change the unit from radian to degree. 1/4 is another calibration factor derived by Mueller matrix formalism (see Appendix A). This equation is eventually important to derive the MCD signal by a different approach called rigid band shift mode, which will be further explained in the next section.

On the other hand, the Eq. (2.4) shows the MCD signal in terms of the decadic absorption (A_{MCD}),

$$\theta_{deg} = \frac{45}{\pi}\ln[10]\,\Delta A_{MCD} \tag{2.4}$$

$$\Delta A_{MCD} = -\frac{1}{J_1[\delta_0]\ln[10]}\frac{\Delta I_w}{\bar{I}} \tag{2.5}$$

where $J_1[\delta_0]$ is the first-order of the *Bessel* function, δ_0 is the amplitude of the phase retardation ($\delta = \delta_0 \sin(wt)$, where w is an angular frequency, and t is the time varying for sinusoidal wave) generated in *PEM*, ΔI_w is the *AC* signal modulate by *PEM*, and $\bar{I}$ is the *DC* signal without any phase modulation [135]–[138]. The ΔI_w and $\bar{I}$ are experimentally measurable values. As it can be seen in Eq. (2.5), the first-order of Bessel function $J_1$is as a function of phase retardation amplitude δ_0 [135]–[138]. Therefore, one can find out the amplitude of J_1 of specific phase retardation amplitude δ_0 using Fig. 2-1 for calibration of the experimentally measured signal $\Delta I_w/\bar{I}$ and express it as the MCD [deg] signal.

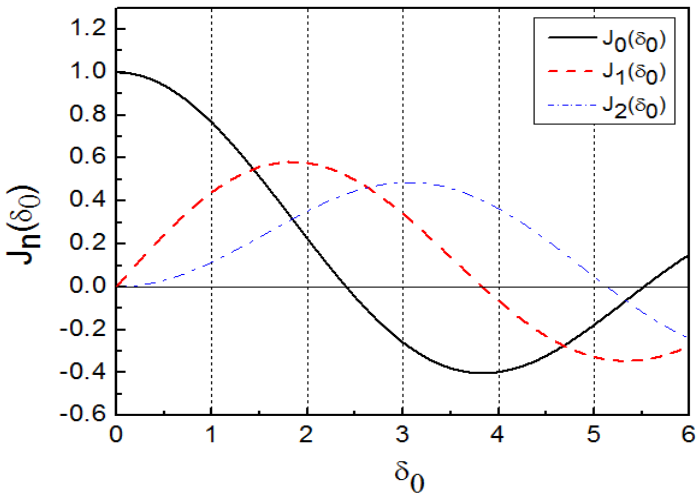

Figure 2-2 Plots for the three lowest order Bessel functions of the first kind as a function of phase retardation amplitude δ_0. (Plotted using MATLAB).

In general, any values of phase retardation amplitude δ_0 can be used for MCD measurement as long as it does not generate J_1= 0 [135]–[138]. In most of the MCD experiments, the phase retardation amplitude δ_0 is equal to 1.571 radian (90 degree, 0.25λ where λ is wavelength of incident light) in *PEM* to make right and left circularly polarized light [135]–[138]. In such a case, the amplitude of the Bessel function is $J_1[\delta_0]$ = 0.567. Having the right and left circularly polarized light in MCD spectroscopy is especially important to meet the selection rule of optical transitions in the DMSs. If the phase retardation amplitude δ_0 is not properly chosen, *PEM* will generate different types of polarized light (*e.g.* linear or elliptically polarized light). Therefore, deriving the equation representing a Muller matrix for the MCD, one can obtain Eqs. (2.4) and (2.5). The Eq. (2.4) can be used for the derivation of the MCD with the rigid band shift model to describe the physics of DMS. Similarly, the Eq. (2.5) can be used to determine experimental parameters and calibrate the measured signal [unit less] into the MCD [deg] signal. In addition, the plots of the first three order of the Bessel function (see Fig. 2-2) can be used as a reference for the calibration of the measured signal. Moreover, the Bessel function plot is very useful in deriving Eqs. for Kerr rotation and Kerr ellipticity as explained in Appendix B.

It should be noted here that this derivation is specifically based on the transmission-mode MCD. Let us now consider how to derive a set of similar equations for the reflection-mode MCD using the Mueller matrix. In general, such an approach is very challenging and complex due to the fact that one needs to introduce extra Mueller matrices representing the optical mirror and the sample surface which to some extent

induce the light polarization destruction. The induced polarization changes by the extra optical components are relatively small as compared to the polarization changes due to the pure magneto-optical effect generated in the sample. However, this issue may become important in cases of samples exhibiting weak magneto-optical responses (*e.g.* paramagnetic material). This case will be clearly illustrated using collected experimental data discussed in Chapter 6. It was demonstrated by others [70] [72] [75] [99] [139] [140] that the Eqs. (2.3) - (2.5) remain valid in the case of reflection-mode MCD spectroscopy. Thus one can still use the same constant parameters to calibrate the signals measured; however, one should remember that the results obtained by the reflection-mode MCD have less quantitative accuracy as compared to the transmission-mode MCD due to the slight polarization changes by the extra optical components (*e.g.* optical mirror, sample surface, *etc*).

2.1.2 Jones matrix formalism used for designing MOKE experiment setup

Magneto-optical Kerr effect (MOKE) is another type of magneto-optical phenomenon related to light matter interaction in the presence of a magnetic field. In this case, linearly polarized light is incident on a sample surface subjected to a magnetic field. If the sample has the magnetic moment, the polarization of the reflected light can be changed (*i.e.* Kerr rotation) or the amplitude of the reflected ellipticity can be changed (*i.e.* Kerr ellipticity). In contrast to the case of the reflection-mode MCD using the Muller matrix formalism, all optical components involved in a MOKE experimental setup can be represented using the Jones matrix formalism [141].

In general, there are three different types of MOKE geometries; polar, longitudinal or transverse geometries [142]. These configurations are dependent on the magnetic field direction with respect to a sample surface and a plane of incidence.

As shown in Fig. 2-3, the unique point in this MOKE setup is using an optical mirror mounted on a sample holder surface inclined at 45-degree with respect to a surface normal for a polar geometry (the magnetic field is perpendicular to the sample surface and parallel to the incident plane) [142]. For longitudinal geometry (the magnetic field is parallel to both the sample and the incident plane), one can use a conventional sample holder [142]. The advantage of preparing different types of sample holders is that one can easily switch the MOKE setup from one configuration to the other. Therefore, all optical components can be in fixed positions for both polar and longitudinal geometries and the system calibration generally is not necessary when the measurement type is switched between the two different configurations. In addition, this developed MOKE setup is the same experimental setup of the reflection-mode MCD. Having one multifunctional experimental setup one can conduct polar/longitudinal MOKE and reflection-mode MCD measurements as well as can conduct a qualitative analysis of the MCD results using the procedure derived for polar-MOKE with the optical mirror. Detailed explanations of the experimental setup will be discussed in Chapter 4.

In my previous work [142], I have derived detailed equations for the longitudinal MOKE geometry. In this work I have combined the previously obtained solutions with the Jones matrix formalism for demonstrating functionality of the combined mirror based polar/longitudinal MOKE setup. Specifically, optical components involved in the

polar/longitudinal MOKE setup developed in this project include polarizer (P_1), photoelastic modulator (*PEM*), mirror (*M*), sample (*S*), and polarizer (analyzer, P_2), are shown schematically in Fig. 2-3. The detailed explanation and the derivations of the following equations are in Appendix B.

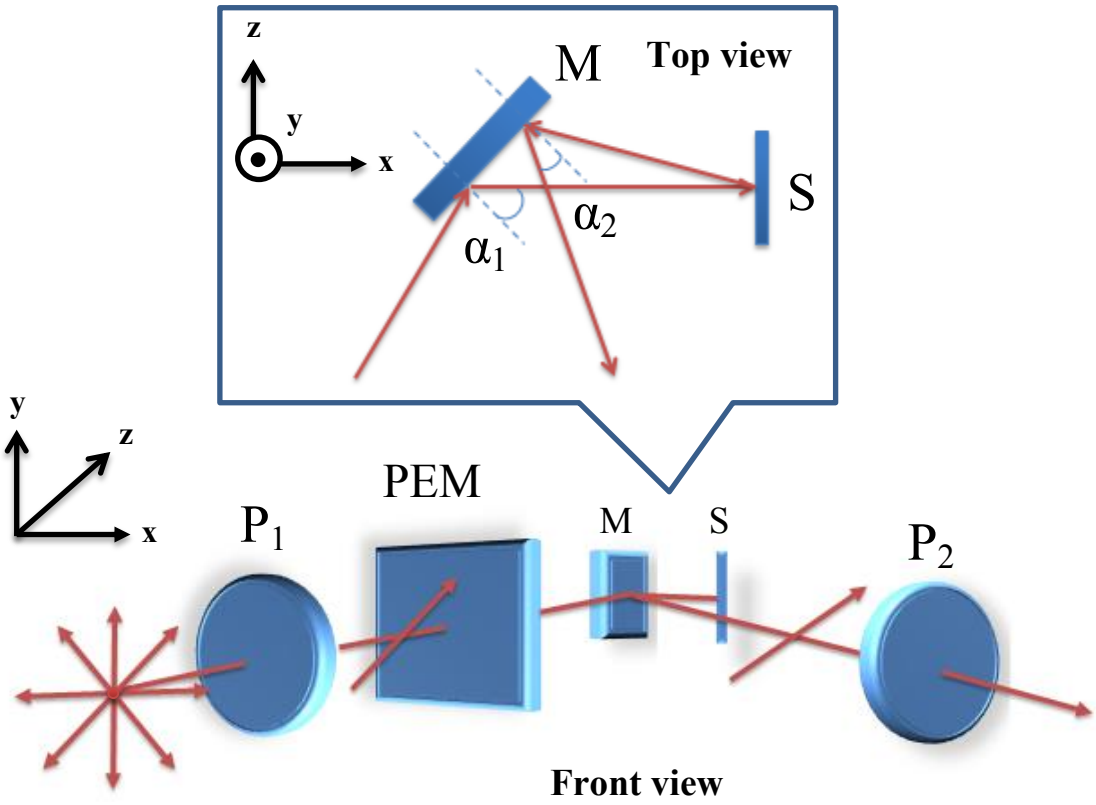

Figure 2-3 Schematic illustration of MOKE principle applied to polar MOKE setup using 45 degree optical mirror, and notation of the Jones matrices for each optical component [141]. P_1: 1st polarizer, *PEM*:photoelastic modulator, *M*: mirror, *S*:sample, P_2: 2nd polarizer (analyzer). The Cartesian coordinates represent that the plane of incidence is *z*-*x* plane and the magnetic field ***B*** is applied along *x* axis direction. A top figure represents the propagation of light with incident light angle ($\boldsymbol{\alpha_1}$) and reflected light angle ($\boldsymbol{\alpha_2}$).

Each optical component including the sample and the -45 degree polarized light can be represented by the Jones matrix [141]. The equation (2.6) represents an incident electric field vector ($\boldsymbol{E}_i$) polarized at -45 degree. The upper bar indicates vector form and bold indicates matrix form,

$$\boldsymbol{E}_i = |E| \begin{pmatrix} \frac{1}{\sqrt{2}} \\ -\frac{1}{\sqrt{2}} \end{pmatrix} \tag{2.6}$$

where $|E|$ represents the electric field amplitude and the vector represents the angle of the polarized light at -45 degree.

Then, the Jones matrix for the PEM can be expressed by Eq. (2-2-2),

$$\widehat{PEM} = \begin{pmatrix} e^{i\delta/2} & 0 \\ 0 & e^{-i\delta/2} \end{pmatrix} \tag{2.7}$$

where δ is the phase retardation generated in the PEM. When the incident angle of light is α, the normalized Jones matrix for the mirror is expressed by,

$$\widehat{M}(\alpha) = \begin{pmatrix} tan\Psi(\alpha)\, e^{i\Delta(\alpha)} & 0 \\ 0 & 1 \end{pmatrix} \tag{2.8}$$

where $tan\Psi(\alpha)$ and $\Delta(\alpha)$ are ellipsometry parameters of the mirror. The $tan\Psi(\alpha)$ term represents the magnitude of the reflectivity ratio between *s*- and *p*-polarized light, the $\Delta(\alpha)$ term represents the phase difference between reflected *s*- and *p*-polarized lights and α parameter is an incident and reflected angle of polarized light at a mirror surface (see Fig. 2-3, top schematic) [141] [143].

Next, the Jones matrix for the sample is given by,

$$\hat{S}(\alpha) = \begin{pmatrix} 1 & -(\emptyset_k + i\eta_k) \\ (\emptyset_k + i\eta_k) & 1 \end{pmatrix} \tag{2.9}$$

where $\emptyset_k$ and η_k represent Kerr rotation and ellipticity, respectively, near normal incident angle α. The last Jones matrix for the 2nd polarizer (analyzer) having an angle $\emptyset$ in the *x*-*y* plane can be represented as,

$$\hat{P}_2(\emptyset) = \begin{pmatrix} cos^2\emptyset & cos\emptyset sin\emptyset \\ sin\emptyset cos\emptyset & sin^2\emptyset \end{pmatrix} \tag{2.10}$$

After multiplying all of the Jones matrices (Eqs. (2.6) - (2.10)), one can derive equations for the Jones vector representing the light reaching at the detector. The detected signal can be eventually calibrated to Kerr rotation $\emptyset_k$ [deg] and Kerr ellipticity η_k [deg] signals in polar geometry as shown in Eqs. (2.11) and (2.12),

$$Kerr\ ellipcity: \quad \frac{I_f}{I_{dc}} = 2\sqrt{2}\, tan\Psi(\alpha_1) J_1(\delta_0) \underbrace{\left(\emptyset_k sin\Delta(\alpha_1) + \eta_k cos\Delta(\alpha_1)\right)}_{\text{Intermixing of Kerr ellipticity } (\eta_k) \text{ and Kerr rotation } (\emptyset_k)} \tag{2.11}$$

$$Kerr\ rotation: \quad \frac{I_{2f}}{I_{dc}} = 2\sqrt{2}\, tan\Psi(\alpha_1) J_2(\delta_0) \underbrace{\left(\emptyset_k cos\Delta(\alpha_1) - \eta_k sin\Delta(\alpha_1)\right)}_{\text{Intermixing of Kerr ellipticity } (\eta_k) \text{ and Kerr rotation } (\emptyset_k)} \tag{2.12}$$

where I_f is the *AC* signal intensity modulated by the first harmonic frequency in *PEM*, I_{dc} is the *DC* signal intensity without any phase modulation, $tan\Psi$ and Δ are ellipsometric parameters of the mirror, $J_1(\delta_0)$ is the first order of Bessel function with specific phase retardation amplitude δ_0 of *PEM* (see Fig. 2-2), α_1 is the incident angle of the light incident on the mirror, I_{2f} is the *AC* signal intensity modulated by a second harmonic frequency in *PEM*, and $J_2(\delta_0)$ is the second order of the Bessel function with specific phase retardation amplitude δ_0 of PEM. The terms $\left(\emptyset_k sin\Delta(\alpha_1) \pm \eta_k cos\Delta(\alpha_1)\right)$ represent intermixing of Kerr ellipticity (η_k) and Kerr rotation $(\emptyset_k)$

parameters induced by the optical mirror. The Eqs. (2.11) and (2.12) include $1/\sqrt{2}$ factor because the lock-in amplifier measures the root-mean-square of the *AC* signal. It should be underlined here that the Eqs. (2.11) and (2.12) indicate that the measured signals are affected by an intermixing of the Kerr ellipticity (η_k) and the Kerr rotation ($\emptyset_k$) components due to the presence of the extra ellipsometry parameters, $tan\Psi$ and Δ from the optical mirror [141] [144]. Because of that, this type of polar MOKE setup suffers from losing the quantitative accuracy of the obtained experimental results due to the ellipsometry parameters of the optical mirror. The same scenario is observed when considering the reflection-mode MCD setup.

In cases where the mirror is not implemented to the polar-MOKE configuration, the terms $tan\Psi = 1$ and $\Delta = 0$ so that one can get rid of the ellipsometry terms from the Eqs. (2.11) and (2.12). Therefore, the Eqs (2.13) and (2.14) show pure Kerr ellipticity (η_k) and Kerr rotation ($\emptyset_k$) signals without any intermixing signals,

$$Kerr\ ellipcity: \qquad \frac{I_f}{I_{dc}} = 2\sqrt{2}\,AJ_1(\delta_0)\eta_k \tag{2.13}$$

$$Kerr\ rotation: \qquad \frac{I_{f2}}{I_{dc}} = 2\sqrt{2}\,BJ_2(\delta_0)\emptyset_k \tag{2.14}$$

where *A* and *B* are calibration factors [141] [145] and the meaning of other parameters remains as defined previously. In addition, $J_1(\delta_0)$ and $J_2(\delta_0)$ values can be found in the plot of the Bessel function (Fig. 2-2). Then, one can calibrate the detected signals into the Kerr ellipticity (η_k) [deg] and the Kerr rotation($\emptyset_k$) [deg] using Eqs. (2.13) and (2.14).

Consequently, Eqs. (2.11) – (2.14) suggests that the intermixing of Kerr ellipticity (η_k) and Kerr rotation ($\emptyset_k$) are due to the ellipsometry parameters ($tan\Psi$ and Δ) and can

be treated as the background noise. To reduce the background noise from the measured signal, Ref. [141] suggests to use a dielectric mirror that has $\Delta \approx 180°$ so that one can reduce the intermixing of $\emptyset_k$ and η_k because the *sine* terms in Eqs. (2.11) and (2.12) can be eliminated. Another way to get rid of the background noise can be conducted by measuring the ellipsometric parameters ($tan\Psi$ and Δ) of the optical mirror using an ellipsometer. Then, one can mathematically correct the measured signal to obtain more precise results using the measured ellipsometric parameter.

The discussion presented in Sections 2.1.1 and 2.1.2 described the Mueller matrix and the Jones matrix formalisms for the MCD and MOKE instrumentation and experimental data calibrations procedures. We would like to emphasize here that, in the case of the transmission-mode MCD measurement; these procedures are straight forward according to the Eqs. (2.1) – (2.5). On the other hand, these routines for the mirror-based reflection-mode MCD and polar MOKE setups are more complicated due to the none zero ellipsometric parameters ($tan\Psi$ and Δ) of the mirror. Thus, one has to pay attention when interpreting the experimental results using these approaches. This aspect is further emphasized in Chapter 4 which focuses on developing an experimental setup and in Chapter 6 where we discuss and interpret obtained experimental results. The detailed explanation and derivations of equations discussed in this section are presented in Appendix B.

2.2 Theory of diluted magnetic semiconductors

This section presents a theoretical framework underlining the physics of diluted magnetic semiconductors (DMSs) needed for analyses of experimental results obtained in this project. First, in Section 2.2.1, I will focus on the mechanism of the *sp-d* exchange interactions, which are the key phenomena in TM-doped II-VI and III-V DMSs. In general, the enhancement of the Zeeman splitting energy in TM-doped II-VI and III-V DMSs is caused by the *sp-d* exchange interactions disregard of the critical points of Brillouin Zone. Therefore, the *sp-d* exchange constants can be used to derive the Zeeman splitting energy in the following section. Section 2.2.2 explains the selection rules for the optical transition in conjunction with the Zeeman splitting effect. It will be shown that by applying the selection rules for the Γ-CPs of the Brillouin zone, one can find out the different optical transition energies in the zinc-blend band gap structure of DMS. Then, using these optical transition energies, Zeeman splitting energy at the Γ-CPs in the DMS can be estimated in terms of the *sp-d* exchange constant. With a similar concept, the Zeeman splitting energy at *L*-CPs of Brillouin Zone will also be shown. In Sections 2.2.3, I will explain the concept of a rigid band shift model which can be used for the analysis of the experimentally obtained results. Finally, in Section 2.2.4, I will show the fitting and deconvolution method to extract the accurate MCD signal at *L*-CP using an energy derivative of the Gaussian function. The detailed derivations of equations discussed in the following are collected in Appendixes C, D, and E.

2.2.1 *sp-d* exchange interaction

When magnetic ions having *d*-orbital are incorporated in the non-magnetic DMS, they substitute the cation site having the *s*-orbital. Also, the *s*-orbital of cation and the *p*-orbital of the anion form the conduction and valence bands in the DMS [99]. It is known that the *s, p* and *d* electrons form sp^3 hybridizations involved in the bonding. In general, the DMS band structure is the same as that of the undoped host semiconductor [99]. There are two types of band structures, namely zinc-blende and wurtzite observed in DMS [99]. The $Ga_{1-x}Mn_xAs$ has the zinc-blende structure, and the direct band gap is at Γ-CPs whereas the indirect band gap is at *L*-CPs.

In DMS, there are two fundamental interaction mechanisms between *sp* electrons in the host semiconductor and *d*-electrons in the magnetic ions, known as the potential exchange and kinetic exchange interactions [99] [146]. The first one, potential exchange interaction, is due to direct Coulomb exchange which tends to make a ferromagnetic spin alignment ($+N_0\alpha$) as shown in Fig. 2-4. The $+N_0\alpha$ indicates ferromagnetic potential *s-d* exchange constant. The N_0 is the number of the cations (magnetic ions) per unit volume, and α is the exchange integral for *s-d* exchange interaction [70].

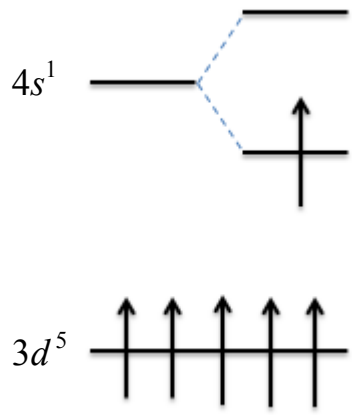

Ferromagnetic
s-d potential exchange interaction

$N_0\alpha > 0$

Figure 2-4 Schematic illustration of ferromagnetic potential *s-d* exchange interaction generated in an ionized Mn atom [99] [146].

On the other hand, the kinetic exchange is due to hybridization of *p*- and *d*-electron's wavefunctions, which causes ferromagnetic ($+N_0\beta$) or anti-ferromagnetic ($-N_0\beta$) spin alignment depending on the number of spins in *d*-electrons. The $+N_0\beta$ indicates ferromagnetic kinetic *p-d* exchange constant and $-N_0\beta$ indicates anti-ferromagnetic kinetic *p-d* exchange constant, respectively. The β parameter is the exchange integral for *p-d* exchange interaction [70]. In the case of the *p-d* hybridization, t_{2g}-orbitals of transition metal ion can only couple with a valence band of *p*-orbitals due to the same Γ_{15} symmetry [73] [99] [147] [148] [149]. The kinetic *p-d* exchange interaction can be explained by a virtual jump of *p*-electrons to *d*-orbital, and vice versa [99].

As shown in Fig. 2-5, if the number of spin-up electrons in the metal ions is less than five (*e.g.* Cr^{2+} (d^4)), then both spin-up and spin-down *p*-electrons can jump to t_{2g}-orbitals of Mn^{2+} ion. Such processes illustrate the ferromagnetic kinetic *p-d* exchange interaction ($+N_0\beta$) and antiferromagnetic kinetic *p-d* exchange interaction ($-N_0\beta$), respectively [99].

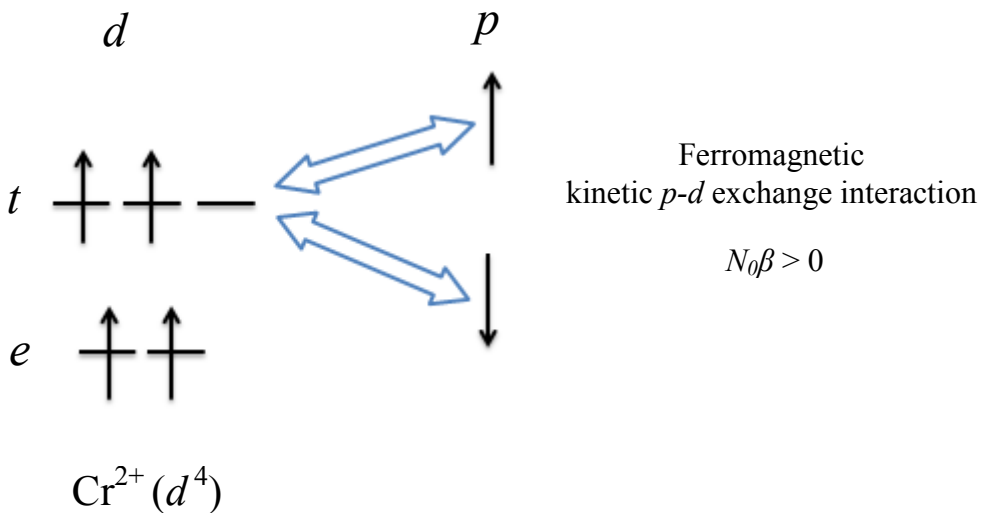

Figure 2-5 Schematic illustration of ferromagnetic *p-d* exchange interaction for Cr^{2+} in the T_d symmetry. Note: only *t*-orbital can mix with *p*-orbitals due to the same Γ_{15} symmetry [73] [99] [146].

However, if more than five spin-up electrons are already occupied in the metal ions (*e.g.* Mn^{2+} (d^5) or Ni^{2+} (d^8)), then only spin-down electron in *p*-orbital can jump to t_{2g}-orbitals of transition metal ions as shown in Fig. 2-6 [99]. Then, one can only expect the antiferromagnetic kinetic *p-d* exchange interaction ($-N_0\beta$) according to the Hund's rule.

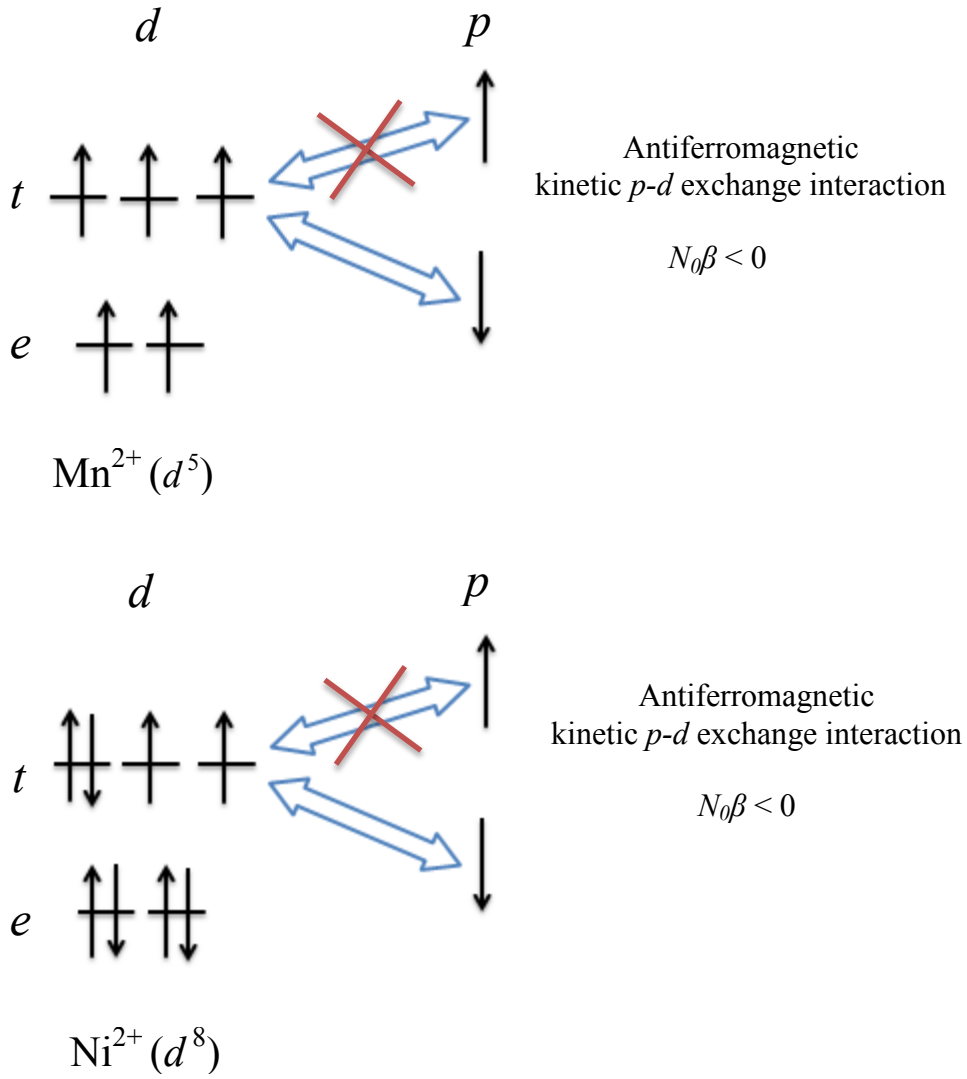

Figure 2-6 Schematic illustration of antiferromagnetic kinetic *p-d* exchange interaction for Mn^{2+} and Ni^{2+} ions in the T_d symmetry. Note: only *t*-orbital can mix with *p*-orbitals due to the same Γ_{15} symmetry [73] [99] [146].

In the case of $Ga_{1-x}Mn_xAs$, Mn^{2+} ion substitutes for Ga^{3+} ion site (*i.e.*it is an acceptor) and the Mn^{2+} ion has the total spin number $S = 5/2$ and total orbital moment $L = 0$ [147]. The process of hole carriers generation by doping $Ga_{1-x}Mn_xAs$ with Mn^{2+} ions is considered as the source of the magnetic moment in this semiconductor [147].

Figure 2-7 shows detailed illustrations of *p*-*d* hybridization in $Ga_{1-x}Mn_xAs$ [147] [148]. The atomic unpolarized levels exist in the *d*-orbital of the magnetic ions before the hybridization (Fig. 2-7 (a)). The energy state of Mn (anion, *d*-orbital) is split with occupied spin-up and unoccupied spin-down electrons states by the atomic exchange (*i.e.* effective on-site 3*d*-3*d* Coulomb interaction) according to the first Hund's rule as shown in Fig. 2-7 (b) [73] [99] [147] [148]. Since the transition metal ion considered here has a tetrahedral structure due to the presence of four anions (Γ_d point symmetry), the Γ_d crystal field further splits the occupied and unoccupied states into a doublet of degenerated e_g states ($3d_{x^2-y^2}$,$3d_{z^2}$) and a triplet of degenerated t_{2g} states ($3d_{xy}$,$3d_{xz}$,$3d_{yz}$), respectively, as shown in Fig. 2-7 (c) and also in Fig. 2-8 [73] [99] [105] [147] [148]. It is known that the e_g doublet is Γ_{12} symmetry whereas the t_{2g} triplet is the Γ_{15} symmetry [149]. Furthermore, the *p*-levels of anions (As^{3-} ions) also are Γ_{15} symmetry. Therefore, the e_g states weakly couple with the energy state of As. On the other hand, the t_{2g} states of Mn hybridizes with the *p*-states of As because they both have Γ_{15} symmetry as shown in Fig. 2-7 (c) [73] [99] [147]–[149]. When the *p*-spins of As (three spin-up) are parallel to the *d*-spins of Mn (three up-spins) at the top of the valence band, the *p*-spins of As are shifted up in energy. On the contrary, when the *p*-spins of As (three spin-down) are antiparallel to the *d*-spins of Mn (three spin-up) at the top of the valence band, the *p*-spins of As are shifted down in energy as shown in Fig. 2-7 (d). Thus, the first effect caused by a single Mn having spin-up at substitutional position in $Ga_{1-x}Mn_xAs$ is introducing three spin-up polarized levels above the top of the valence band and three spin-down polarized levels below the top of the valence band. Here, the three spin-up and spin-down states

predominantly have As *p* character [147]. The second effect caused by single Mn dopant is introducing a hole at the highest of the three antibonding states as schematically indicated by an empty circle in Fig. 2-7 (d). In this way, this hybridization causes antiferromagnetic coupling between localized and itinerant spins by the Zener's kinetic-exchange mechanism as described before [147] [148].

The hybridization process described above is responsible for a kinetic *p-d* exchange interaction represented by the *p-d* exchange $N_0\beta$ constant [73] [99] [147] [148]. At the same time, the potential *s-d* exchange interaction is represented by the *s-d* exchange $N_0\alpha$ constant [73] [99] [147] [148]. On the other hand, there is no kinetic *p-d* exchange interaction ($N_0\beta$) in conduction band, therefore the *s-d* exchange constant ($N_0\alpha$) by potential exchange interaction is more dominant in this case in contrast to the *p-d* exchange constant ($N_0\beta$) by kinetic exchange interaction being more dominant in the valence. It should be mentioned here once more that the - $N_0\alpha$ and -$N_0\beta$ terms indicate antiferromagnetic *s-d* and *p-d* couplings, respectively, whereas the +$N_0\alpha$ and +$N_0\beta$ terms indicate ferromagnetic *s-d* and *p-d* coupling.

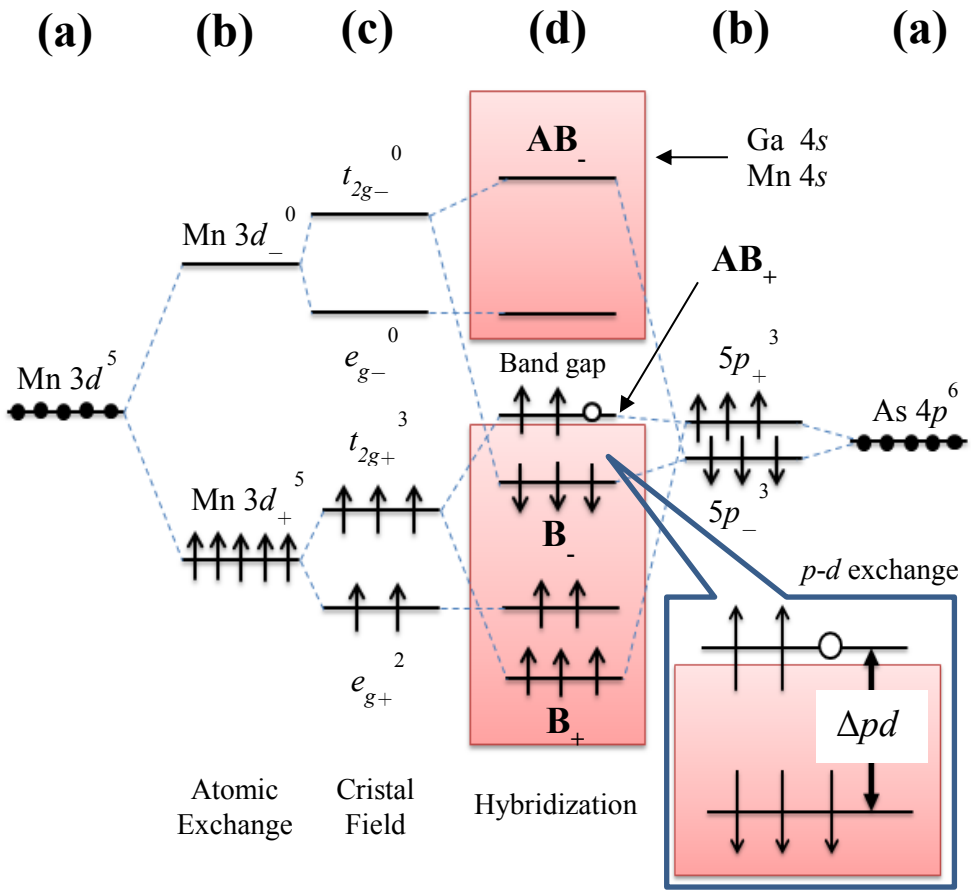

Figure 2-7 A schematic drawing of *p-d* hybridization in $Ga_{1-x}Mn_xAs$. (a) Atomic unpolarized levels (b) The energy state of Mn (anion, *d*-orbital) is split with occupied spin-up and unoccupied spin-down electrons by the atomic exchange according to Hund's first rule as well as the energy state of As. (c) Since the transition metal ion has tetrahedral structure by four anions (Γ_d point symmetry), the Γ_d crystal field further splits the occupied and unoccupied states into doublet of degenerated e_g states and triplet of degenerated t_{2g} states. (d) The e_g states weakly couple with the energy state of As (cation, *p*-orbital). On the other hand, t_{2g} states of Mn hybridizes with *p* states of As. Shaded areas illustrates the host crystal bands [73] [99] [147][148]. + and – indicate up-spin and down-spins, respectively. B and AB represent bonding and antibonding, respectively. Δpd indicates *p-d* exchange energy.

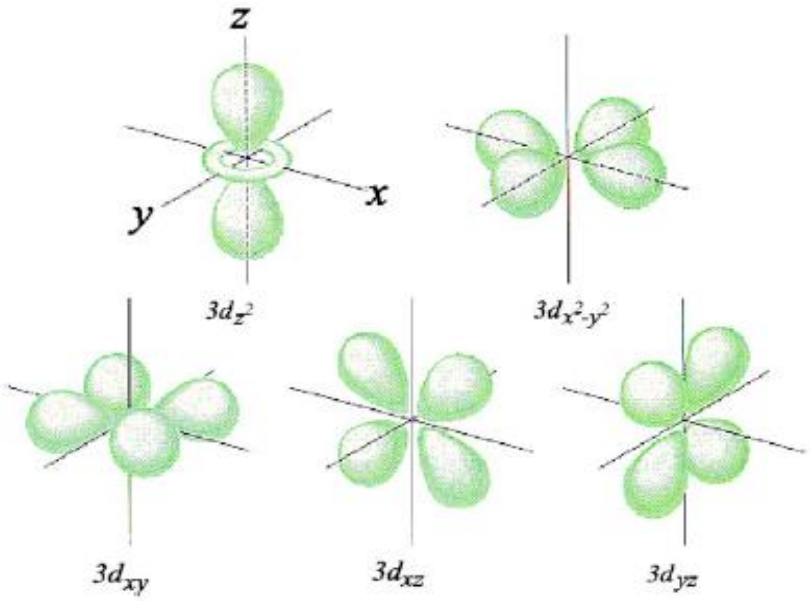

Figure 2-8 Two e_g 3*d* ortibals and three t_{2g} 3*d* orbitals of Mn in $Ga_{1-x}Mn_xAs$ [105]. This figure corresponds to the crystal field splitting shown in the Fig. 2-7 (c).

In this section, we have emphasized the importance of *sp-d* exchange interactions when the $Ga_{1-x}Mn_xAs$ is considered. Specifically, the mechanism of potential *s-d* exchange interactions and kinetic *p-d* exchange interactions was explained. Furthermore, the potential *s-d* exchange constant ($N_0\alpha$) and kinetic *p-d* exchange constant ($N_0\beta$) will be considered later in this discussion as crucial parameters to obtain the Zeeman splitting energy in the DMS.

2.2.2 Zeeman splitting energy at Γ and *L* critical points

One of the main efforts of this work was to estimate the Zeeman splitting energy which indicates strength of the magnetization in the DMS. As mentioned in the previous section, the Zeeman splitting energy can be enhanced by the *sp-d* exchange interaction,

and it can be probed by a magneto-optical technique. Therefore, in the following sections, Zeeman splitting can be explained by different optical transitions for both Γ- and L-CPs of Brillouin zone in a zinc-blende structure DMS. Then, the Zeeman splitting energies will be represented in terms of s-d ($N_0\alpha$) and p-d ($N_0\beta$) exchange constants in the presence of the magnetic field.

2.2.2.1 Γ critical points

Figure 2-9 shows GaAs theoretical energy band structure with indicated inter-band critical points [150] [151]. In the past, most of the magneto-optical investigations involving $Ga_{1-x}Mn_xAs$ were conducted for Γ-CPs due to its direct energy band gap nature which is useful for many practical applications and devices.

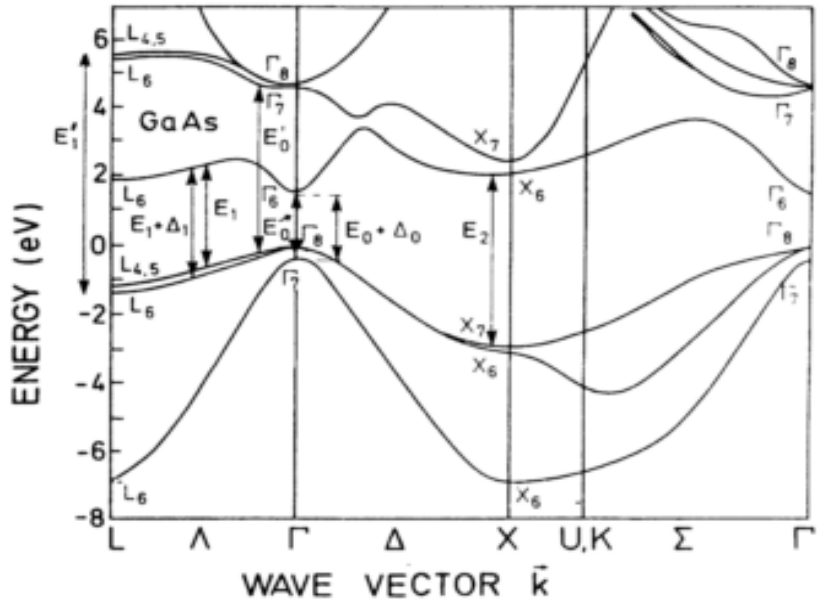

Figure 2-9 Theoretical band structure of GaAs showing main interband critical points [150] [151].

When the DMSs are subjected to the magnetic field, the enhanced Zeeman splitting can be generated in the semiconductor band structure due to the *sp-d* exchange interactions. Under such circumstances, the optical transitions of right circularly polarized light (σ+) and left circularly polarized light (σ-) are allowed between certain energy states based on the selection rules at Γ-CPs [99] [108] [152]. This indicates that spin-up electrons can only be excited to spin-up energy states and spin-down electrons can only be excited to spin-down energy states, respectively. Here, the selection rule is considered as the *conservation of total angular momentum of the electron* which can be expressed, in general, by the Eq. 2-3-1

$$L_{e,ground} + \sigma_{ph} = L_{e,excited} + \sigma_{ph} \tag{2.15}$$

where $L_{e,ground}$ is the total angular momentum of the electron at ground state (*i.e.* initial state), σ_{ph} is the angular momentum of the photon ($\sigma\pm = \pm 1$), and $L_{e,excited}$ is the total angular momentum of the electron at excited state. After the excitation, the angular momentum of the photon (σ_{ph}) is absorbed by the electrons. Thus, the angular momentum of the photon (σ_{ph}) can be considered to be equal to zero after the excitation in the Eq. (2.15). It should be noted here that this selection rule is only applied to Γ-CPs and the reason is described in the next section for *L*-CP [70] [72] [76]. For more detailed discussion of the selection rules applicability please refer to Appendix C.

Figure 2-10 summarizes all total angular momentum quantum numbers for each energy state and the allowed optical transitions between them at Γ-CPs. The optical transitions indicated as (A) and (D) involve the heave holes velence band whereas the (B) and (C) optical transitions involve the light hole valence band, respectively [99]. The E_0

and $E_0+\Delta_0$ parameters represent overall optical transition energies corresponding to the peaks observed in MCD spectra (see Chapter 5 and 6). It can be see in this Fig. 2-10 that the E_0 transition energy receives contribution from multiple optical transitions (A)-(D), where the optical transitions indicated as (E) and (F) due to the spin-orbit split-off band and they contribute to the $E_0+\Delta_0$ transition energy.

As we have mentioned in the earlier section, the $Ga_{1-x}Mn_xAs$ conduction band is formed by the *s*-orbital of the cation (Ga^{3+} ion) for which the *s-d* exchange energy can be represented by the $xN_0\alpha\langle S_z\rangle$ term [71]. Likewise, the valence band is formed by the *p*-orbital of the anion (As^{3-} ion) and the *p-d* exchange energy and can be represented by $xN_0\beta\langle S_z\rangle$ term. In both terms, the x is the magnetic ions concentration, $\langle S_z\rangle$ represents the average energy of magnetic ion's spin along the external magnetic field direction (here z direction) [99] [102] [108] [153] and N_0 and α parameters are the same as defined in Section 2.2.1. Therefore, the order of the total angular momentum for each energy state involved in optical transition, as shown in Fig. 2-10, depends on the average energy $\langle S_z\rangle$ of an electron in the conduction band and the valence band. [71].

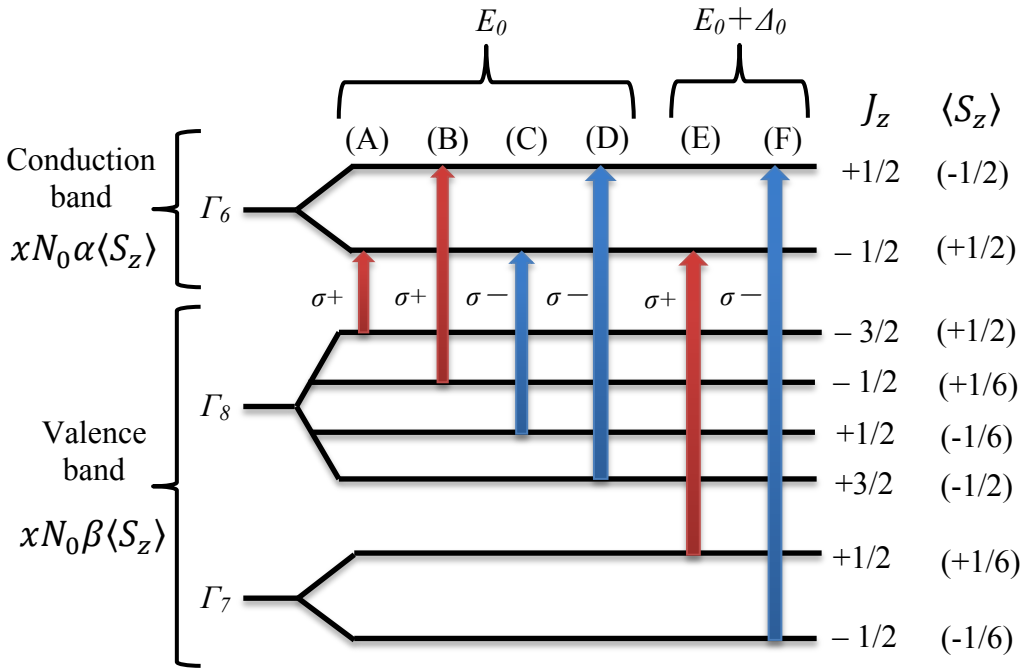

Figure 2-10 Total angular momentum quantum number of each energy state and the optical transitions at Γ critical points. $xN_0\alpha\langle S_z\rangle$ and $xN_0\beta\langle S_z\rangle$ are *s-d* exchange energy and *p-d* exchange energy, respectively. x is the magnetic ions concentration and $\langle S_z\rangle$ is the average energy of an electron in conduction and valence band [71]. Please not that Fig. 2-10 shows total angular momentum $J_z = m_j\hbar$ where Planck's constant $(\hbar)$ is omitted in the figure for simplicity [99].

Now, based on the selection rules and average energies $\langle S_z\rangle$ of the electron for each energy state, one can determine the energies of optical transitions (A) – (D) for E_0 ($\Gamma_8 \rightarrow \Gamma_6$) as shown in Fig. 2-10 [71] [99],

$$E_A(\sigma^+) = E_g - \frac{1}{2}x(N_0\beta - N_0\alpha)\langle S_z\rangle \tag{2.16}$$

$$E_B(\sigma^+) = E_g - \frac{1}{6}x(N_0\beta + 3N_0\alpha)\langle S_z\rangle \tag{2.17}$$

$$E_C(\sigma^-) = E_g + \frac{1}{6}x(N_0\beta + 3N_0\alpha)\langle S_z\rangle \tag{2.18}$$

$$E_D(\sigma^-) = E_g + \frac{1}{2}x(N_0\beta - N_0\alpha)\langle S_z\rangle \tag{2.19}$$

where $E_A(\sigma^+), E_B(\sigma^+), E_C(\sigma^-)$, and $E_D(\sigma^-)$ represents the optical transition energies of (A), (B), (C), and (D) optical transitions as shown in Fig. 2-10. E_g is the bandgap energy of the semiconductor.

Similarly, the energies of optical transitions (E) and (F) for $E_0+\Delta_0$ ($\Gamma_7\rightarrow\Gamma_6$) shown in Fig. 2-10 are given by,

$$E_E(\sigma^-) = E_g + \Delta_{SO} - \frac{1}{6}x(N_0\beta - 3N_0\alpha)\langle S_z\rangle \tag{2.20}$$

$$E_F(\sigma^+) = E_g + \Delta_{SO} + \frac{1}{6}x(N_0\beta - 3N_0\alpha)\langle S_z\rangle \tag{2.21}$$

where $E_E(\sigma^-)$ and $E_F(\sigma^+)$ represent the transition energies of (E) and (F) optical transitions as shown in Fig. 2-10, and Δ_{SO} is the spin-orbit splitting energy of the valence band at Γ-CPs. The meaning of parameters (N_0, α, β and $\langle S_z\rangle$) in Eqs. (2.16) - (2.21) remain as defined previously,

Based on the energies of the optical transitions (Eqs. (2.16) – (2.21)), one can find out the Zeeman splitting energies of E_0 and $E_0+\Delta_0$ transitions at Γ-CPs, which is essentially the energy difference between right circularly polarized light (σ^+) and left circularly polarized light (σ^-) [99] [102] [108] [153] [154]. There are three distinct cases to consider.

1. Zeeman splitting energy ΔE for E_0 transition (heavy-hole),

$$\Delta E = E_D(\sigma^-) - E_A(\sigma^+) = x\,(N_0\beta - N_0\alpha)\,\langle S\rangle \tag{2.22}$$

2. Zeeman splitting energy ΔE for E_0 transition (light-hole),

$$\Delta E \;=\; E_C(\sigma^-) - E_B(\sigma^+) \;=\; \frac{1}{3}\,\mathrm{x}\,(N_0\beta \;+\; 3N_0\alpha)\,\langle S\rangle \qquad (2.23)$$

3. Zeeman splitting energy ΔE for $E_0 + \Delta_0$ transition,

$$\Delta \mathrm{E} \;=\; E_E(\sigma^-) - E_F(\sigma^+) \;=\; \frac{1}{3}\,\mathrm{x}\,(-N_0\beta \;+\; 3N_0\alpha)\,\langle S\rangle \qquad (2.24)$$

Equations (2.22) – (2.24) represents the Zeeman splitting energies at Γ-CPs in terms of the *s-d* exchange constant ($N_0\alpha$) and *p-d* exchange constant ($N_0\beta$). The supplemental explanations of the selection rules and derivations of the Zeeman splitting energies are shown in Appendix C.

2.2.2.2 *L* critical points

It is generally accepted that optical transitions in a semiconductor are most frequently considered at the center of the Brillouin zone (*i.e.* Γ-CPs) for practical reasons. However, our focus in this project is more on *L*-CPs (see Fig. 2-9). As described in the earlier chapter, the impurity bands (IBs) are generated inside of the band gap at Γ-CPs as the concentration of the Mn increases. The IB-related multiple optical transitions make the interpretations of the experimental results much more difficult. Therefore, we intentionally investigate the transitions at *L*-CPs first, then using obtained information, we attempt to conclude the situations at Γ-CPs using some theoretical and experimental assumptions.

Figure 2-11 shows the total angular momentum J_z and the optical transitions at *L* critical points (CPs) [70] [76] [139] [155]. When spin is neglected, the first conduction band is Λ_1 singlet and the upper valence band is a Λ_3 doublet in II-VI or III-V

semiconductors [155]. However, when spin is considered, Λ_1 singlet conduction band becomes the doubly degenerate Λ_6. Similarly, Λ_3 doublet valence band is split by the spin-orbital interaction into two doublets, $\Lambda_{4,5}$ and Λ_6 [155]. In this work, Zeeman splitting energy was investigated by analyzing the optical transition between $\Lambda_{4,5}$ in the valence band and Λ_6 in the conduction band ($\Lambda_{4,5} \rightarrow \Lambda_6$), and the optical transition between Λ_6 in valence band and Λ_6 conduction band ($\Lambda_6 \rightarrow \Lambda_6$) [155]. The optical transition $\Lambda_{4,5} \rightarrow \Lambda_6$, and $\Lambda_6 \rightarrow \Lambda_6$ correspond to E_1 and $E_1+\Delta_1$ structures, respectively [155]. It should be noted that Λ-CPs are often referred to as L-CPs since Λ- and L-CPs are next to each other. It was demonstrated in the past, when studying Mn-doped zinc-blende II-VI DMS, that it is very difficult to apply the selection rules for transitions at L-CPs [70] [72]. The Zeeman splitting in that case at E_1 (*L- CPs*) was theoretically and experimentally estimated to be ~1/4 and ~ 1/16 smaller than one at E_0 (Γ-CPs), respectively [70] [72] [76]. That research's findings demonstrated that accurate optical transitions energies cannot be determined exactly using the selection rule at L-CPs due to the fine electronic levels structure involved. We have adopted in this project the same idea to investigate Mn-doped zinc-blende III-V DMS because this idea was already applied to the III-V semiconductors as shown in Refs. [139] and [155].

Now, the E_1 transition is contributed by multiple optical transitions (A) – (D) and similarly, $E_1+\Delta_1$ transition is contributed by other multiple optical transitions (E) – (H) as shown in Fig. 2-11.

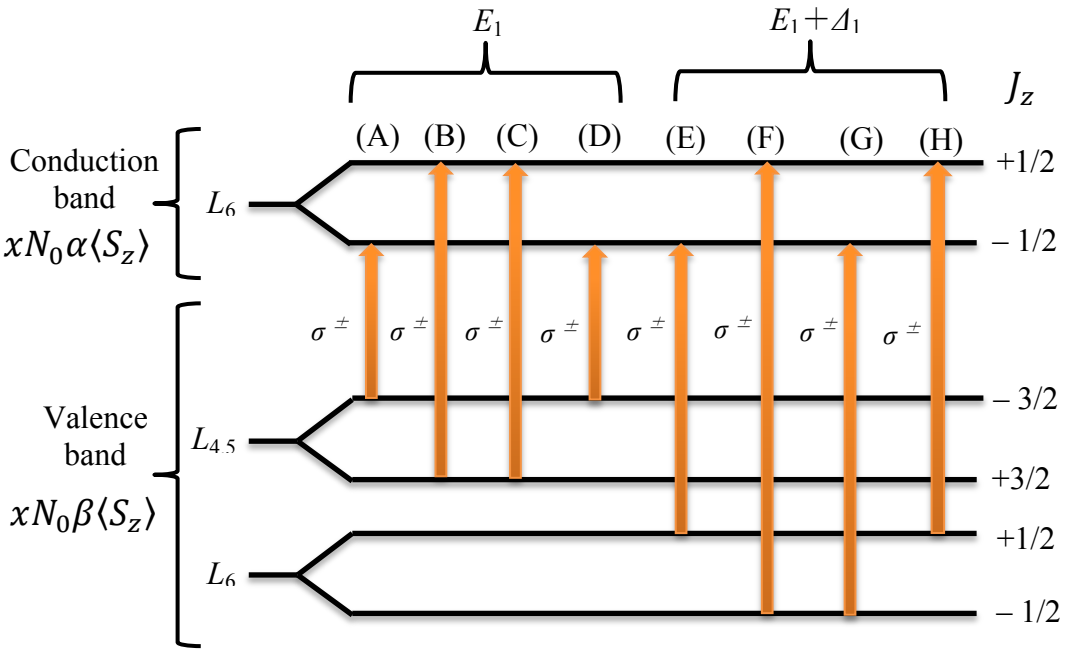

Figure 2-11 Total angular momentum quantum and the optical transitions at *L* critical points. $xN_0\alpha\langle S_z\rangle$ and $xN_0\beta\langle S_z\rangle$ are *s-d* exchange energy and *p-d* exchange energy, respectively. *x* is the magnetic ions concentration and $\langle S_z\rangle$ is the average energy of an electron in the conduction and valence band [71]. Please note that Fig. 2-11 shows the total angular momentum $J_z = m_j\hbar$ where Planck's constant $(\hbar)$ is omitted in the figure for simplicity [70] [76] [139].

We have demonstrated above that the E_1 transition depends on the contribution from multiple (A) – (D) optical transitions as well as the $E_1+\Delta_1$ transition is influenced by multiple (E) – (H) optical transitions (see Fig. 2-11). As a result of that, the Zeeman splitting energies E_1, and $E_1+\Delta_1$ at *L-CPs* can be expressed by Eqs. (2.25) and (2.26) [70] [76] [99],

$$\Delta E_1 \cong r\left(N_0\alpha - \frac{1}{4}N_0\beta\right)\langle S_z\rangle \tag{2.25}$$

$$E_1 + \Delta_1 \cong -rx\left(\frac{1}{4}N_0\beta - N_0\alpha\right)\langle S_z\rangle \tag{2.26}$$

where N_0, α, β and $\langle S_z \rangle$ parameters remain the same as defined in Eqs. (2.16) - (2.21), and r is the numerical factor depending on the magnetic field orientation as shown in equation (2.27),

$$r = \begin{cases} \frac{2}{5}, B \| \langle 111 \rangle \; or \; \langle 110 \rangle \\ \frac{1}{2}, \; B \| \langle 000 \rangle \\ \frac{4-\pi}{2}, B \; is \; randomely \; oriented \end{cases} \tag{2.27}$$

Equations (2.25) – (2.26) represents the Zeeman splitting energies at L-CPs in terms of the *s-d* exchange constant ($N_0\alpha$) and *p-d* exchange constant ($N_0\beta$). We have summarized the expression for estimating the Zeeman splitting energy at E_0 and $E_0+\Delta_0$, (Γ- CPs) and E_1 and $E_1+\Delta_1$ (L-CPs) in Table 2-1[99].

Table 2-1 Summary of Zeeman splitting energy at E_0 and $E_0+\Delta_0$ (Γ-CPs), and E_1, $E_1+\Delta_1$ (L-CPs) critical points involving the *sp-d* exchange interactions in the DMSs [99].

Critical point	Transition	$\Delta E = E(\sigma^-) - E(\sigma^+)$
Γ	E_0 (heavy-hole)	$x\,(N_0\beta - N_0\alpha)\,\langle S \rangle$
	E_0 (light-hole)	$\frac{1}{3}\,x\,(N_0\beta + 3N_0\alpha)\,\langle S \rangle$
	$E_0+\Delta_0$	$\frac{1}{3}\,x\,(-N_0\beta + 3N_0\alpha)\,\langle S \rangle$
L	E_1	$rx\left(\frac{1}{4}N_0\beta - N_0\alpha\right)\langle S_z \rangle$
	$E_1+\Delta_1$	$-rx\left(\frac{1}{4}N_0\beta - N_0\alpha\right)\langle S_z \rangle$

Using Table 2-1, one can estimate separately the potential *s-d* exchange constant ($N_0\alpha$) and kinetic *p-d* exchange constant ($N_0\beta$) when the Zeeman splitting energy of the two different optical transitions is known and the value of the magnetic moment in the DMS is available [99]. It should be mentioned here that the magnitude of the *p-d* exchange constant ($N_0\beta$) is generally larger than that of the potential *s-d* exchange constant ($N_0\alpha$) in typical DMSs. Therefore, if the Zeeman splitting energy of one optical transitions and the value of the magnetic moment are known, one can determine the polarity of $N_0\beta$ which indicates the ferromagnetic or anti-ferromagnetic coupling of *p-d* exchange interaction as mentioned earlier [99]. In general, it has been widely accepted that the *p-d* exchange interaction of $Ga_{1-x}Mn_xAs$ is anti-ferromagnetic coupling ($-N_0\beta$) based both on theoretical and experimental results [109] [156] [157]. In summary, we shall emphasize that understanding the relationship between the Zeeman splitting, optical transitions, and *sp-d* exchange interaction help to comprehend the physics behind the experimental magneto-optical results as discussed in the following chapters.

2.2.3 Rigid band shift model

The rigid band shift model has been frequently applied to the DMSs [99] [158]. It is a very useful model and suitable to investigate this class of materials because of its ability to directly analyze the experimentally obtained MCD signals. In the rigid band shift model, one assumes that the absorption edge of the energy band gap can be modulated by the Zeeman splitting but the shape of the band gap structure itself does not change. This concept is schematically shown in Fig. 2-12. As illustrated there, when the photon energy

reaches to the bandgap energy (E) of the DMS, the light absorption coefficient (k*) increases and it saturates for energies larger than the band gap energy (E). When magnetic field is applied to the DMS, Zeeman splitting (ΔE) can occur and the absorption edge of the energy band gap (E) can be modulated into spin-up ($E_{\uparrow}$) and spin-down ($E_{\downarrow}$) states. Based on the Fig. 2-12, one can derive equations for the MCD representing the rigid band shift model. The detailed explanations and derivations of the following equations are shown in Appendix D. We would like to mention here, that considering it from the historical perspective, when the physics of DMSs is explained using the rigid band shift model, the absorption coefficient often is represented by k whereas when the physics of the optical components is described using the Mueller and Jones matrices, the absorption coefficient is usually represented by α. Therefore, we will adhere to this scheme.

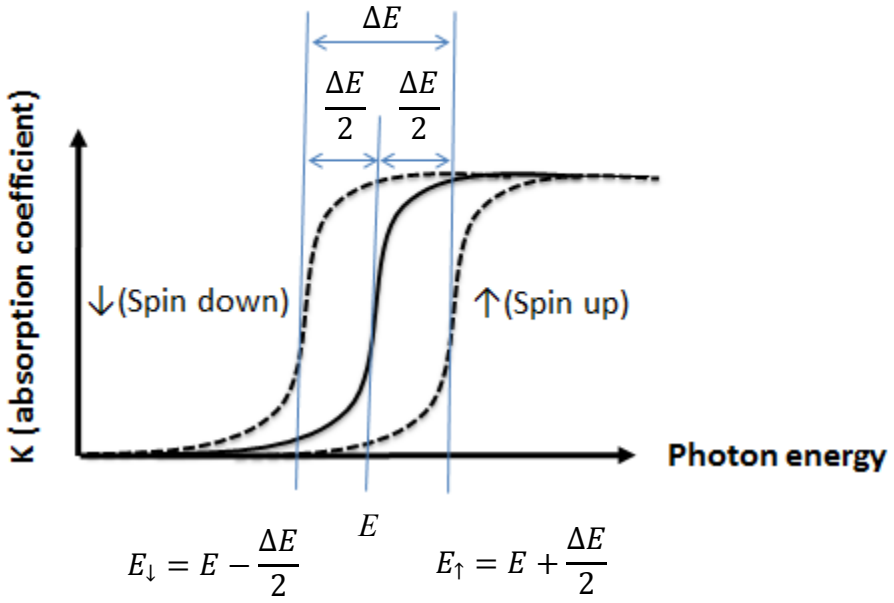

Figure 2-12 Illustration of rigid band shift model. Absorption coefficient k increases when the photon energy reaches to the absorption edge of the semiconductor bandgap E. When magnetic field is applied, the absorption edge splits into two absorption edges for spin-up ($E_\uparrow = E+\Delta E/2$) and spin-down ($E_\downarrow = E+\Delta E/2$). $\Delta E/2$ is the deviation from the semiconductor bandgap E due to the spin-up and spin-down bandgap splitting. ΔE corresponds to Zeeman splitting energy which can be enhanced by *sp-d* exchange interaction.

In the following, we show the final expressions (Eq. (2.28)) of the rigid band shift model which can be used to interpret the experimentally obtained MCD results. The Eq. (2.28) shows the MCD signal as a function of photon energy E and assuming that the $MCD(E)$ is measured in transmission mode for the sample having L thickness [82] [99],

$$MCD(E) = -\frac{45}{\pi}\,\Delta E\,\frac{dkL}{dE} \tag{2.28}$$

where k is the absorption coefficient, and ΔE is the Zeeman splitting energy represented by,

$$\Delta E = -g_{eff}\mu_B H \tag{2.29}$$

where g_{eff} is the effective *g*-factor, μB is the Bohr magneton, and H is the applied magnetic field.

Similarly, the Eq. (2.30) shows the $MCD(E)$ measured in reflection mode for the L thickness sample [75] [104] [139],

$$MCD(E) \approx -\frac{45}{\pi}\,\Delta E\,\frac{dRL}{dE} \tag{2.30}$$

where R is the reflection coefficient, and ΔE is the Zeeman splitting energy represented by Eq. (2.29). Both Eqs. (2.28) and (2.30) are derived based on the rigid band shift model.

The energy derivative of the absorption coefficient k (or reflection coefficient R) can be experimentally obtained using the Eq. (2.31).

$$\frac{dkL}{dE} = -\left[\frac{d}{dE}\left(\log\left(S(E)\right)\right) - \frac{d}{dE}\left(log\left(X(E)\right)\right)\right] \tag{2.31}$$

where $S(E)$ is the intensity after the absorption (or reflection) of light by a sample and $X(E)$ is the initial intensity of the light before the absorption (or reflection) of light by the sample, and L is the sample thickness. The $S(E)$ and $X(E)$ parameters are easily experimentally accessible. Thus, taking the energy derivative of each respective parameter and subtracting them from each other, one can experimentally obtain the $\frac{dkL}{dE}$ and $\frac{dRL}{dE}$ terms. Therefore, by measuring MCD, $\frac{dkL}{dE}$, and $\frac{dRL}{dE}$ signals, one can estimate the Zeeman splitting energy ΔE using the rigid-band shift model (Eqs.(2.28) and (2.30)).

2.2.4 Fitting and deconvolution method using energy derivative of Gaussian function

It was shown previously that the impurity bands (IBs) are created inside of the band gap of $Ga_{1-x}Mn_xAs$ at Γ-CPs. The presence of IB-related multiple optical transitions in DMS disturbs the interpretation of the experimental results at Γ-CPs as compared to the ones at *L*-CPs. Therefore, it would be beneficial, first to try to investigate the magneto-optical results at *L*-CPs and then conclude about their origin at Γ-CPs. However, even though the band structures of the *L*-CPs are much less affected by the IBs, a spectral broadening of the measured MCD spectra can still be observed. In general, the observed broadening is directly related to the material quality strongly affected by the specifics of the material growth method involved (*i.e.* low temperature growth *vs*. high temperature growth method). It is now well established that the $Ga_{1-x}Mn_xAs$ grown at low temperature by molecular beam epitaxy (MBE) does not produce any second phase materials on the surface [8] [83] [94]; however this is achieved at the expense of degrading the material quality which results in MCD spectra broadening [13] [97] [104] [108] [132] [133] [159]–[161]. Therefore, we have introduced a new technique to extract information of the MCD spectra which are free from the broadening effect using the derivative of the Gaussian function.

We will first consider the simplest mode using GaAs to comprehend the process, and then extrapolate this approach on a more complex DMS, which is $Ga_{1-x}Mn_xAs$. In theory, it is known that optical transitions of GaAs at *L*-CPs show two dispersion curves with the opposite polarity due to the two dimensional M_1-type Van Hove singularities as shown in the Fig. 2-13 (a) – (b) [162]. The presence of these two dispersion curves having opposite

polarity has experimentally been confirmed for high quality GaAs grown at high temperature (HT-GaAs) at *L*-CPs [153] and is schematically shown in Fig. 2-13(c). Figure. 2-13(d) shows the magneto-optical signal affected by spectroscopic broadening as typically observed for GaAs or $Ga_{1-x}Mn_xAs$ materials grown at low-temperature (LT-GaAs or $Ga_{1-x}Mn_xAs$) at *L*-CPs. The difference between HT-GaAs and LT-GaAs (or $Ga_{1-x}Mn_xAs$) is that for the former one, deconvolution of magneto-optical spectra is straighter forward due to the clear appearance of the signals at E_1 and $E_1+\Delta E$ optical transitions. In the second case, expected spectral features corresponding to E_1 and $E_1+\Delta E$ peaks are screened out by a broadening effect due to the low temperature growth process involved. The latter scenario is more important here because it is common to observe the broadened spectra in research samples. Thus, to extract accurate values of MCD signals corresponding to E_1 and $E_1+\Delta_1$ peaks from $Ga_{1-x}Mn_xAs$, one has to consider the signal deconvolution procedure.

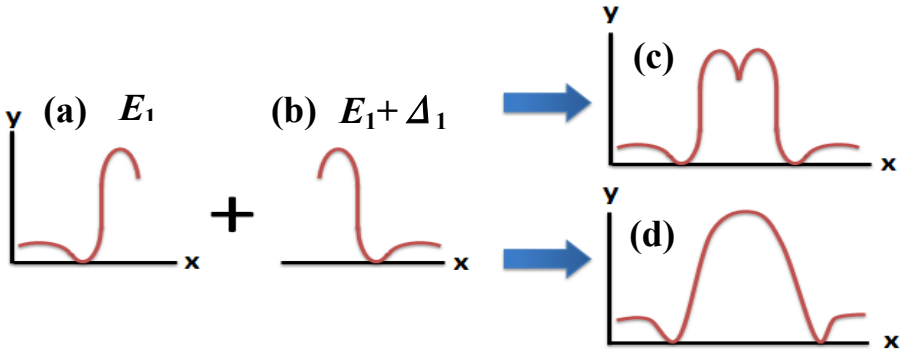

Figure 2-13 (a) - (b) The optical transitions of GaAs at *L*-CPs show two dispersion curves with the opposite polarity due to the two dimensional M_1-type Van Hove singularity [162]. (c) The measured optical transitions of HT-GaAs at *L*-CPs. (d) The measured optical transitions of LT-GaAs or $Ga_{1-x}Mn_xAs$ at *L*-CPs. E_1 and $E_1+\Delta_1$ represent the optical transitions at *L*-CPs. *y*-axis: magneto-optical signal [a.u]. *x*-axis: photon energy [eV].

Considering the above discussion, we have executed a fitting and deconvolution method using the energy derivative of the Gaussian function to extract the information of magneto-optical signals for each optical transition (E_1 and E_1+Δ E_1). Mathematically speaking, the derivative of the Gaussian function represents the dispersion curves. Since E_1 and E_1+Δ E_1 optical transitions are related to each other by a spin–orbit interaction, we assume that they have the same spectral widths and magnitudes but opposite polarities of two derivatives of Gaussian functions. So, the derivative of the Gaussian functions for E_1 and E_1+Δ_1 optical transitions can be represented by,

$$y_1'(E) = -2\frac{Amp}{dE^2}\cdot\left((E-E_1)\cdot exp\left(\frac{-(E-E_1)^2}{dE^2}\right)\right) \tag{2.32}$$

$$y_2'(E) = 2\frac{Amp}{dE^2}\cdot\left((E-E_2)\cdot exp\left(\frac{-(E-E_2)^2}{dE^2}\right)\right) \tag{2.33}$$

where *Amp* is the amplitude of the magneto-optical signal, *dE* is the width of the curve, E_1 is the photon energy of E_1 optical transition, E_2 is the photon energy of E_1+Δ_1 optical transition, and both $y_1'(E)$ and $y_2'(E)$ are functions of photon energy *E*. Thus, using the Eqs. (2.32) and (2.33), one can plot the two dispersion curves as shown in Fig. 2-13 (a)-(b). In practice, the measured magneto-optical signals are the superposition of two dispersion curves. Therefore, the Eqs. (2.32) and (2.33), which are two derivatives of the Gaussian functions, can be combined together as,

$$y_1'(E) + y_2'(E) =$$

$$-2\frac{Amp}{dE^2}\times\left(\left((E-E_1)\cdot exp\left(\frac{-(E-E_1)^2}{dE^2}\right)\right)-\left((E-E_2)\cdot exp\left(\frac{-(E-E_2)^2}{dE^2}\right)\right)\right) \tag{2.34}$$

By means of the Eq. (2.34), one can fit the measured magneto-optical spectrum, and extract all constant values (*i.e. Amp*, *dE*, E_1, and E_2). Subsequently, the two dispersion curves can be plotted using Eqs. (2.32) and (2.33) with the extracted constants from Eq. (2.34). In this way, a spectrally broadened magneto-optical signal can be deconvolved into two dispersion curves corresponding to E_1 and $E_1+\Delta_1$ optical transitions. Figure 2-14 summarizes the fitting and deconvolution method using energy derivative of Gaussian function.

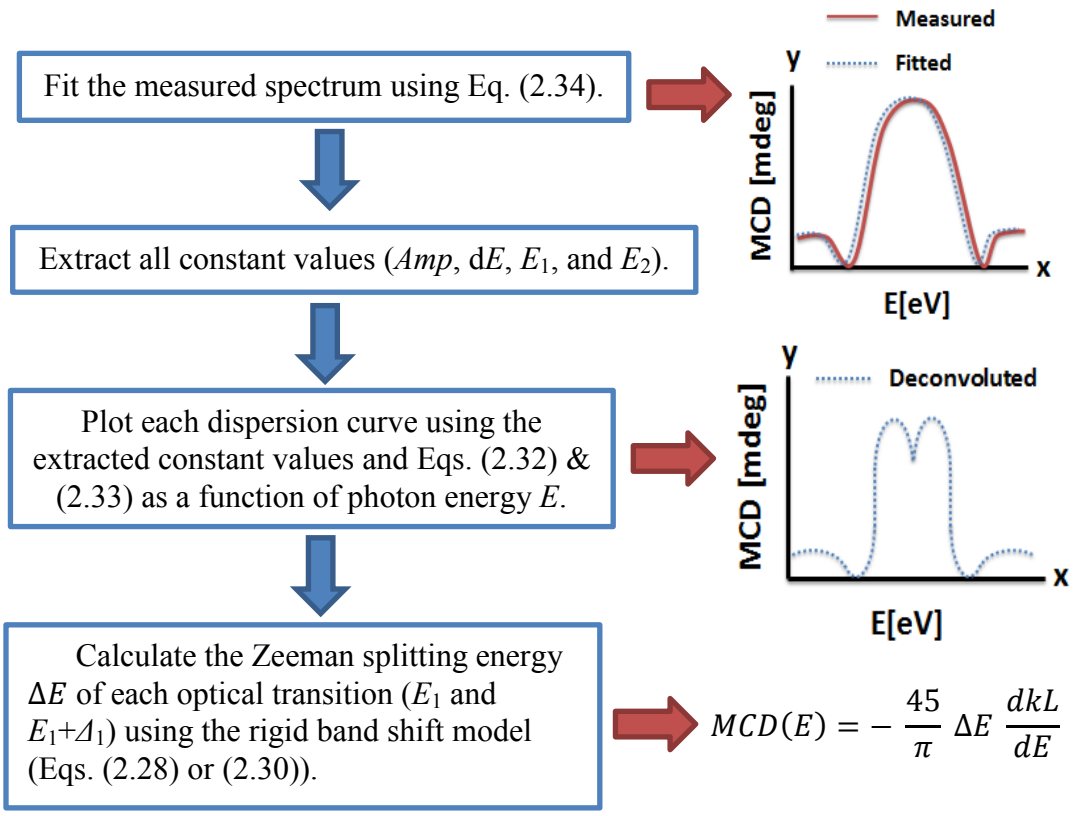

Figure 2-14 Schematic illustrations of fitting and deconvolution procedures applied to MCD spectrum of LT-GaAs and $Ga_{1-x}Mn_xAs$ at *L*-CPs for E_1 and $E_1+\Delta_1$ optical transitions using the energy derivative of Gaussian function [133].

The two dispersion curves corresponding to transitions at *L*-CPs are due to the enhanced Zeeman splitting by *sp-d* exchange interaction. One can calculate the Zeeman splitting energy ΔE of each optical transition (E_1 and $E_1+\Delta_1$) using the rigid band shift model. Then, the true amplitude of the MCD signal can be obtained from the deconvoluted curves and subsequently plugged into the Eqs. (2.28) or (2.29) to calculate the accurate Zeeman splitting energy at *L*-CPs. The fitting method analyzed in this section has applied to the MCD spectroscopic data collected in this project and results are presented in Chapter 6. In addition, it is usually beneficial to do this fitting method after subtracting an IBs-related background. This process will be further discussed and executed in Chapter 6.

3. MATERIAL GROWTH

3.1 General information of $Ga_{1-x}Mn_xAs$ growth

As described in Chapter 2, when Mn ($[Ar]3d^5 4s^2$) is introduced in GaAs host, it resides at the Ga ($[Ar]3d^{10}4s^2p^1$) site compounded with As ($[Ar]3d^{10}4s^2p^3$) to form GaMnAs. Such configuration offers the most stable structure based on fundamental electronic structure of involved elements [163]. The substitutional Mn_{Ga} (predominant) and interstitial Mn_I (less common case) are illustrated in Fig. 3-1. Furthermore, the Mn_{Ga} impurity acts as an acceptor due to missing the valence $4p$ electron by the Mn and as such provides a hole that mediates a ferromagnetic interaction between the local moments of the open d shells in the Mn atoms. It should be mentioned here, that As antisites (As_{Ga}) and Mn_I acting as double donors are responsible for compensating a significant fraction of the free holes generated by Mn_{Ga}. Mn_I also has an effect on reducing the total magnetic moment through anti-ferromagnetic coupling with substitutional Mn_{Ga}. Furthermore, the consequence of the double donor's presence is the reduction of the Curie transition temperature which depends on the density of local moments and density of charge carriers. To achieve a high Curie temperature, one has to maximize the concentration of Mn_{Ga} when minimizing the concentration of double donors.

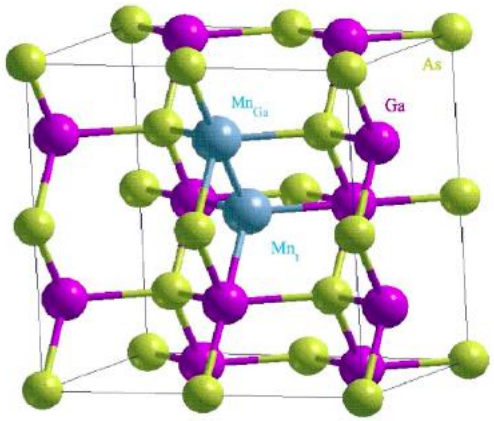

Figure 3-1 Lattice structure showing substitutional Mn_{Ga} and interstitial Mn_I in GaAs host [105].

It is well known that doping concentrations of Mn ions into a III-V semiconductor is limited to approximately 0.1% under equilibrium growth conditions [105]. When Mn ions are introduced more than the doping level, surface segregation and phase separation can be observed. This is due to the fact that the solid solubility limit of Mn ions in III-V host semiconductors is very low. Therefore, it is difficult to incorporate a high concentration of Mn ions into the host material and maintain the single crystal structure under equilibrium growth conditions. However, ferromagnetism can be generally observed when Mn concentration is more than x = 1% and that is well above the Mn solid solubility limit into GaAs under the equilibrium growth condition [83] [164].

Thus, it is required to conduct a nonequilibrium growth which is a low-temperature MBE growth so that one can dope the Mn concentration more than 1% without introducing the Mn precipitation and MnAs second phase formation [8] [83] [94]. The following is the procedure of our material growth.

3.2 $Ga_{1-x}Mn_xAs$ samples investigated in this project

$Ga_{1-x}Mn_xAs$ thin films with (111)-orientation were grown on sapphire (0001) and InP substrates by a low temperature molecular beam epitaxy (MBE) growth technique [133]. The growth temperature of $Ga_{1-x}Mn_xAs$ thin films was at 230 °C to avoid the Mn precipitation and MnAs second phase formation as described before [133]. The film thickness of $Ga_{1-x}Mn_xAs$ samples was 50 nm in order to avoid optical interference effects [133]. In addition, a high temperature growth GaAs (600 °C , HT-GaAs) film and low temperature growth GaAs (230 °C, LT-GaAS) film were grown as a reference [133]. The Mn concentration of x = 0.03 sample was determined from an X-ray photoelectron spectroscopy (XPS), calibrated by an electron probe micro analysis (EPMA). For the other films with smaller Mn content, x values were obtained from a calibrated relation between the amount of Mn beam flux and Mn Knudsen cell temperature, monitored in the growth chamber [133]. During the material growth, the $Ga_{1-x}Mn_xAs$ samples were monitored by a high energy electron diffraction (RHEED) and the surface of the samples showed streaky patterns with (1×2) surface reconstruction [130] [159]. This is an indication that the samples are free from the second phase materials (MnAs precipitations). In addition, an X-ray diffraction (XRD) was also conducted on the (111)-oriented samples and there was no trace of second phase materials on these samples [109] [130].

It should be mentioned here about the selection of the substrates. In principle, $Ga_{1-x}Mn_xAs$ film is grown on sapphire (0001) is to avoid the change of the polarization of light. In the magneto-optical measurement, maintaining a desired polarization is very

important. The optical axis of the sapphire is *c*-axis (0001). When the light transmits along the *c*-axis, there is no birefringence occurring, therefore, there are no polarization changes. On the other hand, if the light transmits along another axis, for example, *a*-axis, the polarization of the light will be destroyed due to the birefringent effect. Therefore, $Ga_{1-x}Mn_xAs$ has to be grown on the *c*-axis of sapphire for MCD measurement in transmission mode. Furthermore, we fabricated different sets of $Ga_{1-x}Mn_xAs$ on InP and free-standing $Ga_{1-x}Mn_xAs$ with various Mn concentrations. For the free-standing film, $Ga_{1-x}Mn_xAs$ was first grown on InP. Then, the InP was chemically etched out so that one can have free-standing $Ga_{1-x}Mn_xAs$ with different concentrations of Mn. Table 3-1, 3-2, and 3-3 summarizes information of all investigated samples developed in this project.

Table 3-1 High temperature growth GaAs (HT-GaAs) films grown by MBE.

Sample	Thickness [nm]	Concentration of Mn [x]	Substrate	Growth temperature [℃]
HT-GaAs	~50	0.0000	Sapphire	600

Table 3-2 Low temperature growth GaAs (LT-GaAs) films grown by MBE.

Sample	Thickness [nm]	Concentration of Mn [*x*]	Substrate	Growth temperature [℃]
LT-GaAs	~50	0.0000	Sapphire	230

Table 3-3 List of $Ga_{1-x}Mn_xAs$ films grown by MBE.

Sample	Thickness [nm]	Concentration of Mn [x]	Substrates	Growth temperature [℃]
$Ga_{1-x}Mn_xAs$	~50	0.0001	Sapphire InP Free-standing	230
		0.0003		
		0.0005		
		0.001		
		0.005		
		0.01		
		0.03		

The magnetization in $Ga_{1-x}Mn_xAs$ depends on the thickness of the material but also the material quality [165]–[167]. In general, the low temperature growth MBE (LT-MBE) degrades the material quality because the low temperature growth creates inevitable defects in the material system [13] [97] [104] [108] [132] [133] [159] [160]. These defects contribute to decreasing the magnetization in $Ga_{1-x}Mn_xAs$. Therefore, a thermal annealing is usually necessary to improve the material quality so that the Curie temperature T_c can be increased [13] [97] [104] [132] [160] [168]. In our case, the sapphire is a hexagonal structure and the $Ga_{1-x}Mn_xAs$ is a cubic structure. Thus, it can be expected that the material quality becomes even worse in $Ga_{1-x}Mn_xAs$/sapphire samples due to the their lattice mismatches (lattice constant of GaAs: ~0.57 nm, lattice constant of sapphire of *c*-plane: ~1.3 nm) [169] [170]. On the other hand, the InP and GaAs are both cubic structures and their lattice constants are relatively closer (lattice constant of InP:

~0.59 nm) [169]. So, the material quality of $Ga_{1-x}Mn_xAs$/InP and Free-standing $Ga_{1-x}Mn_xAs$ are expected to be better. Indeed, one can observe the crystalline structure from $Ga_{1-x}Mn_xAs$/InP, and polycrystalline structure from $Ga_{1-x}Mn_xAs$/sapphire by RHEED monitoring during the growth [82] [133]. Therefore, in general, the amplitude of MCD and *dkL/dE* signals of $Ga_{1-x}Mn_xAs$ grown on InP is expected to be larger than that of $Ga_{1-x}Mn_xAs$/sapphire.

In should be also pointed out here that the main purpose of this project is not the fabrication of high Curie temperature $Ga_{1-x}Mn_xAs$. One of the main objectives in this project is the investigation of the nature of the intrinsic $Ga_{1-x}Mn_xAs$ by analyzing the magneto-optical spectra at *L*-CPs. Therefore, we did not conduct any thermal annealing for our samples.

4. DEVELOPMENT OF MAGNETO-OPTICAL SETUPS

This chapter mainly focuses on the reflection-mode MCD and polar/longitudinal MOKE experimental setups designed and developed at Ohio University (OU). In this project, we have also used the transmission-mode MCD setup available in the Advanced Industrial Science and Technology (AIST) in Japan [99]; however only the fundamentals of theoretical background and the operations of this system are explained in this document.

4.1 Transmission-mode MCD setup

Figure 4-1 shows the schematic illustration of transmission-mode MCD setup available at AIST. The technical details on this MCD setup were also published elsewhere [99] [135]–[138]. Here, in short, we describe its major components and operation. In general, we used two identical MCD setups for measurement in different spectral regions; (1) visible spectral range between 350 nm to 500 nm to investigate MCD spectra around the *L* critical point and (2) infrared spectral ranges between 650 nm to 2000 nm to investigate the MCD spectra around *Γ* critical points or below the bandgap energy of $Ga_{1-x}Mn_xAs$. The light sources used in these systems were Xe lamp (200 nm - 800 nm) or W lamp (650 nm – 2000 nm) generating broad band white light. These lamps were combined with a respective monochromator equipped with a specific diffraction grating to generate monochromatic light. The unpolarized light from the light source passes through a polarizer (*P*) to be linearly polarized light at 45 degree. The light modulated by an optical chopper (*CH*) provides a *DC* signal. The 45 degree linearly

polarized light was modulated to the right and left circularly polarized light using a photoelastic modulator (*PEM*) operating at 50 kHz. Typically, the *PEM* modulation frequency was the same as the first harmonic frequency f due to the direct correspondence of the *MCD* signal to the first-order of Bessel function, $J_1[\delta_0]$ as discussed in Chapter 2 (see Eq. (2.5)). Also, the phase retardation amplitude δ_0 was set to 1.571 radian (90 degree, 0.25λ) in *PEM* to make the right and left circularly polarized light. The light modulated by *PEM* provides an *AC* signal. The modulated light is incident on the sample placed inside of a liquid helium cryostat operating in 6 – 320 K temperature range under the vacuum of 10^{-5} Torr in both setups. The MCD signal (*i.e.* *AC/DC* signals ratio) was detected by a photomultiplier (*PMT*) when Xe lamp was used or by an InSb detector when W lamp was involved, respectively. Here, the *AC* and *DC* signals correspond to ΔI_w and $\bar{I}$ parameters described by Eq. (2.5). All optical components including lens, polarizer, and PEM were inside of a lightproof box to eliminate ambient light background affecting the polarization of detected light. In addition, absorption spectra were also measured by the same systems. After the collection of all absorption spectra with different concentrations of Mn, Eq. (2.31) was used to calibrate the measured absorption spectra into *dkL/dE* (*i.e.* the energy derivative of absorption coefficient) for the data analysis.

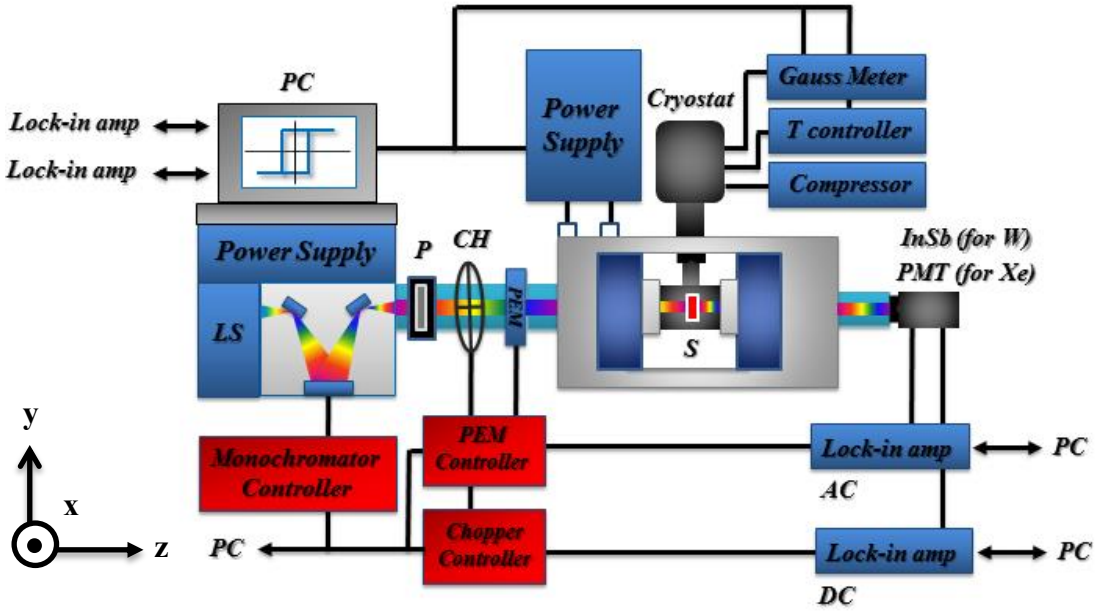

Figure 4-1 MCD setup operating in transmission mode at AIST laboratory. The acronyms in the inset correspond to: *LS*: light source, *P*: polarizer, *PC*: personal computer, *T controller:* temperature controller, *InSb:* detector, *PMT:* Photomultiplier [99] [135]–[138]. The Cartesian coordinates represent the orientation of magnetic field ***B*** and the light propagation direction along the *z* axis. The plane of incidence is *x*-*z* plane.

4.2 Reflection-mode MCD and polar/longitudinal MOKE setups

In this section we will describe our efforts toward the developing of a multifunctional magneto-optical measurement system combining reflection-mode MCD and polar/longitudinal MOKE setups at Ohio University.

The typical polar and longitudinal MOKE setups were built by us in the previous work and the detailed explanations are in Ref. [142]. These setups were primarily designed for operation with laser light source at room temperature. On the basis of the conventional MOKE setups constructed in the previous project, we have also built a new multifunctional magneto-optical measurement system which combines the reflection-mode MCD and polar/longitudinal MOKE setups. The combined MCD and MOKE

setups utilizes broad band white light sources operating in a 300 nm to 2000 nm spectral range with a temperature range between 7 K to 320 K. During the construction of the combined MCD and polar-MOKE setup two major issues arose. The first issue was of the fundamental nature and was related to the destruction of light polarization due to the birefringence of a cryostat quartz window when subjected to the magnetic field during experiments. The second issue was of a technical nature and relates to effective light guiding starting from the lamp to the sample, and eventually to the detector. For the temperature dependent magneto-optical measurements, we used a close-cycled helium duplex cryostat equipped with quartz windows having O.D. of 2 inches and a thickness of ~2 mm. The head of cryostat was placed between electromagnet pole caps separated at least by 2 inches from each other. Special efforts were dedicated to reduce the parasitic light polarization corruption due to the cryostat quartz window birefringence effect when a magnetic field was applied up to 1 Tesla at low temperature (up to 1.5 Tesla at 300 K). However, residual contributions from the windows to light polarization remained present for low temperature polar-MOKE and reflection-mode MCD setups.

This was not the case for a polar-MOKE setup operating at 300 K because the cryostat optical windows were not implemented into the system. Figure 4-2 (a) shows the example of a polar-MOKE hysteresis loop measured by a He-Ne laser at 300 K. The test sample was of AlN:Ni. As it is seen in Fig 4-2 (a), there is no obvious indication of light polarization destruction. However, when the same specimen was in the cryostat and was measured by the He-Ne laser at polar MOKE geometry at 300 K, the deformation of the hysteresis loop was observed due to the birefringence of the quartz window under the

magnetic field as shown in Fig. 4-2 (b). The issues of the light polarization destruction by the quartz windows can be mathematically corrected up to some extent during the post measurement data analysis process. More detailed discussions on AlN:Ni samples were presented in our other publications [171]–[173].

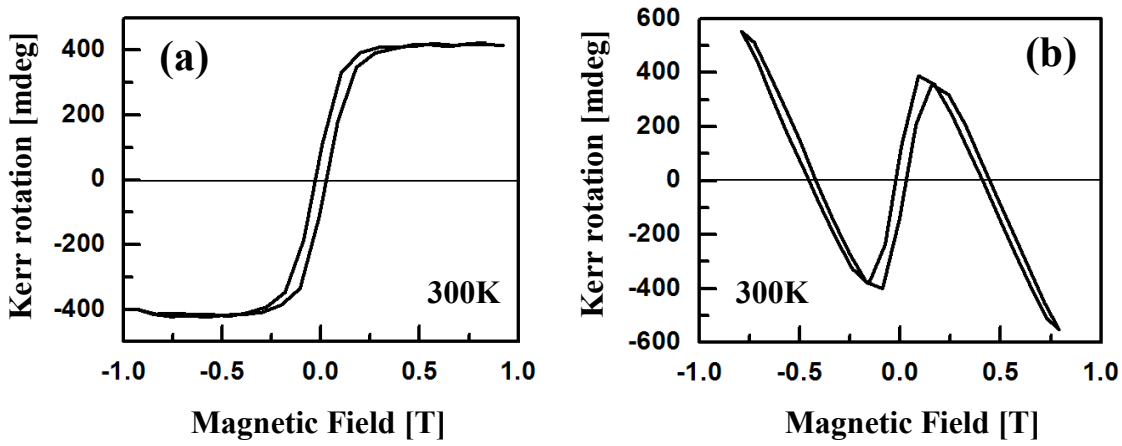

Figure 4-2 (a) Polar MOKE hysteresis loop of AlN:Ni measured by a He-Ne laser without a quartz window at 300 K. (b) Deformation of the polar MOKE hysteresis loop of AlN:Ni measured by a He-Ne laser with a quartz window at 300 K.

The polarization corruption issue in the addressed scenario is intrinsic in the polar–MOKE setup; however it is not a problem for longitudinal-MOKE configuration because the quartz window can be kept out of the magnetic field flux. Also, a typical longitudinal-MOKE setup offers much easier access and arrangement of optical components as compared to a polar-MOKE setup. This is because that the longitudinal-MOKE setup is not restricted by the geometry of electromagnet axial bores needed for light to travel through in the polar-MOKE setup. In such a case, to capitalize on these benefits, an optical mirror can be introduced in the longitudinal-MOKE setup, and the longitudinal-

MOKE with the optical mirror can be converted to the polar-MOKE geometry setup (*i.e.* the incident plain of optical wave is perpendicular to the sample surface and parallel to the magnetic field direction). In this project we used a high quality Al mirror to test the concept mentioned above. Figure 4-3 shows two cases illustrating the positioning of a mirror with respect to a sample (top and front view). The top view shows the optical path of incident and reflected light on *z*-*x* plane, and the front view illustrates how the mirror was installed in the cryostat head. Only the sample is mounted on a holder attached to the cold finger of the cryostat.

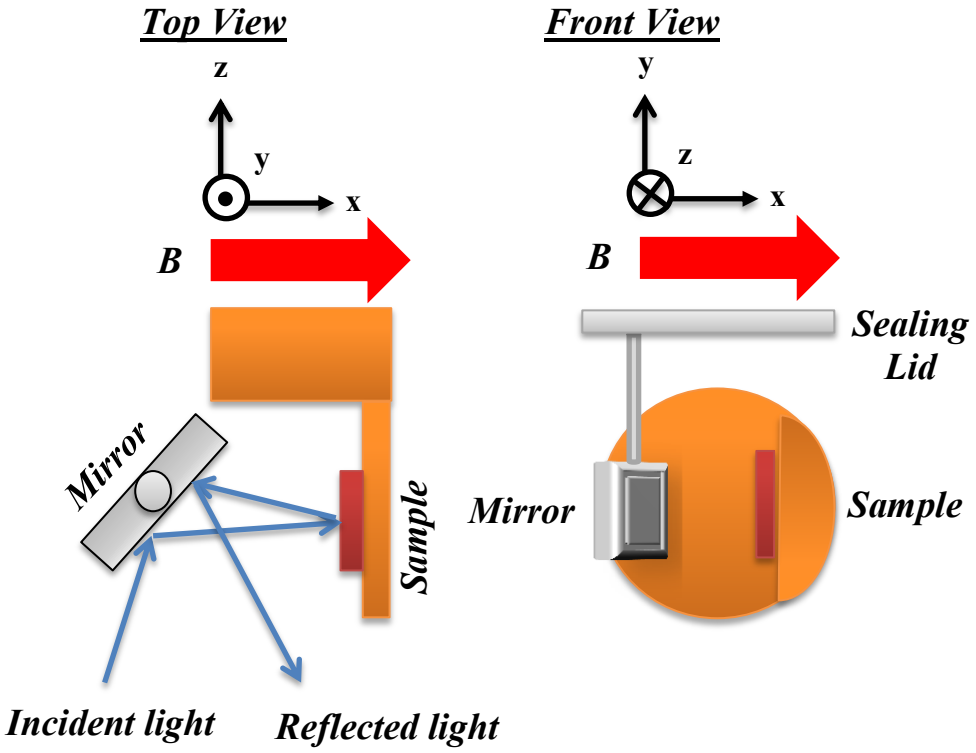

Figure 4-3 Top view and front view of the polar-MOKE and reflection-mode MCD arrangement with an additional optical mirror. The Cartesian coordinates represent that the plane of incidence is *z*-*x* plane and the magnetic field ***B*** is applied along the *x* axis direction.

The operation of the mirror based polar-MOKE setup (reflection-mode MCD setup) using the concept shown in Fig. 4-3 was successfully demonstrated with the test samples at both room (300 K) and cryogenic (20 K) temperature. The representative results are shown in Fig 4-4.

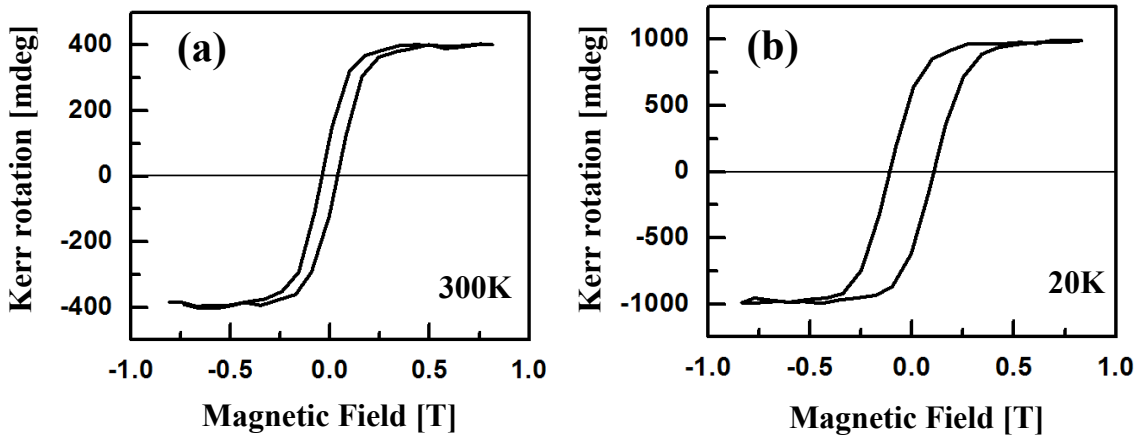

Figure 4-4 (a) Polar MOKE hysteresis loop of AlN:Ni measured by a He-Ne laser with a quartz window and an optical mirror at 300 K. (b) Polar MOKE hysteresis loop of AlN:Ni measured by a He-Ne laser with a quartz window and an optical mirror at 20 K.

During this project, we have tested a few different mirror mounting options for improving the experimental setup functionality. Figure 4-5(a) shows illustrations of another mirror and sample holders [141] (the same Al mirror was used as in the case shown in Fig.4-2); however this time the mirror is physically mounted on a sample holder but kept thermally insulated from the sample ambient temperature. The sample holder is made of non-magnetic copper and the Al mirror is mounted on one side and the sample can be mounted on another side of the holder to maintain the polar MOKE geometry (reflection-mode MCD) as shown in the Fig. 4-6 [141]. For the longitudinal-MOKE setup,

one can use a simple flat samples holder (see Fig.4-5(b)). The direct advantage of using the optical mirror inside of the system is that it is relatively easy and simple to change different configurations between polar-MOKE, longitudinal-MOKE, and reflection-mode MCD geometries without the tedious alignment of the optical components. Selected results related to testing the mirror-based reflection-mode MCD and polar/longitudinal MOKE setup are shown in Appendix E whereas the theoretical framework supporting the implemented concept can be found in Ref.[141].

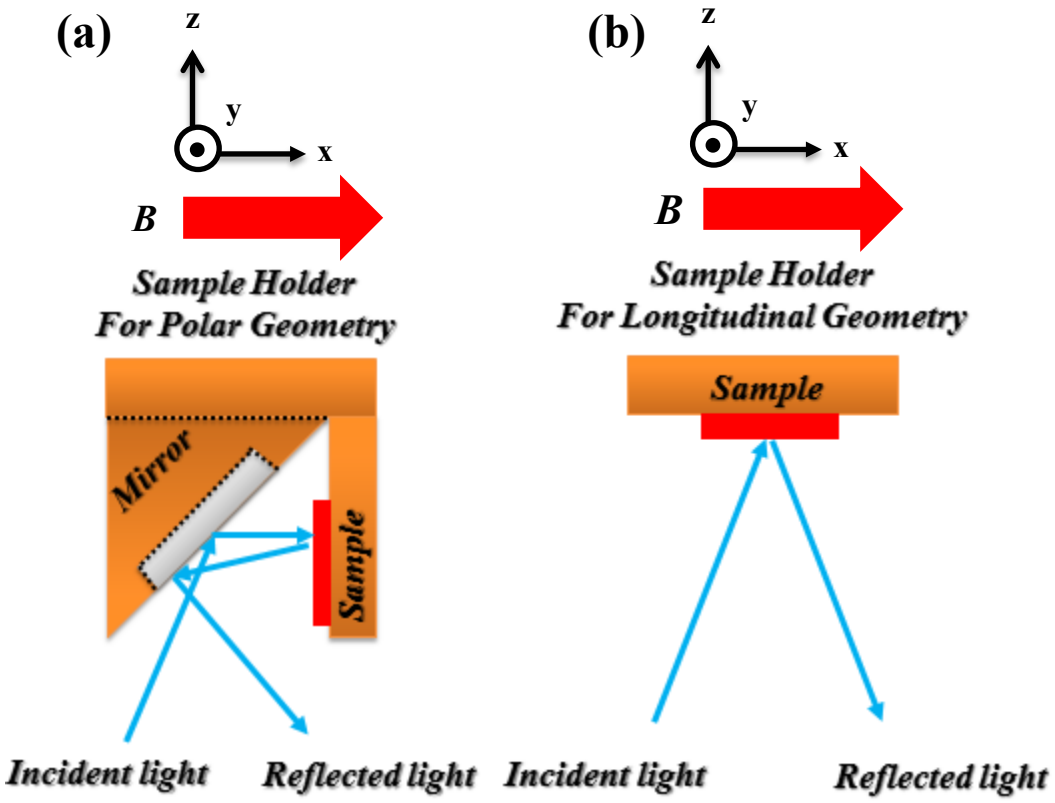

Figure 4-5 (a) A sample holder with a mirror mounted at 45 degrees for reflection-mode MCD and polar MOKE geometry. (b) A sample holder made of copper for longitudinal MOKE geometry [141] [142]. The Cartesian coordinates represent that the plane of incidence is *z*-*x* plane and the magnetic field ***B*** is applied along the *x* axis direction.

In the following we discuss components and operations of the mirror-based reflection-mode MCD and polar/longitudinal MOKE setups developed in this project. The setup is schematically shown in Fig. 4-6. The broad band white light generated by Xe lamp (350 nm - 800 nm) or W lamp (650 nm – 2000 nm) is passing through a dedicated double grating monochromator (Spectral Product, Model CM 110 offering ~1 nm spectral resolution) equipped with a set of different holographic gratings. The unpolarized monochromatic light is then coupled to an optical fiber (*OF*) (Ocean Optics, Model QP600-2-SR) allowing easy light guiding. By choosing correct fiber and optical components parameters (*e.g.* focal length, diameter, curvature, *f*-number, wavelength acceptance region, and *etc*.) we were able to generate light with desired coherence, intensity, and spectral bandwidth at the beginning. As shown in Fig. 4.6, the free space incident monochromatic light passes through a focusing lens (*FL*) then a polarizer (*P1*) (Glan-Thompson polarizer, Model Oriel 25706) polarizing the randomly polarized light into linearly polarized light (±45 degree). Then, the incident light is modulated by an optical chopper (*CH*) (New Focus, Model 3501) for lock-in detection for a *DC* signal, and it is also modulated by a photoelastic modulator (*PEM*) (Hinds Instruments, Model 100) for another lock-in detection for the AC signal.

It should be noted here that the *PEM* frequency and phase values parameters are different depending on which signal: the MCD, Kerr ellipticity or Kerr rotation are detected. As expressed using Eq. (2.5) in Section 2.1, the PEM modulation frequency for MCD should be set as the first harmonic f because the MCD signal correspondence to the first-order of the Bessel function, $J_1[\delta_0]$, and the *PEM* phase retardation amplitude δ_0

should be set to 1.571 radian (90 degree, 0.25λ) to generate right and left circularly polarized light. Similarly, using Eqs. (2.11) – (2.14) the first harmonic *f* and the second harmonic 2*f* of *PEM* modulation frequency are used for Kerr ellipticity and Kerr rotation measurement, respectively. Also, the phase retardation amplitude δ_0 in the MOKE experiment should be set to 2.405 to eliminate the zeroth-order of the Bessel function $J_0(\delta_0)$ in Eq. (B-46) for extraction of the *DC* signal. The *DC* signal is eventually used for the normalization of *AC s*ignals to calibrate the measured signals into the Kerr ellipticity [deg] and Kerr rotation [deg] as show in Chapter 2.

To measure the Kerr ellipticity, a quarter-wave plate should be placed along the incident light path to make fixed 0.25λ retardation to generate elliptically polarized light. Such optical light probes (linearly, circularly, or elliptically polarized light) can be incident onto the mirror, sample surfaces and reflected back as shown in Fig. 2-3. To measure the Kerr rotation, the reflected light passes through two focusing lenses (*FL*) and an analyzer (*P2*) (Glan-Thompson polarizer, Model Oriel 25706). However, the analyzer (*P2*) has to be removed from a reflected light path when the MCD and Kerr ellipticity measurements were considered. This is due to the fact that the MCD signal represents the absorption difference between the right and left circularly polarized light and Kerr ellipticity is the change of amplitude of elliptically polarized light. Therefore, the analyzer (*P2*) in the reflected light path is unnecessary for MCD and Kerr ellipticity measurement. Finally, the reflected light was detected by a silicon detector (Thorlabs, Model DET200) and fed to two identical lock-in amplifiers (Stanford Research, Models SR830). The spectral detection limit of the designed setup in NIR region was 1100 nm.

However, this has not presented any serious constrain to the project because our primary interest was in optical transitions in $Ga_{1-x}Mn_xAs$, at *L*-CPs in 350-800 nm spectral range. Magnetic field was generated by an electromagnet (*EM*) (Lake Shore, Model EM-HVA) driven by a power supply (Lake Shore, Model 642) and magnetic field strength between 0 to 1 Tesla was detected by a Hall probe (Lake Shore, 455-HMNT-4E04-VF) controlled by a Gaussmeter (Lake Shore, Model 475), respectively.

Samples were individually placed in the cryostat (Advanced Research System Inc, Model M/N DE-202NI) operating in a temperature range 6 K to 450 K controlled by a temperature controller (Lake Shore, Model 340).

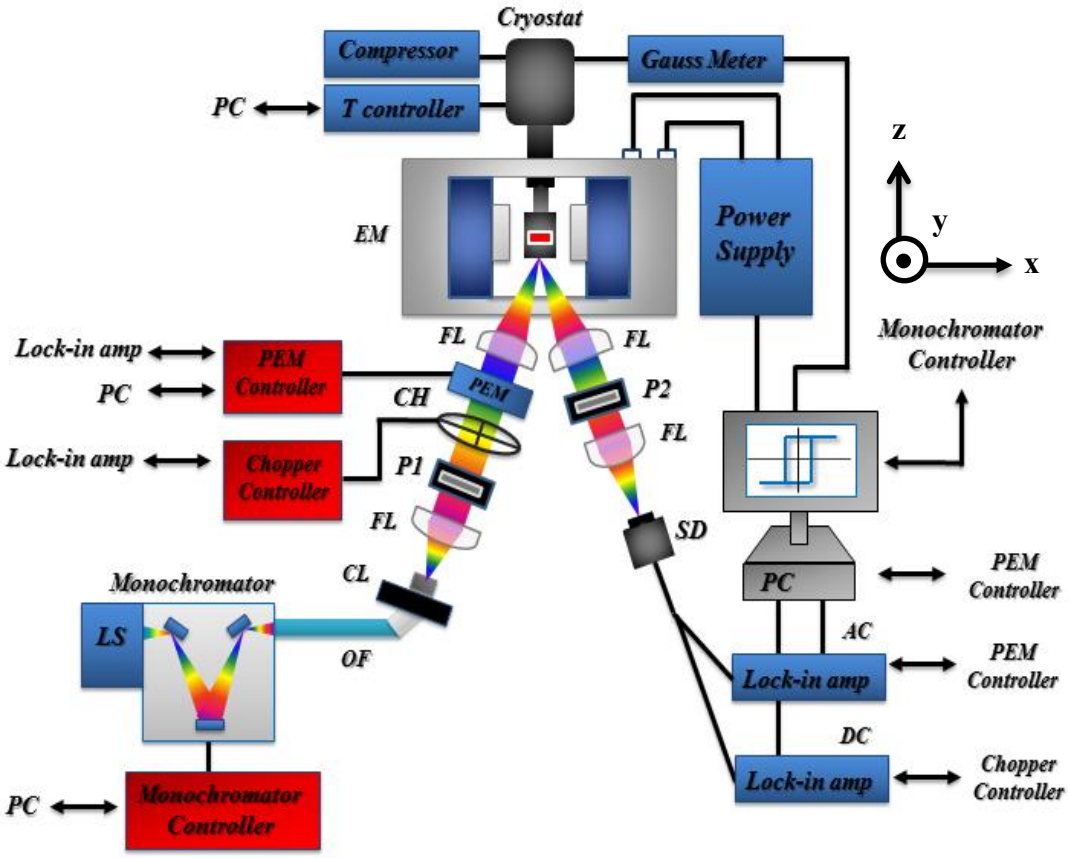

Figure 4-6 Schematic representation of a combined reflection-mode MCD and polar/longitudinal MOKE setup developed at OU. The inset acronyms indicate: *LS*: light source, *CL* and *FL*: lenses, *P1, P2*: polarizers, *PC*: personal computer, *T* controller: temperature controller, *SD*: detector, *OF*: optical fiber, *CH:* optical chopper, *PEM*: photoelastic modulator, *EM*: electromagnet. The Cartesian coordinates represent that the plane of incidence is *z-x* plane and the magnetic field ***B*** is applied along the *x* axis direction. Please note that an optical mirror is involved to maintain the reflection-mode MCD and polar MOKE configurations. (The optical mirror is not shown here. Please see Figs. 4-3 and 4-5.)

Both reflection-mode MCD and polar/longitudinal MOKE experiments are automatically and remotely operated by LabVIEW code. After the collection of the data, the code automatically conducts data processing (averaging, calibrating, plotting, and

saving the measured signals, *etc*) to show final results. The flow charts corresponding to the MCD/MOKE spectra and hysteresis measurements are shown in Figs. 4-7 and 4-8.

In case of MCD/MOKE spectra measurement the LabVIEW code first executes the electromagnet to generate the magnetic field of the desired strength up to 1 Tesla. Subsequently, the monochromator starts scanning the white light with incremental steps (user defined, min. ~1nm) and the PEM simultaneously works for the given wavelength. The reflected light intensity is detected by the detector and the signal is provided to the lock-in amplifier. If the lock-in amplifier does not overload then data is processed and the next measurement loop is initiated until it reaches the desired number of repetitions. When the collected data processing is completed, the LabVIEW code automatically stops the execution and provides the final results.

In the case of the MCD/MOKE hysteresis loop measurement, the LabVIEW code operates in a similar way as described above; however, the wavelength is fixed and the magnetic field strength varies between 0 – 1 Tesla with an increment step not smaller than 0.0001 m Tesla.

It should be noted that all critical calibration parameters necessary for correct data processing are based on the derivations of the equations shown in Chapter 2 and Appendixes A and B and are incorporated into LabVIEW data processing routines. For example, since the retardation amplitude δ_0 has to be 2.405 in a MOKE experiment, the first and second order of the Bessel function should be $J_1(2.405) = 0.52$ and $J_2(2.405) = 0.43$ for Kerr rotation and Kerr ellipticity signals, respectively. Thus, these values (0.52

and 0.43) are used to calibrate the measured signals to the Kerr rotation [deg] and the Kerr ellipticity [deg], respectively.

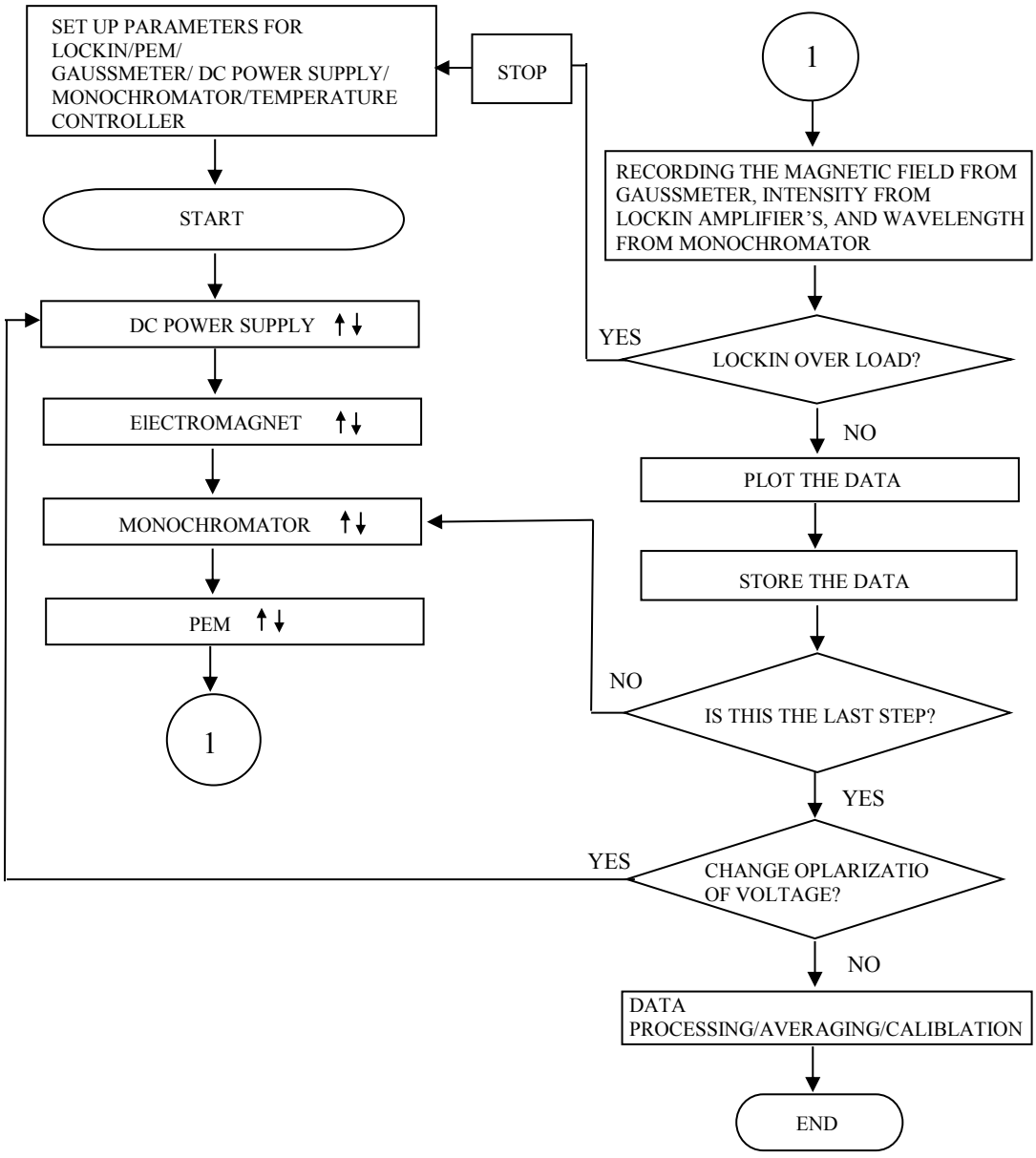

Figure 4-7 Flow chart of the LabVIEW routine for reflection-mode MCD and polar/longitudinal MOKE spectra measurements [175].

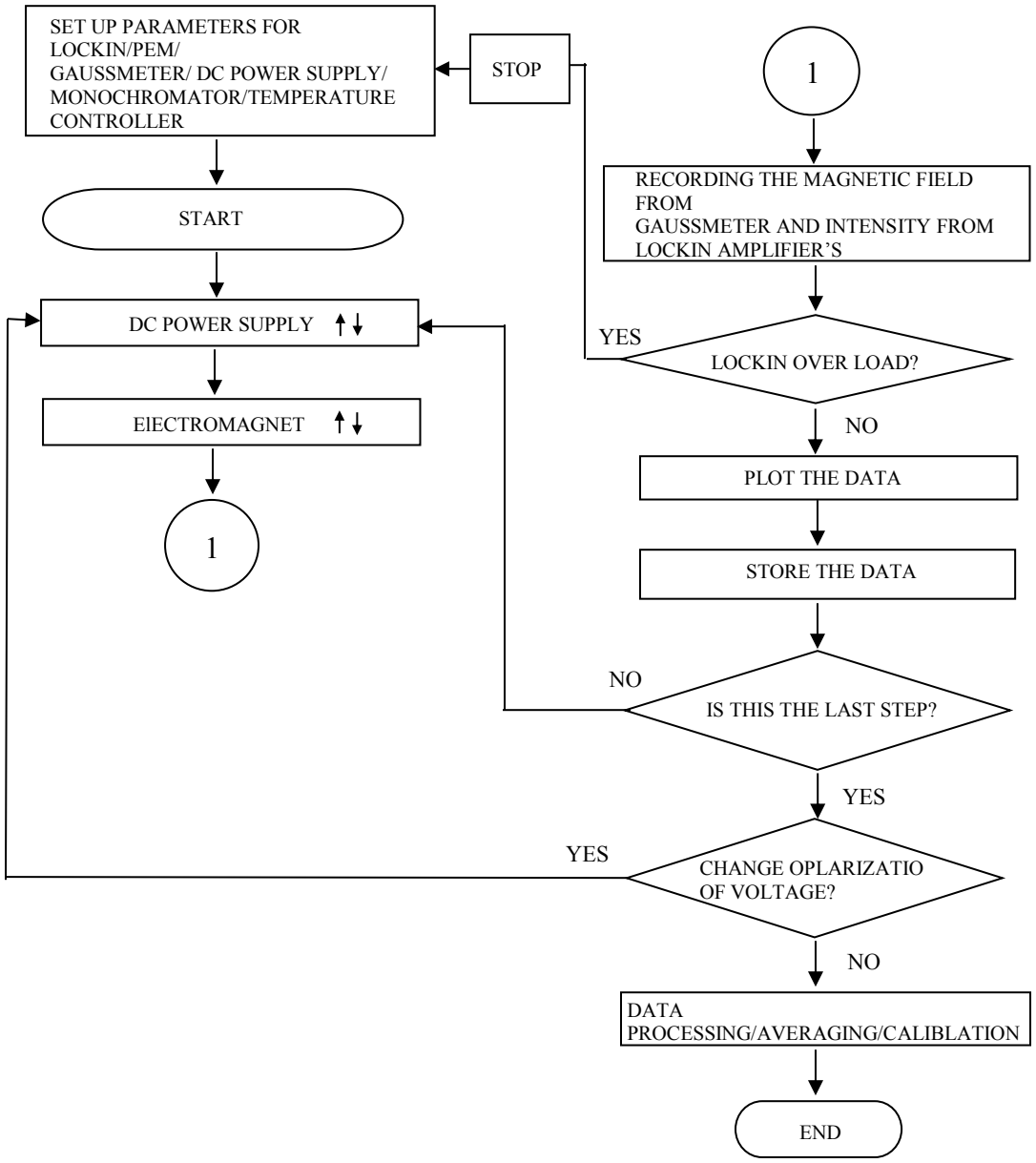

Figure 4-8 Flow chart of the LabVIEW routine for reflection-mode MCD and polar/longitudinal MOKE hysteresis loop measurements [175].

In summary, this chapter described the operation of experimental setups involved in this project including the transmission-mode MCD at AIST and a combined reflection-

mode MCD and polar/longitudinal MOKE setup at Ohio University. The main issue that was crucial for successful development of the multi-functional magneto-optical system at Ohio University was highlighted, namely, the destruction of the light polarization due to an extra optical component involved and physical space limitation for optical components mounting. These problems were solved by introducing an optical mirror to the MCD/MOKE system. It was demonstrated that the developed experimental setup acceptably operates with a magnetic field up to 1 Tesla, in 350 - 800 nm spectral range and in temperatures from 6 K to 320 K. Finally, the operation of the LabVIEW code was briefly explained indicating its ability to automatically control the experiment and to conduct desired data processing.

5. RESULTS

This chapter contains the magneto-optical and energy derivative of absorption (reflection) coefficient results. As indicated in Chapter 3, the research samples studied in this project were HT-GaAs, LT-GaAs, $Ga_{1-x}Mn_xAs$/sapphire, $Ga_{1-x}Mn_xAs$/InP, and free-standing $Ga_{1-x}Mn_xAs$ with different concentrations of Mn. The HT-GaAs, LT-GaAs, $Ga_{1-x}Mn_xAs$/sapphire and free-standing $Ga_{1-x}Mn_xAs$ films were measured by transmission-mode MCD at AIST whereas, $Ga_{1-x}Mn_xAs$/InP films were measured by the reflection-mode MCD at OU.

5.1 High temperature growth GaAs on sapphire

5.1.1 MCD and *dkL*/*dE* spectrum of HT-GaAs on sapphire

Figure 5-1 (a) and (b) shows the transmission-mode MCD and energy derivative of an optical absorption (*dkL/dE*) spectra of high temperature grown GaAs (HT-GaAs) [133] [155].

It is seen that both MCD and *dkL/dE* spectra are composed of two dispersion-type structures centered at E_1 and $E_1+\Delta_1$ optical transitions. Also, we can assume that these spectra representing the two dispersion curves with opposite polarities are due to E_1 and $E_1+\Delta_1$ optical transitions presented in Fig. 2-11 in Section 2.2.2.2 [133] [155] [162]. It is known that optical transitions observed in GaAs at *L*-CPs have a characteristic of the two dimensional M_1-type Van Hove singularity resulting in dispersion-type *dkL/dE* spectral shape at E_1 and $E_1+\Delta_1$ optical transitions [133] [162]. The observed dispersion-type *dkL/dE* peaks in Fig. 5-1 (b) is compatible with the theoretical expectation [133] [162]. Therefore, we can claim here that results presented in Fig. 5-1 (a) and (b) demonstrate a

good correspondence between the MCD and *dkL/dE* structures around the *L*-CPs of HT-GaAs, which satisfies the rigid band shift model [99] [133] [155].

Furthermore, according to Eq (2.28), the MCD and *dkL/dE* spectra should have similar structures. Thus, considering the above constraints, we believe that this data can be further theoretically analyzed using the rigid band shift model. In addition, we will demonstrate the fitting and deconvolution method (see Section 2.2.4) using these results with an energy derivative of the Gaussian function in Chapter 6.

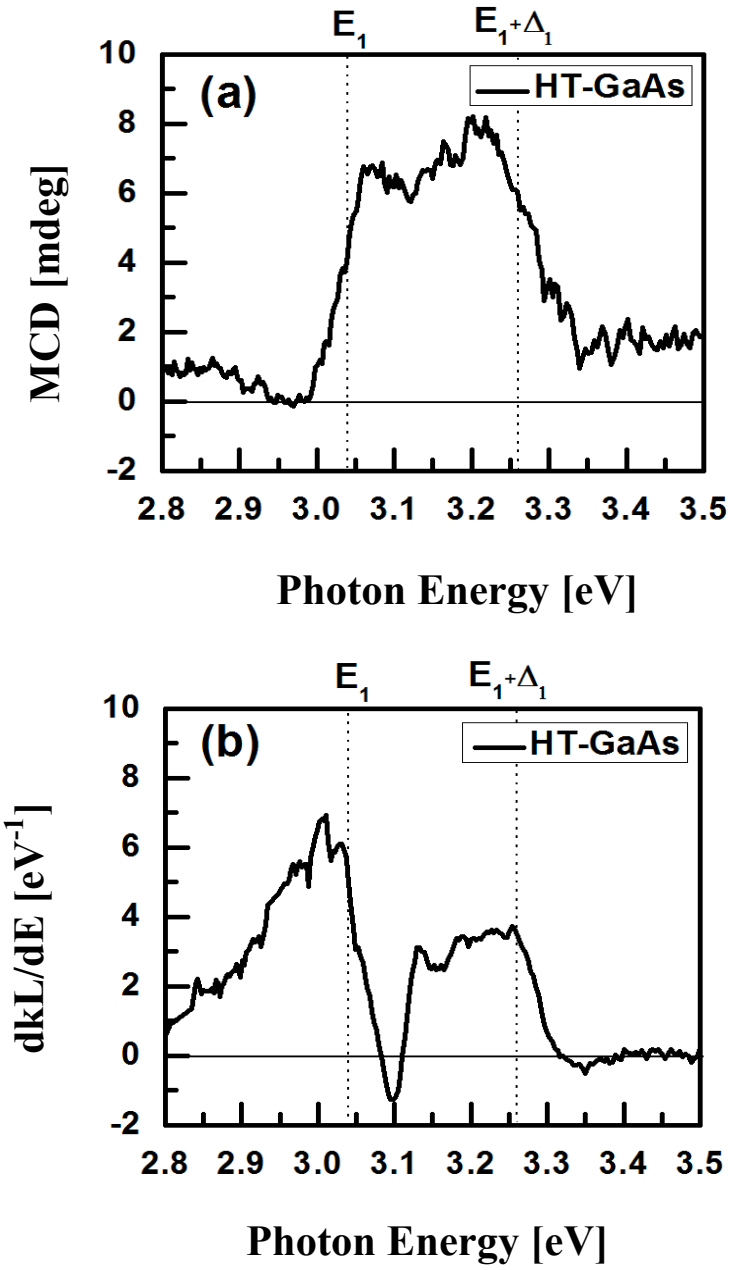

Figure 5-1 (a) MCD and (b) *dkL/dE* spectra of HT-GaAs measured in field of 1 Tesla at 6 K. Both spectra were measured in transmission-mode [133] [155]. Two dispersion curves with opposite polarities due to E_1 and $E_1+\Delta_1$ optical transitions can be observed.

5.2 $Ga_{1-x}Mn_xAs$ on sapphire

5.2.1 Hysteresis loops of $Ga_{1-x}Mn_xAs$ on sapphire

Figure 5-2 (a) shows transmission-mode MCD hysteresis loops measured at 3.04 eV for $Ga_{1-x}Mn_xAs$ films deposited on Sapphire ($Ga_{1-x}Mn_xAs$/Sapphire) with different Mn concentrations. It can be seen that only $Ga_{1-x}Mn_xAs$/Sapphire with x = 0.03 is ferromagnetic material while $Ga_{1-x}Mn_xAs$/Sapphire films with lower Mn concentrations from x = 0.0001 to 0.01 are paramagnetic at 6 K [133]. Figure 5-2 (b) shows a comparison of the normalized MCD and SQUID hysteresis loops. The hysteresis loops shape is identical confirming that results obtained using both methods are compatible with each other [133]. This indicates that all the measured MCD spectra originate only from the single phase of $Ga_{1-x}Mn_xAs$ [109] [158] and are free from other second phase precipitates (*e.g.* MnAs precipitations) [109] [133]. Furthermore, the Curie temperature T_c of $Ga_{1-x}Mn_xAs$ with x = 0.03 was determined from the Arrott plot of MCD intensity for different photon energies and was 20 ± 2 K. For the explanation of the Arrott plot, please refer to Appendix E. The magnetic coercivity of the hysteresis loops shown in Fig. 5-2(b) is very small indicating a good quality of $Ga_{1-x}Mn_xAs$ with x = 0.03 sample for further analysis as well as its prospective practical application *e.g.* for magnetic switching devices.

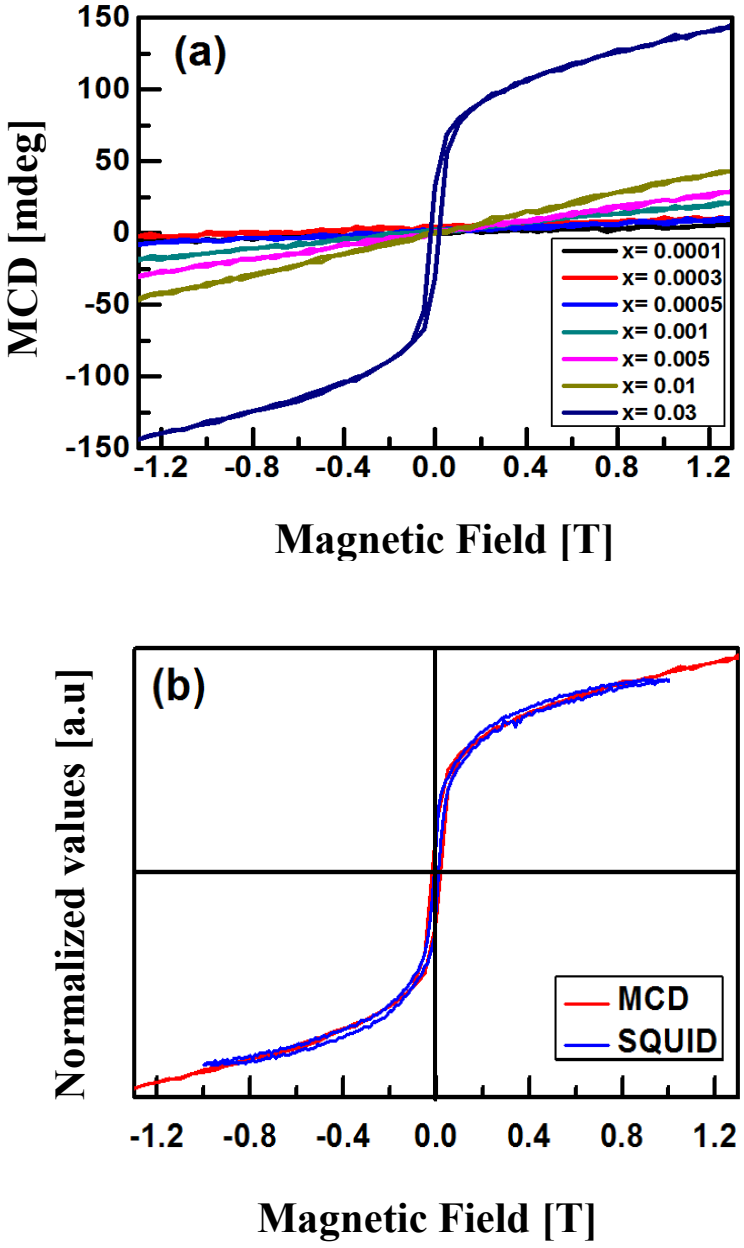

Figure 5-2 (a) Transmission-mode MCD hysteresis loops of $Ga_{1-x}Mn_xAs$ on sapphire with different Mn concentrations monitored at 3.04 eV at 6 K as a function of a magnetic field. (b) Comparison between normalized MCD and SQUID hysteresis loops measured at 6 K [133].

5.2.2 MCD spectra of $Ga_{1-x}Mn_xAs$ on sapphire

Figures in this section show the transmission-mode MCD spectra of $Ga_{1-x}Mn_xAs$/Sapphire with different Mn concentrations as a function of photon energy measured at 6 K and 1T [133].

Figure 5-3 (a)-(c) shows the MCD spectra for (a) a reference LT-GaAs, and $Ga_{1-x}Mn_xAs$ films with (b) $x = 0.0001$, and (c) $x = 0.0003$. Figure 5-4 (d)-(f) shows the MCD spectra for $Ga_{1-x}Mn_xAs$ films with (d) $x = 0.0005$, (e) $x = 0.001$, and (f) $x = 0.005$. Figure 5-5 (g)-(h) shows the MCD spectra for $Ga_{1-x}Mn_xAs$ films with (g) $x = 0.01$ and (h) $x = 0.03$.

5.2.2.1 Γ critical points of $Ga_{1-x}Mn_xAs$ on sapphire

In the MCD spectra of paramagnetic $Ga_{1-x}Mn_xAs$/Sapphire (Figs. 5-3 (a) – 5-5 (g)), one broad peak starts to evolve around the band gap energy of the GaAs host (1.52 eV) and another broad peak also starts to appear even below the band gap energy as the concentration of the Mn increases. One explanation as to why the MCD spectra is below the band gap energy, is that there are multiple optical transitions due to contributions from impurity bands (IBs) [109]. In the MCD spectra of ferromagnetic $Ga_{1-x}Mn_xAs$/Sapphire (Fig. 5-5 (h)), these two broad peaks even have a deviation from a zero-MCD signal due to the strong IB-related multiple optical transitions. Eventually, these IB-related MCD spectra act as a broad positive background for the MCD spectrum around Γ-CPs (E_0 and $E_0+\Delta_0$). However, the IB-related MCD spectra does not contribute much around L-CPs (E_1 and $E_1+\Delta_1$) as shown in Fig. 1-3 [109] [133].

5.2.2.2 *L* critical points of $Ga_{1-x}Mn_xAs$ on sapphire

One broad positive peak is observed for each sample around *L*-CPs (E_1 and $E_1+\Delta_1$), and its magnitude increases with Mn concentration. This is mostly due to the enhancement of the *sp-d* exchange interaction, especially *p-d* exchange interaction ($N_0\beta$), because the IB does not contribute much around *L*-CPs (E_1 and $E_1+\Delta_1$) as shown in Fig. 1-3 [99] [109]. In LT-GaAs (Fig. 5-3 (a)), a broad positive MCD peak around *L*-CPs was observed and it is resulted from the merging of two dispersion-type MCD structures as also mentioned in Section 2.2.4 [133]. On the other hand, in HT-GaAs (Fig. 5-1 (a)), the result clearly shows that an MCD signal is composed of two dispersion-type structures with opposite polarities centered at E_1 and $E_1+\Delta_1$ [133] [155]. These facts suggest that a low temperature growth inevitably degrades the crystal quality of GaAs as well as $Ga_{1-x}Mn_xAs$ [13] [97] [104] [108] [132] [159]–[161]. Especially for $Ga_{1-x}Mn_xAs$, Mn creates defects in the material system, which also contributes to the degrading of the crystal quality. Thus, poor material quality usually causes the broadening of the MCD structures as it can be seen in Fig. 5-3 (a) - 5-5 (h) and these MCD broadening effects are typical observations in $Ga_{1-x}Mn_xAs$ [133] [168] [174].

Furthermore, figure 5-3 (a) – 5-5 (h) also show that the broad positive MCD peak around *L*-CPs shifts its peak position to lower energy as the Mn concentration increases, and the shift seems to saturate with a very small Mn concentration (x = 0. 001).

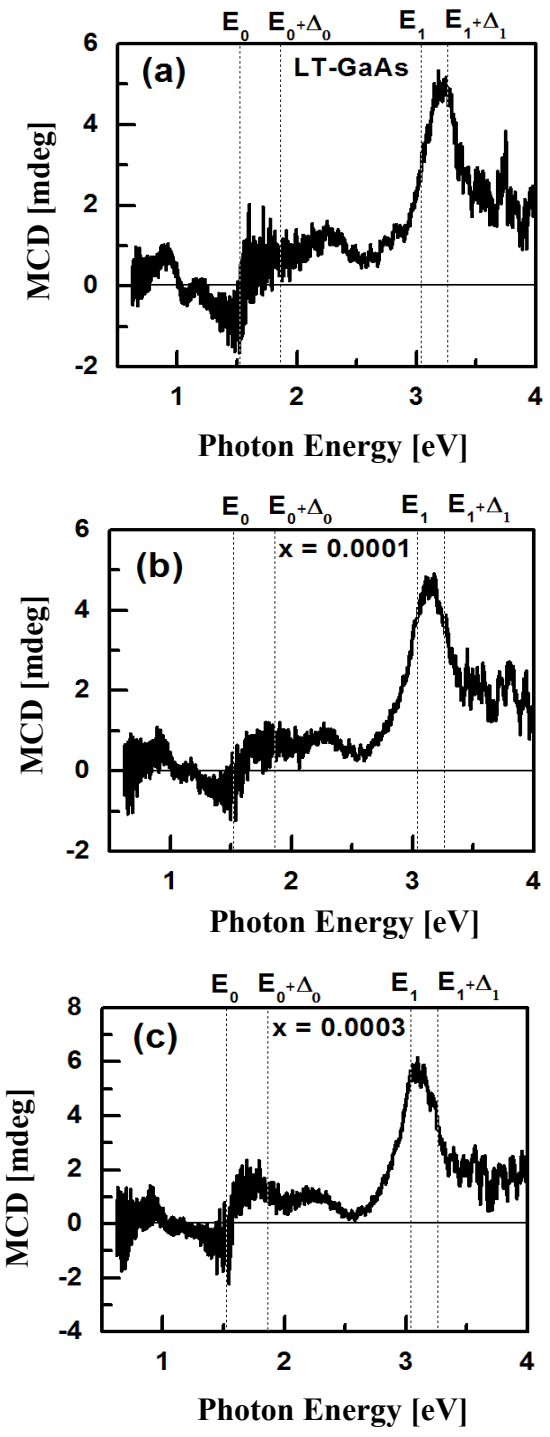

Figure 5-3 (a) - (c) Transmission-mode MCD spectra of $Ga_{1-x}Mn_xAs$ on sapphire with different Mn concentrations measured in a magnetic field of 1 Tesla at 6 K as a function of photon energy. Photon energies corresponding to Γ- (E_0 and $E_0+\Delta_0$) and L- (E_1 and $E_1+\Delta_1$) CPs of GaAs are shown by vertical dotted lines [133].

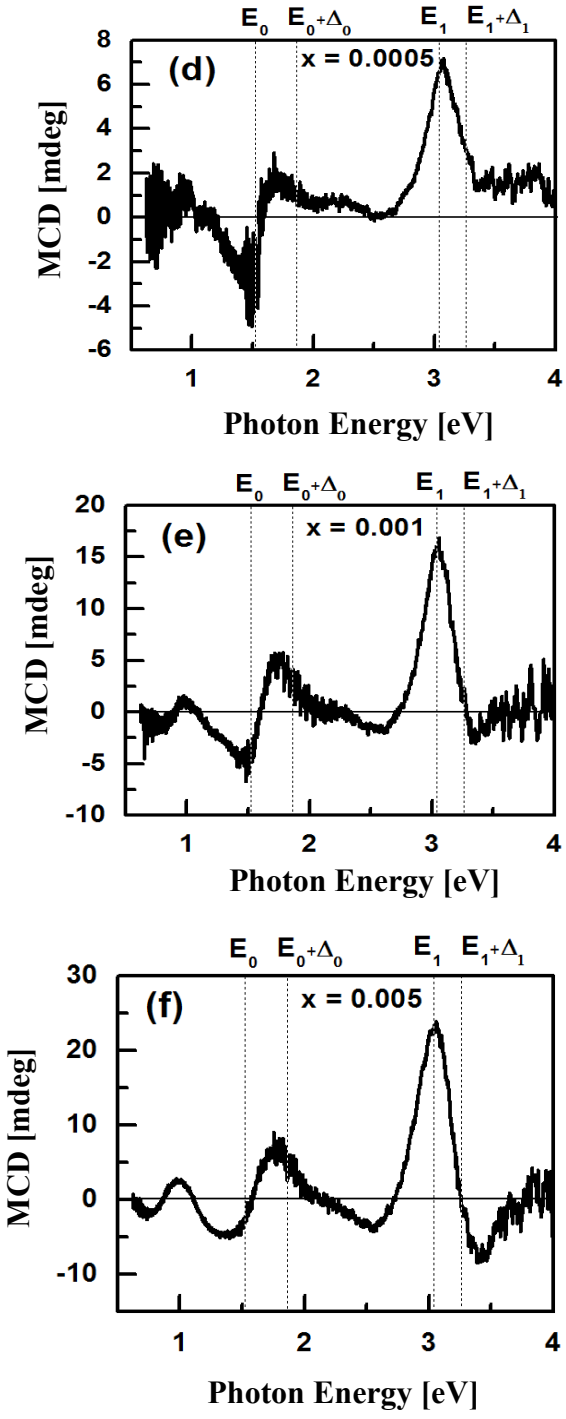

Figure 5-4 (d) - (e) Transmission-mode MCD spectra of $Ga_{1-x}Mn_xAs$ on sapphire with different Mn concentrations measured in a magnetic field of 1 Tesla at 6 K as a function of photon energy. Photon energies corresponding to Γ- (E_0 and $E_0+\Delta_0$) and L- (E_1 and $E_1+\Delta_1$) CPs of GaAs are shown by vertical dotted lines [133].

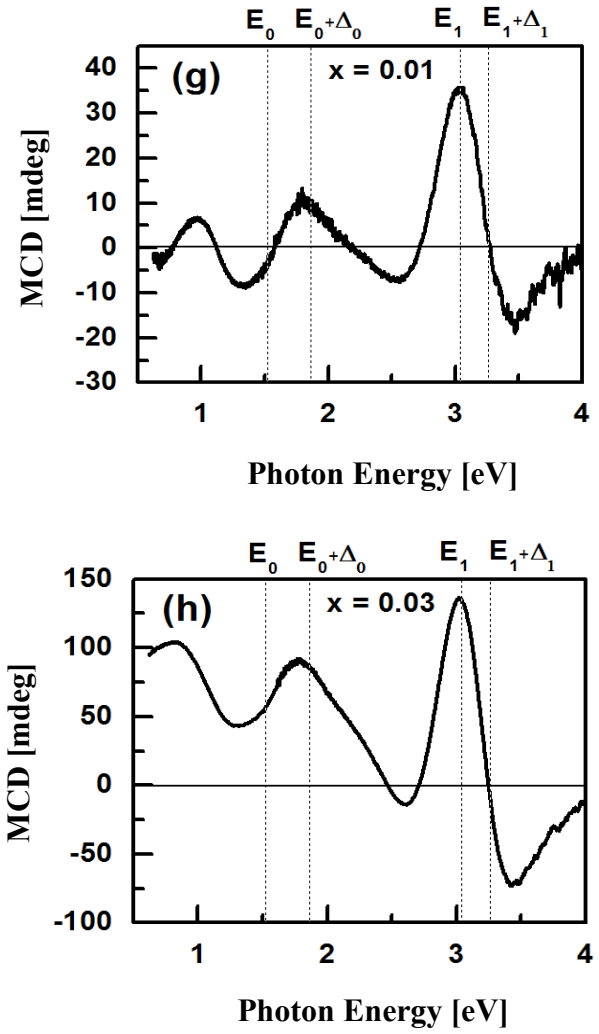

Figure 5-5 (g) - (h) Transmission-mode MCD spectra of $Ga_{1-x}Mn_xAs$ on sapphire with different Mn concentrations measured in a magnetic field of 1 Tesla at 6 K as a function of photon energy. Photon energies corresponding to Γ- (E_0 and $E_0+\Delta_0$) and L- (E_1 and $E_1+\Delta_1$) CPs of GaAs are shown by vertical dotted lines [133].

5.2.3 *dkL/dE* spectra of $Ga_{1-x}Mn_xAs$ on sapphire

Figures in this section show the transmission-mode *dkL/dE* (*i.e.* energy derivative of absorption coefficient) of $Ga_{1-x}Mn_xAs$/Sapphire with different Mn concentrations as a function of photon energy measured at 6 K [133].

Figure 5-6 (a)-(c) shows the *dkL/dE* spectra for (a) a reference LT-GaAs, and $Ga_{1-x}Mn_xAs$ films with (b) x = 0.0001, and (c) x = 0.0003. Figure 5-7 (d)-(f) shows the *dkL/dE* spectra for $Ga_{1-x}Mn_xAs$ films with (d) x = 0.0005, (e) x = 0.001, and (f) x = 0.005. Figure 5-8 (g)-(h) shows the *dkL/dE* spectra for $Ga_{1-x}Mn_xAs$ films with (g) x = 0.01 and (h) x = 0.03.

Comparing these *dkL/dE* spectra with the one from the HT-GaAs shown in Fig. 5-1(b), it is noticeable that the *dkL/dE* spectra of LT-GaAs and $Ga_{1-x}Mn_xAs$ become broader with a less pronounced single peak band shape due to the low temperature growth process inducing a degrading of the semiconductor quality as well as the doping process especially at a high Mn content [13] [97] [104] [108] [132] [133] [159]–[161]. However, *dkL*/*dE* spectra of LT-GaAs and $Ga_{1-x}Mn_xAs$ (x = 0.0001 to x = 0.001) shown in Fig. 5-6 and Fig. 5-7 clearly show a peak around 3.04 eV (E_1) and a shoulder around 3.26 eV ($E_1+\Delta_1$), respectively, both originating from the two dispersion-type MCD structures [133]. The *dkL*/*dE* peaks become broader in $Ga_{1-x}Mn_xAs$ with x larger than x = 0.005 (see Fig. 5-8).

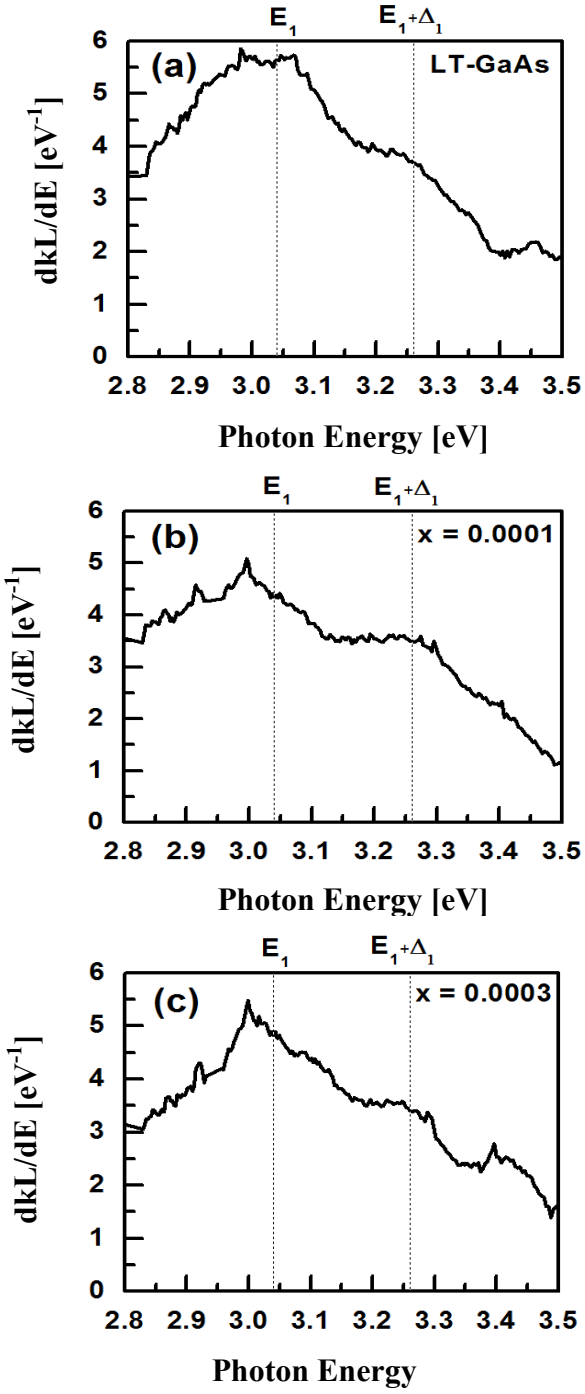

Figure 5-6 (a) - (c) Transmission-mode *dkL/dE* spectra of $Ga_{1-x}Mn_xAs$ on sapphire with different Mn concentrations measured at 6 K as a function of photon energy. Photon energies corresponding to Γ- (E_0 and $E_0+\Delta_0$) and L- (E_1 and $E_1+\Delta_1$) CPs of GaAs are shown by vertical dotted lines [133].

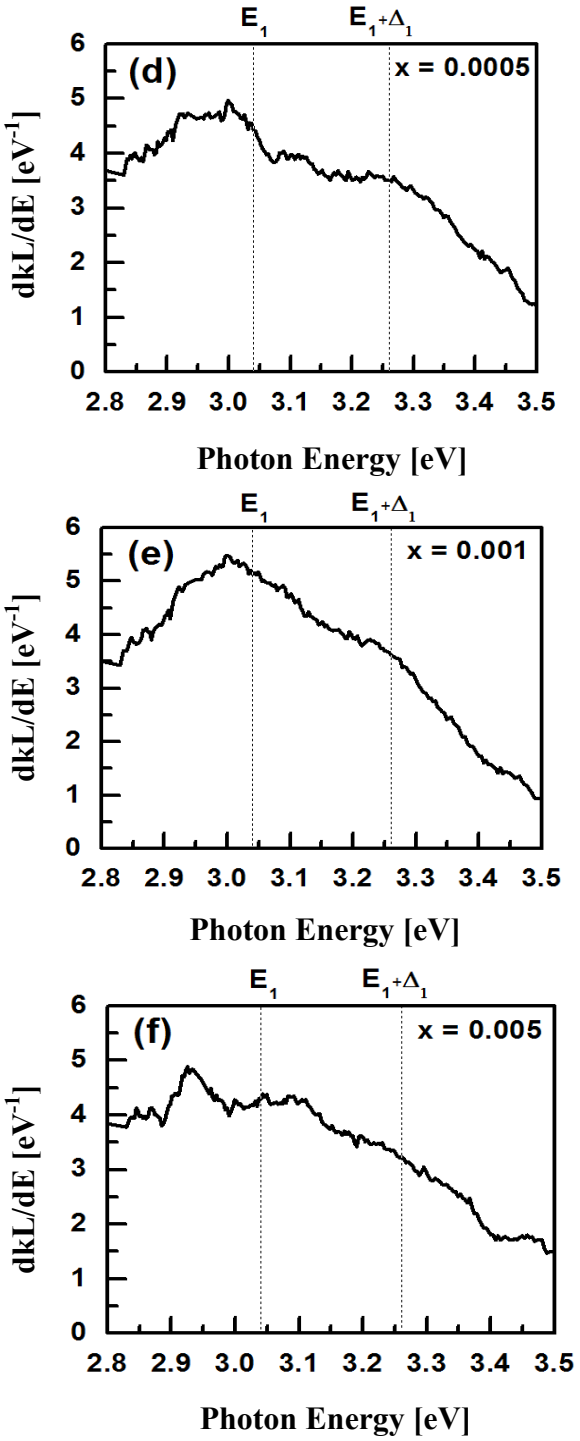

Figure 5-7 (d) - (f) Transmission-mode *dkL/dE* spectra of $Ga_{1-x}Mn_xAs$ on sapphire with different Mn concentrations measured at 6 K as a function of photon energy. Photon energies corresponding to Γ- (E_0 and $E_0+\Delta_0$) and L- (E_1 and $E_1+\Delta_1$) CPs of GaAs are shown by vertical dotted lines [133].

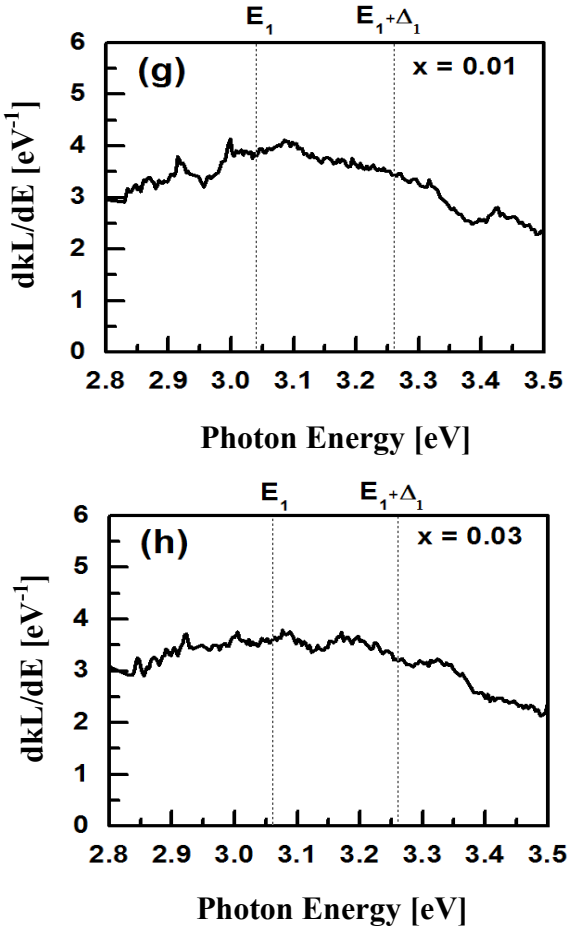

Figure 5-8 (g) - (h) Transmission-mode *dkL/dE* spectra of $Ga_{1-x}Mn_xAs$ on sapphire with different Mn concentrations measured at 6 K as a function of photon energy. Photon energies corresponding to Γ- (E_0 and $E_0+\Delta_0$) and L- (E_1 and $E_1+\Delta_1$) CPs of GaAs are shown by vertical dotted lines [133].

5.3 $Ga_{1-x}Mn_xAs$ on InP

5.3.1 Hysteresis loop of $Ga_{1-x}Mn_xAs$ on InP

Figure 5-9 shows reflection-mode MCD hysteresis loops of $Ga_{1-x}Mn_xAs$ grown on InP ($Ga_{1-x}Mn_xAs$/InP) with different Mn concentrations monitored at 2.78 eV and at 6 K as a function of an applied magnetic field. It is seen that the $Ga_{1-x}Mn_xAs$/InP (x = 0.03) is ferromagnetic while $Ga_{1-x}Mn_xAs$/InP with lower Mn concentrations (x = 0.0001 to 0.01)

are paramagnetic at 6 K. In addition, the estimated Curie temperature T_c of $Ga_{1-x}Mn_xAs$/InP (x = 0.03) was 35 ± 2 K as shown in Appendix E in Fig. E-1 (b).

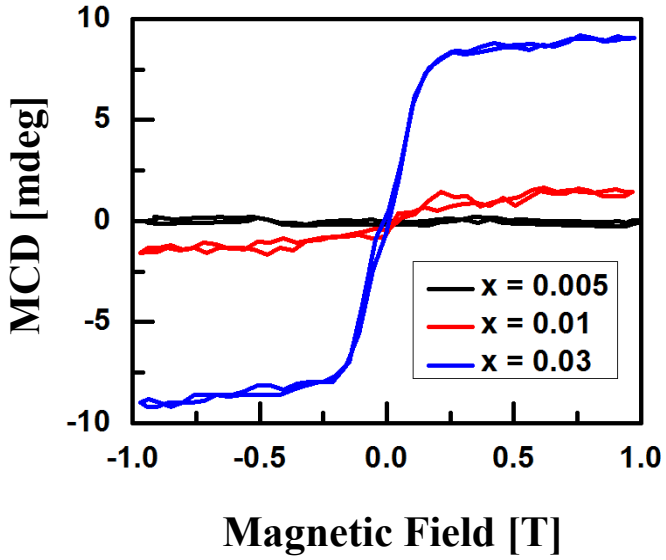

Figure 5-9 Reflection-mode MCD hysteresis loops of $Ga_{1-x}Mn_xAs$ on InP with different Mn concentrations monitored at 2.78 eV at 6 K as a function of a magnetic field.

5.3.2 MCD spectra of $Ga_{1-x}Mn_xAs$ on InP

Figures in this section show the reflection-mode MCD spectra of $Ga_{1-x}Mn_xAs$/InP with different Mn concentrations as a function of photon energy measured at 6 K and 1T [133]. Figure 5-10 (a)-(c) shows the MCD spectra for (a) a reference LT-GaAs, and $Ga_{1-x}Mn_xAs$ films with (b) x = 0.0001, and (c) x = 0.0003. Figure 5-11 (d)-(f) shows the MCD spectra for $Ga_{1-x}Mn_xAs$ films with (d) x = 0.0005, (e) x = 0.001, and (f) x = 0.005. Figure 5-12 (g)-(h) shows the MCD spectra for $Ga_{1-x}Mn_xAs$ films with (g) x = 0.01 and (h) x = 0.03.

The reflection-mode MCD spectra were measured between 1.1 eV and 3.5 eV due to the limitation of the system whereas transmission-mode MCD spectra presented in Section 5.3 were measured in a wider spectral range between 0.6 eV and 6.2 eV. This fact is strictly related to the technical limitation of the developed reflection-mode MCD setup; however it brought certain difficulty to this project in the MCD spectra analysis for photons with energy below the band gap energy. Thus, the detailed analysis of MCD spectra extended toward an infrared spectral region will be conducted in a future work. Although we were not able to investigate the reflection-mode MCD spectra in a similar spectral range as we have done for transmission-mode MCD spectra, we were capable to conduct similar theoretical analysis of collected experimental MCD data. This was possibly due to the fact that in both cases we were primarily focused on optical transitions at *L*-CPs which are accessible in MCD spectroscopy by probing with much larger photon energy.

5.3.2.1 Γ critical points of $Ga_{1-x}Mn_xAs$ on InP

As the concentration of Mn increases in $Ga_{1-x}Mn_xAs$ the amplitude of the MCD peaks are expected to enhance as is shown in Sections 5.2.2 and 5.3.2. However, at the same time, the reflection-mode MCD spectra evolved somehow unexpectedly. The polarity of the MCD spectra of LT-GaAs and $Ga_{1-x}Mn_xAs$/InP with x = 0.001, 0.0003, 0.0001, respectively, are negative whereas, in general, the polarity of MCD spectra for all $Ga_{1-x}Mn_xAs$/sapphire disregard of the Mn content is positive. The origin of this negative polarity is unclear at this time; however it may be due to the effect of InP substrate or due

to the specific nature of the developed reflection-mode MCD system. It is reasonable to assume at this time that the mirror used in the reflection-mode MCD setup introduces extra refractive index changes affecting the MCD signal polarity. It is important to mention that this parasitic effect obscuring the MCD spectra polarity is only important when $Ga_{1-x}Mn_xAs$ samples are doped with low Mn concentrations (*i.e.* for $x < 0.001$). Otherwise, it looks like the effect is less pronounced for $Ga_{1-x}Mn_xAs$ samples with a larger Mn content. Furthermore, even though the polarity of the reflection-mode MCD spectra for $Ga_{1-x}Mn_xAs$/InP samples low Mn content are negative, the absolute value of these MCD spectra structures are very similar to the ones obtained by $Ga_{1-x}Mn_xAs$/sapphire with transmission-mode MCD. Thus, the theoretical analysis of collected reflection-mode MCD spectra presented in the following can still be validated using collected results.

5.3.2.2 *L* critical points of $Ga_{1-x}Mn_xAs$ on InP

Another prominent difference in the MCD spectra structure collected for $Ga_{1-x}Mn_xAs$/InP and $Ga_{1-x}Mn_xAs$/sapphire is the photon energy of the MCD peak(s) position. The MCD peaks from the $Ga_{1-x}Mn_xAs$/sapphire are around 3.04 eV at *L*-CPs (see Figs. 5-3 – 5-5) whereas the corresponding peaks from the $Ga_{1-x}Mn_xAs$/InP are around 2.78 eV at *L*-CPs (see Figs. 5-10 – 5-12), respectively.

Furthermore, in the case of $Ga_{1-x}Mn_xAs$/sapphire the amplitude of MCD peaks around *L*-CPs is larger than the MCD peaks at Γ-CPs (see Figs. 5-3 – 5-5). On the other hand, in $Ga_{1-x}Mn_xAs$/InP the amplitude of MCD peaks around *L*-CPs is smaller than that

at Γ-CPs (see Figs. 5-10 – 5-12). This indicates that the Zeeman splitting energy around L-CPs of $Ga_{1-x}Mn_xAs$/InP is expected to be smaller than that of $Ga_{1-x}Mn_xAs$/sapphire. Moreover, the reduction of the MCD signal amplitude of $Ga_{1-x}Mn_xAs$/InP as compared to that of $Ga_{1-x}Mn_xAs$/sapphire may be due to the differences between involved reflection-mode and the transmission-mode experimental systems.

Recently *Bsatee* has measured [175] using the facility developed in this project the reflection-mode MCD spectrum of $Ga_{1-x}Mn_xAs$/sapphire . It was shown that the value of the reflection-mode MCD peak amplitude was about 22 mdeg whereas the one measured by transmission-mode MCD was about 110 mdeg. This suggests that the reflection-mode MCD setup decreases the MCD spectrum amplitude around L-CPs compared to the ones measured by the transmission-mode MCD setup. As we have considered before, the MCD spectra amplitude reduction may also originate from the extra mirror refractive index changes as well as light absorption. However, the overall structure of the MCD spectra for $Ga_{1-x}Mn_xAs$, especially with a higher concentration of Mn obtained by the reflection-mode setup, appears similar to the ones obtained by the transmission-mode setup. Consequently, the reflection-mode MCD results are still meaningful to analyze.

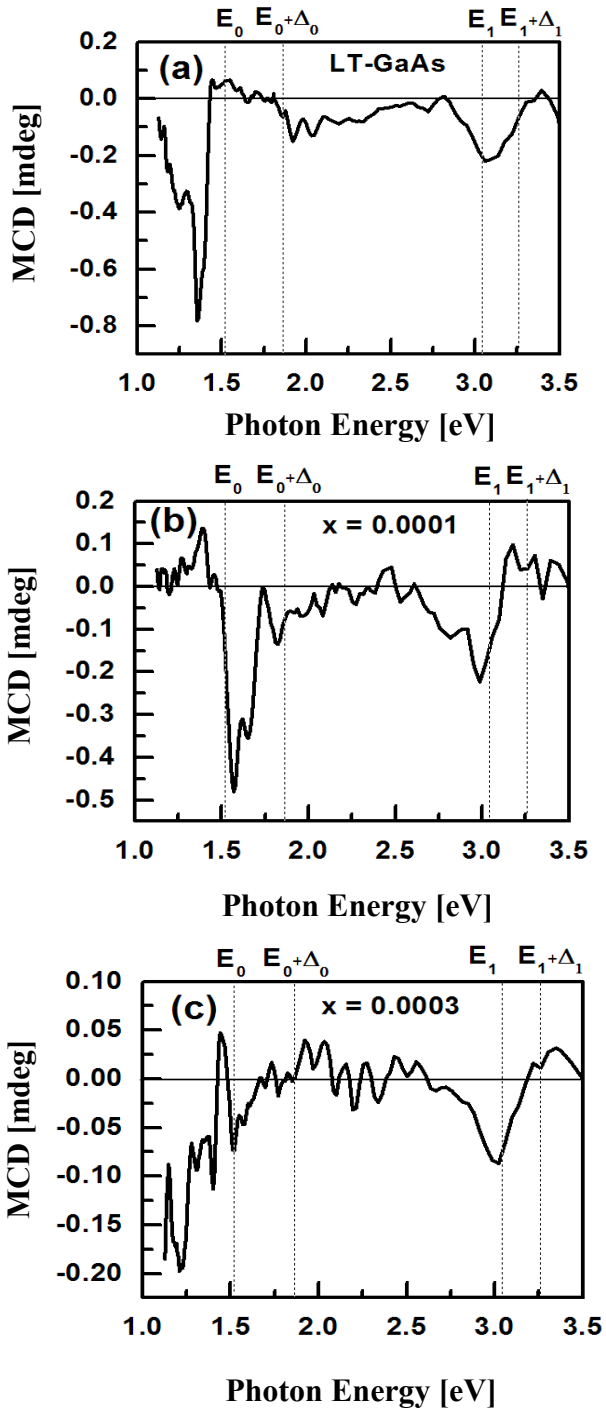

Figure 5-10 (a) - (c) Reflection-mode MCD spectra of $Ga_{1-x}Mn_xAs$ on InP with different Mn concentrations measured in a magnetic field of 1 Tesla at 6 K as a function of photon energy. Photon energies corresponding to Γ- (E_0 and $E_0+\Delta_0$) and L- (E_1 and $E_1+\Delta_1$) CPs of GaAs are shown by vertical dotted lines.

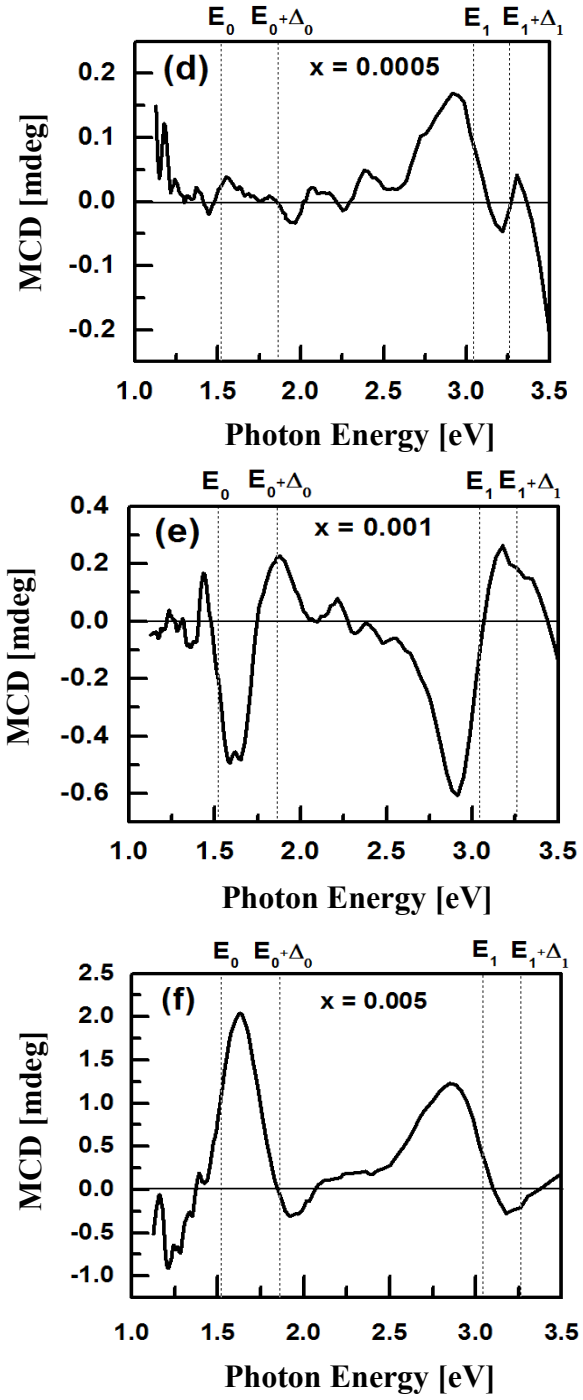

Figure 5-11 (d) - (h) Reflection-mode MCD spectra of $Ga_{1-x}Mn_xAs$ on InP with different Mn concentrations measured in a magnetic field of 1 Tesla at 6 K as a function of photon energy. Photon energies corresponding to Γ- (E_0 and $E_0+\Delta_0$) and L- (E_1 and $E_1+\Delta_1$) CPs of GaAs are shown by vertical dotted lines.

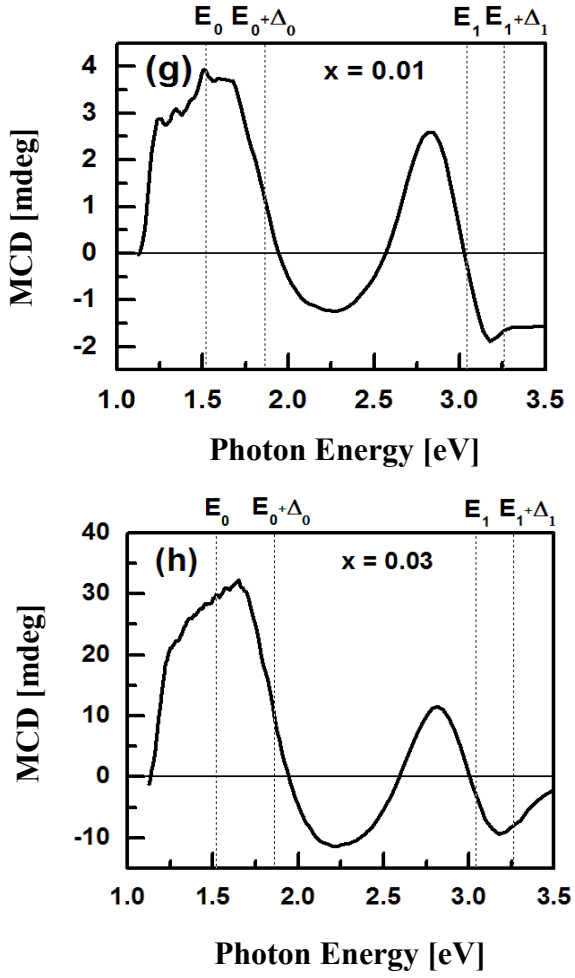

Figure 5-12 (g) - (h) Reflection-mode MCD spectra of $Ga_{1-x}Mn_xAs$ on InP with different Mn concentrations measured in a magnetic field of 1 Tesla at 6 K as a function of photon energy. Photon energies corresponding to Γ- (E_0 and $E_0+\Delta_0$) and L- (E_1 and $E_1+\Delta_1$) CPs of GaAs are shown by vertical dotted lines.

5.3.3 *dRL/dE* spectra of $Ga_{1-x}Mn_xAs$ on InP

Figures in this section show the reflection-mode *dRL/dE* (*i.e.* energy derivative of reflection coefficient) of $Ga_{1-x}Mn_xAs$/InP with different Mn concentrations as a function of photon energy measured at 6 K.

Figure 5-13 (a)-(c) shows the *dRL/dE* spectra for (a) a reference LT-GaAs, and $Ga_{1-x}Mn_xAs$ films with (b) x = 0.0001, and (c) x = 0.0003. Figure 5-14 (d)-(f) shows the *dRL/dE* spectra for $Ga_{1-x}Mn_xAs$ films with (d) x = 0.0005, (e) x = 0.001, and (f) x = 0.005. Figure 5-15 (g)-(h) shows the *dRL/dE* spectra for $Ga_{1-x}Mn_xAs$ films with (g) x = 0.01 and (h) x = 0.03.

It is seen in these figures that there is a consistent tendency for the *dRL/dE* spectra shape changes and that all *dRL/dE* spectra have the same peak around 2.78 eV. The position of this *dRL/dE* spectra peak is the same in all MCD spectra measured for $Ga_{1-x}Mn_xAs$/InP samples (see Figs. 5-10 – 5-12). This was expected due to the rigid band shift model (Eq. (2.30)). However, there is no consistent tendency for change of the *dRL/dE* spectra amplitude with a different concentration of Mn. At x = 0.03, 0.05, 0.001, and 0.0005 of Mn concentration, the *dRL/dE* spectra amplitudes are relatively larger than the ones at x = 0.01, 0.0003, 0.0001, and LT-GaAs. The reason is unclear at this point.

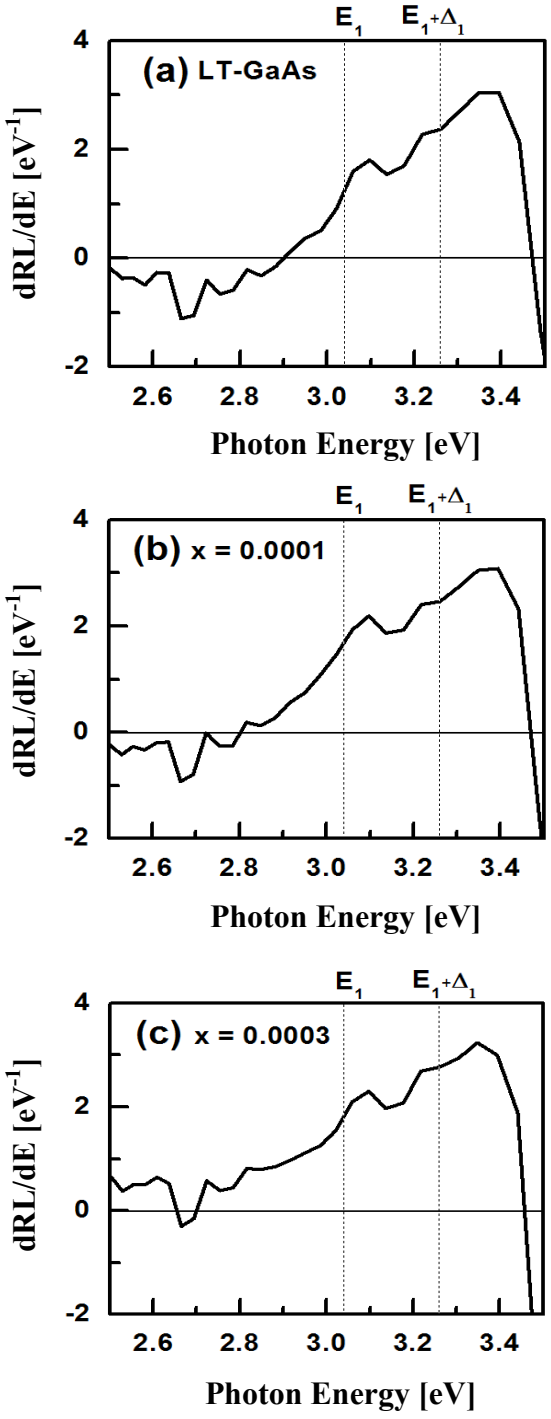

Figure 5-13 (a) – (c) Reflection-mode *dRL/dE* spectra of $Ga_{1-x}Mn_xAs$ on InP with different Mn content measured at 6 K as a function of photon energy. Photon energies corresponding to *Γ*- (E_0 and $E_0+\Delta_0$) and *L*- (E_1 and $E_1+\Delta_1$) CPs of GaAs are shown by vertical dotted lines.

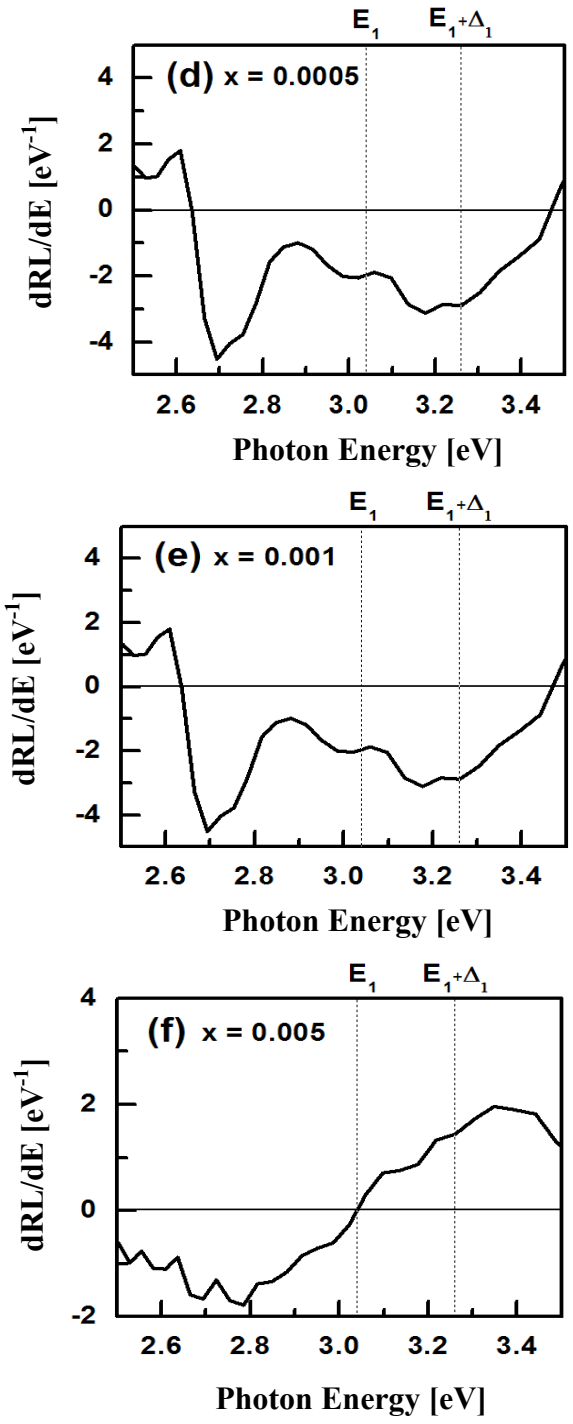

Figure 5-14 (d) – (f) Reflection-mode *dRL/dE* spectra of $Ga_{1-x}Mn_xAs$ on InP with different Mn content measured at 6 K as a function of photon energy. Photon energies corresponding to Γ- (E_0 and $E_0+\Delta_0$) and L- (E_1 and $E_1+\Delta_1$) CPs of GaAs are shown by vertical dotted lines.

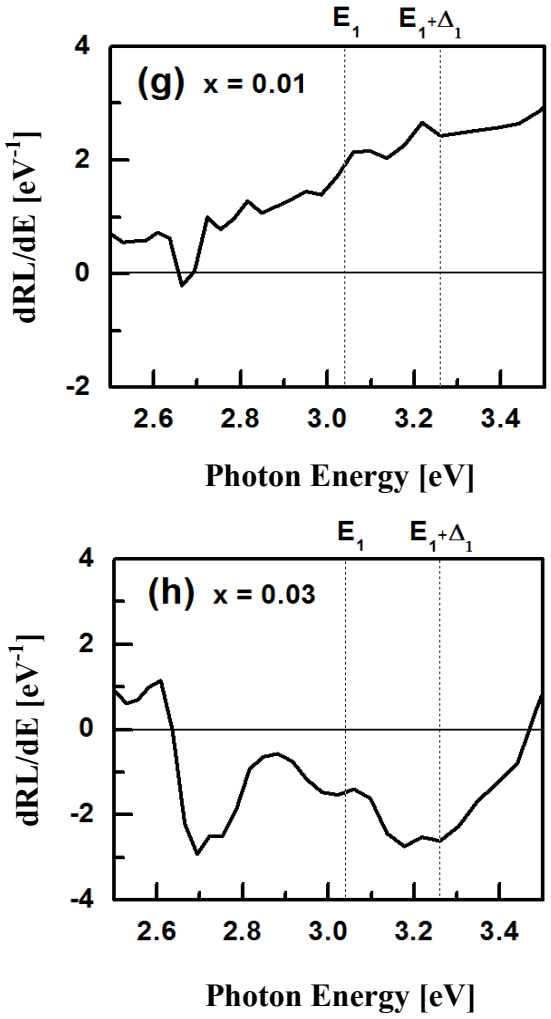

Figure 5-15 (g) – (h) Reflection-mode *dRL/dE* spectra of $Ga_{1-x}Mn_xAs$ on InP with different Mn content measured at 6 K as a function of photon energy. Photon energies corresponding to *Γ*- (E_0 and $E_0+\Delta_0$) and *L*- (E_1 and $E_1+\Delta_1$) CPs of GaAs are shown by vertical dotted lines.

5.4 Free-standing $Ga_{1-x}Mn_xAs$ grown on InP

We have investigated free-standing $Ga_{1-x}Mn_xAs$ originally grown on InP substrate using transmission-mode MCD spectroscopy. The observed spectral features were very similar to the ones observed for $Ga_{1-x}Mn_xAs$/sapphire measured by transmission-mode

MCD. Therefore, in the following section we will consider only selected major results for the free-standing $Ga_{1-x}Mn_xAs$ sample measure using transmission-mode MCD setup.

5.4.1 Hysteresis loop of free-standing $Ga_{1-x}Mn_xAs$

Figure 5-16 shows a transmission-mode MCD hysteresis loop of free-standing $Ga_{1-x}Mn_xAs$ measured at 6 K as a function of an applied magnetic field [176]. As it was expected, the free-standing $Ga_{1-x}Mn_xAs$ sample with x = 0.03 shows ferromagnetic hysteresis behavior at 2.96 eV (Fig. 5-16) The Curie temperature T_c of this sample was determined from the Arrott plot of MCD intensity at different photon energies and it was 36 ± 1 K.

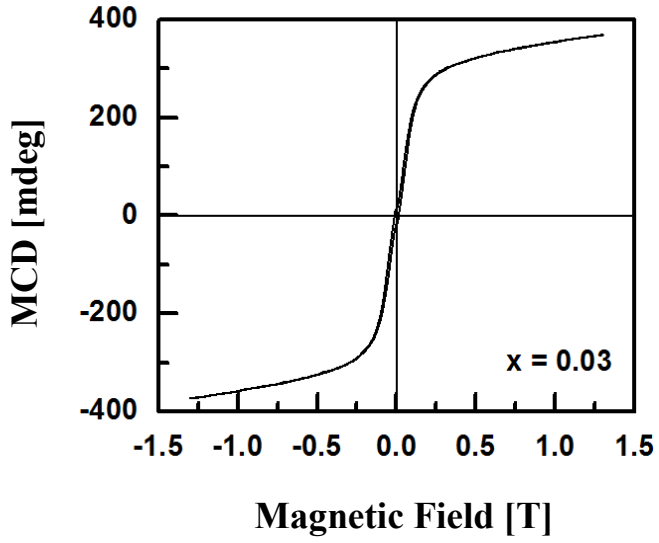

Figure 5-16 Transmission-mode MCD hysteresis loops of free-standing $Ga_{1-x}Mn_xAs$ removed from InP. The photon energy was fixed at 2.96 eV and hysteresis was measured at 6 K as a function of a magnetic field [176].

5.4.2 Comparison between free-standing $Ga_{1-x}Mn_xAs$, and $Ga_{1-x}Mn_xAs$ on sapphire

Figure 5-17 shows the comparison between transmission-mode MCD spectra of the free-standing $Ga_{1-x}Mn_xAs$ film and $Ga_{1-x}Mn_xAs$ film grown on sapphire and measured in the magnetic field of 1 Tesla measured at 6 K as a function of photon energy. It is interesting to note that the amplitude of the MCD spectrum from the free-standing $Ga_{1-x}Mn_xAs$ is about 3 times larger than that of the $Ga_{1-x}Mn_xAs$/sapphire around *L*-CPs. In addition, the peak position of the free-standing $Ga_{1-x}Mn_xAs$ around *L*-CPs is about 2.96 eV whereas that of the $Ga_{1-x}Mn_xAs$/sapphire is about 3.04 eV. Furthermore, the IB-related MCD spectra from the free-standing $Ga_{1-x}Mn_xAs$ around *Γ*-CPs are larger than that of the $Ga_{1-x}Mn_xAs$/sapphire around *Γ*-CPs.

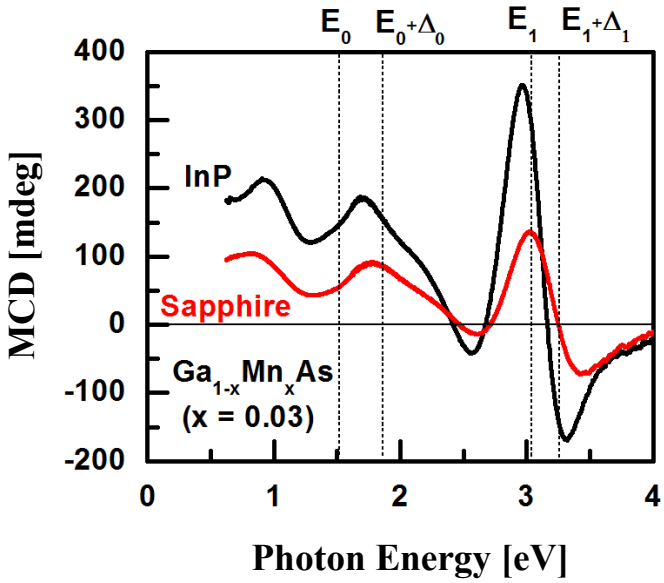

Figure 5-17 Comparison of transmission-mode MCD spectra for free-standing $Ga_{1-x}Mn_xAs$ removed from InP and $Ga_{1-x}Mn_xAs$ grown on sapphire measured in a magnetic field of 1 Tesla at 6 K as a function of photon energy. Photon energies corresponding to *Γ*- (E_0 and $E_0+\Delta_0$) and *L*- (E_1 and $E_1+\Delta_1$) CPs of GaAs are shown by vertical dotted lines.

5.4.3 MCD and *dkL*/*dE* spectra of free-standing $Ga_{1-x}Mn_xAs$

Figure 5-18 (a) - (c) show transmission-mode MCD and *dkL/dE* spectra of free-standing $Ga_{1-x}Mn_xAs$ with x = 0.03, 0.01 and 0.0003, respectively. Before discussing these results it should be noted here that a sharp MCD peak around 3.6 eV seen in Figs. 5-18 (a) and (b) does not come from $Ga_{1-x}Mn_xAs$. This peak is due to the presence of remaining residues after the InP substrate was chemically etched out and as such will not be considered in the following discussion.

The amplitude of both MCD and *dkL/dE* from the free-standing $Ga_{1-x}Mn_xAs$ (see Fig. 5-18) is larger than that of $Ga_{1-x}Mn_xAs$/sapphire (see Figs. 5-3 - 5-8) due to the improved quality of the material crystalline structure resulting from the original growth of free-standing sample on the InP substrate. It is known, that both GaAs and InP have a cubic crystal structure. Thus $Ga_{1-x}Mn_xAs$ film grown on InP should have a smaller lattice mismatch resulting in improved quality. On the other hand, the sapphire has a hexagonal structure, thus, the crystal quality of GaMnAs on sapphire becomes worse and the amplitude of MCD and *dkL/dE* eventually decreases due to defects. These arguments are also mentioned in Section 3.2 with relevant references.

Figure 5-18 (a) and (b) shows that both the MCD and *dkL/dE* spectra from free-standing $Ga_{1-x}Mn_xAs$ with x = 0.03 and x = 0.01exhibit broadened peaks. Interestingly enough, in both MCD and *dkL/dE* spectra for free-standing $Ga_{1-x}Mn_xAs$ with x = 0.0003 (see Fig. 5-18) one can identify two peaks originating from two dispersion curves due to the two dimensional M_1-type Van Hove singularity [133] [162]. As described in Section 3.2, Since the free-standing $Ga_{1-x}Mn_xAs$ has a better crystal structure, structures of both

MCD and *dkL/dE* spectra for the free-standing $Ga_{1-x}Mn_xAs$ ($x = 0.0003$) are similar to the corresponding spectra for HT-GaAs (see Figs. 5-1 (a) and (b)). Also, both MCD and *dkL/dE* spectral structures of the free-standing $Ga_{1-x}Mn_xAs$ ($x = 0.0003$) shift toward the lower energy side as compared to HT-GaAs.

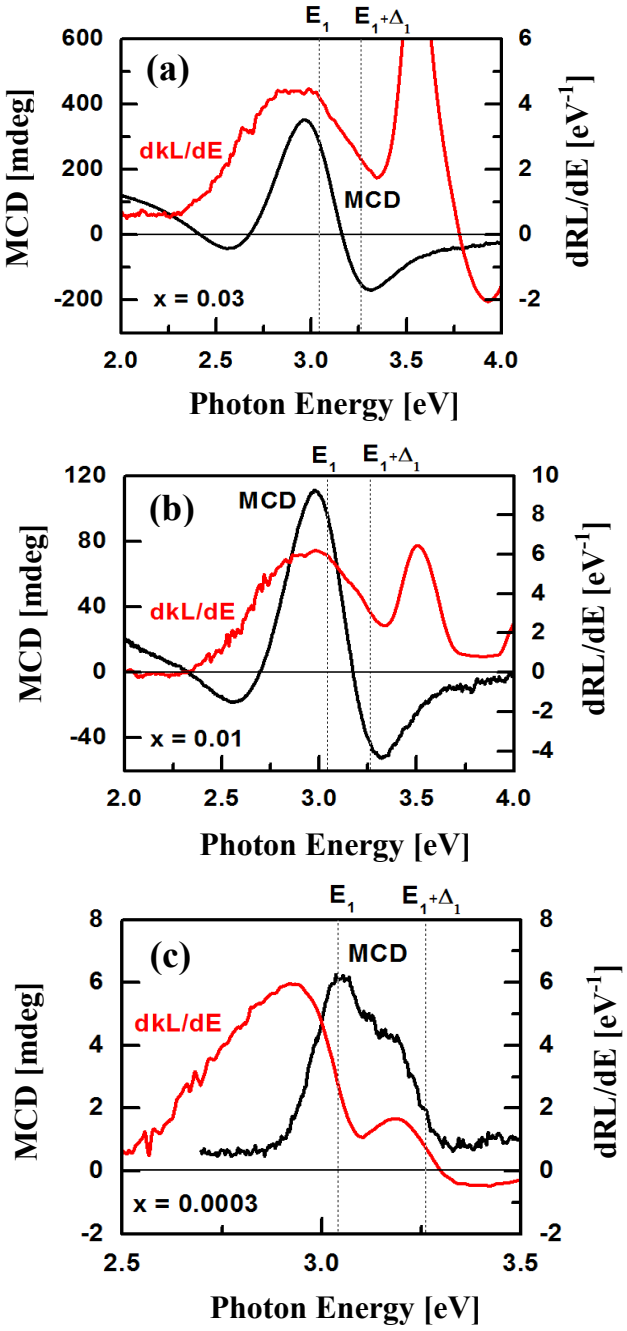

Figure 5-18 Transmission-mode MCD and *dkL/dE* spectra of free-standing $Ga_{1-x}Mn_xAs$ removed from InP substrates with Mn content equal: (a) x = 0.03, (b) x = 0.01, (c) x = 0.0003. Spectra were measured in a magnetic field of 1 Tesla at 6 K as a function of photon energy. Photon energies corresponding to Γ- (E_0 and $E_0+\Delta_0$) and L- (E_1 and $E_1+\Delta_1$) CPs of GaAs are shown by vertical dotted lines. [176].

5.5 MOKE spectroscopy results

During the course of this project we have considered and developed an upgraded magneto-optical Kerr effect (MOKE) measurement setup for studying $Ga_{1-x}Mn_xAs$ samples. However, despite our best efforts we have not observed any MOKE signals for these samples. Lang *et al.* [156] measured the MOKE signals from $Ga_{1-x}Mn_xAs$ epilayers; however specimens studied by them in the project were not matching. Their samples had 300 nm thickness and GaAs buffer layer with Mn content between $x = 0.14$ and $x = 0.03$ whereas our samples are 50 nm thick, do not have a buffer layer wand Mn content between $x = 0.0001$ and $x = 0.03$, respectively. The buffer layer allows a deposited film to have better quality that enhances the overall magnetization. However, one constraint when developing materials for this project was to systematically investigate the optical transitions at *L*-CPs of the Brillouin zone for structurally simple cases of $Ga_{1-x}Mn_xAs$ material system (*i.e.* no buffer layers, small film thickness, *etc.*). When considering these constraints, we were able to avoid in recorded MCD spectra an interference effect (*i.e.* the films thickness was ~50 nm) and uncertainty in MCD spectra interpretation due to the buffer layer properties affecting small intensity MCD spectral features. Also, at the same time the studied $Ga_{1-x}Mn_xAs$ films having ~50 nm thickness offer a large absorption of light around *L*-CPs needed for achieving the goals of this project. Thus, by giving special considerations to the materials development process as mentioned above we were able to generate $Ga_{1-x}Mn_xAs$ samples suitable for obtaining "unaffected" MCD and *dkL/dE* spectra structures at *L*-CPs. However, the functionality of the developed combined

polar/longitudinal MOKE system was verified in parallel to this project as demonstrated in Ref. [175] and Appendix E.

6. DISCUSSIONS

6.1 MCD background subtraction, fitting, and deconvolution procedure

This section demonstrates the procedure applied for the IB-related MCD signal background subtraction, MCD spectra fitting, and the MCD spectra deconvolution using an energy derivative of the Gaussian function. The goal was to estimate the Zeeman splitting energies at Γ- and L-CPs. The theoretical discussion supporting the experimental MCD data analysis was presented in Section 2.2.4 and the performed spectroscopic data fitting and deconvolution are outlined in Fig. 2-14.

6.1.1 HT-GaAs

One of the main tasks in this project was an estimation of Zeeman splitting energy especially at Γ-CPs for reference GaAs and various $Ga_{1-x}Mn_xAs$ samples. It is known that the estimation of Zeeman splitting energy at Γ-CPs is challenging due to the presence of IB-related multiple optical transitions at Γ-CPs. Therefore, it is beneficial to estimate the Zeeman splitting energy at L-CPs first because of a smaller number of optical transitions observed due to the indirect band gap of GaAs semiconductor at L-CPs. Subsequently, one can calculate the Zeeman splitting energy at Γ-CPs using certain theoretical and experimental assumptions. As we have mentioned already (see Section 2.2.4), the measured MCD spectra structure around L-CPs is composed of a superposition of two dispersion-type components originating from the two dimensional M_1-type Van Hove singularity of E_1 and $E_1+\Delta_1$ optical transitions. Because of that the first task in MCD spectra analysis is to see how to extract these two dispersion MCD curves using a fitting

method. To do that we have used an energy derivative of the Gaussian function (see Eqs. 2.32 – 2.34) and first fitted the MCD signal from HT-GaAs as shown by line 1 in Fig. 6-1 [133]. Then, we extracted all constants of the derivative of the Gaussian function from the fitted MCD spectrum (line 1) and successfully deconvolved it into a sum of two dispersion curves (line 2 and 3) and a linear background (line 4), respectively. The two dispersion components have the same spectral widths and magnitudes but opposite polarities due to E_1 and $E_1+\Delta_1$ optical transitions as shown in Fig 6-1.

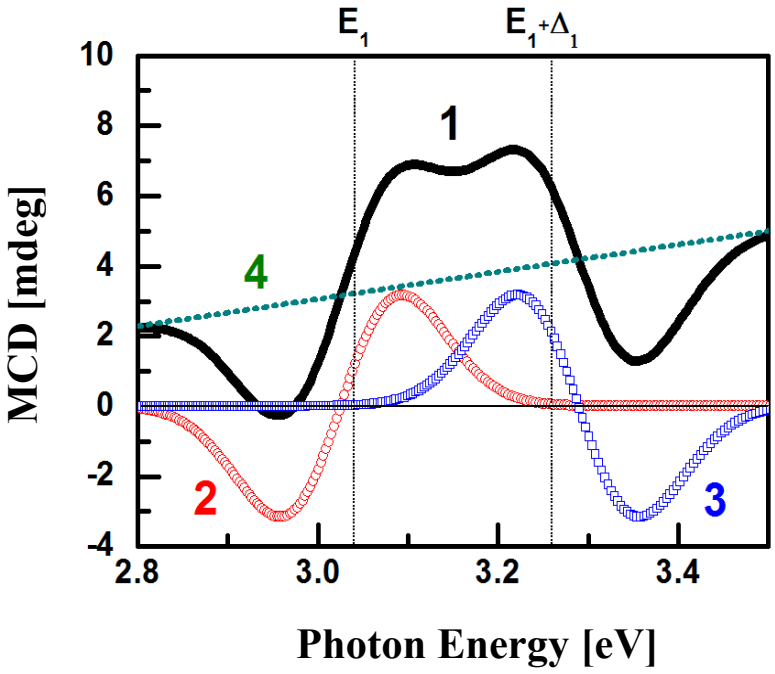

Figure 6-1 Deconvolution of theoretically fitted MCD spectrum (line 1) being a sum of two dispersion curves (line 2 and 3) and a linear background (line 4) of HT-GaAs using an derivative of the Gaussian function. Please notice the opposite polarities of dispersion curves are due to E_1 and $E_1+\Delta_1$ optical transitions [133] [162].

6.1.2 $Ga_{1-x}Mn_xAs$ on sapphire

The MCD spectrum of a $Ga_{1-x}Mn_xAs$/sapphire (x = 0.03) sample shows a very weak kink structure around 2.2 eV (see Fig. 5-5(h)). It should be interesting to note that Boschoten *et al.* [131] also reported that an MCD spectrum of $Ga_{1-x}Mn_xAs$/sapphire (x = 0.05) sample showed a very similar kink structure between 2.0 eV and 2.2 eV but they did not discuss its origin. To clarify the origin of this kink structure, we first analyzed the MCD spectrum of $Ga_{1-x}Mn_xAs$/sapphire (x = 0.005) in shown Fig. 5-4 (f) [133]. When the MCD spectrum around 2.0 eV – 2.2 eV is considered, a positive MCD signal below 2.0 eV is apparently generated from the $E_0+\Delta_0$ optical transition and a negative MCD signal above 2.2 eV is generated from the E_1 optical transition. Consequently, there is no MCD spectrum observed between 2.0 eV and 2.2 eV. It was shown by Ando *et al.* [109] that the $Ga_{1-x}Mn_xAs$/sapphire (x = 0.004) sample with a 10 times larger thickness showed more clearly the absence of an MCD signal between 2.0 eV and 2.2 eV. Hence, this fact indicates that the energy range between 2.0 eV and 2.2 eV can be considered as a boundary between observed optical transitions at Γ-CPs and L-CPs [133]. Also, the zero MCD signal around 2.2 eV is observed in paramagnetic $Ga_{1-x}Mn_xAs$/sapphire with very small Mn concentrations (*e.g.* x = 0.005) whereas the non-zero MCD signal around 2.2 eV is observed in ferromagnetic $Ga_{1-x}Mn_xAs$/sapphire with higher Mn concentration (*e.g.* x = 0.03). We believe that this type of evidence indicating the large positive MCD signal (*i.e.* non-zero MCD signal) around 2.2 eV comes from the impurity band (IB) related optical transitions of the ferromagnetic samples [133]. Therefore, as the first approximation, we assumed that the large positive MCD background due to the IB-

related optical transitions can be represented by a straight dotted line in Fig. 6-2 (a) [109] [133]. This line should start with a positive MCD peak around 1 eV and connect to the MCD signal at 2.2 eV because both of the MCD signals must be zero after the background subtraction. It should be emphasized that the applicable optical selection rules are relaxed due to the IB-related optical transitions at Γ-CPs, hence, the broad MCD spectral shape around Γ-CPs with a long tail toward L-CPs can be reasonably accepted as illustrated in Fig. 1-3 [109].

Line 1 shown in Fig 6-2 (b) represents an MCD spectrum after subtracting the IB-related MCD background. This modified MCD spectrum is considered as being almost free from the contributions from the IB-related optical transitions [133]. After the subtraction of the IB signal contribution, one can observe a negative peak around E_0, a positive peak around $E_0+\Delta_0$, and one large positive peak around L-CPs (E_1 and $E_1+\Delta_1$), respectively, in MCD spectrum of ferromagnetic $Ga_{0.97}Mn_{0.03}As$/sapphire. The obtained shape of the MCD spectrum represents a typical structure of standard paramagnetic II-VI DMSs having antiferromagnetic *p-d* exchange interaction [99] [130]. Thus, we conclude that the observed MCD spectrum of ferromagnetic $Ga_{0.97}Mn_{0.03}As$/sapphire have a very typical MCD spectrum structure except for its strong and broad positive background originated from the IB-related optical transitions. This observation, as we emphasize this fact here once more, suggests that the IB cannot be neglected in MCD analysis and it contributes significantly to a better understanding of the origin of the ferromagnetism in $Ga_{1-x}Mn_xAs$ [109] [118] [129] [168] [177].

Throughout the course of the performed MCD spectra deconvolution procedure, we have subtracted the IB-related MCD signal (see Fig. 6-2 (a)) as explained above. Then, using Eqs. (2.32), (2.33), and (2.34), we applied the energy derivative of the Gaussian function fitting and deconvolution procedures to MCD spectrum of the selected $Ga_{1-x}Mn_xAs$/sapphire (x = 0.03) (see Fig. 6-2 (b)). As a result of that we obtained the fitted MCD spectrum (line 2) around L-CPs, which is the superposition of two energy derivatives of Gaussian functions (line 3 and 4). We assumed that the derivative of the two Gaussian functions have the same width and magnitudes with opposite polarities because E_1 and $E_1+\Delta_1$ optical transitions are related with each other by a spin-orbit interaction. In addition to the two dispersion curves, we have also observed a weak linear background (line 5), which indicates that the nature of the IB-related MCD background is more complex when considered over a wide photon energy range. However, we believe that the presence of a weak linear MCD background shall not significantly affect our following discussions because, anyhow, in the following analysis we extract the total background signals from the MCD signal.

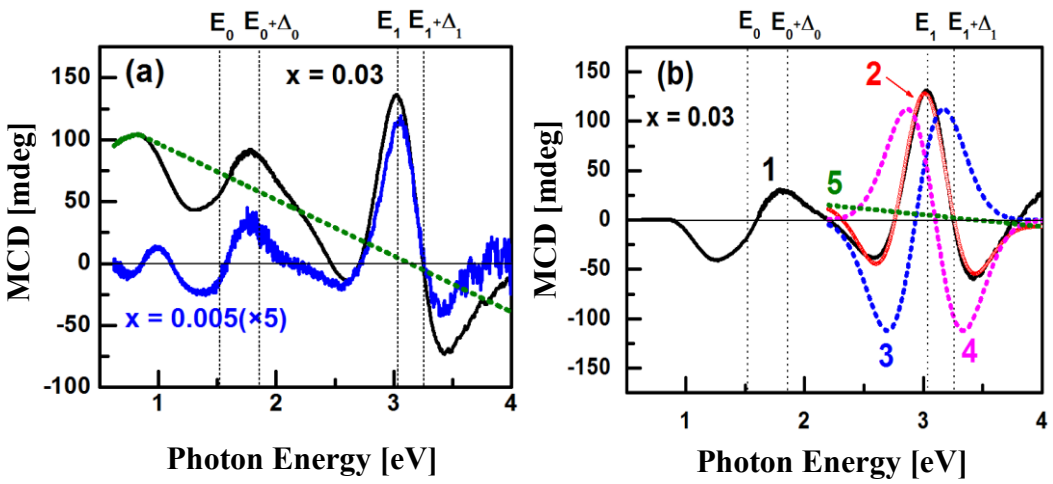

Figure 6-2 (a) Transmission-mode MCD spectrum of $Ga_{1-x}Mn_xAs$ on sapphire with x = 0.03 and x = 0.005. The anticipated MCD linear background is shown by a short dotted line. (b) MCD spectrum of $Ga_{1-x}Mn_xAs$/sapphire with x = 0.03 (line 1) after background subtraction. The fitted curve (line 2) is a sum of a linear background (line 5) and two dispersion curves (line 3 and 4) with same widths and same magnitudes but opposite polarities due to E_1 and $E_1+\Delta_1$ optical transitions. [133].

6.1.3 $Ga_{1-x}Mn_xAs$ on InP

Similar to the procedure outlined in the previous section, we have applied the fitting and deconvolution procedures to analyze the reflection-mode MCD spectra of $Ga_{1-x}Mn_xAs$ (x = 0.03)/InP sample by extracting two dispersion curves for E_1 and $E_1+\Delta_1$ optical transitions as shown in Fig. 6-3. However, this time, there is no IB background subtraction processed because the linear IB-related background cannot be estimated effectively due to the experimental system limitation discussed in Chapter 4. To estimate the expected IB background, one needs to use two points which are around 2.2 eV and below 1.0 eV for linear plotting. However, as is seen in Fig. 6-3 only one such point is available around 2.2 eV when conducting the reflection-mode MCD spectra in this project. Nevertheless, using Eqs. (2.32), (2.33), and (2.34), we have deconvolved the

selected MCD spectrum of $Ga_{1-x}Mn_xAs/InP$ (x = 0.03) into two dispersion curves for E_1 and $E_1+\Delta_1$ optical transitions to roughly estimate the Zeeman splitting energy as shown in Fig 6-3; however these two dispersion curves include small portions of the IB-related background in this case.

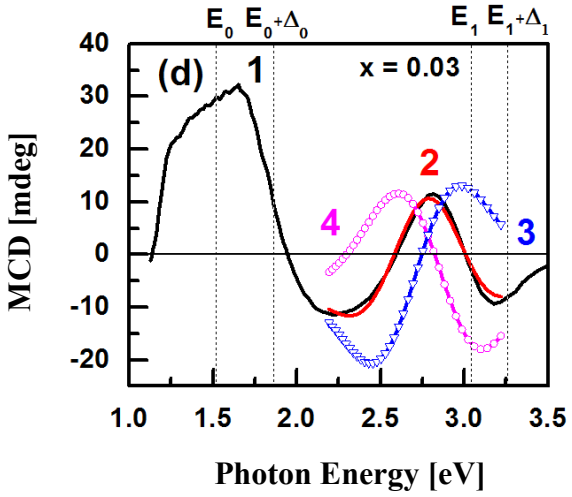

Figure 6-3 MCD spectrum of $Ga_{1-x}Mn_xAs/InP$ sample with x = 0.03 (line 1) prior background subtraction. The fitted curve (line 2) is a sum of two dispersion curves (line 3 and 4) having the same widths and magnitudes but opposite polarities due to E_1 and $E_1+\Delta_1$ optical transitions.

6.1.4 Free-standing $Ga_{1-x}Mn_xAs$

Figure 6-4 (a) shows transmission-mode MCD spectrum of free-standing $Ga_{1-x}Mn_xAs$ initially deposited on InP with x = 0.03 together with a dotted line representing an IB-related background due to multiple optical transitions [176]. Again, we have applied the fitting and deconvolution method described previously and plotted the fitted MCD spectrum (line 2) around L-CPs as shown in Fig. 6-4 (b). The fitted MCD spectrum was deconvolved into two dispersion components (line 3 and 4) using the two energy

derivatives of the Gaussian functions (Eqs. (2.32) and (2.33)). In addition to these components we have also observed another linear background (line 5) which indicates the presence of the IB-related MCD background. As we have mentioned already, complete elimination of the IB-related background is difficult over a wide photon energy range which results in some background residue affecting through a MCD spectra analysis.

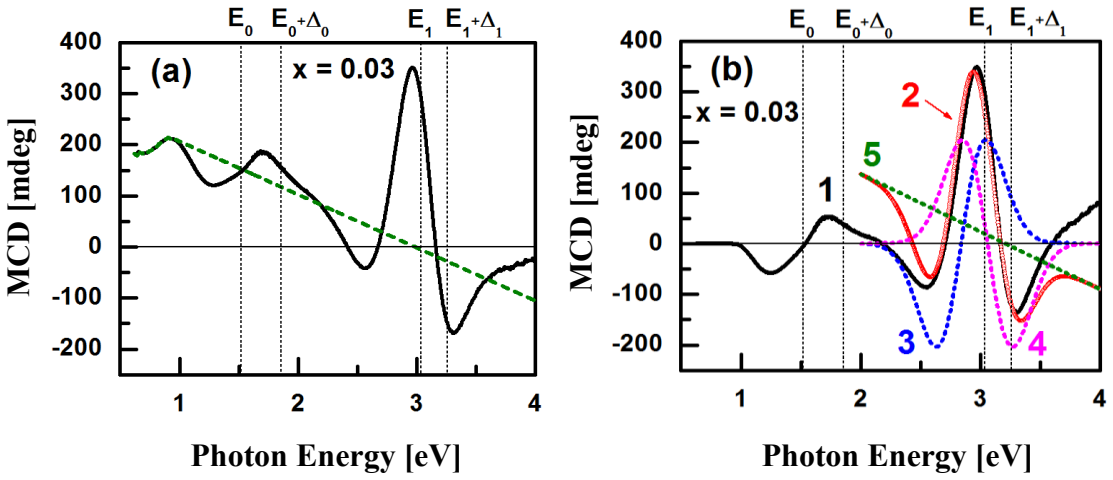

Figure 6-4 (a) Transmission-mode MCD spectrum of free-standing of $Ga_{1-x}Mn_xAs$ film with x = 0.03 removed from InP substrates. A short dotted line presents assumed MCD linear background. (b) MCD spectrum free-standing of the same $Ga_{1-x}Mn_xAs$ film (line 1) after background correction. The fitted curve (line 2) is a sum of a linear background (line 5) and two dispersion curves (line 3 and 4) with same spectral widths and magnitudes but opposite polarities due to E_1 and $E_1+\Delta_1$ optical transitions [176].

6.2 Estimation of Zeeman splitting energies at Γ and L critical points

6.2.1 Proof of concept for estimation method with HT-GaAs

Having decomposed MCD spectra into two dispersion curves for E_1 and $E_1+\Delta_1$ optical transitions for a given sample, one can calculate the Zeeman splitting ΔE of the E_1 optical transitions using the Eqs. (2.28) and (2.29).

To justify this approach we have calculated the effective *g*-values for HT-GaAs sample. The obtained values are (-1.0) and (+2.0) for E_1 and $E_1+\Delta_1$, respectively [133]. The values of effective *g*-values are reasonable [139] [155] and confirmed the validity of our methodology.

In the following, relying on that, we have also calculated the Zeeman splitting energy ΔE of the E_1 for $Ga_{1-x}Mn_xAs$ (x = 0.03) samples. To calculate the Zeeman splitting energy at *L*-CP, we have obtained *dkL*/*dE* (or *dRL*/*dE*) from Figs. 5-8 (h), 5-15 (h), and 5-18 (a) and MCD values from Figs. 6-2, 6-3 and 6-4, respectively. The obtained values have been used along with the Eq. (2.28) to calculate the Zeeman splitting energy at *L*-CP which can eventually be used to calculate the Zeeman splitting energy at Γ-CP as well. It should be emphasized here that obtained Zeeman splitting energy should not be considered as an exact value but rather an estimate due to assumptions we have made during the fitting procedure.

6.2.2 Zeeman splitting energy of $Ga_{0.97}Mn_{0.03}As$ on sapphire

Figure 6-2 (b) shows the MCD spectra of ferromagnetic $Ga_{0.97}Mn_{0.03}As$/sapphire. The fitted MCD signal magnitude and spectral width are 110 mdeg and 0.47 eV, respectively [133]. These values are about 35 times larger and 3.5 times wider than those of HT-GaAs.

Figures 5-6 (a) – 5-8 (h) show that the *dkL/dE* spectra for $Ga_{0.97}Mn_{0.03}As$/sapphire do not strongly depend on the Mn concentration whereas the MCD signal drastically changes with Mn content change. To calculate here the value of *dkL/dE* as defined by Eq.

(2.28) we picked up a half of the *dkL/dE* peak width value centered around 3.0 eV. This step can be justified by considering that the *dkL/dE* (*dRL/dE*) spectra are very broadened and can be considered as a superposition of two broad spectra originating from E_1 and $E_1+\Delta_1$ optical transitions [133]. Thus, the estimated MCD and *dkL/dE* values can be used to calculate the Zeeman splitting energy ΔE of the E_1 in selected samples by transmission-mode MCD. The Zeeman splitting energy ΔE at E_1 obtained here for the $Ga_{0.97}Mn_{0.03}As$/sapphire sample was ~4 meV at *L*-CP. It is known that Zeeman splitting energy ΔE at E_1 of paramagnetic $Cd_{1-x}Mn_xTe$ (x = 0.01 - 0.39) when subjected to magnetic field of 1 Tesla at 4.5 K is between few meV and 20 meV [70] [72], and that of paramagnetic $Zn_{1-x}Mn_xTe$ (x = 0.02 - 0.17) is between 10 meV and 20 meV, respectively [75]. Interestingly enough, the obtained values of ΔE at E_1 of $Ga_{1-x}Mn_xAs$ (x = 0.03), despite its ferromagnetic nature, are smaller than the reported Zeeman splitting energies in paramagnetic $Cd_{1-x}Mn_xTe$ and $Zn_{1-x}Mn_xTe$.

Knowing the estimated Zeeman splitting energy ΔE of $Ga_{0.97}Mn_{0.03}As$/sapphire at *L*-CPs, one can now calculate the Zeeman splitting energy ΔE at Γ-CPs. In fact, the Zeeman splitting of ferromagnetic $Ga_{1-x}Mn_xAs$ at Γ-CPs supported by commonly accepted and convinced theories or models has not been reported in the literature yet because it is very difficult to analyze the MCD spectral shape around Γ-CPs due to the strong broadening of the MCD spectra typically overlapping with IB-related optical transitions [109]. In addition, semiconductor optical absorption is also strongly affected by the IB-related optical transitions.

It should be mentioned here that the electronic states at Γ- and L-CPs of a zinc-blend structure material are related to each other because they are originating from the same s and p orbitals in the material. Let's consider some relationships between the Zeeman splitting at Γ- and L-CPs that can be used to estimate the Zeeman splitting energy at Γ-CPs when the same at L-CPs is known. In $Cd_{1-x}Mn_xTe$ (II-VI DMS), the Zeeman splitting energy at E_0 (Γ-CP) was experimentally observed to be approximately ~16 times larger than that at E_1 (L-CP) [72] [76] [82]. It indicates that Zeeman splitting energy rapidly decreases as one goes away from the Γ-CPs in the Brillouin zone center. This argument is further supported by a theoretical argument which takes into account the contribution of the kinetic exchange effect on the conduction band properties [76] [178]. Therefore, the estimated Zeeman splitting for $Ga_{0.97}Mn_{0.03}As$/sapphire sample at E_0 is a factor of 16 times larger than the already estimated Zeeman splitting at E_1.

To further support the proposed approach we consider fundamental similarities between the electronic structures of $Cd_{1-x}Mn_xTe$ and $Ga_{1-x}Mn_xAs$ compounds. In case of $Cd_{1-x}Mn_xTe$ the E_0, E_1, $E_1+\Delta_1$ energies as well as the $e_d^{+\sigma}$ level energy corresponding to Mn ion occupying an energy level below the top of the valence band are ~1.6 eV, ~3.4 eV, ~ 4.0 eV, and 3.5 eV, respectively [103] [109] [179]. Similarly, for $Ga_{1-x}Mn_xAs$, the energies of E_0, E_1, $E_1+\Delta_1$, and $e_d^{+\sigma}$ level are ~1.5 eV, ~3.0 eV, ~3.2 eV, and ~4.5 eV, respectively [109] [180]. Furthermore, the ratio of absolute value of the MCD area between the Γ-CPs (1.5eV~2.9eV) and the L-CPs (2.9eV~4.1eV) in $Cd_{0.95}Mn_{0.05}Te$ [82] is 0.8 whereas in $Ga_{0.97}Mn_{0.03}As$ the same ratio between the Γ-CPs (0.5eV~2.2eV) and the L-CPs (2.2eV~3.8eV) is 0.4. These estimates are the same order of magnitude

indicating that assessed energies ratio for $Cd_{0.95}Mn_{0.05}Te$ and $Ga_{0.97}Mn_{0.03}As$ after subtracting the IB-related background are, in our opinion, fairly reasonable.

Therefore, the estimated Zeeman splitting of ferromagnetic $Ga_{0.97}Mn_{0.03}As$/sapphire is ~64 meV at E_0 (Γ-CP). The Zeeman splitting of interband optical transitions discussed specifically here is the combination of the Zeeman splitting of the valence and conduction bands. In DMSs with zinc blend structure, Zeeman splitting of the valence band is more dominant than that of the conduction band because *p-d* exchange interactions (*i.e.* exchange interaction between valence band electrons and *d*-electrons) are stronger than *s-d* exchange interaction (*i.e.* exchange interaction between conduction band electrons and *d*-electrons) [71] [99]. The obtained results indicate the Zeeman splitting energies of the valence band of ferromagnetic $Ga_{1-x}Mn_xAs$.

In summary of this section, the estimated Zeeman splitting energy ΔE at E_1 critical point (L-CP) for $Ga_{0.97}Mn_{0.03}As$/sapphire was ~4.0 meV and for the ΔE at E_0 critical point (Γ-CP) was ~64 meV, respectively

6.2.3 Zeeman splitting energy of $Ga_{0.97}Mn_{0.03}As$ on InP

Figure 6-3 shows that the fitted MCD signal amplitude and spectral width of ferromagnetic $Ga_{0.97}Mn_{0.03}As$/InP are 13 mdeg and 0.56 eV, respectively. These values are about 4.4 times larger and 4.1 times wider than those of HT-GaAs. However, it should be noted here again that the magnitude of the fitted MCD from $Ga_{0.97}Mn_{0.03}As$/InP includes a small contribution of IB-related background. Therefore, we expect that the expected real value of the MCD signal magnitude should be smaller.

Figures 5-13 (a) – 5-15 (h) show that *dRL/dE* spectra do not strongly depend on the Mn concentration whereas MCD signal drastically changes with Mn content. To elucidate the value of *dRL/dE* using Eq. (2.30), we picked up half of the *dRL/dE* peak value around 2.78 eV because, as we have done for the $Ga_{0.97}Mn_{0.03}As$/sapphire, the broadened *dRL/dE* spectra can be considered as a superposition of two broad spectra originating from E_1 and $E_1+\Delta_1$ optical transitions.

Thus, again the estimated MCD and *dRL/dE* values in conjunction with Eq. (2.30) can be used to calculate the Zeeman splitting energy ΔE of the E_1 in $Ga_{0.97}Mn_{0.03}As$/InP measured by reflection-mode MCD. In this way, the calculated Zeeman splitting energy ΔE at E_1 in $Ga_{0.97}Mn_{0.03}As$/InP was ~0.6 meV at *L*-CP. Using the same value of calibration factor (*i.e*. 16) estimated for the ratio of Zeeman splitting energy between Γ-CP and *L*-CP in $Cd_{1-x}Mn_xTe$, we have estimated the Zeeman splitting of ferromagnetic $Ga_{0.97}Mn_{0.03}As$/InP at E_0 (Γ-CP) as ~9.6 meV. This value is much smaller than the corresponding one for $Ga_{0.97}Mn_{0.03}As$/sapphire measured by transmission-mode MCD. We believe, that this reduction of Zeeman splitting energy of ferromagnetic $Ga_{0.97}Mn_{0.03}As$/InP is reasonable to accept here; however further analysis is required, because the magnitude of the MCD signal at *L*-CP in conducted experiments from $Ga_{0.97}Mn_{0.03}As$/InP is smaller than one from the $Ga_{0.97}Mn_{0.03}As$/sapphire. Based on the Eq. (2.30) and the rigid band shift mode, one can argue that the Zeeman splitting energy is proportional to the MCD signal. Therefore, the reduction of the MCD signal of $Ga_{0.97}Mn_{0.03}As$/InP measured by the reflection-mode can cause a reduction of the Zeeman splitting energy. In summary of this section, the estimated Zeeman splitting energy ΔE at

E_1 critical point (L-CPs) for $Ga_{0.97}Mn_{0.03}As$/InP was ~0.6 meV and for the ΔE at E_0 critical point (Γ-CPs) was ~9.6 meV, respectively.

6.2.4 Zeeman splitting energy of free-standing $Ga_{0.97}Mn_{0.03}As$

Figure 6-4 (b) shows that the fitted MCD signal amplitude and spectral width of the free-standing ferromagnetic $Ga_{0.97}Mn_{0.03}As$ are 205 mdeg and 0.42 eV, respectively. These values are about 68.3 times larger and 3.1 times wider than those of HT-GaAs.

To elucidate the value of *dkL/dE* using Eq. (2.28) we picked up half of the *dkL/dE* peak value around 2.96 eV as it was done in the preceding case. Thus, once more the estimated MCD and *dkL/dE* values in conjunction with Eq. (2.28) can be used to calculate the Zeeman splitting energy ΔE of the E_1 in the free-standing $Ga_{0.97}Mn_{0.03}As$ measured by transmission-mode MCD. The calculated Zeeman splitting energy ΔE at E_1 (L-CP) in the free-standing $Ga_{0.97}Mn_{0.03}As$ was ~6.5 meV. Once again, using the same value of the calibration factor (*i.e.* 16) for the ratio of Zeeman splitting energy between Γ-CP and L-CP in $Cd_{1-x}Mn_xTe$, we have estimated the Zeeman splitting of free-standing film $Ga_{0.97}Mn_{0.03}As$ at E_0 (Γ-CP) as ~104 meV. This value is larger than the corresponding one from $Ga_{0.97}Mn_{0.03}As$/sapphire measured by transmission-mode MCD.

The observed enhancement of the Zeeman splitting energy in free-standing film is most likely due to the better quality of the $Ga_{0.97}Mn_{0.03}As$ crystal grown on InP substrate as explained in the earlier discussion. Also, the internal strain developed at the interface boundary in heteroepitaxialy grown $Ga_{0.97}Mn_{0.03}As$/sapphire may affect the Zeeman splitting magnitude whereas for free-standing $Ga_{0.97}Mn_{0.03}As$ this argument is absent. In

summary of this section, the estimated Zeeman splitting energy ΔE at E_1 critical point (L-CP) for free-standing $Ga_{0.97}Mn_{0.03}As$ was ~6.5 meV and for the ΔE at E_0 critical point (Γ-CP) was ~104 meV, respectively.

Table 6-1 summarizes the estimated Zeeman splitting energies ΔE at E_1 (Γ-CP) and E_0 (L-CP) for $Ga_{0.97}Mn_{0.03}As$/sapphire, $Ga_{0.97}Mn_{0.03}As$/InP, and free-standing $Ga_{0.97}Mn_{0.03}As$ samples.

Table 6-1 Zeeman splitting energies ΔE at E_1 (Γ-CP) and E_0 (L-CP) for $Ga_{0.97}Mn_{0.03}As$.

Sample	Zeeman splitting energy ΔE at E_0 (Γ-CP) (meV)	Zeeman splitting energy ΔE at E_1(L-CP) (meV)
$Ga_{0.97}Mn_{0.03}As$/sapphire	~64	~4.0
$Ga_{0.97}Mn_{0.03}As$/InP	~9.6	~0.6
Free-standing $Ga_{0.97}Mn_{0.03}As$	~104	~6.5

Interestingly enough, recently Ohya *et al.* have reported a very small (*i.e.* only a several meV) Zeeman splitting of the valence band in a ferromagnetic $Ga_{1-x}Mn_xAs$ with high T_c of 154 K by electrical tunneling spectroscopy [118]. In contrast to that our MCD spectra analysis has shown that the Zeeman splitting at the band gap is much larger even for a sample with a lower T_c of 20 K. The reason for this discrepancy is not clear at this point.

6.3 Localized *sp-d* exchange interaction

Figure 6-5 (a) and (b) show photon energies of MCD and *dkL/dE* peaks obtained experimentally as well as photon energies of E_1 and $E_1+\Delta_1$ dispersion curve peaks obtained by a fitting and deconvolution method [133]. As we have mentioned before, the MCD peaks at *L*-CPs shift to lower energy and then start to saturate when Mn concentration reaches around $x = 0.001$. On the contrary, the *dkL/dE* peak position does not shift as Mn concentration changes. According to Eq. (2.28) which is derived based on an assumption that the spin-dependent band structure is uniform throughout an entire sample, the MCD structures are expected to behave in the same manner as *dkL/dE* structures behave on the energy scale.

It has been reported in the past that Mn atoms in $Ga_{1-x}Mn_xAs$ are actually inhomogeneously distributed throughout the sample on an atomic scale and that causes an atomic-scale fluctuation in the local electronic density of state [132] [181]. Thus, we propose that the different behaviors of MCD and *dkL/dE* spectra found in this study can be explained by this microscopic inhomogeneity of an electronic structure. The MCD technique selectively detects signals from energy bands which are affected by *sp-d* exchange interaction. On the other hands, *dkL/dE* signal captures the characteristics of the entire sample.

Similarly, Fig. 6-6 (a) and (b) shows photon energies of MCD, and *dRL/dE* peak obtained by a measurement and photon energies of E_1 and $E_1+\Delta_1$ extracted by fitting of MCD peaks as a function of the Mn concentration *x*; as shown in Fig. 6-6 (a) and (b), MCD, E_1 and $E_1+\Delta_1$ peaks shift to lower energy (red shift). On the other hand, *dRL/dE*

peaks do not have noticeable shifts of photon energy. The tendency of peaks' shift of MCD, E_1, $E_1+\Delta_1$ and *dRL/dE* in energy scale from $Ga_{1-x}Mn_xAs$/InP is similar to one from $Ga_{1-x}Mn_xAs$/sapphire. However, Fig. 6-6 (c) shows that the *dRL/dE* value suddenly increases at x = 0.0005 and 0.001 and starts to decrease x = 0.005 and 0.01 and then, it again increases at x = 0.03. This inconsistent behavior of the amplitude change of the *dRL/dE* is not fully understood yet. On the contrary, the amplitude of the MCD signal consistently increases with Mn concentrations as expected.

Figure 6-7 (a) - (c) shows an empirical model to explain the relationship between MCD and *dkL/dE* (or *dRL/dE*) of $Ga_{1-x}Mn_xAs$ as a function of Mn concentration [133]. In this model, a rigid sphere of influence appears around Mn atoms, and *d*-electrons of Mn atoms generate exchange interaction with *s,p*-electrons of GaAs host to increase an MCD effect inside the sphere. The *d*-electrons do not influence outside of the sphere, hence, they do not cause enhancement of the MCD signal. Thus, this model suggests that the spin-polarized band structure of $Ga_{1-x}Mn_xAs$ has a strongly localized nature. It should be noted that the inhomogeneity discussed here is not on a macroscopic scale, in addition, the spatial variations of the optical properties should be very small because the sample is pure $Ga_{1-x}Mn_xAs$ and is free from second phase materials which have large optical property differences. This means that our MCD and *dkL/dE* data are free from some optical interference effects observed in macroscopic inhomogeneous materials with large optical property variations.

Based on our model mentioned above, Fig. 6-7 (a) – (c) schematically shows that MCD probes only some parts of the sample affected by Mn atoms whereas *dkL/dE* probes

the entire sample response [133]. In this case, the absorbance kL can be represented as $kL = k_{Mn}L_{Mn} + k_{nonMn}(L-L_{Mn})$, where k_{Mn} is the absorption coefficient, L_{Mn} is the effective length of the Mn affecting area and k_{nonMn} is the absorption coefficient of a non-Mn affecting area on the sample. Hence, one can expect that observed dkL/dE should be larger than the real expected value, $dk_{Mn}L_{Mn}/dE$, for the spin-polarized part of $Ga_{1-x}Mn_xAs$ if the broadening due to the low temperature growth is reasonably assumed to be uniform. This means that when $kL = k_{Mn}L_{Mn} + k_{nonMn}(L-L_{Mn})$ is considered together with Eq. (2.28), the Zeeman splitting energy eventually becomes smaller. Therefore, the estimated Zeeman splitting energy ΔE, for example $\Delta E =$ ~64 mdeg for the E_1 optical transition in $Ga_{0.97}Mn_{0.03}As$/sapphire, should be considered as the minimum limit, which is calculated by using the Eq. (2.28).

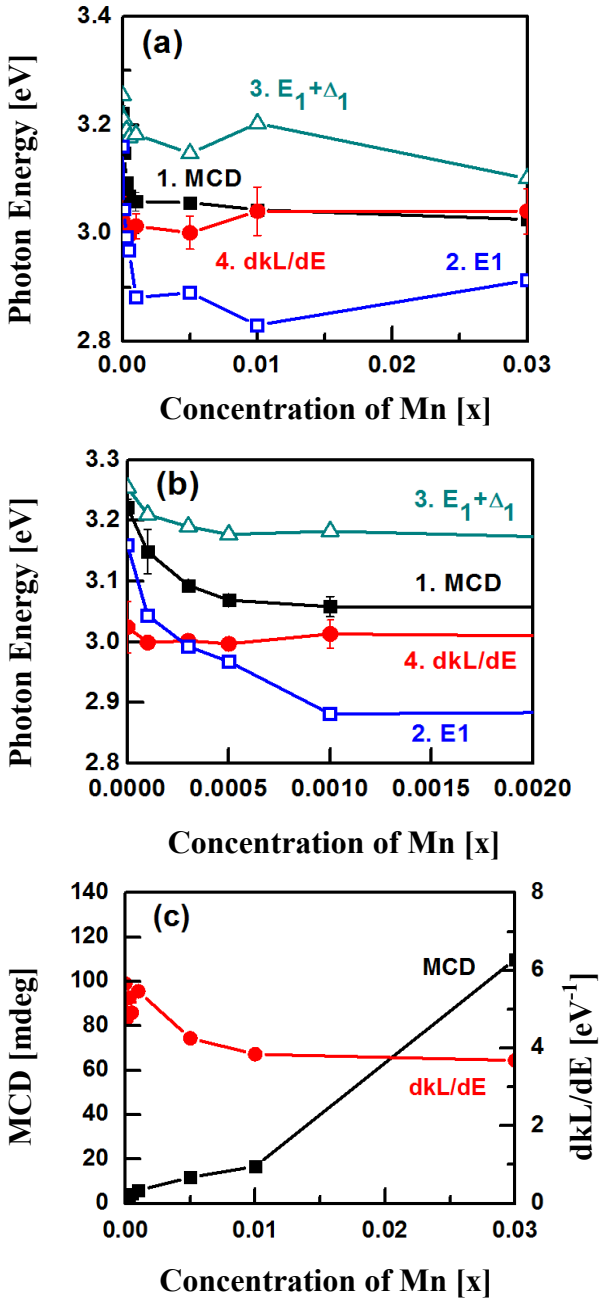

Figure 6-5 (a) Energies of (1) MCD peak, (2) E_1, (3) $E_1+\Delta_1$, and (4) *dkL/dE* peak extracted from Fig. 5-3 – Fig. 5-8 at 6 K as a function of Mn concentration *x*. E_1 and $E_1+\Delta_1$ were obtained by fitting the MCD spectral shape. (b) Magnification of data shown in (a) presented for lower Mn content. (c) Fitted MCD amplitude of the E_1 component and measured *dkL/dE* value around 3 eV as a function of Mn content [133].

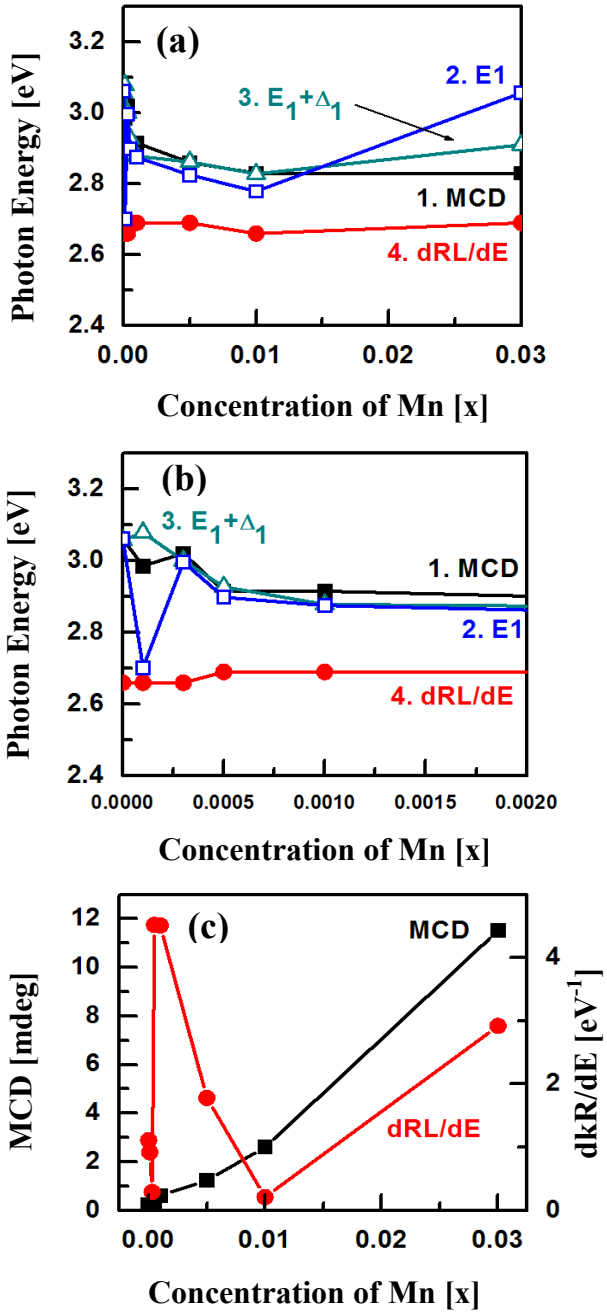

Figure 6-6 (a) Energies of (1) MCD peak, (2) E_1, (3) $E_1+\Delta_1$, and (4) *dRL/dE* peak extracted from Fig. 5-10 – Fig. 5-15 at 6K as a function of Mn concentration *x*. E_1 and $E_1+\Delta_1$ were obtained by fitting the MCD spectral shape. (b) Magnification of data shown in (a) presented for lower Mn content. (c) Fitted MCD amplitude of the E_1 component and measured *dRL/dE* value around 3 eV as a function of Mn content [133].

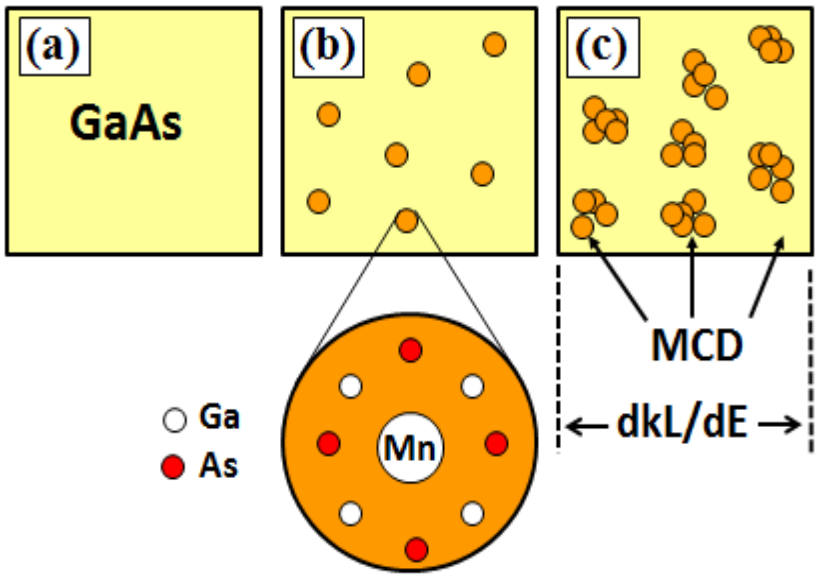

Figure 6-7 Empirical model to describe a relationship between MCD and *dkL/dE* signals for (a) pure GaAs, (b) $Ga_{1-x}Mn_xAs$ with lower Mn concentrations and (c) $Ga_{1-x}Mn_xAs$ with higher Mn concentrations [133].

7. CONCLUSIONS

This work has focused on conducting magneto-optical characterizations of the transition metal (TM)-doped III-V ferromagnetic diluted magnetic semiconductor. Mainly, the investigated samples were $Ga_{1-x}Mn_xAs$/sapphire, $Ga_{1-x}Mn_xAs$/InP, and free-standing $Ga_{1-x}Mn_xAs$ having different Mn content. In the course of this project we have also investigated other selected material systems primarily as references.

This dissertation started with the reviewing selected contemporary silicon technologies and an introduction of the prospective novel technology related to spintronics. Specifically, different applications and devices utilizing the spin properties were considered. Furthermore, the historical perspective on development of the diluted magnetic semiconductor (DMS) was discussed, especially, related to the $Ga_{1-x}Mn_xAs$ as one of the major contender for DMS science and technology. Special attention was given to the characterization technique suitable for DMSs as this aspect is currently under heated debate for gaining insight to the origin of ferromagnetism in DMSs.

Subsequently, different types of theoretical approaches were presented. The first one focused on Mueller and Jones' matrix formalisms needed for developing an experimental facility in this project and the second one was a theoretical framework for analyzing the measured data with special considerations given to *s*, *p*-*d* exchange interaction, selection rule, Zeeman splitting energy; rigid band shift model, and the selected fitting and deconvolution method.

Materials studied in this project were $Ga_{1-x}Mn_xAs$/sapphire, $Ga_{1-x}Mn_xAs$/InP, and free-standing $Ga_{1-x}Mn_xAs$ fabricated using growth facility and technological processes developed at AIST, Japan.

Samples were tested primarily using transmission-mode MCD setups available at AIST, and reflection-mode MCD and combined polar/longitudinal MOKE setups developed in this project at Ohio University.

We have systematically investigated the ferromagnetic properties of $Ga_{1-x}Mn_xAs$/sapphire, $Ga_{1-x}Mn_xAs$/InP and free-standing $Ga_{1-x}Mn_xAs$ doped with different Mn concentrations up to x = 0.03. For ferromagnetic $Ga_{0.97}Mn_{0.03}As$ samples, we successfully deconvolved MCD spectrum into two dispersion curves by an energy derivative of the Gaussian function and have estimated the Zeeman splitting energy at E_1 (L-CP) using the fitted MCD and *dkL/dE* (*dRL/dE*) spectra with the rigid band shift model. This calculation was conducted after taking out the strong background signal originated from the impurity band (IB) related optical transitions.

In our theoretical analysis, we have relied on the known Zeeman splitting energy in $Cd_{1-x}Mn_xTe$ (TM-doped II-VI DMS) at E_0 (Γ-CP) being ~16 times larger than that at E_1 (L-CP). Using this ratio, we have estimated the Zeeman splitting energies in various $Ga_{1-x}Mn_xAs$ films. The Zeeman splitting energies at E_0 (Γ-CP) from $Ga_{0.97}Mn_{0.03}As$/sapphire, $Ga_{0.97}Mn_{0.03}As$/InP, and free-standing $Ga_{0.97}Mn_{0.03}As$ removed from InP were ~64 meV, ~9.6 meV, and ~104 meV, respectively, indicating that the valence band of studied ferromagnetic $Ga_{1-x}Mn_xAs$ semiconductor should demonstrate a sizeable Zeeman splitting.

In addition, the obtained results showed that the MCD structures at *L*-CPs shift to lower energy side as Mn concentration increases. On the other hand, the corresponding *dkL/dE* (*dKR/dE*) spectral structures do not show any significant shift to lower energy side with Mn concentration. However, the MCD and *dkL/dE* (*dkR/dE*) spectra should behave in the same manner as a function of Mn concentrations according to the rigid band shift mode. This unexpected behavior can be explained by an empirical model which is a sphere of influence, indicating that MCD locally detects certain areas affected by *d*-electrons while the *dkL/dE* spectrum results from the overall sample response. This indicates that we have a strongly localized nature of a spin-affected band structure in the ferromagnetic $Ga_{1-x}Mn_xAs$.

8. FUTURE WORK

8.1 Investigation of RE-doped DMSs

Initial attempts to observe ferromagnetism in transition metals (TMs)-doped DMSs [83] recently motivated researchers to investigate also rare earth (RE)-doped DMSs due to their unique electronic property of generating large magnetic moments caused by the successive filling of localized 4*f* shell electrons. The magnetic moments in RE ions are generated by exchange interaction because of a coupling between the localized 4*f* electron spins and conduction electrons [182] [183]. In addition, the coupling generates not only the exchange interaction but as well a huge spin-splitting in the electronic state, and the splitting is proportional to the magnetization of the spins [182]. Furthermore, the highly localized 4*f* electrons generally dominate magnetic property of an RE ions while itinerant *s*-*d* electrons dominate electronic properties in RE-doped materials [184]. However, in general, it is expected that the strength of *f*-orbital magnetic coupling in RE-doped semiconductors is much weaker than that of *d*-orbital magnetic coupling in TM-doped semiconductors because of the deeper localization of the *f*-electrons [185].

Despite a weak magnetic coupling, in general, in RE-doped semiconductors, Gd-doped III-Ns exhibits a colossal magnetic moment [186]. In these materials, the Gd^{3+} ion 4*f* electrons spins induce a positive local 5*d* spin moment caused by intra-ion 4*f*-5*d* exchange interaction followed by inter-ion 5*d*-5*d* coupling mediated by conduction carriers or anion orbital [187]. This complex many-body interaction/exchange mechanism is not well understood presently. In the past, the first significant efforts in studying of Gd-doped III-Ns came from Prof. Ploog's group reporting on the room temperature magnetic

moment of 4000μ_B per Gd atom observed in Gd-doped GaN epitaxial layers [185]. This result was very interesting because the atomic moment of the Gd atom is only 8μ_B. Currently, the observed colossal magnetic moment in Gd-doped GaN is quantitatively explained by a phenomenological model introducing the "*sphere of influence*" approach [186]. In short, when Gd atoms are introduced in a GaN matrix, it is expected that the Gd generates defects in the host matrix because a neutral Gd atom has a larger atomic size than ones in GaN matrix. Subsequently, the defects in the host matrix are polarized by randomly positioned Gd atoms. However, each Gd atom spherically influences the host matrix atoms and matrix atoms are polarized by equal amounts within the sphere. On the contrary, the host matrix atoms located outside of the sphere are not affected by the Gd atoms. Therefore, the overlap of the spheres of influences generates a long-range coupling between the individual spheres as the concentration of Gd increases, then the Gd-doped GaN eventually shows a colossal magnetic moment [185]. However, in this model, the exact nature of the defect(s) type(s) which creates a sphere of influence is still unknown.

Moreover, Gd-doped AlN exhibits very similar magnetic behavior as Gd-doped GaN epilayers [188]. Furthermore, ferromagnetic behavior was observed in high quality crystalline epitaxial structures including Eu-doped GaN [189], Yb-doped GaN [190], GdN, DyN, ErN, and SmN, respectively [191]–[194]. More recently, some highly disordered REN thin films of GdN, DyN, ErN, and SmN have been made using ion assisted deposition techniques [195]–[197]. Despite strong technological relevance for using these materials for spintronics and spin-polarized optoelectronics [198], the

detailed mechanism responsible for the resulting magnetic properties has not been fully explored yet.

RE:III-N/III-N and REN/III-Ns and multilayer quantum structures such as InGaGdN/GaN, and DyN/GaN superlattice were investigated in the past [199] [200]. It is believed that such quantum structures can be beneficial in spin manipulation. They will provide a unique opportunity to understand the impact of the material interface and heteroboundary, strongly affected by the internal stress/strain, on magnetic interactions between RE elements and the semiconductor host. Unfortunately, experimental studies, especially magneto-optical spectroscopy, on the RE:III-N and REN epilayers and quantum structures are very limited; however highly required to support recent theoretical investigations [158]. Therefore, to engineer the desired RE:III-Ns or RENs DMSs, one has to have a good understanding of the role that the RE^{3+} ion plays in inducing defects and the resulting complexes, internal stress/strain as well as how the magnetic moments of incorporated RE ions affect the semiconductor electronic bands structures due to the *s*, *p*, *d* and *f* exchange interactions The last one can be effectively investigated by systematic magneto-optical studies conducted on a wide range of RE ions concentrations and semiconductor parameters (*e.g.* morphology, carriers' type and concentrations, interface-induced strain/stress *etc.*). Only few magneto-optical measurements (*e.g.* X-ray magnetic circular dichroism (XMCD)) were conducted in the past and the obtained results agree with results obtained by other magnetic measurement techniques at cryogenic temperature [201]. The XMCD demonstrated that Gd-doped GaN behaves like a dilute magnetic nitride at 7 K. However, it does not explain why a large

portion of the overall magnetization in this material is only activated by the dopant/defect complexes. Thus, the MCD studies proposed here, conducted in suitable UV-visible-NIR spectral range, may reveal the role of the GaN host matrix for the overall magnetic properties of this and other RE-doped III-Ns. Since the knowledge on magneto-optics of RE:III-Ns and RENs materials is limited [202], it will be very interesting to conduct MCD and MOKE spectroscopy for the investigations of RE:III-Ns and RENs materials in the future.

REFERENCES

[1] W. Shockley, J. Bardeen, and W. H. Brattain, "The electronic theory of the transistor," *Science*, vol. 108, pp. 678–679, 1948.

[2] W. Shockley, "Transistor technology evokes new physics," *Nobel Lect.*, p. 31, 1956.

[3] J. Barden, "Semiconductor Research Leading to the Point Contact Transistor," *Nobel Lect. Phys. 1942-1962*, 1964.

[4] W. H. Brattain, "Surface Properties of Semiconductors.," *Science*, vol. 126, no. 3265, pp. 151–153, 1957.

[5] G. E. Moore, "Creaming more components onto integrated circuits," *Electronics*, vol. 38, no. 8, pp. 114–117, 1965.

[6] R. C. Jaeger, *Introduction to Microelectronic Fabrication: Volume 5 of Modular Series on Solid State Devices (2nd Edition)*. New Jersey: Prentice-Hall, Inc., 2002.

[7] S. D. Sarma, "Spintronics A new class of device based on electron spin, rather than on charge, may yield the next generation of microelectronics," *Ame. Sce.*, vol. 89, pp. 516–523, 2001.

[8] H. Ohno, "Making Nonmagnetic Semiconductors Ferromagnetic," *Science (80-.).*, vol. 281, no. 5379, pp. 951–956, Aug. 1998.

[9] D. L. Peterson, D. U. Bartholomew, U. Debska, A. K. Ramdas, and S. Rodriguez, "Spin-flip Raman scattering in n-type diluted magnetic semiconductors," *Phys. Rev. B*, vol. 32, no. 1, pp. 323–340, 1985.

[10] H. Ohno, H. Munekata, S. von Molnar, and L. L. Chang, "New III-V diluted magnetic semiconductors (invited)," *J. Appl. Phys.*, vol. 69, p. 6103, 1991.

[11] H. Ohno, H. Munekata, T. Penney, S. Vonmolnar, and L. L. Chang, "Magnetotransport Properties of P-Type (In,Mn)As Diluted Magnetic Iii-V Semiconductors," *Phys. Rev. Lett.*, vol. 68, no. 17, pp. 2664–2667, 1992.

[12] T. Dietl, A. Haury, and Y. Merle d'Aubigné, "Free carrier-induced ferromagnetism in structures of diluted magnetic semiconductors," *Phys. Rev. B*, vol. 55, no. 6, pp. R3347–R3350, 1997.

[13] K. Khazen, “Ferromagnetic Resonance Investigation of GaMnAs Nanometric Layers,” university pierre et marie curie, 2008.

[14] H. Ohno, D. Chiba, F. Matsukura, T. Omiya, E. Abe, T. Dietl, Y. Ohno, and K. Ohtani, “Electric-field control of ferromagnetism.,” *Nature*, vol. 408, pp. 944–6, 2000.

[15] S. A. Wolf, D. D. Awschalom, R. A. Buhrman, J. M. Daughton, S. von Molnár, M. L. Roukes, A. Y. Chtchelkanova, and D. M. Treger, “Spintronics: a spin-based electronics vision for the future.,” *Science*, vol. 294, pp. 1488–95, Nov. 2001.

[16] I. Zuic, J. Fabian, and S. D. Sarma, “Spintronics : Fundamentals and applications,” *Rev. Mod. Phys.*, vol. 76, p. 423, 2004.

[17] V. A. Ivanov, T. G. Aminov, V. M. Novotortsev, and V. T. Kalinnikov, “Spintronics and spintronics materials,” *Russ. Chem. Bull.*, vol. 53, no. 11, p. 2357, 2004.

[18] J. Fabian, A. M. Abiague, C. Ertler, P. Stano, and I. Zutic, “Semiconductor Spintronics,” *Acta Phys. Slovaca*, vol. 57, pp. 567–907, 2007.

[19] A. Fert, “Nobel Lecture: Origin, development, and future of spintronics,” *Rev. Mod. Phys.*, vol. 80, pp. 1517–1530, Dec. 2008.

[20] S. D. Bader and S. S. P. Parkin, “Spintronics,” *Annu. Rev. Condens. Matter Phys.*, vol. 1, no. 1, pp. 71–88, Aug. 2010.

[21] G.-X. Miao, M. Münzenberg, and J. S. Moodera, “Tunneling path toward spintronics,” *Rep. Prog. Phys.*, vol. 74, p. 036501, Mar. 2011.

[22] A. Hirohata and K. Takanashi, “Future perspectives for spintronic devices,” *J. Phys. D. Appl. Phys.*, vol. 47, no. 19, p. 193001, 2014.

[23] P. Grünberg, R. Schreiber, Y. Pang, M. B. Brodsky, and H. Sowers, “Layered Magnetic Structures: Evidence for Antiferromegnetic Coupling of Fe Layers across Cr Interlayers,” *Phys. Rev. Lett.*, vol. 57, no. 19, p. 2442, 1986.

[24] G. Binasch, P. Grünberg, F. Saurenbach, and W. Zinn, “Enhanced magnetoresistance in layered magnetic structures with antiferromagnetic interlayer exchange,” *Phys. Rev. B*, vol. 39, no. 7, pp. 4828–4830, 1989.

[25] M. N. Baibich and J. M. Broto, “Giant Magnetosresistance of (001)Fe/(001)Cr Magnetic Superlattices,” *Phys. Rev. Lett.*, vol. 61, no. 001, pp. 2472–2475, 1988.

[26] S. S. P. Parkin, W. Road, and S. Jose, "Giant magnetoresistance in antiferromagnetic Co/Cu multilayer," vol. 58(23), pp. 2710–2712, 1991.

[27] B. Dieny, V. S. Speriosu, S. S. P. Parkin, B. a. Gurney, D. R. Wilhoit, and D. Mauri, "Giant magnetoresistive in soft ferromagnetic multilayers," *Phys. Rev. B*, vol. 43, no. 1, pp. 1297–1300, 1991.

[28] S. S. P. Parkin, R. Bhadra, and K. P. Roche, "Oscillatory magnetic exchange coupling through thin copper layers," *Phys. Rev. Lett.*, vol. 66, no. 16, pp. 2152–2155, 1991.

[29] S. S. P. Parkin, "Origin of enhanced magnetoresistance of magnetic multilayers: Spin-dependent scattering from magnetic interface states," *Phys. Rev. Lett.*, vol. 71, no. 10, pp. 1641–1644, 1993.

[30] R. City, S. P. Parkin, S. Jose, R. Cited, and U. S. P. Documents, "Magnetoresistive spin valve sensor with improved pinned ferromagnetic layer and magnetic recording system using the sensor," 5465185, 1995.

[31] C. Tsang, R. E. Fontana, T. Lin, D. E. Heim, V. S. Speriosu, B. A. Gurney, and M. L. Mason, "Design, Fabrication and Testing of Spin-Valve Read Heads for High-Density Recording," *Ieee Trans. Magn.*, vol. 30, no. 6, pp. 3801–3806, 1994.

[32] M. Julliere, "Tunneling between ferromagnetic films," *Phys. Lett. A*, vol. 54, no. 3, pp. 225–226, 1975.

[33] T. Miyazaki, T. Yaoi, and S. Ishio, "Large magnetoresistance effect in 82Ni-Fe/Al-Al2O3/Co magnetic tunneling junction," *J. Magn. Magn. Mater.*, vol. 98, no. 1–2, pp. L7–L9, 1991.

[34] T. Miyazaki and N. Tezuka, "Giant magnetic tunneling effect in $Fe/Al_2O_3/Fe$ junction," *J. Magn. Magn. Mater.*, vol. 139, no. 3, pp. L231–L234, 1995.

[35] Y. Huai, F. Albert, P. Nguyen, M. Pakala, and T. Valet, "Observation of spin-transfer switching in deep submicron-sized and low-resistance magnetic tunnel junctions," *Appl. Phys. Lett.*, vol. 84, no. 16, pp. 3118–3120, 2004.

[36] L. Berger, "Low-field magnetoresistance and domain drag in ferromagnets," *Journal of Applied Physics*, vol. 49, no. 3. pp. 2156–2161, 1978.

[37] D. C. Ralph and M. D. Stiles, "Spin transfer torques," *J. Magn. Magn. Mater.*, vol. 320, no. 7, pp. 1190–1216, 2008.

[38] S. S. P. Parkin, C. Kaiser, A. Panchula, P. M. Rice, B. Hughes, M. Samant, and S.-H. Yang, "Giant tunnelling magnetoresistance at room temperature with MgO (100) tunnel barriers.," *Nat. Mater.*, vol. 3, no. 12, pp. 862–867, 2004.

[39] S. Yuasa, T. Nagahama, A. Fukushima, Y. Suzuki, and K. Ando, "Giant room-temperature magnetoresistance in single-crystal Fe/MgO/Fe magnetic tunnel junctions.," *Nat. Mater.*, vol. 3, no. 12, pp. 868–871, 2004.

[40] H. Yoda, "No Potential of MRAM for High Speed & High Density ApplicationTitle," Dresden, 2007.

[41] M. Nakayama, T. Kai, N. Shimomura, M. Amano, E. Kitagawa, T. Nagase, M. Yoshikawa, T. Kishi, S. Ikegawa, and H. Yoda, "Spin transfer switching in TbCoFe/CoFeB/MgO/CoFeB/TbCoFe magnetic tunnel junctions with perpendicular magnetic anisotropy," *J. Appl. Phys.*, vol. 103, no. 7, pp. 105–108, 2008.

[42] L. Thomas, G. Jan, J. Zhu, H. Liu, Y. J. Lee, S. Le, R. Y. Tong, K. Pi, Y. J. Wang, D. Shen, R. He, J. Haq, J. Teng, V. Lam, K. Huang, T. Zhong, T. Torng, and P. K. Wang, "Perpendicular spin transfer torque magnetic random access memories with high spin torque efficiency and thermal stability for embedded applications (invited)," *J. Appl. Phys.*, vol. 115, no. 17, 2014.

[43] S. Ikeda, J. Hayakawa, Y. Ashizawa, Y. M. Lee, K. Miura, H. Hasegawa, M. Tsunoda, F. Matsukura, and H. Ohno, "Tunnel magnetoresistance of 604% at 300 K by suppression of Ta diffusion in CoFeB/MgO/CoFeB pseudo-spin-valves annealed at high temperature," *Appl. Phys. Lett.*, vol. 93, no. 8, 2008.

[44] M. Johnson and R. H. Silsbee, "Interfacial charge-spin coupling: Injection and detection of spin magnetization in metals," *Phys. Rev. Lett.*, vol. 55, no. 17, pp. 1790–1793, 1985.

[45] M. Johnson, "The all-metal spin transistor," *IEEE Spectr.*, vol. 31, no. 5, pp. 47–51, 1994.

[46] S. Datta and B. Das, "Electronic analog of the electro-optic modulator," *Appl. Phys. Lett.*, vol. 56, no. 7, pp. 665–667, 1990.

[47] P. Chuang, S. Ho, L. W. Smith, F. S, M. Pepper, C. Chen, J. Fan, J. P. Grif, I. Farrer, H. E. Beere, G. a C. Jones, D. a Ritchie, and T. Chen, "All-electric all-semiconductor spin field-effect transistors," *Nat. Nanotechnol.*, vol. 10, no. 1, pp. 35–39, 2014.

[48] E. I. Rashba, “Properties of semiconductors with an extremum loop I. Cyclotron and combinational resonance in amagnetic field perpendicular to the plane of the loop,” *Sov. Phys. Solid State*, vol. 2, pp. 1109–1122, 1960.

[49] Y. A. Bychkov and E. I. Rashba, “Oscillatory effects and the magnetic susceptibility of carriers in inversion layers,” *J. Phys. C Solid State Phys.*, vol. 17, no. 33, pp. 6039–6045, 1984.

[50] C. Betthausen, T. Dollinger, H. Saarikoski, V. Kolkovsky, G. Karczewski, T. Wojtowicz, K. Richter, and D. Weiss, “Spin-Transistor Action via Tunable Landau-Zener Transitions,” *Science*, vol. 337, no. 6092. pp. 324–327, 2012.

[51] G. A. Prinz, “Magnetoelectronics,” *Science*, vol. 282, pp. 1660–1663, 1998.

[52] J. J. Krebs, B. T. Jonker, and G. A. Prinz, “Properties of Fe single-crystal films grown on (100)GaAs by molecular-beam epitaxy,” *Journal of Applied Physics*, vol. 61, no. 7. pp. 2596–2599, 1987.

[53] C. Daboo, R. J. Hicken, E. Gu, M. Gester, S. J. Gray, D. E. P. Eley, E. Ahmad, J. A. C. Bland, R. Ploessl, and J. N. Chapman, “Anisotropy and orientational dependence of magnetization reversal processes in epitaxial ferromagnetic thin films,” *Phys. Rev. B*, vol. 51, no. 22, pp. 15964–15973, 1995.

[54] A. Filipe, A. Schuhl, and P. Galtier, “Structure and magnetism of the Fe/GaAs interface,” *Esprit*, vol. 70, no. January, pp. 129–131, 1997.

[55] D. O. Demchenko and A. Y. Liu, “Influence of interface structure on electronic properties and Schottky barriers in Fe/GaAs magnetic junctions,” p. 9, 2006.

[56] Q. O. Hu, E. S. Garlid, P. A. Crowell, and C. J. Palmstrøm, “Spin accumulation near Fe/GaAs (001) interfaces: The role of semiconductor band structure,” *Phys. Rev. B - Condens. Matter Mater. Phys.*, vol. 84, no. 8, pp. 1–5, 2011.

[57] J. Freeland, Y. B. Xu, E. T. M. Kernohan, M. Tselepi, and J. A. C. Bland, “Scaling behaviour and evolution of ferromagnetism in epitaxial Fe/GaAs(100) and Fe/InAs(100),” vol. 341, pp. 343–344, 1999.

[58] F. Bensch, G. Garreau, R. Moosbühler, G. Bayreuther, and E. Beaurepaire, “Onset of ferromagnetism in Fe epitaxially grown on GaAs(001) (4×2) and (2×6),” *J. Appl. Phys.*, vol. 89, no. 11 II, pp. 7133–7135, 2001.

[59] G. Wastlbauer and J. A. C. Bland, “Structural and magnetic properties of ultrathin epitaxial Fe films on GaAs(001) and related semiconductor substrates,” *Adv. Phys.*, vol. 54, no. 2, pp. 137–219, 2005.

[60] H. J. Zhu, M. Ramsteiner, H. Kostial, M. Wassermeier, H. P. Schönherr, and K. H. Ploog, "Room-temperature spin injection from Fe into GaAs.," *Phys. Rev. Lett.*, vol. 87, no. 1, p. 016601, 2001.

[61] A. T. Hanbicki, B. T. Jonker, G. Itskos, G. Kioseoglou, and A. Petrou, "Efficient electrical spin injection from a magnetic metal/tunnel barrier contact into a semiconductor," *Appl. Phys. Lett.*, vol. 80, no. 7, pp. 1240–1242, 2002.

[62] A. T. Hanbicki, O. M. J. Van't Erve, R. Magno, G. Kioseoglou, C. H. Li, B. T. Jonker, G. Itskos, R. Mallory, M. Yasar, and A. Petrou, "Analysis of the transport process providing spin injection through an Fe/AlGaAs Schottky barrier," *Appl. Phys. Lett.*, vol. 82, no. 23, pp. 4092–4094, 2003.

[63] O. Wunnicke, P. Mavropoulos, R. Zeller, and P. H. Dederichs, "Ballistic Spin Injection from Fe into ZnSe and GaAs with a (001), (111), and (110) orientation," vol. 4643–4659, p. 12, 2004.

[64] N. Orlean, K. Sakiyama, W. P. Company, G. W. Neudeck, R. Cited, M. Oestreich, Z. Wang, W. Wang, L. Spinu, W. Zhou, and J. Tang, "Spin transistor magnetic random access memory device," US 6753562 B1, 2004.

[65] T. Dietl, "A ten-year perspective on dilute magnetic semiconductors and oxides.," *Nat. Mater.*, vol. 9, no. 12, pp. 965–74, Dec. 2010.

[66] H. Saito, S. Yuasa, and K. Ando, "Origin of the tunnel anisotropic magnetoresistance in $Ga_{(1-x)}Mn_{(x)}As/ZnSe/Ga_{(1-x)}Mn_{(x)}As$ magnetic tunnel junctions of II-VI/III-V heterostructures.," *Phys. Rev. Lett.*, vol. 95, no. 8, p. 086604, 2005.

[67] K. Onodera, T. Masumoto, and M. Kimura, "980 nm compact optical isolators using $Cd_{1-x-y}Mn_xHg_yTe$ single crystals for high power pumping laser diodes," *Electron. Lett.*, vol. 30, no. 23, pp. 1954–1955, 1994.

[68] P. K. Baltzer, P. J. Wojtowicz, M. Robbins, and E. Lopatin, "Exchange Interactions in Ferromagnetic Chromium Chalcogeide Spinels," *Phys. Rev.*, vol. 151, p. 367, 1966.

[69] T. Kasuya and A. Yanase, "Anomalous Transport Phenomena in Eu-Chalcogenide Alloys," *Rev. Mod. Phys.*, vol. 40, p. 1968, 1968.

[70] J. Ginter, J. A Gaj, and S. Le Dang, "Exchange splittings of reflectivity maxima E1 and E1 + Δ1 in $Cd_{1-x}Mn_xTe$," *Solid State Commun.*, vol. 48, no. 10, pp. 849–852, 1983.

[71] A. K. Bhattacharjee, G. Fishman, and B. Coqblin, "Virtual Bound State Model for The Exchange Interaction in Semimagnetic Semiconductors such as $Cd_{1-x}Mn_xTe$," *Pysica 117B 118B*, pp. 449–451, 1983.

[72] D. Coquillat, J. P. Lascaray, M. C. D. Deruelle, J. A. Gaj, and R. Triboulet, "Magnetoreflectivity of $Cd_{1-x}Mn_xTe$ at L point of the Brillouin zone," *Solid State Commun.*, vol. 59, no. 1, pp. 25–28, Jul. 1986.

[73] S. H. Wei and A. Zunger, "Total-energy and band structure calculations for the semimagnetic $Cd_{1-x}Mn_xTe$ Semiconductor alloy and its binary constituents," *Phy. Rev. B.*, vol. 35, no. 5, p. 2340, 1987.

[74] J. K. Furdyna, "Diluted magnetic semiconductors," *J. Appl. Phys.*, vol. 64, no. 4, p. R29, 1988.

[75] D. Coquilat, J. P. Lascaray, J. A. Gaj, J. Deportes, and J. K. Furdyna, "Zeeman splittings of optical transitions at the L point of the Brillouin zone in semimagnetic semiconductors," *Phy. Rev. B.*, vol. 39, no. 14, pp. 88–93, 1989.

[76] A. K. Bhattacharjee, "Magneto-optics near the L point of the Brillouin zone in semimagnetic semiconductors," *Phy. Rev. B.*, vol. 41, no. 9, pp. 5696–5700, 1990.

[77] K. Ando, K. Takahashi, and T. Okuda, "Magnetic circular dichroism of zinc-blende-phase MnTe," *Phy. Rev. B.*, vol. 46, p. 12289, 1992.

[78] A. K. Bhattacharjee, "Interaction between band electrons and transition-metal ions in diluted magnetic semiconductors," *Phy. Rev. B.*, vol. 46, pp. 5266–5273, 1992.

[79] K. Ando and H. Akinaga, "Optical study of the magnetic phase transition in $Cd_{1-x}Mn_xTe$," *J. Magn. Magn. Mater.*, vol. 140–144, pp. 2029–2030, 1995.

[80] H. Saito, V. Zayets, S. Yamagata, and K. Ando, "Magneto-optical studies of ferromagnetism in the II-VI diluted magnetic semiconductor $Zn_{1-x}Cr_xTe$," *Phy. Rev. B.*, vol. 66, p. 081201, Aug. 2002.

[81] H. Saito, V. Zayets, S. Yamagata, and K. Ando, "Room-Temperature Ferromagnetism in a II-VI Diluted Magnetic Semiconductor $Zn_{1-x}Cr_xTe$," *Phys. Rev. B.*, vol. 90, p. 207202, May 2003.

[82] K. Ando, H. Saito, and V. Zayets, "Anomalous Zeeman splittings of II–VI diluted magnetic semiconductors at L-critical points," *J. Appl. Phys.*, vol. 109, no. 7, p. 07C304, 2011.

[83] H. Munekata, H. Ohono, S. von Molnar, A. Segmüller, L. L. Chang, and L. Ezaki, "Diluted Magnetic III-V Semiconductors," *Phys. rev. lett.*, vol. 63, pp. 1849–1852, 1989.

[84] M. E. Overberg, B. P. Gila, G. T. Thaler, C. R. Abernathy, S. J. Pearton, N. a. Theodoropoulou, K. T. McCarthy, S. B. Arnason, a. F. Hebard, S. N. G. Chu, R. G. Wilson, J. M. Zavada, and Y. D. Park, "Room temperature magnetism in GaMnP produced by both ion implantation and molecular-beam epitaxy," *J. Vac. Sci. Technol. B Microelectron. Nanom. Struct.*, vol. 20, no. 3, p. 969, 2002.

[85] S. Basu and T. Adhikari, "Bulk growth, composition and morphology of gallium manganese antimonide — a new ternary alloy system," *Journal of Alloys and Compounds*, vol. 205, no. 1–2. pp. 81–85, 1994.

[86] S. Basu and T. Adhikari, "Variation of band gap with Mn concentration in $Ga_{1-x}Mn_xSb$ — A new III–V diluted magnetic semiconductor," *Solid State Commun.*, vol. 95, no. 1, pp. 53–55, 1995.

[87] M. L. Reed, N. A. El-Masry, H. H. Stadelmaier, M. K. Ritums, M. J. Reed, C. A. Parker, J. C. Roberts, and S. M. Bedair, "Room temperature ferromagnetic properties of (Ga, Mn)N," *Appl. Phys. Lett.*, vol. 79, no. 21, pp. 3473–3475, 2001.

[88] N. Theodoropoulou, A. F. Hebard, M. E. Overberg, C. R. Abernathy, S. J. Pearton, S. N. G. Chu, and R. G. Wilson, "Unconventional carrier-mediated ferromagnetism above room temperature in ion-implanted (Ga, Mn)P:C.," *Phys. Rev. Lett.*, vol. 89, no. 10, p. 107203, 2002.

[89] K. Ando, "Magneto-optical studies of s,p-d exchange interactions in GaN:Mn with room-temperature ferromagnetism," *Appl. Phys. Lett.*, vol. 82, no. 1, pp. 100–102, 2003.

[90] N. Kim, S. J. Lee, and T. W. Kang, "Magnetic properties of p-doped GaMnN diluted magnetic semiconductors containing clusters," *Solid State Commun.*, vol. 133, no. 10, pp. 629–633, 2005.

[91] K. Ganesan and H. L. Bhat, "Magnetic and magnetotransport properties of diluted magnetic semiconductor (Ga,Mn)Sb crystals," *J. Supercond. Nov. Magn.*, vol. 21, no. 7, pp. 391–397, 2008.

[92] A. Alsaad and I. A. Qattan, "Effects of disorder on the Curie temperature of GaMnN, GaCrN, InCrN, and InMnN diluted magnetic semiconductors," *Phys. B Condens. Matter*, vol. 406, no. 22, pp. 4233–4239, 2011.

[93] B. Hu, B. Y. Man, C. Yang, M. Liu, C. S. Chen, X. G. Gao, S. C. Xu, C. C. Wang, and Z. C. Sun, "The important role of Mn^{3+} in the room-temperature ferromagnetism of Mn-doped GaN films," *Appl. Surf. Sci.*, vol. 258, no. 1, pp. 525–529, 2011.

[94] H. Ohno, A. Shen, F. Matsukura, A. Oiwa, A. Endo, S. Katsumoto, and Y. Iye, "(Ga,Mn)As: A new diluted magnetic semiconductor based on GaAs," *Appl. Phy. Lett.*, vol. 69, p. 363, 1996.

[95] F. Matsukura, H. Ohno, A. Shen, and Y. Sugawara, "Transport properties and origin of ferromagnetism in (Ga,Mn)As," *Phys. Rev. B*, vol. 57, no. 4, pp. R2037–R2040, 1998.

[96] K. Y. Wang, R. P. Campion, K. W. Edmonds, M. Sawicki, T. Dietl, C. T. Foxon, and B. L. Gallagher, "Magnetism in (Ga , Mn) As Thin Films With T C Up To 173K," *AIP Conf. Proc.*, vol. 772, p. 333, 2005.

[97] K. Ohno, S. Ohya, and M. Tanaka, "Properties of heavily Mn-doped GaMnAs with curie temperature of 172.5 K," *J. Supercond. Nov. Magn.*, vol. 20, no. 6, pp. 417–420, 2007.

[98] M. Wang, R. A. Marshall, K. W. Edmonds, a. W. Rushforth, R. P. Campion, and B. L. Gallagher, "Determining Curie temperatures in dilute ferromagnetic semiconductors: High Curie temperature (Ga,Mn)As," *Appl. Phys. Lett.*, vol. 104, no. 13, 2014.

[99] K. Ando, in Magneto-Optics, S. Sugano, N. Kojima, and Eds, *Magneto-Optics of Diluted Magnetic Semiconductors: New Materials and Applications*, vol. 128. Springer-Verlag Berlin Heidelberg New York, 2000.

[100] C. Zener, "Interaction between the d-shells in the transition metals. II. Ferromagnetic compounds of manganese with Perovskite structure," *Phys. Rev.*, vol. 82, no. 3, pp. 403–405, 1951.

[101] T. Dietl, H. Ohno, F. Matsukura, J. Cibert, and D. Ferrand, "Zener Model Description of Ferromagnetism in Zinc-Blende Magnetic Semiconductors," *Science*, vol. 287, pp. 1019–1022, Feb. 2000.

[102] J. Szczytko, W. Mac, A. Stachow, A. Twardowski, P. Becla, and J. Tworzydlo, "The s,p-d exchange interaction in GaAs heavily doped with Mn," *Solid State Commun.*, vol. 99, pp. 927–931, 1996.

[103] J. K. Furdyna, "Diluted magnetic semiconductors," *J. Appl. Phys.*, vol. 64, no. 4, p. R29, 1988.

[104] M. Tanaka, S. Ohya, and P. Nam Hai, "Recent progress in III-V based ferromagnetic semiconductors: Band structure, Fermi level, and tunneling transport," *Appl. Phys. Rev.*, vol. 1, no. 1, 2014.

[105] T. Jungwirth, J. Sinova, J. Mašek, J. Kučera, and A. H. MacDonald, "Theory of ferromagnetic (III,Mn)V semiconductors," *Rev. Mod. Phys.*, vol. 78, no. 3, pp. 809–864, 2006.

[106] T. Dietl, "Ferromagnetic semiconductors," *Semicond. Sci. Technol.*, vol. 17, no. 4, pp. 377–392, 2002.

[107] J. Szczytko, W. Mac, A. Twardowski, F. Matsukura, and H. Ohno, "Antiferromagnetic p-d exchange in ferromagnetic Ga1-x MnxAs epilayers," *Phys. Rev. B.*, vol. 59, pp. 935–939, 1999.

[108] J. Szczytko, W. Bardyszewski, and A. Twardowski, "Optical absorption in random media: Application to $Ga_{1-x}Mn_xAs$ epilayers," *Phys. Rev. B*, vol. 64, no. 7, pp. 1–8, 2001.

[109] K. Ando, H. Saito, K. Agarwal, M. Debnath, and V. Zayets, "Origin of the Anomalous Magnetic Circular Dichroism Spectral Shape in Ferromagnetic $Ga_{1-x}Mn_xAs$: Impurity Bands inside the Band Gap," *Phys. Rev. Lett.*, vol. 100, no. 6, p. 067204, Feb. 2008.

[110] T. Dietl, H. Ohno, and F. Matsukura, "Hole-mediated ferromagnetism in tetrahedrally coordinated semiconductors," *Phy. Rev. B.*, vol. 63, p. 195205, 2001.

[111] T. Jungwirth, K. Y. Wang, J. Mašek, K. W. Edmonds, J. König, J. Sinova, M. Polini, N. A. Goncharuk, a. H. MacDonald, M. Sawicki, A. W. Rushforth, R. P. Campion, L. X. Zhao, C. T. Foxon, and B. L. Gallagher, "Prospects for high temperature ferromagnetism in (Ga,Mn)As semiconductors," *Phys. Rev. B - Condens. Matter Mater. Phys.*, vol. 72, no. 16, pp. 1–13, 2005.

[112] D. Neumaier, M. Turek, U. Wurstbauer, A. Vogl, M. Utz, W. Wegscheider, and D. Weiss, "All-electrical measurement of the density of states in (Ga,Mn)As," *Phys. Rev. Lett.*, vol. 103, no. 8, pp. 1–4, 2009.

[113] Y. Nishitani, D. Chiba, M. Endo, M. Sawicki, F. Matsukura, T. Dietl, and H. Ohno, "Curie temperature versus hole concentration in field-effect structures of $Ga_{1-x}Mn_xAs$," *Phys. Rev. B - Condens. Matter Mater. Phys.*, vol. 81, no. 4, pp. 1–8, 2010.

[114] I. Muneta, H. Terada, S. Ohya, and M. Tanaka, "Anomalous Fermi level behavior in GaMnAs at the onset of ferromagnetism," *Appl. Phys. Lett.*, vol. 103, no. 3, 2013.

[115] M. Kobayashi, I. Muneta, Y. Takeda, Y. Harada, A. Fujimori, J. Krempaský, T. Schmitt, S. Ohya, M. Tanaka, M. Oshima, and V. N. Strocov, "Unveiling the impurity band induced ferromagnetism in the magnetic semiconductor (Ga,Mn)As," *Phys. Rev. B - Condens. Matter Mater. Phys.*, vol. 89, no. 20, pp. 1–8, 2014.

[116] H. Akai, "Ferromagnetism and its stability in the diluted magnetic semiconductor (In, Mn) As," *Phys. Rev. Lett.*, vol. 81, no. 14, pp. 3002–3005, 1998.

[117] M. Khalid, E. Weschke, W. Skorupa, M. Helm, and S. Zhou, "Ferromagnetism and impurity band in a magnetic semiconductor: InMnP," *Phys. Rev. B - Condens. Matter Mater. Phys.*, vol. 89, no. 12, pp. 1–5, 2014.

[118] S. Ohya, K. Takata, and M. Tanaka, "Nearly non-magnetic valence band of the ferromagnetic semiconductor GaMnAs," *Nat. Phys.*, vol. 7, p. 342, 2011.

[119] P. Kacman, "Spin interactions in diluted magnetic semiconductors and magnetic semiconductor structures," *Semicond. Sci. Technol.*, vol. 16, no. 4, pp. R25–R39, 2001.

[120] P. W. Anderson and H. Hasegawa, "Considerations on double exchange," *Phys. Rev.*, vol. 100, no. 2, pp. 675–681, 1955.

[121] T. W. Preist and D. F. Pettengill, "Screening effects in doped semiconductors," *J. Phys. C Solid State Phys.*, vol. 6, no. 22, pp. 3268–3274, 1973.

[122] K. Alberi, J. Wu, W. Walukiewicz, K. M. Yu, O. D. Dubon, S. P. Watkins, C. X. Wang, X. Liu, Y. J. Cho, and J. Furdyna, "Valence-band anticrossing in mismatched III-V semiconductor alloys," *Phys. Rev. B - Condens. Matter Mater. Phys.*, vol. 75, no. 4, pp. 1–6, 2007.

[123] J. Fujii, B. R. Salles, M. Sperl, S. Ueda, M. Kobata, K. Kobayashi, Y. Yamashita, P. Torelli, M. Utz, C. S. Fadley, A. X. Gray, J. Braun, H. Ebert, I. Di Marco, O. Eriksson, P. Thunström, G. H. Fecher, H. Stryhanyuk, E. Ikenaga, J. Minár, C. H. Back, G. Van Der Laan, and G. Panaccione, "Identifying the electronic character and role of the Mn states in the valence band of (Ga,Mn)As," *Phys. Rev. Lett.*, vol. 111, no. 9, pp. 1–5, 2013.

[124] J. Okabayashi, A. Kimura, O. Rader, T. Miyazaki, A. Fujimori, T. Hayashi, and M. Tanaka, "Angle-resolved photoemission study of $Ga_{1-x}Mn_xAs$," *Phy. Rev. B.*, vol. 64, p. 125304, 2001.

[125] V. F. Sapega, M. Moreno, M. Ramsteiner, L. Däweritz, and K. H. Ploog, "Polarization of valence band holes in the (Ga,Mn)as diluted magnetic semiconductor," *Phys. Rev. Lett.*, vol. 94, no. 13, pp. 8–11, 2005.

[126] V. F. Sapega, M. Ramsteiner, O. Brandt, L. Däweritz, and K. H. Ploog, "Hot-electron photoluminescence study of the (Ga,Mn)As diluted magnetic semiconductor," *Phys. Rev. B - Condens. Matter Mater. Phys.*, vol. 73, no. 23, pp. 1–9, 2006.

[127] S. Ohya, P. N. Hai, Y. Mizuno, and M. Tanaka, "Quantum size effect and tunneling magnetoresistance in ferromagnetic-semiconductor quantum heterostructures," *Phy. Rev. B.*, vol. 75, p. 155328, 2007.

[128] K. S. Burch, J. Stephens, R. K. Kawakami, D. D. Awschalom, and D. N. Basov, "Ellipsometric study of the Electronic Structure of GaMnAs and LT-GaAs," vol. 205208, p. 21, 2004.

[129] K. S. Burch, D. B. Shrekenhamer, E. J. Singley, J. Stephens, B. L. Sheu, R. K. Kawakami, P. Schiffer, N. Samarth, D. D. Awschalom, and D. N. Basov, "Impurity Band Conduction in a High Temperature Ferromagnetic Semiconductor," *Phys. Rev. Lett.*, vol. 97, no. 8, p. 087208, Aug. 2006.

[130] K. Ando, T. Hayashi, M. Tanaka, A. Twardowski, and I. Introduction, "Magneto-optic effect of the ferromagnetic diluted magnetic semiconductor $Ga_{1-x}Mn_xAs$," *J. Appl. Phys.*, vol. 83, no. 11, pp. 6548–6551, 1998.

[131] B. Beschoten, P. A. Crowell, I. Malajovich, and D. D. Awschalom, "Magnetic Circular Dichroism Studies of Carrier-Induced Ferromagnetism in ($Ga_{1-x}Mn_xAs$)," *Phys. Rev. Lett.*, vol. 83, pp. 3073–3076, 1999.

[132] A. Richardella, P. Roushan, S. Mack, B. Zhou, D. A. Huse, D. D. Awschalom, and A. Yazdani, "Visualizing critical correlations near the metal-insulator transition in $Ga_{(1-x)}Mn_{(x)}As$.," *Science*, vol. 327, no. 5966, pp. 665–9, Feb. 2010.

[133] H. Tanaka, W. M. Jadwisienczak, H. Saito, V. Zayets, S. Yuasa, and K. Ando, "Localized sp–d exchange interaction in ferromagnetic $Ga_{1-x}Mn_xAs$ observed by magnetic circular dichroism spectroscopy of L critical points," *J. Phys. D. Appl. Phys.*, vol. 47, no. 35, p. 355001, 2014.

[134] D. W. Abraham, M. M. Frank, and S. Guha, "Absence of magnetism in hafnium oxide films," *Appl. Phys. Lett.*, vol. 87, no. 25, pp. 1–3, 2005.

[135] G. Osborne, J. C. Cheng, and P. J. Stephens, "A Near-Infrared Circular Dichroism and Magnetic Circular Dichroism Instrument," *Rev. Sci. Instrum.*, vol. 44, no. 1, p. 10, 1973.

[136] W. R. Mason, *A Practical Guide to Magnetic Circular Dichroism Spectroscopy*. Hoboken: John Wiley & Sons, Inc., 2007.

[137] J. C. Sutherland, "Measurement of circular dichroism and related spectroscopies with conventional and synchrotron light sources: Theory and instrumentation," *Adv. Biomed. Spectrosc.*, vol. 1, no. 2009, pp. 19–72, 2009.

[138] J. C. Sutherland, "Dichrometer Erros Resulting from Large Signals or Improper Modulator Phasing," *Chirality*, vol. 24, no. 9, pp. 706–717, 2012.

[139] A. Fujimori, H. Fukutani, and G. Kuwabara, "Magnetic Circular Dichroism at E1 Edges in Semiconductors," *J. Phys. Soc. Jpn.*, vol. 45, p. 910, 1978.

[140] T. Hayashi, "III – V based magnetic (GaMnAs)/nonmagnetic (AlAs) semiconductor superlattices," *Appl. Phy. Lett.*, vol. 71, no. September, pp. 1825–1827, 1997.

[141] A. Arora, S. Ghosh, and V. Sugunakar, "A mirror based polar magneto-optical Kerr effect spectroscopy arrangement," *Rev. Sci. Instrum.*, vol. 82, no. 12, 2011.

[142] H. Tanaka, "Development of MOKE Spectrometer for Magneto-optical Studies of Novel Magnetic Materials and Quantum Structures," Ohio University, 2008.

[143] H. G. Tompkins, *Handbook of Ellipsometry*, vol. 30, no. 7. 2005.

[144] M. Zvàra, "Faraday Rotation and Faraday Ellipticity in the Exciton Absorption Region of GaAs ," *Physica Status solidi*, vol. 36. p. 785, 1969.

[145] S. Lee, "Optical and magneto-optical properties of single crystals of RFe_2 (R=Gd, Tb, Ho, and Lu) and $GdCo_2$ intermetallic compounds," Iowa State University, 1998.

[146] J. Bilnowski and P. Kacman, "Kinetic exchange in diluted magnetic semiconductors," *Phy. Rev. B.*, vol. 46, pp. 298–304, 1992.

[147] T. O. Strandberg, C. M. Canali, and a. H. MacDonald, "Magnetic interactions of substitutional Mn pairs in GaAs," *Phys. Rev. B - Condens. Matter Mater. Phys.*, vol. 81, no. 5, 2010.

[148] Y. J. Zhao, P. Mahadevan, and A. Zunger, "Comparison of predicted ferromagnetic tendencies of Mn substituting the Ga site in III-V's and in I-III-VI_2 chalcopyrite semiconductors," *Appl. Phys. Lett.*, vol. 84, no. 19, pp. 3753–3755, 2004.

[149] M. Taniguchi, M. Fujimori, M. Fujisawa, T. Mori, I. Souma, and Y. Oka, "Mn 3d partial density-of-states and p-d hybridization in $Cd_{1-x}Mn_xY$ (Y = S, Se, and Te)," *Solid State Commun.*, vol. 62, no. 6, pp. 431–434, 1987.

[150] M. L. C. James R. Chelikowsky, "Nonlocal pseudopotential calculations for electronic structure of eleven diamond and znc-blende semiconductor," *Phys. Rev. B*, vol. 14, no. 2, pp. 556–582, 1976.

[151] P. Lautenschlager, M. Garriga, S. Logothetidis, and M. Cardona, "Interband critical points of GaAs and their temperature dependence," *Phy. Rev. B.*, vol. 35, pp. 9174–9189, 1987.

[152] S. Iba, S. Koh, K. Ikeda, and H. Kawaguchi, "Circularly polarized lasing over wide wavelength range in spin-controlled (110) vertical-cavity surface-emitting laser," *Solid State Commun.*, vol. 152, no. 16, pp. 1518–1521, 2012.

[153] W. Mac, A. Twardowski, and M. Demianiuk, "s,p-d exchange interaction in Cr-based diluted magnetic semiconductors.," *Phy. Rev. B.*, vol. 54, pp. 5528–5535, Aug. 1996.

[154] M. Arciszewska and M. Nawrocki, "Determination of the band structure parameters of $Cd_{0.95}Mn_{0.05}Se$ from magnetoabsorption measurements," *J. Phys. Chem. Solids*, vol. 47, no. 3, pp. 309–314, 1986.

[155] K. Ando, H. Saito, M. Debnath, V. Zayets, and a. Bhattacharjee, "Zeeman splittings near the L point of the Brillouin zone in zinc-blende semiconductors," *Phys. Rev. B*, vol. 77, no. 12, p. 125123, Mar. 2008.

[156] R. Lang, A. Winter, H. Pascher, H. Krenn, X. Lui, and J. K. Furdyna, "Polar Kerr effect studies of $Ga_{1-x}Mn_xAs$ epitaxial films," *Phy. Rev. B.*, vol. 72, p. 024430, 2005.

[157] R. Chakarvorty, S. Shen, K. J. Yee, T. Wojtowicz, R. Jakiela, A. Barcz, X. Liu, J. K. Furdyna, and M. Dobrowolska, "Common origin of ferromagnetism and band

edge Zeeman splitting in GaMnAs at low Mn concentrations," *Appl. Phy. Lett.*, vol. 91, no. 17, p. 171118, 2007.

[158] K. Ando, "Seeking Room-Temperature Ferromagnetic Semiconductors," *Science*, vol. 312, no. June, pp. 1883–1885, 2006.

[159] M. Tanaka, H. Shimizu, T. Hayashi, H. Shimada, and K. Ando, "Ferromagnetic semiconductor heterostructures based on (GaMn)As," *J. Vac. Sci. Technol. A*, vol. 18, p. 1247, 2000.

[160] S. Ohya, K. Ohno, and M. Tanaka, "Magneto-optical and magnetotransport properties of heavily Mn-doped GaMnA," *Appl. Phy. Lett.*, vol. 90, p. 112503, 2007.

[161] K. C. Agarwal, H. Saito, S. Yuasa, and K. Ando, "Growth and Transport Studies in M/I/p-SC Magnetic Tunnel Diodes Containing Different Tunnel Barrier Materials," *IEEE Trans. Magn.*, vol. 43, no. 6, pp. 2809–2811, 2007.

[162] P. Y. Yu and M. Cardona, *Fundamentals of Semiconductors Physics and Materials Properties*, 4th ed. heidelberg: Springer, 2010.

[163] T. O. Strandberg, C. M. Canali, and a. H. MacDonald, "Magnetic properties of substitutional Mn in (110) GaAs surface and subsurface layers," *Phys. Rev. B - Condens. Matter Mater. Phys.*, vol. 81, no. 2, p. 054401, 2010.

[164] Y. S. Tver'yanovich, D. Kim, and A. Rusnak, "Effect of Light on the Magnetic Properties of Semiconductors," *Gla. Phys. Chem.*, vol. 31, pp. 563–582, 2005.

[165] B. S. Sorensen, J. Sadowski, S. E. Andresen, and P. E. Lindelof, "Dependence of Curie Temperature on the Thickness of Epitaxial (Ga,Mn)As Film," *Phy. Rev. B.*, vol. 66, p. 233313, 2002.

[166] O. Proselkov, D. Sztenkiel, W. Stefanowicz, M. Aleszkiewicz, J. Sadowski, T. Dietl, and M. Sawicki, "Thickness dependent magnetic properties of (Ga,Mn)As ultrathin films," *Appl. Phys. Lett.*, vol. 100, no. 26, 2012.

[167] S. Bac, H. Lee, S. Lee, S. Choi, T. Yoo, S. Lee, X. Liu, and J. Furdyna, "Thickness dependence of uniaxial anisotropy fields in GaMnAs films," *Appl. Phys. Express 8*, vol. 8, p. 033201, 2015.

[168] M. Dobrowolska, K. Tivakornsasithorn, X. Liu, J. K. Furdyna, M. Berciu, K. M. Yu, and W. Walukiewicz, "Controlling the Curie temperature in (Ga,Mn) As impurity band," *Nat. Mater.*, vol. 11, no. February, p. 444, 2012.

[169] B. G. Streetman and S. K. Banerjee, *Solid State Electronic Devices*, 6th ed. New Jersey: Prentice-Hall, Inc., 2006.

[170] M. Lucht, M. Lerche, H. Wille, Y. V Shvyd, and H. D. R, "Precise Measurement of the Lattice Parameters of Sapphire in the Temperature Range 4.5 K - 250 K Using the M ossbauer Wavelength Standard 1 Introduction 2 Method," *J. Appl. Crystallogr.*, vol. 36, pp. 1075–1081, 2003.

[171] W. M. Jadwisienczak, H. Tanaka, M. Kordesch, A. Khan, S. Kaya, and V. Vuppuluri, "Studies of Ni and Co Doped Amorphous AlN for Magneto-Optical Applications," in *Mater. Res. Soc. Symp. Proc*, 2010, p. 1202.

[172] W. M. Jadwisienczak, H. Tanaka, G. Chen, M. Kordesch, and A. Khan, "Morphology and Magnetio-optical Properties of Amorphous AlN Films Doped with Nickel," in *Mater. Res. Soc. Symp. Proc*, 2011, p. 1290.

[173] H. Tanaka, W. M. Jadwisienczak, S. Kaya, G. Chen, C. Wan, and M. E. Kordesch, "Cluster and thickness dependence of ferromagnetism in nickel in situ-doped amorphous AlN thin films," *J. Electron. Mater.*, vol. 42, no. 5, pp. 844–848, 2013.

[174] R. Chakarvorty, S. Shen, K. J. Yee, T. Wojtowicz, R. Jakiela, A. Barcz, X. Liu, J. K. Furdyna, and M. Dobrowolska, "Common origin of ferromagnetism and band edge Zeeman splitting in GaMnAs at low Mn concentrations," *Appl. Phy. Lett.*, vol. 91, no. 17, p. 171118, 2007.

[175] M. Bsatee, "The Development of Experimental Setup for Various Magneto-Optical Studies," Ohio University, 2015.

[176] K. Ando, H. Tanaka, V. Zayets, and H. Saito, "Magnetic band splitting of $Ga_{1-x}Mn_xAs$ estimated by magnetic circular dichroism (MCD) spectroscopy," *Poster ICM Barcelona*, 2015.

[177] S. Ohya, I. Muneta, P. N. Hai, and M. Tanaka, "Valence-Band Structure of the Ferromagnetic Semiconductor GaMnAs Studied by Spin-Dependent Resonant Tunneling Spectroscopy," *Phys. Rev. Lett.*, vol. 104, p. 167204, 2010.

[178] A. K. Bhattacharjee and J. Perez-Conde, "Hybridization-induced exchange interaction between the conduction band electrons and Mn ions in diluted magnetic semiconductors," in *Proc. 25th Int. Conf. Phys. Semicond.*, 2000, p. 242.

[179] M. Zimmnal-Starnawska, M. Podgorny, A. Kisiel, A. Giriat, and Demina, "Reflectivity spectra of $Cd_{1-x}Mn_xTe$, $Zn_{1-x}Mn_xS$ and $Zn_{1-x}Mn_xSe$ in the 0.7-8.1 eV energy range," *J. Phys. C Solid State Phys.*, vol. 17, p. 615, 1984.

[180] J. Okabayashi, A. Kimura, T. Mizokawa, A. Fujimori, T. Hayashi, and M. Tanaka, "Mn 3d partial density of states in $Ga_{1-x}Mn_xAs$ studied by resonant photoemission spectroscopy," *Phys. Rev. B.*, vol. 59, p. R2486, 1999.

[181] G. Mahieu, P. Condette, B. Grandidier, J. P. Nys, G. Allan, D. Stiévenard, P. Ebert, H. Shimizu, and M. Tanaka, "Compensation mechanisms in low-temperature-grown $Ga_{1-x}Mn_xAs$ investigated by scanning tunneling spectroscopy," *Appl. Phy. Lett.*, vol. 82, no. 5, p. 712, 2003.

[182] T. Dietl, "Ecole Franco-Roumaine: Magnétisme des systèmes nanoscopiques et structures hybrides- Brasov," *Eco. Fran. Roun. Mag. Sem.*, pp. 1–5, 2003.

[183] J. L. Erskine and E. A. Stern, "Magneto-Optic Kerr Effects in Gadolinium," *Phys. Rev. B.*, vol. 8, pp. 1239–1255, 1973.

[184] J. Jensen and A. R. Mackintosh, *Rare Earth Magnetism: Structures and Excitations (International Series of Monographs on Physics)*. Oxford University Press, USA, 1991.

[185] S. Dhar, L. Pérez, O. Brandt, A. Trampert, K. Ploog, J. Keller, and B. Beschoten, "Gd-doped GaN: A very dilute ferromagnetic semiconductor with a Curie temperature above 300 K," *Phys. Rev. B.*, vol. 72, no. 24, pp. 1–9, Dec. 2005.

[186] S. Dhar, O. Brandt, M. Ramsteiner, V. Sapega, and K. Ploog, "Colossal Magnetic Moment of Gd in GaN," *Phys. Rev. Lett.*, vol. 94, no. 3, pp. 1–4, Jan. 2005.

[187] T. Story, M. Górska, A. Lusakowski, M. Arciszewska, W. Dobrowolski, E. Grodzicka, Z. Golacki, and R. Galazka, "New Mechanism of f-f Exchange Interactions Controlled by Fermi Level Position.," *Phys. rev. lett.*, vol. 77, no. 16, pp. 3447–3450, Oct. 1996.

[188] S. Y. Han, J. Hite, G. T. Thaler, R. M. Frazier, C. R. Abernathy, S. J. Pearton, H. K. Choi, W. O. Lee, Y. D. Park, J. M. Zavada, and R. Gwilliam, "Effect of Gd implantation on the structural and magnetic properties of GaN and AlN," *Appl. Phy. Lett.*, vol. 88, p. 042102, 2006.

[189] J. Hite, G. T. Thaler, R. Khanna, C. R. Abernathy, S. J. Pearton, J. H. Park, A. J. Steckl, and J. M. Zavada, "Optical and magnetic properties of Eu-doped GaN," *Appl. Phys. Lett.*, vol. 89, no. 13, p. 132119, 2006.

[190] W. M. Jadwisienczak, J. Wang, H. Tanaka, J. Wu, R. Palai, H. Huhtinen, and A. Anders, "Optical and magnetic properties of GaN epilayers implanted with ytterbium," *J. Rar. Ear.*, vol. 28, pp. 931–935, Dec. 2010.

[191] W. R. McKenzie, P. R. Munroe, F. Budde, B. J. Ruck, S. Granville, and H. J. Trodahl, "TEM characterisation of GdN thin films," *Curr. Appl. Phys.*, vol. 6, no. 3, pp. 407–410, Jun. 2006.

[192] J. W. Gerlach, J. Mennig, and B. Rauschenbach, "Epitaxial gadolinium nitride thin films," *Appl. Phys. Lett.*, vol. 90, no. 6, p. 061919, 2007.

[193] F. Leuenberger, A. Parge, W. Felsch, K. Fauth, and M. Hessler, "GdN thin films: Bulk and local electronic and magnetic properties," *Phys. Rev. B*, vol. 72, no. 1, pp. 1–8, Jul. 2005.

[194] J. Kennedy, S. Granville, A. Markwitz, B. J. Ruck, and H. J. Trodahl, "Ion beam analysis of rare earth nitride thin films," *Nucl. Instruments Methods Phys. Res. Sect. B Beam Interact. with Mater. Atoms*, vol. 266, no. 8, pp. 1558–1561, Apr. 2008.

[195] A. Bittar, H. J. Trodahl, N. T. Kemp, and A. Markwitz, "Ion-assisted deposition of amorphous GaN: Raman and optical properties," *Appl. Phys. Lett.*, vol. 78, no. 5, p. 619, 2001.

[196] B. Ruck, A. Koo, U. Lanke, F. Budde, S. Granville, H. Trodahl, A. Bittar, J. Metson, V. Kennedy, and A. Markwitz, "Quantitative study of molecular N2 trapped in disordered GaN:O films," *Phys. Rev. B*, vol. 70, no. 23, pp. 1–5, Dec. 2004.

[197] H. J. Trodahl, F. Budde, B. J. Ruck, S. Granville, A. Koo, and A. Bittar, "Raman spectroscopy of nanocrystalline and amorphous GaN," *J. Appl. Phys.*, vol. 97, no. 8, p. 084309, 2005.

[198] T. Dietl and S. D. Sarma, "Spintronics," *Res. Prog. Soli. Stat. Phys.*, vol. 89, pp. 28–30, 2005.

[199] H. Asahi, S. Hasegawa, Y.-K. Zhou, and S. Emura, "Rare-earth doped III-nitride semiconductors for semiconductor spintronics," *J. Lumi.*, pp. 1–5, Dec. 2011.

[200] Y. K. Zhou, M. S. Kim, N. Teraguchi, A. Suzuki, Y. Nanishi, and H. Asahi, "Optical and magnetic properties of the DyN/GaN superlattice," *Phys. Status Solidi*, vol. 240, no. 2, pp. 440–442, Nov. 2003.

[201] A. Ney, T. Kammermeier, E. Manuel, V. Ney, S. Dhar, K. H. Ploog, F. Wilhelm, and A. Rogalev, "Element specific investigations of the structural and magnetic properties of Gd:GaN," *Appl. Phys. Lett.*, vol. 90, no. 25, p. 252515, 2007.

[202] A. L. Sukhachev, A. V. Malakhovskii, I. S. Edelman, V. N. Zabluda, V. L. Temerov, and I. Y. Makievskii, "Magneto-optical spectroscopy of Yb^{3+} ions in huntite structure," *J. Magn. Magn. Mater.*, vol. 322, no. 1, pp. 25–29, Jan. 2010.

[203] A. Arrott, "Criterion for ferromagnetism from observations of magnetic isotherms," *Phys. Rev.*, vol. 108, no. 6, pp. 1394–1396, 1957.

[204] I. Yeung, R. M. Roshko, and G. Williams, "Arrott-plot criterion for ferromagnetism in disordered systems," *Phys. Rev. B*, vol. 34, no. 5, pp. 3456–3457, 1986.

[205] K. Ando, H. Saito, V. Zayets, and M. C. Debnath, "Optical properties and functions of dilute magnetic semiconductors," *J. Phys. Condens. Matter*, vol. 16, no. 48, pp. S5541–S5548, Dec. 2004.

[206] M. Venkatesan, C. B. Fitzgerald, and J. M. D. Coey, "Thin films: unexpected magnetism in a dielectric oxide.," *Nature*, vol. 430, no. 7000, p. 630, 2004.

APPENDIX A. MUELLER MATRIX FORMALISM FOR MCD SETUP

This section contains detailed explanations and derivations of equations related to the Mueller matrix formalism for a transmission-mode MCD. Again, the Mueller matrix formalism is closely related to the development process of the reflection-mode MCD and combined polar/longitudinal MOKE experimental facility described in Chapter 4. It should be mentioned here that throughout this dissertation we have observed the following notation style in equations: *e.g.* the $\boldsymbol{I_{-45}}$ (in **bold**) represents a vector, the $\widehat{M}_{PEM}$ (in upper accent like ^) represents a matrix and all other symbols are scalars (in *Italic* font style).

As discussed in Section 2.1.1, the optical components used in the transmission-mode MCD setup can be represented by the Mueller matrix whereas linearly polarized light can be represented by the Stokes vector. For the schematic illustration of the discussed principles and MCD setup see Fig. 2-1[135]–[138]. The detected MCD signal can be derived by the multiplication of the Mueller matrix and the Stokes vector. In the transmission-mode MCD only the Stokes vector representing (-45) degree polarized light ($\boldsymbol{I_{-45}}$) and the Mueller matrix at (0) degree representing PEM ($\widehat{M}_{PEM}$) are necessary as shown below,

$$\boldsymbol{I_{-45}} = I_0 \begin{pmatrix} 1 \\ 0 \\ -1 \\ 0 \end{pmatrix} \qquad (\mathrm{A}-1)$$

$$\widehat{M}_{PEM} = \begin{pmatrix} 1 & 0 & 0 & 0 \\ 0 & 1 & 0 & 0 \\ 0 & 0 & cos\delta & sin\delta \\ 0 & 0 & -sin\delta & cos\delta \end{pmatrix} \qquad (\mathrm{A}-2)$$

where δ is the phase retardation in PEM.

Thus, the light intensity reaching to the detector ($\boldsymbol{I}_{\mathbf{det}}$) can be achieved by multiplying Eq. (A-1) and (A-2). Such a signal will include right (I_R) and left (I_L) circularly polarized light as described by Eq. (A-3),

$$\boldsymbol{I}_{\boldsymbol{det}} = \widehat{M}_{PEM}\boldsymbol{I}_{\mathbf{-45}} = I_0 \begin{pmatrix} 1 & 0 & 0 & 0 \\ 0 & 1 & 0 & 0 \\ 0 & 0 & cos\delta & sin\delta \\ 0 & 0 & -sin\delta & cos\delta \end{pmatrix} \begin{pmatrix} 1 \\ 0 \\ -1 \\ 0 \end{pmatrix} = I_0 \begin{pmatrix} 1 \\ 0 \\ -cos\delta \\ sin\delta \end{pmatrix} \quad (\mathrm{A}-3)$$

where I_0 is the initial intensity of light before being absorbed by optical components. The phase retardation δ in PEM can make right and left circularly polarized light, respectively. The intensity of right and left circularly polarized light can be extracted from Eq. (A-3) using a unit vector of right ($\boldsymbol{I}_{\mathbf{R\_unit}}$) and left ($\boldsymbol{I}_{\mathbf{L\_unit}}$) circularly polarized light as,

$$\boldsymbol{I}_{\mathbf{R\_unit}} = \begin{pmatrix} 1 \\ 0 \\ 0 \\ 1 \end{pmatrix} \quad (\mathrm{A}-4)$$

$$\boldsymbol{I}_{\mathbf{L\_unit}} = \begin{pmatrix} 1 \\ 0 \\ 0 \\ -1 \end{pmatrix} \quad (\mathrm{A}-5)$$

The light intensity reaching to the detector ($\boldsymbol{I}_{\mathbf{det}}$, Eq. (A-3)) is achieved by multiplying $\boldsymbol{I}_{\boldsymbol{det}}$ by either the unit vector of the right ($\boldsymbol{I}_{\mathbf{R\_unit}}$, Eq. (A-4)) or left ($\boldsymbol{I}_{\mathbf{L\_unit}}$, Eq. (A-5)) circularly polarized light. Then, one can obtain the right (I_R) and left (I_L) circularly polarized light intensity parameters, separately using,

$$I_R = I_0(1 \quad 0 \quad -cos\delta \quad sin\delta) \begin{pmatrix} 1 \\ 0 \\ 0 \\ 1 \end{pmatrix} = I_0(1 + sin\delta) \quad (\mathrm{A}-6)$$

$$I_L = I_0(1 \quad 0 \quad -cos\delta \quad sin\delta)\begin{pmatrix} 1 \\ 0 \\ 0 \\ -1 \end{pmatrix} = I_0(1 - sin\delta) \qquad (A-7)$$

As mentioned in Section 2.1.1, the measured MCD signal is the absorption difference between right circularly polarized light and left circularly polarized light (*AC* signal). Using the Eqs. (A-6) and (A-7), one can find out $I_R + I_L$ (*DC* signal) and $I_R - I_L$ (*AC* signal) using,

$$I_R + I_L = I_0(1 + sin\delta) + I_0(1 - sin\delta) = 2I_0 \qquad (A-8)$$

$$I_R - I_L = I_0(1 + sin\delta) - I_0(1 - sin\delta) = 2I_0 sin\delta \qquad (A-9)$$

At the end of the derivation, one has to take the ratio of $I_R + I_L$ and $I_R - I_L$ for the normalization process. Thus, the factor 2 in the Eqs. (A-8) and (A-9) can be omitted to simplify the derivation as,

$$I_R + I_L = I_0 \qquad (A-10)$$

$$I_R - I_L = I_0 sin\delta \qquad (A-11)$$

Now, one can represent the I_R and I_L in terms of the phase difference δ using the Eqs. (A-10) and (A-11). The Eq. (A-11) can be presented in terms of I_R as shown in Eq. (A-12),

$$I_R - I_L = I_0 sin\delta \;\Rightarrow\; I_R = I_L + I_0 sin\delta \qquad (A-12)$$

Now, the equation (A-12) can be plugged into the Eq. (A-10) to obtainI_L,

$$(I_L + I_0 sin\delta\,) + I_L = I_0$$

$$I_L = \frac{I_0}{2}\,(1 - sin\delta\,) \qquad (A-13)$$

Similarly, the Eq. (A-11) can be rewritten in terms of I_L as shown in Eq. (A-14),

$$I_R - I_L = I_0 sin\delta \;\Rightarrow\; I_L = I_R - I_0 sin\delta \qquad (A-14)$$

Now, the equation (A-14) can be plugged into the Eq. (A-10) to obtain $I_{R,}$

$$I_R + (I_R - I_0 sin\delta) = I_0$$

$$I_R = \frac{I_0}{2}(1 + sin\delta) \qquad (A-15)$$

Equations (A-14) and (A-15) show the intensity of the right (I_R) and left (I_L) circularly polarized light in terms of the phase difference δ.

The final goal for the presented analytical derivation is to show the MCD signal in terms of a decadic absorption coefficient difference $\Delta A_{MCD} = A_R - A_L$. Term A_R is a decadic absorption coefficient for right circularly polarized light, and A_L is a decadic absorption coefficient of left circularly polarized light. However, it is mathematically convenient to consider first the Eulerian absorption coefficient (α), and converts the equation in terms of decadic absorption coefficient (A) at the end of the derivation process. Definition of the decadic absorption and Eulerian absorption are described in Section 2.1.1 in this dissertation. In addition, it should be noted that the whole derivation of equations for MCD can also be applied to circular dichroism (CD) because their corresponding theoretical frameworks measurement principles are identical. The only difference between MCD and CD signals is whether a magnetic field is applied during the measurement or not.

The intensity in form of a decadic absorption and Eulerian absorption can be shown as,

$$I = I_0 10^{-A} \qquad (A-16)$$

$$I = I_0 e^{-\alpha} \qquad (A-17)$$

Using the Eqs. (A-17), the intensity of right (I_R) and left (I_L) circularly polarized light can be represented in the form of Eulerian absorption as,

$$I_R = I_0 e^{-\alpha_R} \quad (A-18)$$

$$I_L = I_0 e^{-\alpha_L} \quad (A-19)$$

where α_R and α_L are Eulerian absorption coefficients for right and left circularly polarized light, respectively. Using the Eqs. (A-18) and (A-19), the mean intensity and intensity differences between I_R and I_L can be expressed as,

$$I = \frac{I_R + I_L}{2} \quad (A-20)$$

$$\Delta I = I_R - I_L \quad (A-21)$$

Similarly, the average absorption coefficient and the absorption coefficient differences between α_R and α_R are expressed by,

$$\bar{\alpha} = \frac{\alpha_R + \alpha_L}{2} \quad (A-22)$$

$$\Delta\alpha_{MCD} = \alpha_R - \alpha_L \quad (A-23)$$

Using the Eqs. (A-22) and (A-23), one can find out the absorption coefficient for the right (α_R) and left (α_L) circularly polarized light in terms of the Eulerian absorption coefficient difference ($\Delta\alpha_{MCD}$) as,

$$\alpha_R = \bar{\alpha} + \frac{\Delta\alpha_{MCD}}{2} \quad (A-24)$$

$$\alpha_L = \bar{\alpha} - \frac{\Delta\alpha_{MCD}}{2} \quad (A-25)$$

Now, the intensity reaching to the detector in terms of Eulerian absorption coefficient can be expressed by Eq. (A-26),

$$I(t) = I_R e^{-\alpha_R} + I_L e^{-\alpha_L} \quad (A-26)$$

Since the phase retardation δ is a function of time varying ($\delta = \delta_0 \sin(wt)$, where δ_0 is the amplitude of the phase retardation and w is an angular frequency), the intensity of light reaching to the detector also can be a function of time $I(t)$. Plugging the Eqs. (A-13) and (A-15) into the Eq. (A-26), the equation (A-27) shows the intensity reaching to the detector including the phase retardation δ,

$$I(t) = I_R e^{-\alpha_R} + I_L e^{-\alpha_L} = \left(\frac{I_0}{2}(1 + sin\delta)\right)e^{-\alpha_R} + \left(\frac{I_0}{2}(1 - sin\delta)\right)e^{-\alpha_L}$$

$$= \frac{I_0}{2}(e^{-\alpha_R} + e^{-\alpha_L} + (e^{-\alpha_R} - e^{-\alpha_L})sin\delta) \quad (A-27)$$

Plug the Eqs. (A-24) and (A-25) into the Eq. (A-27),

$$I(t) = \frac{I_0}{2}\left(e^{-(\bar{\alpha}+\frac{\Delta\alpha_{MCD}}{2})} + e^{-(\bar{\alpha}-\frac{\Delta\alpha_{MCD}}{2})} + \left(e^{-(\bar{\alpha}+\frac{\Delta\alpha_{MCD}}{2})} - e^{-(\bar{\alpha}-\frac{\Delta\alpha_{MCD}}{2})}\right)sin\delta\right)$$

$$= \frac{I_0}{2}\left(e^{-\bar{\alpha}}e^{-\frac{\Delta\alpha_{MCD}}{2}} + e^{-\bar{\alpha}}e^{+\frac{\Delta\alpha_{MCD}}{2}} + \left(e^{-\bar{\alpha}}e^{-\frac{\Delta\alpha_{MCD}}{2}} - e^{-\bar{\alpha}}e^{+\frac{\Delta\alpha_{MCD}}{2}}\right)sin\delta\right)$$

$$= \frac{I_0}{2}e^{-\bar{\alpha}}\left(e^{-\frac{\Delta\alpha_{MCD}}{2}} + e^{+\frac{\Delta\alpha_{MCD}}{2}} + \left(e^{-\frac{\Delta\alpha_{MCD}}{2}} - e^{+\frac{\Delta\alpha_{MCD}}{2}}\right)sin\delta\right) \quad (A-28)$$

Since $\delta = \delta_0 \sin(wt)$, the Eq. (A-28) becomes,

$$I(t) = \frac{I_0}{2}e^{-\bar{\alpha}}\left(e^{-\frac{\Delta\alpha_{MCD}}{2}} + e^{+\frac{\Delta\alpha_{MCD}}{2}} + \left(e^{-\frac{\Delta\alpha_{MCD}}{2}} - e^{+\frac{\Delta\alpha_{MCD}}{2}}\right)\sin(\delta_0 \sin(wt))\right) \quad (A-29)$$

Now, the sine term can be expanded using the odd-order Bessel function of the first kind, which is,

$$\sin(\delta_0 \sin(wt) = 2J_1[\delta_0]\sin[wt] + 2J_3[\delta_0]\sin[3wt] + \cdots \quad (A-30)$$

where $J_1[\delta_0]$ and $J_3[\delta_0]$ are the first- and third-order Bessel functions as shown in Fig. 2-2. Plugging the Eq. (A-30) into the Eq. (A-29),

$$I(t) = \frac{I_0}{2} e^{-\bar{\alpha}} \left(e^{-\frac{\Delta\alpha_{MCD}}{2}} + e^{+\frac{\Delta\alpha_{MCD}}{2}} + \left(e^{-\frac{\Delta\alpha_{MCD}}{2}} - e^{+\frac{\Delta\alpha_{MCD}}{2}} \right) 2J_1[\delta_0] \sin[wt] + \cdots \right) \quad (A-31)$$

It should be noted here that only the lowest term ($2J_1[\delta_0] \sin[wt]$) of the Eq. (A-30) was plugged into the Eq. (A-29). This is because the system only detects the signal modulated by a given frequency, not because the lower term is much larger than the higher term. In the actual experiment, the first harmonic of frequency (I_f) has to be set in PEM to detect the lowest term ($2J_1[\delta_0] \sin[wt]$) in Eq. (A-31).

Now, the equation (A-31) is expressed by,

$$I(t) = \bar{I} + \Delta I_w \sin(wt) + \Delta I_{2w} \sin(2wt) + \cdots \quad (A-32)$$

where

$$\bar{I} = \frac{I_0}{2} e^{-\bar{\alpha}} \left(e^{-\frac{\Delta\alpha_{MCD}}{2}} + e^{+\frac{\Delta\alpha_{MCD}}{2}} \right) \quad (A-33)$$

$$\Delta I_w = \frac{I_0}{2} e^{-\bar{\alpha}} \left(e^{-\frac{\Delta\alpha_{MCD}}{2}} - e^{+\frac{\Delta\alpha_{MCD}}{2}} \right) 2J_1[\delta_0] \quad (A-34)$$

where ΔI_w is the AC signal modulated by PEM, and $\bar{I}$ is the DC signal without any phase modulation. Thus, the Eq. (A-32) shows the light intensity reaching the detector including both *AC* and *DC* signals and it is essentially the same as expressed by Eq. (A-26). Now, one can take the ratio of the *AC* (Eq. (A-34)) and the *DC* (Eq. (A-33)) signal, and show it as,

$$\frac{\Delta I_w}{\bar{I}} = \frac{\frac{I_0}{2} e^{-\bar{\alpha}} \left(e^{-\frac{\Delta\alpha_{MCD}}{2}} - e^{+\frac{\Delta\alpha_{MCD}}{2}} \right) 2J_1[\delta_0]}{\frac{I_0}{2} e^{-\bar{\alpha}} \left(e^{-\frac{\Delta\alpha_{MCD}}{2}} + e^{+\frac{\Delta\alpha_{MCD}}{2}} \right)}$$

$$= \frac{-\left(e^{+\frac{\Delta\alpha_{MCD}}{2}} - e^{-\frac{\Delta\alpha_{MCD}}{2}}\right) 2J_1[\delta_0]}{\left(e^{-\frac{\Delta\alpha_{MCD}}{2}} + e^{+\frac{\Delta\alpha_{MCD}}{2}}\right)} \qquad (A-35)$$

Now, by using the hyperbolic tangent which is expressed as,

$$tanhx = \frac{e^x - e^{-x}}{e^x + e^{-x}}$$

one can simplify the Eq. (A-35) as,

$$\frac{\Delta I_w}{\bar{I}} = -2J_1[\delta_0] tanh\left[\frac{\Delta\alpha_{MCD}}{2}\right] \qquad (A-36)$$

In addition, when $\Delta\alpha_{MCD}$ is sufficiently small, the Eq. (A-36) can be further simplified into,

$$\frac{\Delta I_w}{\bar{I}} \approx -2J_1[\delta_0]\left(\frac{\Delta\alpha_{MCD}}{2}\right) \qquad (A-37)$$

Using the Eqs. (A-16) and (A-17) and Eq. (A-37) one can represente it in terms of decadic absorption. Thus, Eq. (A-38) shows the relationship between the Eulerian absorption and the decadic absorption as,

$$I = I_0 10^{-A} = I_0 e^{-\alpha} \Rightarrow 10^{-A} = e^{-\alpha} \Rightarrow -\alpha = \ln[10^{-A}] \qquad (A-38)$$

Now, using the logarithm power rule,

$$log_b(x^y) = y log_b(x)$$

The equation (A-38) becomes,

$$\alpha = A \ln[10] \qquad (A-39)$$

Plugging the Eq. (A-39) into the Eq. (A-37), one can finally obtain the MCD signal in form of the decadic absorbance unit as,

$$\frac{\Delta I_w}{\bar{I}} \approx -2J_1[\delta_0]\left(\frac{\Delta A_{MCD} \ln[10]}{2}\right) \qquad (A-40)$$

It should be recalled here that ΔI_w / $\bar{I}$ is an actual measured MCD signal. ΔI_w is the *AC* signal which is phase-modulated by PEM. $\bar{I}$ is the *DC* signal without any phase modulation. By taking the ratio of *AC* and *DC* signals, one can normalize the detected signal which is necessary to convert the measured signals [unit less] to the MCD [deg] signal for quantitative analysis.

Using the Eq. (A-40), the decadic absorption coefficient difference (ΔA_{MCD}) can be represented by,

$$\Delta A_{MCD} = -\frac{1}{J_1[\delta_0]\ln[10]}\frac{\Delta I_w}{\bar{I}} \qquad (A-41)$$

ΔI_w / $\bar{I}$ can be measured and $J_1[\delta_0]$ can be determined by Fig. 2-2.

As represented in the Eq. (A-41), the MCD can be expressed by the decadic absorbance unit but it is more convenient to express it with a unit of degrees of ellipticity. Figure A-1 shows ellipticity angle θ made by the electric field vector of right and left circularly polarized light. The angle θ is an arctangent of semi-minor axis (E_L-E_R) and semi-major axis (E_L+E_R). In addition, the angle α shows the rotation of the major axis of the ellipsoid with respecte to the incident beam made by two circularly polarized light.

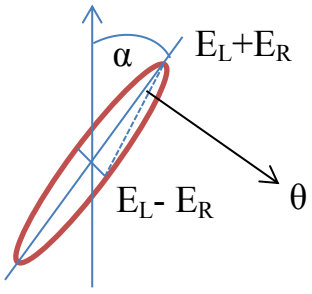

Figure A-1 Ellipticity angle θ made by the electric field vector ***E*** of right and left circularly polarized light.

Using the Eq. (A-27), one can represent the electric field vector of right and left circularly polarized light as,

$$I = {E_R}^2 = \frac{I_0}{2} e^{-\alpha R} \Rightarrow E_R = \sqrt{\frac{I_0}{2} e^{-\alpha R}} \qquad (A-42)$$

$$I = {E_L}^2 = \frac{I_0}{2} e^{-\alpha L} \Rightarrow E_R = \sqrt{\frac{I_0}{2} e^{-\alpha L}} \qquad (A-43)$$

Using the Eqs. (A-42) and (A-43), and illustration of Fig. A-1 one can have,

$$\theta_{rad} = arctan\left[\frac{E_L - E_R}{E_L + E_R}\right] \qquad (A-44)$$

$$= arctan\left[\frac{\sqrt{\frac{I_0}{2} e^{-\alpha L}} - \sqrt{\frac{I_0}{2} e^{-\alpha R}}}{\sqrt{\frac{I_0}{2} e^{-\alpha L}} + \sqrt{\frac{I_0}{2} e^{-\alpha R}}}\right] \qquad (A-45)$$

Plug Eqs. (A-24) and (A-25) into Eq. (A-45),

$$\theta_{rad} = arctan\left[\frac{\sqrt{\frac{I_0}{2} e^{-\left(\bar{\alpha} - \frac{\Delta\alpha_{MCD}}{2}\right)}} - \sqrt{\frac{I_0}{2} e^{-\left(\bar{\alpha} + \frac{\Delta\alpha_{MCD}}{2}\right)}}}{\sqrt{\frac{I_0}{2} e^{-\left(\bar{\alpha} - \frac{\Delta\alpha_{MCD}}{2}\right)}} + \sqrt{\frac{I_0}{2} e^{-\left(\bar{\alpha} + \frac{\Delta\alpha_{MCD}}{2}\right)}}}\right]$$

$$= arctan\left[\frac{\sqrt{\frac{I_0}{2} e^{-\bar{\alpha}} e^{+\frac{\Delta\alpha_{MCD}}{2}}} - \sqrt{\frac{I_0}{2} e^{-\bar{\alpha}} e^{-\frac{\Delta\alpha_{MCD}}{2}}}}{\sqrt{\frac{I_0}{2} e^{-\bar{\alpha}} e^{+\frac{\Delta\alpha_{MCD}}{2}}} + \sqrt{\frac{I_0}{2} e^{-\bar{\alpha}} e^{-\frac{\Delta\alpha_{MCD}}{2}}}}\right]$$

$$= arctan\left[\frac{\sqrt{e^{+\frac{\Delta\alpha_{MCD}}{2}}} - \sqrt{e^{-\frac{\Delta\alpha_{MCD}}{2}}}}{\sqrt{e^{+\frac{\Delta\alpha_{MCD}}{2}}} + \sqrt{e^{-\frac{\Delta\alpha_{MCD}}{2}}}}\right]$$

$$= arctan\left[\frac{\left(e^{+\frac{\Delta\alpha_{MCD}}{2}}\right)^{\frac{1}{2}} - \left(e^{-\frac{\Delta\alpha_{MCD}}{2}}\right)^{\frac{1}{2}}}{\left(e^{+\frac{\Delta\alpha_{MCD}}{2}}\right)^{\frac{1}{2}} + \left(e^{-\frac{\Delta\alpha_{MCD}}{2}}\right)^{\frac{1}{2}}}\right]$$

$$= arctan\left[\frac{\left(e^{+\frac{\Delta\alpha_{MCD}}{2}}\right)^{\frac{1}{4}} - \left(e^{-\frac{\Delta\alpha_{MCD}}{2}}\right)^{\frac{1}{4}}}{\left(e^{+\frac{\Delta\alpha_{MCD}}{2}}\right)^{\frac{1}{4}} + \left(e^{-\frac{\Delta\alpha_{MCD}}{2}}\right)^{\frac{1}{4}}}\right] \qquad (A-46)$$

By using the hyperbolic tangent,

$$tanhx = \frac{e^{x} - e^{-x}}{e^{x} + e^{-x}}$$

The equation (A-46) becomes,

$$\theta_{rad} = arctan\left[tanh\left[\frac{\Delta\alpha_{MCD}}{4}\right]\right] \approx \frac{\Delta\alpha_{MCD}}{4} \qquad (A-47)$$

If the $\Delta\alpha_{MCD}$ is sufficiently small, the Eq. (A-47) can be approximated as $\approx \frac{\Delta\alpha_{MCD}}{4}$. Thus, this equation can be expressed in terms of an Eulerian absorption coefficient (α_{MCD}) with a unit of degree as,

$$\theta_{deg} = \frac{180}{\pi}\frac{\Delta\alpha_{MCD}}{4} \qquad (A-48)$$

As described in the main discussion (Section 2.2.1), the Eq. (A-48) can be used for a derivation of the rigid band shift model.

Furthermore, plug the Eq. (A-39) into the Eq. (A-48), and one can finally present an MCD [deg] signal in terms of a decadic absorption coefficient (A_{MCD}) with a unit of degree expressed as,

$$\theta_{deg} = \frac{180}{\pi}\frac{(\Delta A_{MCD}\ln[10]\,)}{4} = \frac{45}{\pi}\ln[10]\,\Delta A_{MCD} \qquad (A-49)$$

where

$$\Delta A_{MCD} = -\frac{1}{J_1[\delta_0]\ln[10]}\frac{\Delta I_w}{\bar{I}}$$

ΔA_{MCD} is from the Eq. (A-41). The Eqs. (A-49) and (A-41) can be used as a calibration of the detected signal into a MCD [deg] signal.

In summary, the presented derivation procedure was conducted in terms of the Eulerian absorption coefficient (α) because it is, in principle, mathematically more convenient. Then, the final equation for measured light intensity was represented in terms of a decadic absorption coefficient (A) so that one can conveniently convert the measured signal [unit less] into the MCD [deg] signal.

APPENDIX B. JOHNES MATRIX FORMALISM FOR MOKE SETUP

The derivation of a set of MOKE equations when using a 45 degree reflecting mirror presented in this section is based on Ref. [141]. This Jones matrix formalism starts by considering a linearly polarized light at (-45) degrees. Since the unpolarized light becomes linearly polarized after the first polarizer ($\boldsymbol{P}_1$) (see Fig. 2-3), the corresponding Jones matrix for the first polarizer ($\boldsymbol{P}_1$) does not need to be included in this Jones matrix formalism. The Jones vector which expresses the reflected light ($\boldsymbol{E}_r$) intensity reaching to the detector can be derived by a dot product of Jones matrices of the optical component as shown in Fig. 2-3 and Eq. (B-1),

$$\boldsymbol{E}_r = \hat{P}_{\mathbf{2}}(90°) \cdot \widehat{M}(\alpha_2) \cdot \hat{S} \cdot \widehat{M}(\alpha_1) \cdot \widehat{PEM} \cdot \boldsymbol{E}_{\boldsymbol{i}}(-45°) \qquad (\mathrm{B}-1)$$

where $\hat{P}_{\mathbf{2}}$ (90°), $\widehat{M}(\alpha_2)$, $\hat{S}$, $\widehat{M}(\alpha_1)$, $\widehat{PEM}$, and $\boldsymbol{E}_{\boldsymbol{i}}$(-45°) are Jones matrices for the 2nd polarizer (analyzer) at 90 degrees with respected to the 1st polarizer, the mirror for light incident path, the sample, the mirror for light reflected path, the photo elastic modulator (PEM), and the incident linearly polarized light at (-45) degree after the first polarizer ($\boldsymbol{P}_1$), respectively. Now, let us in the following consider each Jones matrix separately. An electric field vector of incident linearly polarized light ($\boldsymbol{E}_{\boldsymbol{i}}$) at (-45) degree after the first polarizer ($\boldsymbol{P}_1$) is illustrated in the Fig. (B-1). In the Jones matrix formalism, *cos*(-45) and *sin*(-45) eventually becomes constant values, $1/\sqrt{2}$ and - $1/\sqrt{2}$, respectively.

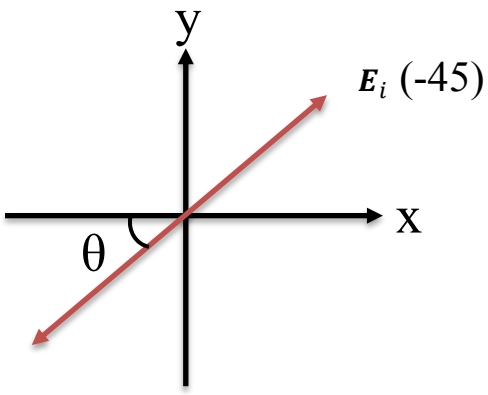

Figure B-1 Illustration of incident linearly polarized light at (-45) degree.

Equation (B-2) shows the electric field vector of the incident linearly polarized light ($\boldsymbol{E_i}$) at (-45) degrees after the first polarizer ($\boldsymbol{P}_1$),

$$\boldsymbol{E_i} = \begin{pmatrix} E_{ox} \\ E_{oy} \end{pmatrix} = |E| \begin{pmatrix} cos\theta \\ sin\theta \end{pmatrix} = |E| \begin{pmatrix} \cos(-45) \\ \cos(-45) \end{pmatrix} = |E| \begin{pmatrix} \frac{1}{\sqrt{2}} \\ -\frac{1}{\sqrt{2}} \end{pmatrix} \qquad (B-2)$$

Next, the Jones matrix of PEM is expressed by,

$$\widehat{PEM} = \begin{pmatrix} e^{i\delta/2} & 0 \\ 0 & e^{-i\delta/2} \end{pmatrix} \qquad (B-3)$$

$$\delta = \delta_0 \cos(2\pi f t) \qquad (B-4)$$

where δ is the sinusoidal retardation, δ_0 is the amplitude of the sinusoidal retardation, f is modulation frequency, t is time. In the Eq. (B-3), the modulation axis is in the x-z plane [141].

The next Jones matrix should be for an optical mirror with incident angle α. When linearly polarized light is incident on the optical mirror, the reflected light becomes weak elliptically polarized due to the nature of an optical mirror as shown in Fig. B-2.

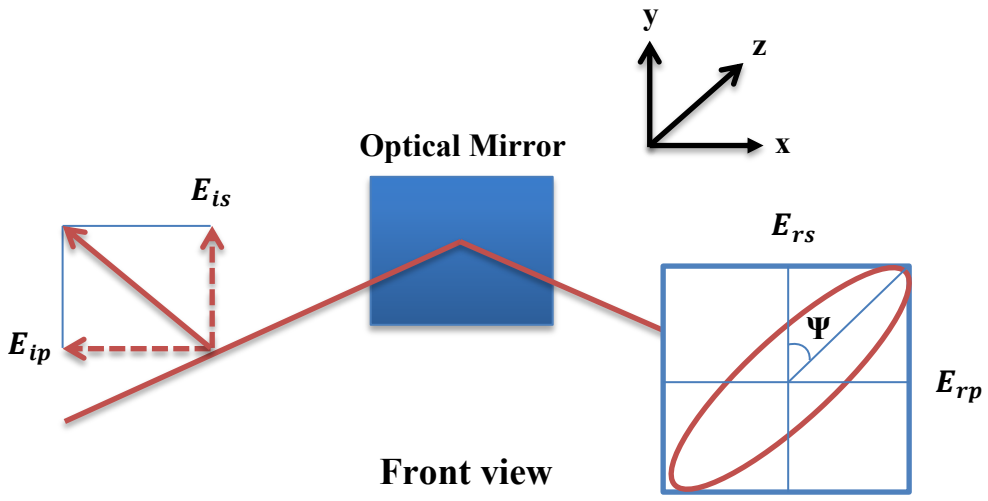

Figure B-2 Formation of a polarization ellipse with ellipsometric angle Ψ and phase difference Δ from linearly polarized light. The plane of incidence is in *x*-*z* plane. Magnetic field $\boldsymbol{B}$ is applied along *x* axis direction.

So, the Fresnel reflection matrix of the optical mirror with an incident angle α is shown in Fig. B-2,

$$\widehat{M}(\alpha) = \begin{pmatrix} r_{pp} & 0 \\ 0 & r_{ss} \end{pmatrix} \qquad (B-5)$$

where r_{pp} and r_{ss} are the Fresnel reflection coefficients which are the ratio of incident *p*-, (*s*-) polarized electric vector and the reflected *p*-, (*s*-) polarized electric vector as shown in Eqs. (B-6) and (B-7),

$$\begin{cases} r_{pp} = \dfrac{\boldsymbol{E_{rp}}}{\boldsymbol{E_{ip}}} \\ r_{ss} = \dfrac{\boldsymbol{E_{rs}}}{\boldsymbol{E_{is}}} \end{cases} \qquad (B-6)$$

where E_{rp} is an electric field vector of reflected *p*-polarized light, E_{ip} is an electric field vector of incident *p*-polarized light, E_{rs} is an electric field vector of reflected *s*-polarized light, and E_{is} is an electric field vector of incident *s*-polarized light as shown in Fig. B-2. The indexes *i* and *r* indicates incident and reflected light, respectively. These four electric field vectors are shown in Eqs. (B-7) – (B-10),

$$\begin{cases} \boldsymbol{E_{rp}} = E_{rpo}e^{i\emptyset xr} \\ \boldsymbol{E_{ip}} = E_{ipo}e^{i\emptyset xi} \end{cases} \quad (\mathrm{B}-7)$$

$$\begin{cases} \boldsymbol{E_{rs}} = E_{rso}e^{i\emptyset yr} \\ \boldsymbol{E_{is}} = E_{iso}e^{i\emptyset yi} \end{cases} \quad (\mathrm{B}-8)$$

where E_{rpo}, E_{ipo}, E_{rso}, and E_{iso} are the amplitude of the four electric field vectors, and $\emptyset_{xr}$, $\emptyset_{xi}$, $\emptyset_{yr}$, and $\emptyset_{yi}$ are phases of the four electric field vectors for the *x* and *y* components.

Plugging the Eqs. (B-7) and (B-8) into the Eq. (B-6), these Fresnel reflection coefficients can be expressed in terms of the phase of the electric field vector as indicated by Eqs. (B-9) and (B-10),

$$r_{pp} = \frac{\boldsymbol{E_{rp}}}{\boldsymbol{E_{ip}}} = \frac{E_{rpo}e^{i\emptyset xr}}{E_{ipo}e^{i\emptyset xi}} \quad (\mathrm{B}-9)$$

$$r_{ss} = \frac{\boldsymbol{E_{rs}}}{\boldsymbol{E_{is}}} = \frac{E_{rso}e^{i\emptyset yr}}{E_{iso}e^{i\emptyset yi}} \quad (\mathrm{B}-10)$$

Now, one can multiply $\frac{r_{ss}}{r_{ss}}$ with Eq. (B-5) to normalize $\widehat{M}(\alpha)$.

$$\widehat{M}(\alpha) = \frac{r_{ss}}{r_{ss}}\begin{pmatrix} r_{pp} & 0 \\ 0 & r_{ss} \end{pmatrix} = r_{ss}\begin{pmatrix} \frac{r_{pp}}{r_{ss}} & 0 \\ 0 & \frac{r_{ss}}{r_{ss}} \end{pmatrix} = r_{ss}\begin{pmatrix} \frac{r_{pp}}{r_{ss}} & 0 \\ 0 & 1 \end{pmatrix} \quad (\mathrm{B}-11)$$

where

$$\frac{r_{pp}}{r_{ss}} = \frac{\left(\frac{\boldsymbol{E_{rp}}}{\boldsymbol{E_{ip}}}\right)}{\left(\frac{\boldsymbol{E_{rs}}}{\boldsymbol{E_{is}}}\right)} = \frac{E_{rpo}e^{i\emptyset xr}}{E_{ipo}e^{i\emptyset xi}}\frac{E_{iso}e^{i\emptyset yi}}{E_{rso}e^{i\emptyset yr}} = \frac{E_{rpo}}{E_{rso}}\frac{e^{i\emptyset xr}}{e^{i\emptyset yr}}\frac{E_{iso}}{E_{ipo}}\frac{e^{i\emptyset yi}}{e^{i\emptyset xi}} \qquad (\mathrm{B}-12)$$

Since $\frac{E_{rpo}}{E_{rso}} = tan\Psi(\alpha)$ based on the Fig. B-2, the Eq. (B-12) becomes,

$$\frac{r_{pp}}{r_{ss}} = \frac{\left(\frac{\boldsymbol{E_{rp}}}{\boldsymbol{E_{ip}}}\right)}{\left(\frac{\boldsymbol{E_{rs}}}{\boldsymbol{E_{is}}}\right)} = tan\Psi(\alpha)\frac{e^{i\emptyset xr}}{e^{i\emptyset yr}}\frac{E_{iso}}{E_{ipo}}\frac{e^{i\emptyset yi}}{e^{i\emptyset xi}} = tan\Psi(\alpha)\, e^{i(\emptyset xr-\emptyset yr)}\frac{E_{iso}}{E_{ipo}}e^{i(\emptyset xi-\emptyset yi)}$$

$$(\mathrm{B}-13)$$

In general, the amplitude of the electric field vectors for *s*- and *p*- polarized light can be assumed to be equal ($E_{\mathrm{iso}} = E_{\mathrm{ipo}}$). Also, since the 2nd term of the Eq. (B-13) is lineally polarized light there is no phase difference, *e.g.* $\emptyset xi - \emptyset yi = 0$. Thus, the 2nd term of the Eq. (B-13) becomes an equal one and it eventually converges to Eq. (B-14),

$$\frac{r_{pp}}{r_{ss}} = tan\Psi(\alpha)\, e^{i(\emptyset xr-\emptyset yr)}\frac{E_{iso}}{E_{ipo}}e^{i(\emptyset xi-\emptyset yi)} = tan\Psi(\alpha)\, e^{i\Delta}1e^{0} \qquad (\mathrm{B}-14)$$

Thus, the Eq. (B-12) finally can be represented as Eq. (B-15),

$$\frac{r_{pp}}{r_{ss}} = tan\Psi(\alpha)\, e^{i\Delta} \qquad (\mathrm{B}-15)$$

where $\Delta = \emptyset xr - \emptyset yr$ represents a phase difference between the *x*- and *y*-component of the electric field vector.

Now, the Eq. (B-15) can be plugged into the Eq. (B-11),

$$\widehat{M}(\alpha) = \frac{r_{ss}}{r_{ss}}\begin{pmatrix} r_{pp} & 0 \\ 0 & r_{ss} \end{pmatrix} = r_{ss}\begin{pmatrix} \frac{r_{pp}}{r_{ss}} & 0 \\ 0 & \frac{r_{ss}}{r_{ss}} \end{pmatrix} = r_{ss}\begin{pmatrix} \frac{r_{pp}}{r_{ss}} & 0 \\ 0 & 1 \end{pmatrix} = r_{ss}\begin{pmatrix} tan\Psi\,(\alpha)e^{i\Delta(\alpha)} & 0 \\ 0 & 1 \end{pmatrix}$$

$$(\mathrm{B}-16)$$

Consequently, the normalized Jones matrix for the mirror is given by,

$$\widehat{M}(\alpha) = \begin{pmatrix} tan\Psi(\alpha)\, e^{i\Delta(\alpha)} & 0 \\ 0 & 1 \end{pmatrix} \quad (B-17)$$

where $tan\Psi(\alpha)$ and $\Delta(\alpha)$ are ellipsometry parameters of the mirror that depends on α [141]. The $tan\Psi(\alpha)$ is the magnitude of the reflectivity ratio of *s*- and *p*-polarized light and $\Delta(\alpha)$ is the phase difference between reflected *s*- and *p*-polarized light.

The Fresnel reflection matrix for the sample can be expressed by,

$$\hat{S}(\alpha) = \begin{pmatrix} r_{pp} & r_{ps} \\ r_{sp} & r_{ss} \end{pmatrix} \quad (B-18)$$

When incident light is close to normal angle, $r_{ss} \approx r_{pp}$. Therefore, Eq. (B-18) can be converted to Eq. (B-19),

$$\hat{S}(\alpha) = \frac{r_{pp}}{r_{pp}}\begin{pmatrix} r_{pp} & r_{ps} \\ r_{sp} & r_{pp} \end{pmatrix} = r_{pp}\begin{pmatrix} \frac{r_{pp}}{r_{pp}} & \frac{r_{ps}}{r_{pp}} \\ \frac{r_{sp}}{r_{pp}} & \frac{r_{pp}}{r_{pp}} \end{pmatrix} = r_{pp}\begin{pmatrix} 1 & -(\emptyset_k - i\eta_k) \\ (\emptyset_k - i\eta_k) & 1 \end{pmatrix} \quad (B-19)$$

After the normalization step of Eq. (B-19) it becomes,

$$\hat{S}(\alpha) = \begin{pmatrix} 1 & -(\emptyset_k + i\eta_k) \\ (\emptyset_k + i\eta_k) & 1 \end{pmatrix} \quad (B-20)$$

where $r_{ps}/r_{pp} = -r_{sp}/r_{pp} = -(\emptyset_k + i\eta_k)$ The $\emptyset_k$ and η_k parameters represent Kerr rotation and ellipticity, respectively, at a normal incident angle.

The last Jones matrix is for the 2nd polarizer (analyzer) with an angle ∅ in the *x*-*z* plane, and it can be represented as,

$$\hat{P}_2(\emptyset) = \begin{pmatrix} cos^2\emptyset & cos\emptyset sin\emptyset \\ sin\emptyset cos\emptyset & sin^2\emptyset \end{pmatrix} \quad (B-21)$$

Now, one can plug Eqs. (B-2), (B-3), (B-17), (B-20) (B-21) into the Eq. (B-1) in order to obtain the Jones vector of the light reaching at the detector. Just for clear visualization, these equations are listed below again as,

$$\boldsymbol{E_r} = \hat{P}_{\mathbf{2}}(90°) \cdot \widehat{M}(\alpha_2) \cdot \hat{S} \cdot \widehat{M}(\alpha_1) \cdot \widehat{PEM} \cdot \boldsymbol{E_i}(-45°) \qquad (\mathrm{B}-1)$$

$$\boldsymbol{E_i} = \begin{pmatrix} E_{ox} \\ E_{oy} \end{pmatrix} = |E| \begin{pmatrix} cos\theta \\ sin\theta \end{pmatrix} = |E| \begin{pmatrix} \cos(-45) \\ \cos(-45) \end{pmatrix} = |E| \begin{pmatrix} \frac{1}{\sqrt{2}} \\ -\frac{1}{\sqrt{2}} \end{pmatrix} \qquad (\mathrm{B}-2)$$

$$\widehat{PEM} = \begin{pmatrix} e^{i\delta/2} & 0 \\ 0 & e^{-i\delta/2} \end{pmatrix} \qquad (\mathrm{B}-3)$$

$$\widehat{M}(\alpha) = \begin{pmatrix} tan\Psi(\alpha)\, e^{i\Delta(\alpha)} & 0 \\ 0 & 1 \end{pmatrix} \qquad (\mathrm{B}-17)$$

$$\hat{S}(\alpha) = \begin{pmatrix} 1 & -(\emptyset_k + i\eta_k) \\ (\emptyset_k + i\eta_k) & 1 \end{pmatrix} \qquad (\mathrm{B}-20)$$

$$\hat{P}_{\mathbf{2}}(\emptyset) = \begin{pmatrix} cos^2\emptyset & cos\emptyset sin\emptyset \\ sin\emptyset cos\emptyset & sin^2\emptyset \end{pmatrix} \qquad (\mathrm{B}-21)$$

In the following we have shown step-by-step detailed derivations of the Eq. (B-1).

<u>(A) Multiplication of the Eqs. (B-21) and (B-17)</u>

$$\hat{P}_{\mathbf{2}}(90°) \cdot \widehat{M}(\alpha 2) = \begin{pmatrix} cos^2\emptyset & cos\emptyset sin\emptyset \\ sin\emptyset cos\emptyset & sin^2\emptyset \end{pmatrix} \begin{pmatrix} tan\Psi(\alpha_2)\, e^{i\Delta(\alpha_2)} & 0 \\ 0 & 1 \end{pmatrix}$$

$$= \begin{pmatrix} cos^2(90°) & \cos(90°)\sin(90°) \\ \sin(90°)\cos(90°) & sin^2(90°) \end{pmatrix} \begin{pmatrix} tan\Psi\,(\alpha_2) e^{i\Delta(\alpha_2)} & 0 \\ 0 & 1 \end{pmatrix}$$

$$= \begin{pmatrix} 0 & 0 \\ 0 & 1 \end{pmatrix} \begin{pmatrix} tan\Psi(\alpha_2)\, e^{i\Delta(\alpha_2)} & 0 \\ 0 & 1 \end{pmatrix} = \begin{pmatrix} 0 & 0 \\ 0 & 1 \end{pmatrix} \qquad (\mathrm{B}-22)$$

Note that the effect of the second mirror is dismissed because there is no α_2 term in the Eq. (B-22).

<u>(B) Multiplication of the Eqs. (B-22) and (B- 20)</u>

$$\hat{P}_{\mathbf{2}}(90°)\cdot\widehat{M}(\alpha_2)\cdot\hat{S}=\begin{pmatrix}0 & 0\\ 0 & 1\end{pmatrix}\begin{pmatrix}1 & -(\emptyset_k+i\eta_k)\\ (\emptyset_k+i\eta_k) & 1\end{pmatrix}$$

$$=\begin{pmatrix}0 & 0\\ (\emptyset_k+i\eta_k) & 1\end{pmatrix} \qquad (\mathrm{B}-23)$$

(C) Multiplication of the Eqs. (B-23) and (B-17)

$$\hat{P}_{\mathbf{2}}(90°)\cdot\widehat{M}(\alpha_2)\cdot\hat{S}\cdot\widehat{M}(\alpha_1)=\begin{pmatrix}0 & 0\\ (\emptyset_k+i\eta_k) & 1\end{pmatrix}\begin{pmatrix}tan\Psi(\alpha_1)e^{i\Delta(\alpha_1)} & 0\\ 0 & 1\end{pmatrix}$$

$$=\begin{pmatrix}0 & 0\\ (\emptyset_k+i\eta_k)tan\Psi(\alpha_1)e^{i\Delta(\alpha_1)} & 1\end{pmatrix} \qquad (\mathrm{B}-24)$$

(D) Multiplication of the Eqs. (B-24) and (B-3)

$$\hat{P}_{\mathbf{2}}(90°)\cdot\widehat{M}(\alpha_2)\cdot\hat{S}\cdot\widehat{M}(\alpha_1)\cdot\widehat{PEM}=\begin{pmatrix}0 & 0\\ (\emptyset_k+i\eta_k)tan\Psi(\alpha_1)\,e^{i\Delta(\alpha_1)} & 1\end{pmatrix}\begin{pmatrix}e^{\frac{i\delta}{2}} & 0\\ 0 & e^{-\frac{i\delta}{2}}\end{pmatrix}$$

$$=\begin{pmatrix}0 & 0\\ e^{\frac{i\delta}{2}}(\emptyset_k+i\eta_k)tan\Psi(\alpha_1)\,e^{i\Delta(\alpha_1)} & e^{-\frac{i\delta}{2}}\end{pmatrix} \qquad (\mathrm{B}-25)$$

(E) Multiplication of the Eqs. (B-25) and (B- 2)

$$\hat{P}_{\mathbf{2}}(90°)\cdot\widehat{M}(\alpha_2)\cdot\hat{S}\cdot\widehat{M}(\alpha_1)\cdot\widehat{PEM}\cdot\boldsymbol{E_i}(-45°)$$

$$=\begin{pmatrix}0 & 0\\ e^{\frac{i\delta}{2}}(\emptyset_k+i\eta_k)tan\Psi\,(\alpha_1)e^{i\Delta(\alpha_1)} & e^{-\frac{i\delta}{2}}\end{pmatrix}|E|\begin{pmatrix}\frac{1}{\sqrt{2}}\\ -\frac{1}{\sqrt{2}}\end{pmatrix}$$

$$=|E|\begin{pmatrix}0\\ \frac{1}{\sqrt{2}}e^{\frac{i\delta}{2}}(\emptyset_k+i\eta_k)tan\Psi(\alpha_1)\,e^{i\Delta(\alpha_1)}-\frac{1}{\sqrt{2}}e^{-\frac{i\delta}{2}}\end{pmatrix}$$

$$=\frac{e^{-\frac{i\delta}{2}}}{\sqrt{2}}|E|\begin{pmatrix}0\\ -1+e^{i\delta}e^{i\Delta(\alpha_1)}(\emptyset_k+i\eta_k)tan\Psi(\alpha_1)\end{pmatrix}$$

$$=|E|\frac{e^{-\frac{i\delta}{2}}}{\sqrt{2}}\begin{pmatrix}0\\ -1+e^{i[\delta+\Delta(\alpha_1)]}(\emptyset_k+i\eta_k)tan\Psi(\alpha_1)\end{pmatrix} \qquad (\mathrm{B}-26)$$

Therefore, the Jones vector of reflected light reaching to the detector can be expressed as,

$$\boldsymbol{E_r} = \hat{P}_{\mathbf{2}}(90°) \cdot \widehat{M}(\alpha_2) \cdot \hat{S} \cdot \widehat{M}(\alpha_1) \cdot \widehat{PEM} \cdot \boldsymbol{E_i}(-45°)$$

$$= |E| \frac{e^{-\frac{i\delta}{2}}}{\sqrt{2}} \begin{pmatrix} 0 \\ -1 + e^{i[\delta + \Delta(\alpha_1)]} tan\Psi(\alpha_1)(\emptyset_k + i\eta_k) \end{pmatrix} \qquad (\mathrm{B}-27)$$

As mentioned above, there is no effect of the second mirror because the Eq. (B-27) does not include α_2. This indicates that one of the mirrors does not affect the measurement in this configuration.

Now, the exponential term in the Eq. (B-27) can be represented by *sine* and *cosine* functions using the following identity,

$$e^{i\Delta} = cos(\Delta) + isin(\Delta) \qquad (\mathrm{B}-28)$$

Thus, the Eq. (B-27) becomes,

$$\boldsymbol{E_r} = |E| \frac{e^{-\frac{i\delta}{2}}}{\sqrt{2}} \begin{pmatrix} 0 \\ -1 + (\cos(\delta + \Delta(\alpha_1)) + isin(\delta + \Delta(\alpha_1)))tan\Psi(\alpha_1)(\emptyset_k + i\eta_k) \end{pmatrix} \qquad (\mathrm{B}-29)$$

Also, the complex conjugate of ***Er*** is given by,

$$\boldsymbol{E_r^*} = |E| \frac{e^{+\frac{i\delta}{2}}}{\sqrt{2}} \begin{pmatrix} 0 \\ -1 + (\cos(\delta + \Delta(\alpha_1)) - isin(\delta + \Delta(\alpha_1)))tan\Psi(\alpha_1)(\emptyset_k - i\eta_k) \end{pmatrix} \qquad (B-30)$$

Now, the measured intensity (*I*) of the light can be represented by the multiplication of $\boldsymbol{E_r^*}$ and $\boldsymbol{E_r}$,

$$I = \boldsymbol{E}_{\boldsymbol{r}}^{*}\boldsymbol{E}_{\boldsymbol{r}} =$$

$$\left(0 \quad \left(-|E|\frac{e^{+\frac{i\delta}{2}}}{\sqrt{2}} + |E|\frac{e^{+\frac{i\delta}{2}}}{\sqrt{2}}(\cos(\delta + \Delta(\alpha_1)) - isin(\delta + \Delta(\alpha_1)))tan\Psi(\alpha_1)(\emptyset_k - i\eta_k)\right)\right)$$

$$\times \begin{pmatrix} 0 \\ \left(-|E|\frac{e^{-\frac{i\delta}{2}}}{\sqrt{2}} + |E|\frac{e^{-\frac{i\delta}{2}}}{\sqrt{2}}(\cos(\delta + \Delta(\alpha_1)) + isin(\delta + \Delta(\alpha_1)))tan\Psi(\alpha_1)(\emptyset_k + i\eta_k)\right) \end{pmatrix}$$

$$= \underbrace{|E|^2\frac{e^0}{2} - |E|^2\frac{e^0}{2}\left(-1 + (\cos(\delta + \Delta(\alpha_1)) - isin(\delta + \Delta(\alpha_1)))tan\Psi(\alpha_1)(\emptyset_k - i\eta_k)\right)}_{\text{(a)}}$$

$$\underbrace{- |E|^2\frac{e^0}{2}\left(\cos(\delta + \Delta(\alpha_1)) - isin(\delta + \Delta(\alpha_1))\right)tan\Psi(\alpha_1)(\emptyset_k - i\eta_k)}_{\text{(b)}}$$

$$\underbrace{+ |E|^2\frac{e^0}{2}\left[\left(\left(\cos(\delta + \Delta(\alpha_1)) - isin(\delta + \Delta(\alpha_1))\right)tan\Psi(\alpha_1)(\emptyset_k - i\eta_k)\right)\right.}_{\text{(c)}}$$

$$\underbrace{\left.\times\left((\cos(\delta + \Delta(\alpha_1)) + isin(\delta + \Delta(\alpha_1)))tan\Psi(\alpha_1)(\emptyset_k + i\eta_k)\right)\right]}_{\text{(d)}}$$

$$(B - 31)$$

Now, the partial calculation of the Eq. (B-31) is shown in the following as,

$$-(a)-(b)=-|E|^2\frac{1}{2}\Big[\Big((\cos(\delta+\Delta(\alpha_1))+isin(\delta+\Delta(\alpha_1)))tan\Psi(\alpha_1)(\emptyset_k+i\eta_k)\Big)$$

$$+\Big(\Big(\cos(\delta+\Delta(\alpha_1))-isin(\delta+\Delta(\alpha_1))\Big)tan\Psi(\alpha_1)(\emptyset_k-i\eta_k)\Big)\Big]$$

$$=-|E|^2\frac{1}{2}\big[co\,s(\delta+\Delta(\alpha_1))\,tan\Psi(\alpha_1)\emptyset_k$$

$$+co\,s(\delta+\Delta(\alpha_1))\,tan\Psi(\alpha_1)i\eta_k+isin(\delta+\Delta(\alpha_1))tan\Psi(\alpha_1)\emptyset_k$$

$$+isin(\delta+\Delta(\alpha_1))tan\Psi(\alpha_1)i\eta_k+co\,s(\delta+\Delta(\alpha_1))\,tan\Psi(\alpha_1)\emptyset_k$$

$$-co\,s(\delta+\Delta(\alpha_1))\,tan\Psi(\alpha_1)i\eta_k-isin(\delta+\Delta(\alpha_1))tan\Psi(\alpha_1)\emptyset_k$$

$$+isin(\delta+\Delta(\alpha_1))tan\Psi(\alpha_1)i\eta_k\big]$$

$$=-|E|^2\frac{1}{2}\left[co\,s(\delta+\Delta(\alpha_1))\,tan\Psi(\alpha_1)\emptyset_k-sin(\delta+\Delta(\alpha_1))tan\Psi(\alpha_1)\eta_k\right.$$

$$\left.+co\,s(\delta+\Delta(\alpha_1))\,tan\Psi(\alpha_1)\emptyset_k-sin(\delta+\Delta(\alpha_1))tan\Psi(\alpha_1)\eta_k\right]$$

$$=-|E|^2\tfrac{1}{2}\left[2co\,s(\delta+\Delta(\alpha_1))\,tan\Psi(\alpha_1)\emptyset_k-2sin(\delta+\Delta(\alpha_1))tan\Psi(\alpha_1)\eta_k\right]$$

$$(B-32)$$

The next step is (c)×(d),

$$(c)\times(d)=\frac{|E|^2}{2}\big[(\cos(\delta+\Delta(\alpha_1))tan\Psi(\alpha_1)\emptyset_k$$

$$-\cos(\delta+\Delta(\alpha_1))tan\Psi(\alpha_1)i\eta_k-isin(\delta+\Delta(\alpha_1))tan\Psi(\alpha_1)\emptyset_k$$

$$+isin(\delta+\Delta(\alpha_1))tan\Psi(\alpha_1)i\eta_k\big)$$

$$\times\big(\cos(\delta+\Delta(\alpha_1))tan\Psi(\alpha_1)\emptyset_k$$

$$+\cos(\delta+\Delta(\alpha_1))tan\Psi(\alpha_1)i\eta_k+isin(\delta+\Delta(\alpha_1))tan\Psi(\alpha_1)\emptyset_k$$

$$+isin(\delta+\Delta(\alpha_1))tan\Psi(\alpha_1)i\eta_k\big)\big]$$

$$= |E|^2 \frac{1}{2} \times$$

$$\left[\left(\cos\left(\delta + \Delta(\alpha_1)\right) tan\Psi(\alpha_1)\emptyset_k\right)\left(\cos\left(\delta + \Delta(\alpha_1)\right) tan\Psi(\alpha_1)\emptyset_k\right)\right.$$

$$+\left(\cos\left(\delta + \Delta(\alpha_1)\right) tan\Psi(\alpha_1)\emptyset_k\right)\left(\cos\left(\delta + \Delta(\alpha_1)\right) tan\Psi(\alpha_1) i\eta_k\right)$$

$$+\left(\cos\left(\delta + \Delta(\alpha_1)\right) tan\Psi(\alpha_1)\emptyset_k\right)\left(isin\left(\delta + \Delta(\alpha_1)\right) tan\Psi(\alpha_1)\emptyset_k\right)$$

$$+\left(\cos\left(\delta + \Delta(\alpha_1)\right) tan\Psi(\alpha_1)\emptyset_k\right)\left(isin\left(\delta + \Delta(\alpha_1)\right) tan\Psi(\alpha_1)\emptyset_k\right)$$

$$+\left(-\cos\left(\delta + \Delta(\alpha_1)\right) tan\Psi(\alpha_1) i\eta_k\right)\left(\cos\left(\delta + \Delta(\alpha_1)\right) tan\Psi(\alpha_1)\emptyset_k\right)$$

$$+\left(-\cos\left(\delta + \Delta(\alpha_1)\right) tan\Psi(\alpha_1) i\eta_k\right)\left(\cos\left(\delta + \Delta(\alpha_1)\right) tan\Psi(\alpha_1) i\eta_k\right)$$

$$+\left(-\cos\left(\delta + \Delta(\alpha_1)\right) tan\Psi(\alpha_1) i\eta_k\right)\left(isin\left(\delta + \Delta(\alpha_1)\right) tan\Psi(\alpha_1)\emptyset_k\right)$$

$$+\left(-\cos\left(\delta + \Delta(\alpha_1)\right) tan\Psi(\alpha_1) i\eta_k\right)\left(isin\left(\delta + \Delta(\alpha_1)\right) tan\Psi(\alpha_1) i\eta_k\right)$$

$$+\left(-isin\left(\delta + \Delta(\alpha_1)\right) tan\Psi(\alpha_1)\emptyset_k\right)\left(\cos\left(\delta + \Delta(\alpha_1)\right) tan\Psi(\alpha_1)\emptyset_k\right)$$

$$+\left(-isin\left(\delta + \Delta(\alpha_1)\right) tan\Psi(\alpha_1)\emptyset_k\right)\left(-\cos\left(\delta + \Delta(\alpha_1)\right) tan\Psi(\alpha_1) i\eta_k\right)$$

$$+\left(-isin\left(\delta + \Delta(\alpha_1)\right) tan\Psi(\alpha_1)\emptyset_k\right)\left(isin\left(\delta + \Delta(\alpha_1)\right) tan\Psi(\alpha_1)\emptyset_k\right)$$

$$+\left(-isin\left(\delta + \Delta(\alpha_1)\right) tan\Psi(\alpha_1)\emptyset_k\right)\left(isin\left(\delta + \Delta(\alpha_1)\right) tan\Psi(\alpha_1) i\eta_k\right)$$

$$+\left(isin\left(\delta + \Delta(\alpha_1)\right) tan\Psi(\alpha_1) i\eta_k\right)\left(\cos\left(\delta + \Delta(\alpha_1)\right) tan\Psi(\alpha_1)\emptyset_k\right)$$

$$+\left(isin\left(\delta + \Delta(\alpha_1)\right) tan\Psi(\alpha_1) i\eta_k\right)\left(\cos\left(\delta + \Delta(\alpha_1)\right) tan\Psi(\alpha_1) i\eta_k\right)$$

$$+\left(isin\left(\delta + \Delta(\alpha_1)\right) tan\Psi(\alpha_1) i\eta_k\right)\left(isin\left(\delta + \Delta(\alpha_1)\right) tan\Psi(\alpha_1)\emptyset_k\right)$$

$$\left.+\left(isin\left(\delta + \Delta(\alpha_1)\right) tan\Psi(\alpha_1) i\eta_k\right)\left(isin\left(\delta + \Delta(\alpha_1)\right) tan\Psi(\alpha_1) i\eta_k\right)\right]$$

$$= \frac{|E|^2}{2}\Big[cos^2\big(\delta + \Delta(\alpha_1)\big)tan\Psi^2(\alpha_1){\emptyset_k}^2$$

$$- 2\cos\big(\delta + \Delta(\alpha_1)\big)sin\big(\delta + \Delta(\alpha_1)\big)tan\Psi^2(\alpha_1)\emptyset_k i\eta_k$$

$$+ cos^2\big(\delta + \Delta(\alpha_1)\big)tan\Psi^2(\alpha_1){\eta_k}^2$$

$$+ 2\cos\big(\delta + \Delta(\alpha_1)\big)sin\big(\delta + \Delta(\alpha_1)\big)tan\Psi^2(\alpha_1)\emptyset_k i\eta_k$$

$$+ sin^2\big(\delta + \Delta(\alpha_1)\big)tan\Psi^2(\alpha_1){\emptyset_k}^2 + sin^2\big(\delta + \Delta(\alpha_1)\big)tan\Psi^2(\alpha_1){\eta_k}^2\Big]$$

$$= \frac{|E|^2}{2}\Big[cos^2\big(\delta + \Delta(\alpha_1)\big)tan\Psi^2(\alpha_1){\emptyset_k}^2 + sin^2\big(\delta + \Delta(\alpha_1)\big)tan\Psi^2(\alpha_1){\emptyset_k}^2$$

$$+ cos^2\big(\delta + \Delta(\alpha_1)\big)tan\Psi^2(\alpha_1){\eta_k}^2 + sin^2\big(\delta + \Delta(\alpha_1)\big)tan\Psi^2(\alpha_1){\eta_k}^2\Big]$$

$$= \frac{|E|^2}{2}\Big[tan\Psi^2(\alpha_1){\emptyset_k}^2\Big(cos^2\big(\delta + \Delta(\alpha_1)\big) + sin^2\big(\delta + \Delta(\alpha_1)\big)\Big)$$

$$+ tan\Psi^2(\alpha_1){\eta_k}^2\Big(cos^2\big(\delta + \Delta(\alpha_1)\big) + sin^2\big(\delta + \Delta(\alpha_1)\big)\Big)\Big]$$

$$= \frac{|E|^2}{2}\Big[tan\Psi^2(\alpha_1){\emptyset_k}^2 + tan\Psi^2(\alpha_1){\eta_k}^2\Big]$$

$$= \frac{|E|^2}{2}\Big[tan\Psi^2(\alpha_1)\big({\emptyset_k}^2 + {\eta_k}^2\big)\Big] \qquad (\mathrm{B}-33)$$

Plugging in the Eqs. (B-32) and (B-33) into the Eq. (B-31),

$$I = \boldsymbol{E_r^* E_r} = |E|^2\frac{1}{2}$$

$$-|E|^2\frac{1}{2}\Big[2co\,s\big(\delta + \Delta(\alpha_1)\big)\,tan\Psi(\alpha_1)\emptyset_k - 2sin\big(\delta + \Delta(\alpha_1)\big)tan\Psi(\alpha_1)\eta_k\Big]$$

$$+\frac{|E|^2}{2}\Big[tan\Psi^2(\alpha_1)\big({\emptyset_k}^2 + {\eta_k}^2\big)\Big] \qquad (\mathrm{B}-34)$$

It is known that when using the lock-in technique, the lowest *sine* and *cosine* terms of Fourier components are detected because they are referenced by a modulator. Taking this into consideration,

$$I = \boldsymbol{E_r^* E_r} = \frac{|E|^2}{2}\left(1 - 2tan\Psi(\alpha_1)\left[\emptyset_k cos\left(\delta + \Delta(\alpha_1)\right) - \eta_k sin\left(\delta + \Delta(\alpha_1)\right)\right]\right)$$

$$= I_0\left(1 - 2tan\Psi(\alpha_1)\left[\emptyset_k cos\left(\delta + \Delta(\alpha_1)\right) - \eta_k sin\left(\delta + \Delta(\alpha_1)\right)\right]\right) \quad (B-35)$$

where I_0 is the initial light intensity which is wavelength dependent. Now, the phase, *cosine*, and *sine* terms can be expressed as,

$$\delta = \delta_0 \cos(2\pi f t) \quad (B-36)$$

$$sin\left(\delta + \Delta(\alpha_1)\right) = cos\delta sin\Delta(\alpha_1) + sin\delta cos\Delta(\alpha_1) \quad (B-37)$$

$$cos\left(\delta + \Delta(\alpha_1)\right) = cos\delta cos\Delta(\alpha_1) - sin\delta sin\Delta(\alpha_1) \quad (B-38)$$

Plug the Eq. (B-36) into the Eqs. (B-37) and (B-38),

$$cos\left(\delta + \Delta(\alpha_1)\right) = \cos(\delta_0 \cos(2\pi f t))\, cos\Delta(\alpha_1) - \sin(\delta_0 \cos(2\pi f t))\, sin\Delta(\alpha_1) \quad (B-39)$$

$$sin\left(\delta + \Delta(\alpha_1)\right) = cos(\delta_0 \cos(2\pi f t))\, sin\Delta(\alpha_1) + sin(\delta_0 \cos(2\pi f t))\, cos\Delta(\alpha_1) \quad (B-40)$$

Now, the expansion formulas of *cosine* and *sine* terms are,

$$\sin(\delta_0\, cos(2\pi f t)) = 2J_1(\delta_0)\cos(2\pi f t) + \cdots \quad (B-41)$$

$$\cos(\delta_0\, cos(2\pi f t)) = J_0(\delta_0) - 2J_2(\delta_0) cos(4\pi f t) + \cdots \quad (B-42)$$

where $J_0(\delta_0)$, $J_1(\delta_0)$, and $J_2(\delta_0)$ are zeroth-, first-, and second-order Bessel function as shown in the Fig 2-2.

Then, plug the Eqs. (B-41) and (B-42) into the Eqs. (B-39) and (B-40),

$$sin\big(\delta + \Delta(\alpha_1)\big) = (J_0(\delta_0) - 2J_2(\delta_0)cos(4\pi ft) + \cdots)sin\Delta(\alpha_1)$$
$$+(2J_1(\delta_0)\cos(2\pi ft) + \cdots)cos\Delta(\alpha_1) \qquad (\mathrm{B}-41)$$

$$cos\big(\delta + \Delta(\alpha_1)\big) = (J_0(\delta_0) - 2J_2(\delta_0)cos(4\pi ft) + \cdots)cos\Delta(\alpha_1)$$
$$-(2J_1(\delta_0)\cos(2\pi ft) + \cdots)sin\Delta(\alpha_1) \qquad (\mathrm{B}-42)$$

Next, plug the Eqs. (B-41) and (B-42) into the Eq. (B-35),

$$I = \boldsymbol{E_r^* E_r} = I_0\big(1 - 2tan\Psi(\alpha_1)\big[\emptyset_k cos\big(\delta + \Delta(\alpha_1)\big) - \eta_k sin\big(\delta + \Delta(\alpha_1)\big)\big]\big)$$
$$= I_0\{1 - 2tan\Psi(\alpha_1) \times \emptyset_k[J_0(\delta_0) - 2J_2(\delta_0)cos(4\pi ft) + \cdots)cos\Delta(\alpha_1)$$
$$-(2J_1(\delta_0)\cos(2\pi ft) + \cdots)sin\Delta(\alpha_1)]$$
$$-\eta_k[(J_0(\delta_0) - 2J_2(\delta_0)cos(4\pi ft) + \cdots)sin\Delta(\alpha_1)$$
$$+(2J_1(\delta_0)\cos(2\pi ft) + \cdots)cos\Delta(\alpha_1)]\} \qquad (B-43)$$

Now, one can rearrange the Eq. (B-43) in terms of J_0, J_1 and J_2 as,

$$I = \boldsymbol{E_r^* E_r} = I_0[1 - 2tan\Psi(\alpha_1) \times (J_0(\delta_0)cos\Delta(\alpha_1)\emptyset_k - J_0(\delta_0)sin\Delta(\alpha_1)\eta_k$$
$$-(2J_1(\delta_0)\cos(2\pi ft))sin\Delta(\alpha_1)\emptyset_k + \cdots - 2J_1(\delta_0)\cos(2\pi ft))cos\Delta(\alpha_1)\eta_k + \cdots$$
$$-2J_2(\delta_0)cos(4\pi ft)cos\Delta(\alpha_1)\emptyset_k + \cdots + 2J_2(\delta_0)cos(4\pi ft))sin\Delta(\alpha_1)\eta_k + \cdots]$$
$$= I_0[1 - 2tan\Psi(\alpha_1)J_0(\delta_0)\big(\emptyset_k cos\Delta(\alpha_1) - \eta_k sin\Delta(\alpha_1)\big)$$
$$+4tan\Psi(\alpha_1)J_1(\delta_0)\cos(2\pi ft)\big(\emptyset_k sin\Delta(\alpha_1) + \eta_k cos\Delta(\alpha_1)\big) + \cdots$$
$$+4tan\Psi(\alpha_1)J_2(\delta_0)\cos(4\pi ft)\big(\emptyset_k cos\Delta(\alpha_1) - \eta_k sin\Delta(\alpha_1)\big) \qquad (B-44)$$

The Eq. (B-44) can be simplified into,

$$I = I_0\big[I_{dc} + I_f cos(2\pi ft) + I_{2f}\cos(4\pi ft) + \cdots\big] \qquad (\mathrm{B}-45)$$

The Eq. (B-45) represents the detected light intensity. Thus the detected signal can be processed using a lock-in amplifier to increase the signal-to-noise ratio.

The I_{dc}, I_f, and I_{2f} are shown below as,

$$I_{dc} = 1 - 2tan\Psi(\alpha_1)J_0(\delta_0)\left(\emptyset_k cos\Delta(\alpha_1) - \eta_k sin\Delta(\alpha_1)\right) \quad (B-46)$$

$$I_f = 4tan\Psi(\alpha_1)J_1(\delta_0)\left(\emptyset_k sin\Delta(\alpha_1) + \eta_k cos\Delta(\alpha_1)\right) \quad (B-47)$$

$$I_{2f} = 4tan\Psi(\alpha_1)J_2(\delta_0)\left(\emptyset_k cos\Delta(\alpha_1) - \eta_k sin\Delta(\alpha_1)\right) \quad (B-48)$$

where I_{dc} is the *DC* signal which is modulated by the optical chopper in our system as shown in the Fig. 4-2. Both I_f and I_{2f} are the *AC* signals modulated by PEM. The modulation frequencies f (1st harmonic) and $2f$ (2nd harmonic) are for the Kerr ellipticity and Kerr rotation, respectively, and these modulation frequencies are generated specifically by a PEM. Therefore, the modulation frequency has to be carefully chosen in PEM depending on the Kerr ellipticity or the Kerr rotation measurement based on the Eq. (B-45).

To obtain the *DC* signal only, the 2nd term of the Eq. (B-46) has to be zero. This means that $J_0(\delta_0)$ (*i.e.* zeroth order of Bessel function) has to be zero in the Eq. (B-46). To eliminate the $J_0(\delta_0)$ term the phase retardation amplitude δ_0 has to be 2.405 as shown in Fig.2-2. Thus, the phase retardation amplitude δ_0 in PEM should be 2.405 for the actual MOKE experiment. When the $J_0(2.405) = 0$, the 2nd term of the Eq. (B-46) becomes zero as well. So, the *DC* signal becomes $I_{dc} = I_0$. By normalizing the Eqs. (B-47) and (B-48), the Kerr ellipticity and rotation can be represented by,

$$Kerr\ ellipcity \qquad \frac{I_f}{I_{dc}} = \frac{1}{\sqrt{2}} \frac{4tan\Psi(\alpha_1)J_1(\delta_0)\left(\emptyset_k sin\Delta(\alpha_1) + \eta_k cos\Delta(\alpha_1)\right)}{1} \quad (B-49)$$

$$Kerr\ rotation \qquad \frac{I_{2f}}{I_{dc}} = \frac{1}{\sqrt{2}} \frac{4tan\Psi(\alpha_1)J_2(\delta_0)\left(\emptyset_k cos\Delta(\alpha_1) - \eta_k sin\Delta(\alpha_1)\right)}{1} \quad (B-50)$$

It should be noted that the $1/\sqrt{2}$ factor is included in the above equations because the lock-in amplifier measures the root-mean-square of *AC* signal. The Eqs. (B-49) and (B-50) can be rearranged into,

$$\frac{I_f}{I_{dc}} = \frac{1}{\sqrt{2}}\frac{\sqrt{2}}{\sqrt{2}}\frac{4tan\Psi(\alpha_1)J_1(\delta_0)\left(\emptyset_k sin\Delta(\alpha_1) + \eta_k cos\Delta(\alpha_1)\right)}{1}$$

$$= 2\sqrt{2}\, tan\Psi(\alpha_1)J_1(\delta_0)\left(\emptyset_k sin\Delta(\alpha_1) + \eta_k cos\Delta(\alpha_1)\right) \qquad (B-51)$$

$$\frac{I_{f2}}{I_{dc}} = \frac{1}{\sqrt{2}}\frac{\sqrt{2}}{\sqrt{2}}\frac{4tan\Psi(\alpha_1)J_2(\delta_0)\left(\emptyset_k cos\Delta(\alpha_1) - \eta_k sin\Delta(\alpha_1)\right)}{1}$$

$$= 2\sqrt{2}\, tan\Psi(\alpha_1)J_2(\delta_0)\left(\emptyset_k cos\Delta(\alpha_1) - \eta_k sin\Delta(\alpha_1)\right) \qquad (B-52)$$

The Eqs. (B-51) and (B-52) suggests that the measured signal at the detector is affected by intermixing the signals of $\emptyset_k$, and η_k in addition to the ellipsometry parameters $tan\Psi$ and Δ from the mirror, as reported in Refs.[141] and [144]. When the mirror is not implemented into the system, $tan\Psi = 1$ and $\Delta = 0$. Therefore, the Eqs. (B-51) and (B-52) can be further simplified as,

$$Kerr\ ellipcity \qquad \frac{I_f}{I_{dc}} = 2\sqrt{2}\, AJ_1(\delta_0)\eta_k \qquad (B-53)$$

$$Kerr\ rotation \qquad \frac{I_{f2}}{I_{dc}} = 2\sqrt{2}\, BJ_2(\delta_0)\emptyset_k \qquad (B-54)$$

where A and B are calibration factors [145]. Finally, when $J_0(2.405) = 0$, then$J_1(2.405) = 0.52$ for Kerr ellipticity and $J_2(2.405) = 0.43$ for Kerr rotation as shown in the Fig. 2-2. Using the Eqs. (B-52) and (B-53), these values (0.52 and 0.43) can be used to calibrate the measured signals [unit less] to the Kerr rotation [deg] and the Kerr ellipticity [deg] signals, respectively.

APPENDIX C. ZEEMAN SPLITTING ENERGY

This is a supplemental section to derive the mathematical expression of the Zeeman splitting energy as shown in Section 2.2.2. Sections of *C.1* and *C.2* explain how to obtain the Zeeman splitting energy in terms of the *s*-*d* exchange constant ($N_0\alpha$) and *p*-*d* exchange constant ($N_0\beta$) for Γ critical points and for *L* critical points of the Brillouin Zone.

C.1 Γ critical points

As mentioned in Section 2.2.2.1, the selection rule can be applied to Γ -CPs to determine the different optical transitions from each energy state (Fig. 2-10).

As illustrated in Fig. 2-10, one has to know the total angular momentum of an electron at each energy state to find out the allowed optical transitions.

At first, the total angular momentum quantum number is expressed by,

$$j = l \pm s$$

where l is the orbital angular momentum quantum number and s is the spin angular momentum quantum number.

Then, the *z*-component of total angular momentum J_z is,

$$J_z = m_j\hbar, \qquad m_j = -j, -j+1, -j+2 \ldots\ldots j-1, j, \quad \text{or} \quad m_j = m_l + m_s$$

where m_l is the magnetic quantum number (projection of orbital quantum number) and m_s is the spin projection quantum number.

Now, since the conduction band is formed by the *s*-orbital of the cation, $m_j = 0 \pm 1/2$, and the total angular momentum of the conduction band is,

$$J_z = \pm \frac{1}{2}\hbar$$

Similarly, since the valence band is formed by *p*-orbital of the anion, $m_j = 0 \pm 1/2$ and $m_j = \pm 1 \pm 1/2$. The total angular momentum of the valence band is,

$$J_z = \pm \frac{1}{2}\hbar, \quad J_z = \left(\pm 1 \pm \frac{1}{2}\right)\hbar$$

Therefore, the total angular momentum number at each energy state under the magnetic field is represented in Fig. C-1.

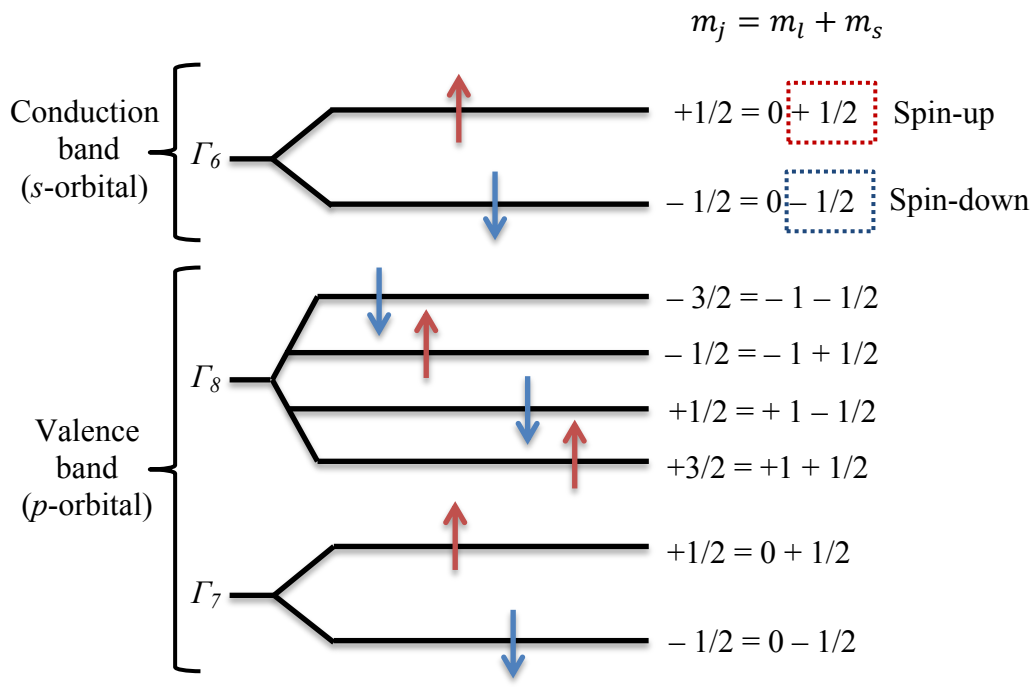

Figure C-1 Total angular momentum quantum number of each energy state at Γ critical point under an external magnetic field.

Now, based on Figs. 2-10 and C-1, the optical transitions of the right circularly polarized light (σ^+) and left circularly polarized light (σ^-) can be decided. So, the angular momentum of photon for right (σ^+) and left (σ^-) circularly polarized light is defined as:

Right circularly polarized light: $\sigma+ = +1$

Left circularly polarized light: $\sigma- = -1$

Now, one can use Eq. (2.15) to determine the allowed optical transitions.

1. $\Gamma_8 - \Gamma_6$ optical transitions

As illustrated in Fig. 2-10 and C-1, the total angular momentum of an electron at an initial state is -3/2, the angular momentum of a photon is ±1, and the total angular momentum of an electron at an excited state (allowed optical transition) is given by,

$-3/2 + (\sigma-) = -3/2 + (-1) = -3/2 \ -2/2 = -5/2 \quad \Rightarrow$ Not allowed

$-3/2 + (\sigma+) = -3/2 + (+1) = -3/2 + 2/2 = -1/2 \quad \Rightarrow$ Allowed (A)

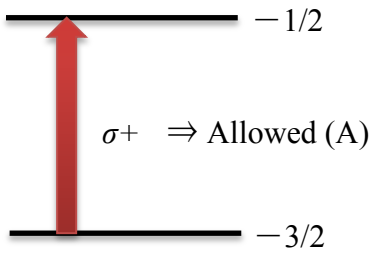

Figure C-2 Illustration of allowed $\Gamma_8 - \Gamma_6$ optical transitions due to the selection rule.

As shown in the Fig. C-1, the $-5/2$ does not exist in the conduction band. Therefore, the σ^+ optical transition can be allowed but σ^- optical transition cannot be allowed in this

case as shown in Fig. C-2. In this way, one can figure out other allowed $\Gamma_8 - \Gamma_6$ optical transitions as well,

$-1/2 + (\sigma\text{-}) = -1/2 + (-1) = -1/2 \ -2/2 = -3/2 \quad \Rightarrow$ Not allowed

$-1/2 + (\sigma+) = -1/2 + (+1) = -1/2 + 2/2 = +1/2 \quad \Rightarrow$ Allowed (B)

$+1/2 + (\sigma\text{-}) = -1/2 + (-1) = 1/2 \ -2/2 = -1/2 \quad \Rightarrow$ Allowed (C)

$+1/2 + (\sigma+) = -1/2 + (+1) = 1/2 + 2/2 = +3/2 \quad \Rightarrow$ Not Allowed

$+3/2 + (\sigma\text{-}) = +3/2 + (-1) = +3/2 \ -2/2 = +1/2 \quad \Rightarrow$ Allowed (D)

$+3/2 + (\sigma+) = +3/2 + (+1) = +3/2 + 2/2 = +5/2 \quad \Rightarrow$ Not Allowed

2. $\Gamma_7 - \Gamma_6$ optical transitions

Similarly, the $\Gamma_7 - \Gamma_6$ optical transitions can be determined by,

$+1/2 + (\sigma\text{-}) = -1/2 + (-1) = 1/2 \ -2/2 = -1/2 \quad \Rightarrow$ Allowed (E)

$+1/2 + (\sigma+) = -1/2 + (+1) = 1/2 + 2/2 = +3/2 \quad \Rightarrow$ Not Allowed

$-1/2 + (\sigma\text{-}) = -1/2 + (-1) = -1/2 \ -2/2 = -3/2 \quad \Rightarrow$ Not allowed

$-1/2 + (\sigma+) = -1/2 + (+1) = -1/2 + 2/2 = +1/2 \quad \Rightarrow$ Allowed (F)

The Fig. 2-10 summarizes all total angular momentum quantum for each energy state and the allowed optical transitions (A) – (F). The detailed explanations for Fig. 2-10 can be found in the Section 2.2.2.1. So, using the selection rule, one can find out the optical transition energies between different energy states as shown in Eqs. (2.16) – (2.21).

Now, based on the energies of the optical transitions (Eqs. (2.16) – (2.21)), one can find out the Zeeman splitting energies of E_0 and $E_0+\Delta_0$ transitions (Γ-CPs) and that is

nothing but the energy difference between right circularly polarized light (σ^+) and left circularly polarized light (σ^-) [99] [102] [108] [153] [154].

1. Zeeman splitting energy ΔE for E_0 transition (heavy-hole),

$$\begin{aligned}\Delta E &= E_D(\sigma^-) - E_A(\sigma^+) \\ &= \left(E_g + \frac{1}{2}\,\mathrm{x}\,(N_0\beta - N_0\alpha)\,\langle S\rangle\right) - \left(E_g - \frac{1}{2}\,\mathrm{x}\,(N_0\beta - N_0\alpha)\,\langle S\rangle\right) \\ &= \mathrm{x}\,(N_0\beta - N_0\alpha)\,\langle S\rangle \end{aligned} \qquad (\mathrm{C}-1)$$

2. Zeeman splitting energy ΔE for E_0 transition (light-hole),

$$\begin{aligned}\Delta E &= E_C(\sigma^-) - E_B(\sigma^+) \\ &= \left(E_g + \frac{1}{6}\,\mathrm{x}\,(N_0\beta + N_0\alpha)\,\langle S\rangle\right) - \left(E_g - \frac{1}{6}\,\mathrm{x}\,(N_0\beta + N_0\alpha)\,\langle S\rangle\right) \\ &= \frac{1}{3}\,\mathrm{x}\,(N_0\beta + 3N_0\alpha)\,\langle S\rangle \end{aligned} \qquad (\mathrm{C}-2)$$

3. Zeeman splitting energy ΔE for $E_0 + \Delta_0$ transition,

$$\begin{aligned}\Delta \mathrm{E} &= E_E(\sigma^-) - E_F(\sigma^+) \\ &= \left(E_g + \frac{1}{6}\,\mathrm{x}\,(N_0\beta + N_0\alpha)\,\langle S\rangle\right) - \left(E_g - \frac{1}{6}\,\mathrm{x}\,(N_0\beta + N_0\alpha)\,\langle S\rangle\right) \\ &= \frac{1}{3}\,\mathrm{x}\,(-N_0\beta + 3N_0\alpha)\,\langle S\rangle \end{aligned} \qquad (\mathrm{C}-3)$$

Equations (C-1) – (C-3) represents the Zeeman splitting energies at Γ-CPs in terms of the *s-d* exchange constant ($N_0\alpha$) and *p-d* exchange constant ($N_0\beta$), and they are summarized in Table 2-1. The main discussions of selection rules and the Zeeman splitting energies at Γ-CPs are shown in Section 2.2.2.1.

C.2 *L* critical points

As already mentioned in Section 2.2.2.2, it is very difficult to apply the selection rules at *L* critical points (CPs). In Mn-doped zinc-blende II-VI DMS, the Zeeman splitting at E_1 (*L*-CP) is theoretically and experimentally ~1/4 and ~ 1/16 smaller than the one at E_0 (Γ-CP), respectively. Thus, an accurate optical transitions cannot be determined for such a fine structure using the selection rule at *L*-CPs and the same idea can be also applied to Mn-doped zinc-blende III-V DMS [70] [76] [139] [155].

The total angular momentum quantum J_z and the optical transitions at *L*-CPs as shown in the Fig. 2-11 [70] [76] [139] [155].

Now, the Zeeman splitting energies for E_1 and $E_1+\Delta_1$ optical transitions (*L*-CPs) can be derived in the following [70] [76] [99] [155]. When the magnetic field *B* is applied along $\hat{n}$ (unit vector), the effective Zeeman Hamiltonian can be expressed as [76],

$$H^i = K^i(\mathrm{s}\cdot\hat{n}) \qquad (\mathrm{C}-4)$$

$$K^i = -\mu_B g^i \mathrm{B} - J^i_{kk} M \qquad (\mathrm{C}-5)$$

where superscript $i = c, v$ indicates the conduction and valence band, respectively, and *s* is the electron spin [76]. The first term in an Eq. (C-5) represents the effective *g* factor due to the direct effect of a magnetic field. The second term is due to the *e*-Mn^{2+} exchange and the diagonal exchange parameter at critical points *k*, which are represented by J^i_{kk} [76]. *M* is the magnetization, which is represented by $M = N_0 x \langle S\rangle$, where N_0 is the number of the cations (magnetic ions) per unit volume, *x* is the concentration of magnetic ions, *S* is the Mn ion spin ($S = 5/2$), and $\langle S\rangle$ is the average energy of magnetic ion's spin along the external magnetic field direction [76]. The *z* axis along the <111> direction was

chosen and the symmetry group of k is chosen C_{3v} at the Λ and L critical points of Brillouin zone [76]. As illustrated in the Fig. 2-11, E_1 and $E_1+\Delta_1$ splits into four components that can allow both σ^+ and σ^- transitions. In practice such a fine structure cannot be experimentally observed but one can eventually obtain the Zeeman splitting energy ΔE_1 by the weighted average $< E >$ of the energy of the four component given by σ^+ and σ^- transitions [155]. Thus, one can derive the average Zeeman splitting energies for ΔE_1 and $\Delta E_1+\Delta_1$ optical transitions (L-CPs) from the Eq. (C-4) [76] [155],

$$\langle \Delta E_1 \rangle = \langle E_1(\sigma^-) \rangle - \langle E_1(\sigma^+) \rangle$$

$$= 2\frac{cos^2\theta}{1 + cos^2\theta}(K^c - K^v) \qquad (C-6)$$

$$\langle \Delta E_1 + \Delta_1 \rangle = \langle (E_1 + \Delta_1)(\sigma^-) \rangle - \langle (E_1 + \Delta_1)(\sigma^+) \rangle$$

$$= -2\frac{cos^2\theta}{1 + cos^2\theta}(K^c - K^v) \qquad (C-7)$$

θ is the angle between the given L direction and the applied magnetic field, and K is given in the Eq. (C-5).

Now, the Eqs. (C-6) and (C-7) should be average over four L points and one can have [76],

$$\Delta E_1 = r(K^c - K^v) \qquad (C-8)$$

where r is the numerical factor depending on the magnetic field orientation and it is represented by,

$$\mathrm{r} = \begin{cases} \frac{2}{5}, B \| \langle 111 \rangle \; or \; \langle 110 \rangle \\ \frac{1}{2}\,, \; B \| \langle 000 \rangle \\ \frac{4-\pi}{2}, B \; is \; randomely \; oriented \end{cases} \qquad (\mathrm{C}-9)$$

Now, using the Eq. (C-5) and $g^c \approx g^v \approx 2$, the Eq. (C-8) becomes,

$$\begin{aligned} \Delta E_1 &= r(K^c - K^v) \\ &= r\{(-\mu_B g^c \mathrm{B} - J^c_{kk} M\,) - (-\mu_B g^v \mathrm{B} - J^v_{kk} M\,)\} \\ &= r\{(-2\mu_B \mathrm{B} - J^c_{kk} M\,) - (-2\mu_B \mathrm{B} - J^v_{kk} M\,)\} \\ &= r(J^v_{kk} - J^c_{kk}) M \end{aligned} \qquad (C-10)$$

where

$$J^c_{LL} \approx \alpha \qquad (\mathrm{C}-11)$$

$$J^v_{LL} \approx \frac{1}{4}\,\beta \qquad (\mathrm{C}-12)$$

where α and β are exchange integrals for *s*-*d* and *p*-*d* exchange interaction, respectively [70].

Using the Eqs. (C-10)– (C-12), finally the Zeeman splitting energies E_1, and E_1+Δ_1 at *L* critical points can be derived [70] [76] [99],

$$\Delta E_1 \cong r\left(N_0\alpha - \frac{1}{4}\,N_0\beta\right)\langle S_z \rangle \qquad (\mathrm{C}-13)$$

$$E_1 + \Delta_1 \cong -rx\left(\frac{1}{4}N_0\beta - N_0\alpha\right)\langle S_z \rangle \qquad (\mathrm{C}-14)$$

where $N_0\alpha$ and $N_0\beta$ are *s*-*d* and *p*-*d* exchange constant, respectively.

Finally, the table 2-1 summarizes the Zeeman splitting energy at E_0, $E_0+\Delta_0$, and E_1, $E_1+\Delta_1$ critical points from the Eqs. (2.22) – (2.24), and the Eqs. (2.25) – (2.26) [99].

It should be noted here that the effective *g*-factor of the valence band and conduction band were approximated to be equal in this time ($g^c \approx g^v \approx 2$) to simplify the Eq. (C-10) [76]. Then, one can relatively easily estimate the *s-d* ($N_0\alpha$) and *p-d* ($N_0\beta$) exchange constant using the Eqs. (C-13) and (C-14) if the Zeeman splitting energy is known. The accurate *g*-factor usually includes some extra terms *Xs* (*i.g*, $g = 2 + Xs$) which are dependent of E_1 and $E_1+\Delta_1$ energies [139] [155]. So, the accurate *g*-factor is not exactly a factor of 2 and the *g*-factor of the valence band and conduction band is not usually the same. However, if they are assumed to be the same the accuracy of the *g*-factor may be reduced but one can obtain the information of the *s-d* ($N_0\alpha$) and *p-d* ($N_0\beta$) exchange interaction constant in a simpler manner using the Eqs. (C-13) and (C-14).

Another important fact that should be mentioned here is that the quality of g^c and g^v (effective *g*-factor of conduction and valence bands) are different from that of g_{eff} (effective *g*-factor shown in Eq. (2.29): $\Delta E = -g_{eff}\mu_B H$). The effective *g*-factor in the Eq. (2.29) is given by $g_{eff} = g^c - g^v$ and this is actually called the effective interband *g*-factor [139] [155]. More specifically, the effective interband *g*-factor for ΔE_1 optical transition is given by $g_{eff} = g^c - g_{45}$ where g_{45} is the effective *g*-factor for the Zeeman splitting of $L_{4,5}$ energy state as shown in the Fig. 2-11 [139] [155]. Similarly, the effective interband *g*-factor for $\Delta E_1 + \Delta_1$ optical transition is given by $g_{eff} = g^c - g_6$ where g_6 is the effective *g*-factor for the Zeeman splitting of the L_6 energy state as shown in the Fig. 2-11 [139] [155]. In addition, the effective interband *g*-factor can be estimated

using the Eqs. (2.28) and (2.29) because the MCD and dkL/dE (or dRL/dE) values can be experimentally obtained. This calculation method to find out the effective interband *g*-factor was successfully demonstrated for the TM-doped II-VI DMSs [82].

APPENDIX D. RIGID BAND SHIFT MODEL

When the diluted magnetic semiconductors (DMSs) are investigated by the MCD technique, the rigid band shift model is often used [99] [158]. The model simply states that the absorption edge of an energy band gap can be modulated by the Zeeman splitting effect but the shape of the band gap structure itself does not change as shown in the Fig. 2-12. As illustrated in the Fig. 2-12, when the photon energy reaches the band gap energy (E) of the DMS, the absorption coefficient (k) of light increases and it saturates beyond the first band gap energy (E) until it reaches the next bandgap energy. When a magnetic field is applied to the DMS, Zeeman splitting (ΔE) can occur and the absorption edge of an energy band gap (E) can be modulated into spin-up ($E_{\uparrow}$) and spin-down ($E_{\downarrow}$) states. Based on the Fig. 2-12, one can derive MCD[θ]. As explained in an earlier section, the MCD[θ] is a ratio of AC and DC signal. The AC signal is the absorption difference between the right and left circularly polarized light and the DC signal is the mean intensity of the right and left circularly polarized light as,

$$\mathrm{AC} = I^{+} - I^{-} \qquad (D-1)$$

$$\mathrm{DC} = \frac{I^{+} + I^{-}}{2} \qquad (D-2)$$

From the Eqs. (A-47), (D-1) and (D-2), the MCD[θ] becomes,

$$MCD[\theta] = \frac{1}{4}\frac{AC\ signal}{DC\ signal} = \frac{2}{4}\frac{I^{+} - I^{-}}{I^{+} + I^{-}}$$

$$= \frac{(MCD(+H) + CD) - (MCD(-H) + CD)}{2} \qquad (\mathrm{D}-3)$$

where $MCD(+H)$ is the MCD signal as a function of the positive magnetic field ($+H$), $MCD(-H)$ is the MCD signal as a function of the negative magnetic field ($-H$), and CD is

a circular dichroism (CD). In AC signal ($I^+ - I^-$), the CD signal is included. The CD signal does not depend on magnetic field and it acts as background noise. Therefore, if (*MCD* (+*H*) + *CD*) – (*MCD* (-*H*) + *CD*) is processed, only CD cancels out each other and (*MCD* (+*H*)- *MCD* (-*H*))/2 provides the averaged *AC* signal. This is the reason why the MCD signal is measured in a both positive (+*H*) and negative (-*H*) magnetic field and divided by a factor of 2 as shown in Eq. (D-3). The Eq. (D-3) simply becomes Eq. (D-4) in the unit of degree as,

$$MCD\ (\text{degree}) = \frac{180}{\pi}\frac{1}{2}\frac{I^+ - I^-}{I^+ + I^-} = \frac{90}{\pi}\frac{I^+ - I^-}{I^+ + I^-} \qquad (\text{D}-4)$$

Now, when light is incident onto the sample, it is absorbed exponentially. Thus, an Eq. (D-5) simply shows the transmitted light intensity through a sample without the applied magnetic field [99],

$$I = I_o exp(-k(E)L) \qquad (\text{D}-5)$$

where I_0 is the initial intensity before being absorbed by the sample, $k(E)$ is the absorption coefficient at the bandgap energy E, and L is the sample thickness. Now, it is assumed that the bandgap energy (E) splits into half ($\pm\ \Delta/2$) [99]. This means that the magnetic field changes the optical absorption energy without changing the spectrum shape (*i.e*. rigid band shift model). When right and left circularly polarized light are shined onto the sample, the absorption coefficient $k+$ and $k-$ are introduced and the Eq. (D-5) becomes [99],

$$I^+ = I_o exp(-k^+(E)L) = I_o \exp\left(-k\left(E + \frac{\Delta E}{2}\right)L\right) \qquad (\text{D}-6)$$

$$I^- = I_o exp(-k^-(E)L) = I_o \exp\left(-k\left(E - \frac{\Delta E}{2}\right)L\right) \qquad (\text{D}-7)$$

where ΔE is the Zeeman splitting energy which includes the effective g-value (g_{eff}),

$$\Delta E = -g_{eff}\mu_B H \qquad (D-8)$$

where μB is the Bohr magneton, and H is the applied magnetic field.

Now, the Taylor expansion is used for $k\left(E + \frac{\Delta E}{2}\right)$ and $k\left(E - \frac{\Delta E}{2}\right)$,

$$f(a+h) = f(a) + f'(a)h + f''(a)\frac{h^2}{2!} + \cdots\cdots\cdots f^{(n)}(a)\frac{h^n}{n!} + 0(h^{n+1})$$

In consequence, we obtain,

$$k\left(E + \frac{\Delta E}{2}\right) = k(E) + \frac{dk}{dE}\frac{\Delta E}{2} + \cdots\cdots \qquad (\mathrm{D}-9)$$

$$k\left(E - \frac{\Delta E}{2}\right) = k(E) - \frac{dk}{dE}\frac{\Delta E}{2} + \cdots\cdots \qquad (\mathrm{D}-10)$$

Now, plugging the Eqs. (D-9) and (D-10) into the Eqs. (D-6) and (D-7) we get,

$$I^+ = I_o \exp\left(-k\left(E + \frac{\Delta E}{2}\right)L\right) = I_o \exp\left(-k(E) - \frac{dk}{dE}\frac{\Delta E}{2}L\right) \qquad (D-11)$$

$$I^- = I_o \exp\left(-k\left(E - \frac{\Delta E}{2}\right)L\right) = I_o \exp(-k(E) + \frac{dk}{dE}\frac{\Delta E}{2}L) \qquad (\mathrm{D}-12)$$

To derive $I^+ - I^-$, and $I^+ + I^-$, another Taylor expansion for an exponential function can be used,

$$e^x = \sum_{n=0}^{\infty}\frac{x^n}{n!} \Rightarrow e^x = \frac{x^0}{0!} + \frac{x'}{1!} + \cdots\cdots = 1 + x$$

$$I^+ - I^- = I_o e^{-k(E)}\left[e^{-\frac{dk\Delta E}{dE\ 2}} - e^{\frac{dk\Delta E}{dE\ 2}}\right]L$$

$$= I_o e^{-k(E)}\left[\left(1 - \frac{dk}{dE}\frac{\Delta E}{2}\right) - \left(1 + \frac{dk}{dE}\frac{\Delta E}{2}\right)\right]L$$

$$= I_o e^{-k(E)}\left(-2\frac{dk}{dE}\frac{\Delta E}{2}\right)L \qquad (\mathrm{D}-13)$$

$$I^+ - I^- = I_o e^{-k(E)} \left[e^{-\frac{dk\Delta E}{dE\ 2}} + e^{\frac{dk\Delta E}{dE\ 2}} \right] L$$

$$= I_o e^{-k(E)} \left[\left(1 - \frac{dk}{dE} \frac{\Delta E}{2} \right) + \left(1 + \frac{dk}{dE} \frac{\Delta E}{2} \right) \right] L$$

$$= I_o e^{-k(E)} [2] L \qquad (\mathrm{D}-14)$$

Using the Eqs. (D-13) and (D-14), one can obtain the following equation,

$$\frac{I^+ + I^-}{I^+ - I^-} = \frac{I_o e^{-k(E)} \left(-2 \frac{dk}{dE} \frac{\Delta E}{2} \right) L}{2 I_o e^{-k(E)} L} = -\frac{1}{2} \frac{dk}{dE} \Delta E \qquad (D-15)$$

Now, the Eq. (D-15) has to be plugged into Eq. (D-4), which is $MCD(E) = -\frac{90}{\pi} \frac{I^+ - I^-}{I^+ + I^-} [deg]$, and the Eq. (D-4) becomes,

$$MCD(E) = \frac{90}{\pi} \frac{I^+ - I^-}{I^+ + I^-} = \frac{90}{\pi} \left(-\frac{1}{2} \frac{dk}{dE} \Delta E \right) = \frac{45}{\pi} \Delta E \frac{dk}{dE} [deg] \qquad (\mathrm{D}-16)$$

Therefore, the equation for the transmission-mode MCD can be derived from the rigid band shift model [82] [99],

$$MCD(E) = -\frac{45}{\pi} \Delta E \frac{dkL}{dE} \qquad (D-17)$$

In the same manner, the equation for reflection-mode MCD can be derived from the rigid band shift model as shown in Eq. (2.30).

Furthermore, to obtain the energy derivative of the absorption (or reflection), one can start to derive the equation with the Eulerian absorption unit,

$$S(E) = X(E) exp(-k(E)L) \qquad (\mathrm{D}-18)$$

where *S(E)* is the intensity after the absorption of light by a sample and *X(E)* is the initial intensity of the light before the absorption of light by the sample, *k* is the absorption coefficient, and *L* is the thickness of the sample.

Therefore, the Eq. (D-18) becomes,

$$k = -\frac{1}{L} log\left(\frac{S(E)}{X(E)}\right) \qquad (\mathrm{D}-19)$$

Now, taking the energy derivative of an Eq. (D-19) we obtain,

$$\frac{dkL}{dE} = -\left[\frac{d}{dE}\left(\log\left(S(E)\right)\right) - \frac{d}{dE}\left(log\left(X(E)\right)\right)\right] \qquad (\mathrm{D}-20)$$

The main discussion supporting the mathematical formalism presented in Appendix D can be located in Section 2.2.2.

APPENDIX E. ADDITIONAL RESULTS FROM MCD AND MOKE SYSTEMS

This Appendix E shows some supplemental results to demonstrate the functionality of the multifunctional magneto-optical system combining Reflection-mode MCD and polar/longitudinal MOKE measurement options. Figure E-1 (a) shows the MCD hysteresis loops with different wavelength generated by a Xe lamp and a monochromator. The tested sample was $Ga_{0.97}Mn_{0.03}As$/InP measured at 8K. These results prove that the developed system can perform the wavelength (or photon energy) dependent measurements. Figure E-1 (b) shows the MCD hysteresis loop collected at different ambient temperatures demonstrating further the correct system functionality.

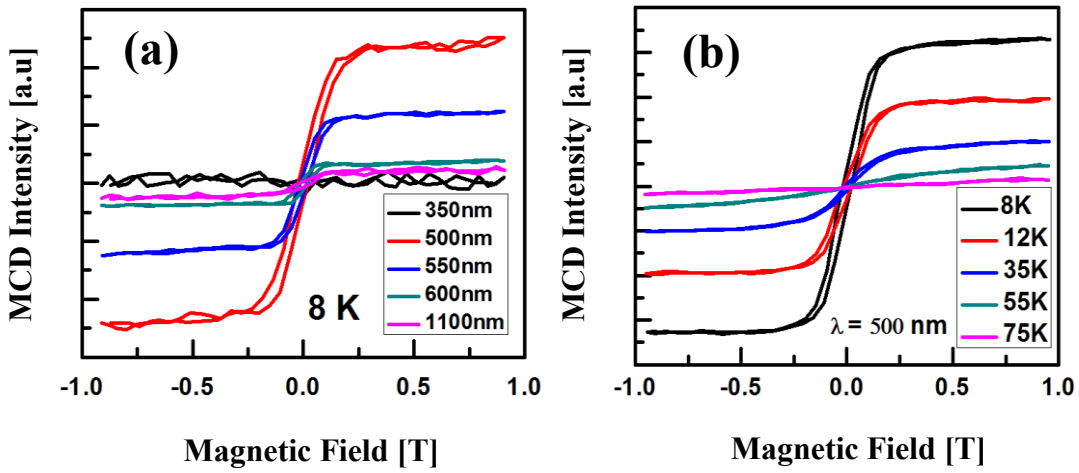

Figure E-1 (a) MCD hysteresis loops of $Ga_{0.97}Mn_{0.03}As$ on InP with different wavelength (b) MCD hysteresis loop of $Ga_{0.97}Mn_{0.03}As$ on InP with different ambient temperature. These results were measured by a reflection-mode MCD setup at OU.

Figure E-2 (a) and (b) shows the room temperature MOKE hysteresis loop and MOKE spectrum of AlN:Ni measured by in polar geometry using a developed

polar/longitudinal MOKE setup based on an extra optical mirror approach. These results confirm the correct functionality of the developed MOKE experimental setup at OU.

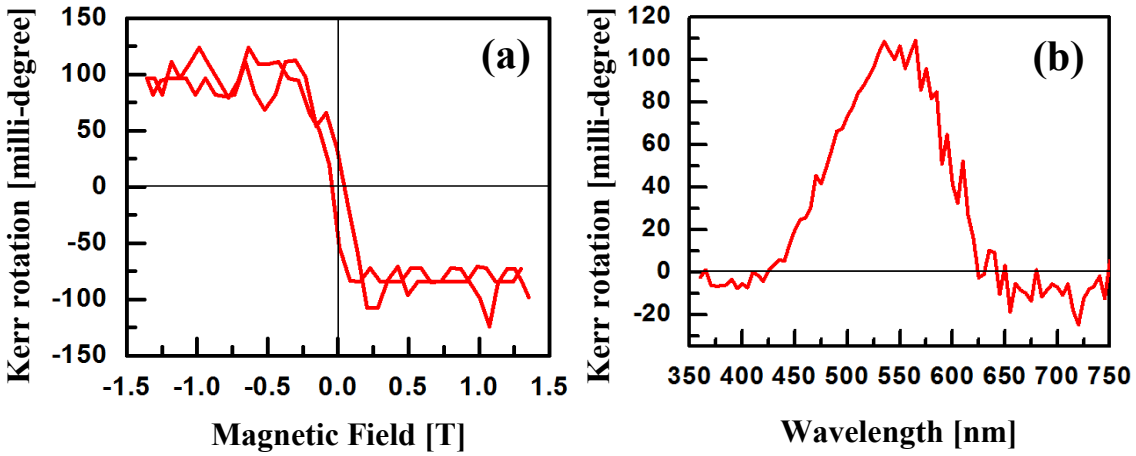

Figure E-2 (a) Kerr rotation of AlN:Ni in polar geometry at room temperature. (b) Kerr spectrum of AlN:Ni in polar geometry at room temperature [175].

APPENDIX F. ARROTT PLOT

Arrott plot is a plot that can be used to relatively easily and accurately determine the Curie temperature T_c of ferromagnetic materials [203] [204]. This technique determining the Curie temperature T_c is named after American physicist Anthony Arrott, who introduced this technique to study magnetism in 1957 [203]. The Arrott plot presents straight-line isotherms of the square of the magnetization M in a magnetic field H as a function of H/M for fixed temperature T [203] [204]. This is based on the Weiss molecular-field theory predicting that a slope of a plot (Arrott plot) becomes a straighter line as temperature T approaches the critical temperature. Then, the plot eventually intercepts at zero magnetization M and zero H/M at a fixed temperature [203] [204]. The temperature where the plot intercepts zero M and H/M can be considered as the Curie temperature T_c of a ferromagnetic material.

In our case, we conducted the Arrott plot with straight-line isotherms of the square of the *MCD* intensity in magnetic field H as a function of H/MCD for fixed temperature T. The examples for the Arrott plots shown in Fig. F-1 were obtained using results collected by transmission-mode MCD at AIST, Japan. Additional examples of the Arrott plot using MCD intensity can be found elsewhere [80] [81] [104] [133] [140] [160] [205].

From the Fig. E-1, the Curie temperature T_c of $Ga_{0.97}Mn_{0.03}As$/sapphire was determined as 17 ± 1 K. However, the displayed temperature in the system has ~3 K deviation from what it should be due to the internal property of the used MCD setup. Therefore, the Curie temperature T_c of tested $Ga_{0.97}Mn_{0.03}As$/sapphire is concluded as 20 ± 2 K.

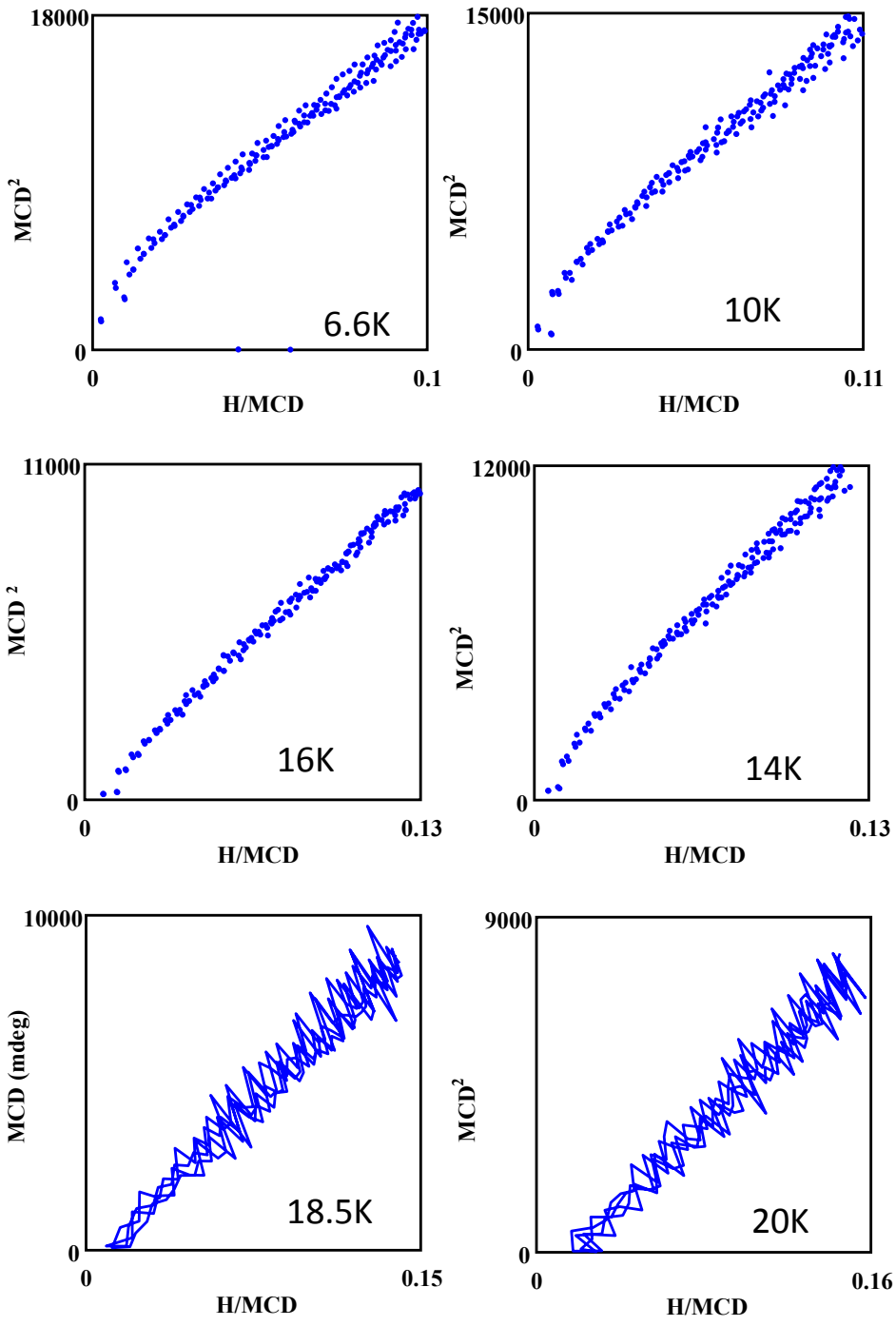

Figure F-1 Arrott plots from $Ga_{0.97}Mn_{0.03}As$ on sapphire measured by a transmission-mode MCD at AIST.

APPENDIX G. MAJOR PROJECT OUTCOMES

The scientific, academic and professional outcomes generated during this project are shown in this appendix.

Papers:

- H. Tanaka,W. M. Jadwisienczak, H. Saito, V. Zayets, S. Yuasa, and K. Ando, "Localized *s,p-d* exchange interaction in ferromagnetic $Ga_{1-x}Mn_xAs$ observed by magnetic circular dichroism spectroscopy of *L* critical point" *J. Phys. D: Appl. Phys*. 47, pp, 355001, Aug. 2014.
- J. B. Huarac, J.Z. Wang, H. Tanaka, W. M. Jadwisienczak, B. Weiner, and G. Morell, "Stability of the Mn pholuminescence in bifunctional ZnS:0.05Mn nanoparticles," *J. Appl. Phys.* 114, pp. 053106, Aug. 2013.
- H. Tanaka, W. M. Jadwisienczak, S. Kaya, G. Chen, C. Wan, M. E. Kordesch, "Ferromagnetism of Cluster and Thickness Dependence in Nickel in situ Doped Amorphous AlN Thin Films," *J. Electron. Matter*., DOI: 10.1007/s11664-013-2493-3, Mar. 2013.
- W. Jadwisienczak, R. Palai, J. Wang, H. Tanaka, J. Wu, A. Rivera, H. Huhtinen, and A. Anders, "Optical properties of ferromagnetic ytterbium-doped III-nitride epilayers," *Phys. Status Solidi C*, vol. 8, pp. 2185–2187, July. 2011.
- W. M. Jadwisienczak, H. Tanaka, G. Chen, M. Kordesch, A. Khan, "Morphology and Magnetio-optical Properties of Amorphous AlN Films Doped with Nickel," *Mater. Res. Soc. Symp. Proc*., pp. 1290, DOI: 10.1557/opl.2011.16 , Jan. 2011.
- W. M. Jadwisienczak, J. Wang, H. Tanaka, J. Wu, R. Palai, H. Huhtinen, and A. Anders, "Optical and Magnetic Properties of GaN Epilayers Implanted with Ytterbium," *J. Rare. Earth.*, vol. 28, pp. 931-937, Dec. 2010.
- W. M. Jadwisienczak, H. Tanaka, M. Kordesch, A. Khan, S. Kaya, and V. Vuppuluri, "Studies of Ni and Co Doped Amorphous AlN for Magneto-Optical Applications." *Mater. Res. Soc. Symp. Proc*., pp. 1202, 1202-I05-06, Jan. 2010.

Presentations/Posters:

- H. Tanaka, M. Bsatee, W. M. Jadwisienczak, "Zeeman Splitting of Ferromagnetic GaMnAs on InP Observed by Magnetic Circular Dichroism in Reflection Mode," *Electronic Materials Conference (EMC),* Columbus, Ohio, Summer 2015.
- K. Ando, H. Tanaka, V. Zayets, and H. Saito, "Magnetic band splitting of Ga1-xMnxAs estimated by magnetic circular dichroism (MCD) spectroscopy," *International Conference on Magnetism (ICM)*, Barcelona, Spain, Spring 2015.
- H. Tanaka,W. M. Jadwisienczak, H. Saito, V. Zayets, S. Yuasa, and K. Ando, "Localized s,p-d exchange interaction in ferromagnetic $Ga_{1-x}Mn_xAs$ observed by magnetic circular dichroism spectroscopy of L critical point," *Condense matter and surface science (CMSS) and Nanoscale Quantum Phenomena Institute (NQPI) joint*

session, Athens, Ohio, Spring 2014.

- H. Tanaka, W. M. Jadwisienczak, S. Kaya, G. Chen, C. Wan , M. Kordesch, "Magneto-optical Properties of Amorphous AlN Thin Films in-situ Doped with Nickel Clusters," *Electronic Materials Conference (EMC)*, Pittsburgh, Pennsylvania, Summer 2012.
- W. M. Jadwisienczak, H. Tanaka, G. Chen, M. Kordesch, A. Khan, "Morphology and Magnetio-optical Properties of Amorphous AlN Films Doped with Nickel," *Material Research Society (MRS) Fall meeting and Exhibit*, Massachusetts, Boston, Fall, 2010.
- H. Tanaka, and W. M. Jadwisienczak, M. Kordesch, A. Khan, S. Kaya, V. Vuppuluri,"Studies of Ni and Co Doped Amorphous AlN for Magneto-Optical Applications," *Material Research Society (MRS) Fall meeting and Exhibit*, Massachusetts, Boston, Fall 2009.

Thesis and Dissertation Services